Structure and Chain Exchange Kinetics of Block Copolymer Micelles in Selective Solvents

A DISSERTATION
SUBMITTED TO THE FACULTY OF THE GRADUATE SCHOOL
OF THE UNIVERSITY OF MINNESOTA
BY

Yuanchi Ma

IN PARTIAL FULFILLMENT OF THE REQUIREMENTS
FOR THE DEGREE OF
DOCTOR OF PHILOSOPHY

Timothy P. Lodge, Advisor

August 2017

Acknowledgements

First and foremost, I would like to thank my advisor, Prof. Timothy P. Lodge for all the advice and support in my five years as a graduate student. Tim's help is like the beacon shining in the mist, which guided me through countless difficulties that I have come across in my research, and eventually led me to the day of Ph.D. graduation. Especially, I am thankful for the tolerance that Tim showed to me during the time I was struggling with the synthesis and could not proceed with the project. This "learning-from mistakes" experience is invaluable to me, and I will always cherish it.

My past five years in the Lodge group has been very fruitful, and I also benefit a lot from the collaboration with many group members. Particularly, I would like to thank Dr. Yuanyan Gu for helping me getting started with my research, as well as Dr. Jie Lu, Dr. Dan Zhao and En Wang for the insightful discussion about the neutron scattering results in my project. I learned a lot from Dr. Soonyong So in interpreting DLS data, and I owed my thanks to his kind help in aligning the old DLS instrument. Dr. Jennifer Laaser, Dr. Megan Hoarfrost and Dr. Andrew Peters taught me a great deal about maths and physics concepts during our discussions. I would also like to thank current and former group members: Dr. Mohammad Savoji, Dr. Rob Hickey, Dr. Hongchul Moon, Dr. Sipei Zhang, Dr. Can Zhou, Dr. Lucas McIntosh, Dr. John McAllister, Dr. Chris Thurber, Dr. Matt Irwin, Dr. Ralm Ricarte, Dr. Amanda Maxwell, Itaru Asano, Boxin Tang, Yiming Zeng, Seyoung Jung, Ziang Li, Yaming Jiang, Peter Schmidt, Paul Chen, Sujay Chopade, Cecilia Hall, Aakriti Kharel, Wenjia Zhang, Shuyi Xie and various others for day to day conversations and discussions. Outside the Lodge group, I appreciate the help and useful advice from Dr. Paul Butler and Dr. Yimin Mao at NIST, and Dr. Lilin He at ORNL.

Finally, I would like to thank Tao Wang from the Hoye group, Yuan Fang from the Stein group, Haoyu Yu and Kaining Duanmu from the Truhlar group, and Danqing Deng

from the Department of Physics for their company during my five years in Minneapolis. Get-togethers on weekends and festivals have been the best recreation for me, and made me recover from the tiresome days of research.

Thank you all!

To My Family

Abstract

Block copolymers can self-assemble into various structures, such as micelles and vesicles. Previous studies have shown that single chain exchange is the main mechanism for block copolymer micelles to achieve equilibrium. In this study, a new lower critical micelle temperature (LCMT) system, poly(methyl methacrylate)-*block*-poly(*n*-butyl methacrylate) in two room temperature ionic liquids, 1-ethyl-3-methylimidazolium bis(trifluoromethylsulfonyl)imide and 1-butyl-3-methylimidazolium bis(trifluoromethylsulfonyl)imide was developed, and its chain exchange kinetics were investigated using time-resolved small-angle neutron scattering (TR-SANS). In order to probe the effect of the core block length, the corona block length and the solvent selectivity on the chain exchange rate, we synthesized two series of protonated and deuterated copolymers, one with identical core block length and one with identical corona block length, as well as systematically varied the Flory-Huggins interaction parameter χ by tuning the ratio of the two ionic liquids in the solvent. Notably, the results show that the solvent selectivity has a remarkable effect on the chain exchange rate, and therefore we proposed a more elaborate function of χ for the energy barrier of chain expulsion, which is rationalized by a calculation in the spirit of Flory−Huggins theory. Besides the kinetic study, complementary dynamic light scattering (DLS) and small-angle X-ray scattering (SAXS) experiments were also conducted to investigate the structure of micelles. Particular emphasis was placed on elucidating the scaling relationship between the micelle core radii and the degree of polymerization of the core block in the copolymers.

Table of Contents

List of Tables

List of Figures

Chapter 1
Introduction and Background

1.1. Overview

Equilibrium of block copolymer micelles has been a long-standing issue in polymer physics. Despite the fact that long time annealing can bring a system closer to its equilibrium state, however, much still remains unclear about the details of the micelle equilibration process.

In order to address this issue, the Lodge and Bates groups have conducted a number of researches on an upper critical micellization temperature (UCMT) system, poly(ethylene-*alt*-propylene)-*block*-poly(styrene) (PEP-*b*-PS) in squalane; the previous results demonstrated that micelle equilibration is primarily accomplished via single chain exchange among the micelles, and that the chain exchange rate is mainly governed by two factors: Rouse relaxation of the core blocks, and the activation barrier for the core block expulsion. Although these findings promoted a giant leap in the knowledge of micelle dynamics, more systems still need to be studied in order to determine whether the dependence of micelle chain exchange rate on the aforementioned factors is universal. Among all, lower critical micellization temperature (LCMT) systems are of greatest interest, because there has not been any study so far that covers this area. On the other hand, polymer-ionic liquid (IL) interactions is an emerging topic, which enables multiple applications, such as ion-conducting membranes. Therefore, we also seek to combine the study of micelle equilibration with that of the phase behavior of polymers in ILs.

In sum, in this study, we aim at developing a new LCMT system, with poly(methyl methacrylate)-*block*-poly(*n*-butyl methacrylate) (PMMA-*b*-PnBMA) as the copolymer micelles and two room-temperature ionic liquids, [EMIM][TFSI] and [BMIM][TFSI] as

the solvent. The chain exchange kinetics of this system is studied by time-resolved small-angle neutron scattering (TR-SANS). Our overarching goal is to determine how the chain exchange rate is affected by various factors, such as temperature, solvent selectivity, core and corona block length, and eventually find a way to estimate how far a given system is away from equilibrium.

1.2. Miscibility of Polymer in Ionic Liquid

Phase behavior of polymers in water and organic solvents has been extensively studied. Both UCST and LCST behavior has been observed in aqueous and organic systems. Most notably, polymer/organic solvent systems usually display a UCST[1–3] (with exceptions[4–6]), while an LCST is prevalent in polymer/water systems[7–10] (with exceptions[11]). The LCST behavior in aqueous systems reflects the impact brought by hydrogen bonding between polymer and water. The negative enthalpy of mixing can be easily understood, since the formation of hydrogen bonds is exothermic; the negative entropy of mixing is a result of the formation of cage-like ordered structures in the solvent.[12–15] For example, in the most well-known aqueous LCST system, poly(*N*-isopropylacrylamide) (PNIPAm)/water, water molecules form hydrated-shells around the isopropyl-groups, thereby leading to a negative entropy of mixing.[16,17]

Ionic liquids (ILs), often referred to as “molten salts”, are a special class of ionic compounds with bulky cations and anions. The bulkiness and flexibility of the cations and anions hinder the formation of lattices in ILs, therefore, ILs have melting points lower than room temperature. Compared with normal organic solvents, ILs have a number of desirable properties, such as non-volatility, high thermal stability, low toxicity, and decent electric conductivity.[18–20] These properties have led to various applications

based on ILs, such as polymer ion gels,[21–23] catalyst supports,[24,25] and dispersion media.[26–29]

Ionic liquids are often seen as the third class of solvents, because ILs have some shared characteristics of both water and organic solvents. ILs are similar to organic solvents in that the cations and anions that form ILs are mostly organic; however, they also resemble water in terms of hydrogen bond formation with solutes (for example, the 1,3-di-substituted imidazolium cations are able to form hydrogen bonds with poly(ethylene oxide)).[30,31] Furthermore, there are various interactions in ionic liquids, including Coulombic forces, hydrogen bonds, van der Waals interactions, and cation-π interactions. These unique characteristics give rise to both UCST and LCST behaviors in polymer/IL systems.

In the past two decades, Winterton *et al.* and Watanabe *et al.* have systematically studied polymer solubility in ionic liquids;[32–34] however, there is still a lack of theories that can precisely interpret or predict the solubility and phase behavior of polymer/IL systems. Noticeably, the Hildebrand solubility parameters often fail to work in polymer/IL systems, because these parameters are significantly affected by the Coulombic characters of ILs, while the solubility of a neutral polymer in ILs does not rely on the Coulombic interaction.[34] Batista *et al.* proposed to separate the Hildebrand solubility parameter (δ) of ionic liquids into a polar part (δ_P) and a nonpolar part (δ_{NP}), and only use the latter to account for the polymer/IL miscibility.[35] Similarly, some other authors proposed to use Hansen solubility parameter (δ_T) as the solubility scale,[36] in which $\delta_T = (\delta_D^2 + \delta_P^2 + \delta_H^2)^{1/2}$, and the three terms on the right side of the equation are the partial solubility parameters contributed from dispersion, polar and hydrogen-bonding interactions, respectively. Nevertheless, none of the attempts have been able to fully rationalize a number of cases, in which two ionic liquids with almost identical solubility

parameters have tremendous difference in the ability to dissolve a single polymer.[34] For example, [BMIM][PF_6] and [BMIM][BF_4] have the solubility parameter of 14.9 and 16.2 $cal^{1/2}cm^{-3/2}$,[37] respectively, but the former is miscible with PMMA (solubility parameter = 8.9 $cal^{1/2}cm^{-3/2}$),[38] while the latter is not. ([BMIM] is the cation, and stands for 1-butyl-3-methylimidazolium; the structure of the anions, [PF_6] and [BF_4], can be seen in Figure 1.1.)

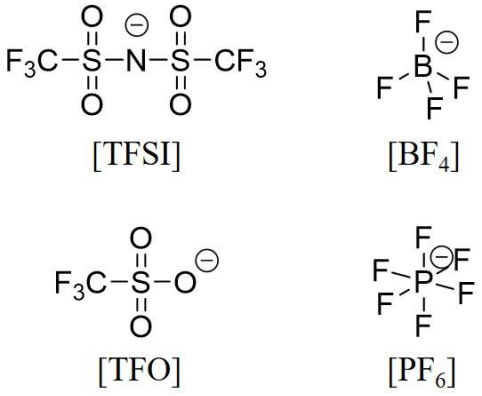

Figure 1.1. Chemical structures of the anions used in this section.

So far, the understanding of polymer/IL miscibility is largely based on empirical rules, as given below:

(1) The polymer solubility in ILs is mainly governed by the anions. For example, the solubility of poly(methyl methacrylate) (PMMA) in imidazolium-based ionic liquids follows the order of [TFSI] > [PF_6] > [TFO] > [BF_4] (chemical structures of these anions are given in Figure 1.1).[39]

(2) Hydrophilic and ionophilic polymers have the greatest solubility in ILs. For example, PEO can be dissolved in most imidazolium-based ionic liquids.[40]

(3) Polymers capable of forming strong intramolecular hydrogen bonds have poor solubility in ILs. For example, poly(acrylic acid) (PAA) is insoluble in nearly all ILs investigated.[34]

Interestingly, even within the same class of polymer, different phase behaviors, i.e., UCST, LCST, and complete miscibility in a broad temperature range, can all be observed in the same ionic liquid. A good example is poly(methacrylates) in 1-ethyl-3-methylimidazolium bis(trifluoromethylsulfonyl)imide ([EMIM][TFSI]). It is well-known that PMMA is soluble in [EMIM][TFSI];[21,34,39,41] however, as the alkyl chain length increases, different phase behaviors start to emerge. Lee and Lodge found that poly(*n*-butyl methacrylate) (PnBMA) has an LCST behavior in [EMIM][TFSI], presumably because of the favorable interaction between the ester group and imidazolium cations at low temerature;[42] similarly, the Watanabe group reported an LCST behavior in the poly(benzyl methacrylate) (PBzMA)/[EMIM][TFSI] system.[43] As the alkyl chain gets longer, such as in the case of poly(octadecyl methacylate) (PODMA), it displays a UCST behavior in [EMIM][TFSI], but for a different reason: high temperature breaks up the crystalline packing of the octadecyl tails, thus enhancing the solubility of PODMA in [EMIM][TFSI].[34]

Despite the huge impact of anions on the miscibility of polymer/ILs, cations also play an important role. Lee and Lodge demonstrated that the addition of 1-butyl-3-methylimidazolium bis(trifluoromethylsulfonyl)imide ([BMIM][TFSI]) into [EMIM][TFSI] can significantly increase the critical temperature of PnBMA in the ionic liquid mixture; and by changing from 100% [EMIM][TFSI] to 100% [BMIM][TFSI], the LCST can be varied by about 250 °C.[42,44] This finding provides a convenient method for tuning the selectivity of IL, that is, by tuning the alkyl chain length on the cation of IL. As the PnBMA in [EMIM][TFSI]/[BMIM][TFSI] is the system of interest studied in this thesis, it will be further described in the following chapters.

1.3. Block Copolymer Micelles: Thermodynamics

General Introduction to Block Copolymer Micelles

Block copolymers are composed of two or more different polymerized monomers in sequential order; their structures can be represented by "AAA−BBB−CCC−…". Specifically, the block copolymers with the structure of "$(A)_n$−$(B)_m$" are called diblock copolymers, which is the main topic of this dissertation. Because the two blocks in diblock copolymers are covalently linked, they will undergo microphase separation into A- and B-rich domains if they are not compatible with each other, which gives periodic nanostructures. The structures (body-centered cubic spheres, hexagonally packed cylinders, gyroid and lamellae) and the domain sizes are determined by the Flory-Huggins interaction parameter (χ_{AB}), the degree of polymerization (N_A, N_B), and the volume fraction of the two blocks (f_A, f_B).[45–47]

The addition of solvent (S) will render the system more complex. Here, we just limit the discussion within a simple case: the solvent is only selective to A block, *i.e.*, A is solvophilic, while B is solvophobic. Under such a scenario, the A block tends to increase its contact with the solvent, while the B block tends to collapse and self-aggregate in order to avoid contact with the solvent. In the dilute regime, the diblock copolymer (A-B) will preferably self-assemble into isolated structures, with A blocks stretching out to form the corona, and B blocks wrapped inside to form the core. This structure is known as a micelle. Compared with small surfactant micelles, block copolymer micelles are similar in structure, but have unique advantages, such as high stability, and tunable size. The applications of block copolymer micelles include drug delivery,[48] oil dispersants and viscosity modifiers.[49]

Micelle Structures and Morphology Transition

Polymorphism is an interesting feature of block copolymer micelles and thus attracts significant attention. The transition from spherical to cylindrical (worm-like) micelles, and that from cylindrical micelles to bilayer vesicles are observed in many polymer/solvent systems, such as poly(ethylene oxide)-*block*-poly(butadiene) (PEO-*b*-PB),[50−52] poly(styrene)-*block*-poly(acrylic acid) (PS-*b*-PAA)[53−56] in polar solvents, and poly(styrene)-*block*-poly(isoprene) (PS-*b*-PI) in alkanes.[57] As can be expected, the change in the volume ratio between the core and corona will result in a change of curvature, thereby inducing the morphology change. A geometric model to understand these morphology transitions was provided by Israelachvili *et al.*, similar to that for small surfactant micelles.[58] In this model, the critical packing parameter (p) is introduced to predict the shape of a micelle, defined by $p = v/(l_c \cdot a_0)$, where a_0 is the effective surface area of hydrophilic heads in a molecule, while v and l_c are the volume and the contour length of hydrophobic tails, respectively. $p = 1/3$ is the threshold for spherical micelles, above which micelles will adopt a cylindrical geometry; when p is further increased to be over 1/2, the cylindrical micelles will convert into bilayer membranes or vesicles. The transitions above are depicted in Figure 1.2. Note that p is just a rough estimate for the morphology boundaries in the case of block copolymer micelles; more exact stability ranges of spherical, cylindrical and bilayer morphologies are available elsewhere.[59]

Various studies have focused on tuning the shape of micelles, mainly by changing volume fraction of the core block (f_B) and solvent selectivity. The first approach has a direct effect on the critical packing parameter (p): by increasing the fraction of core block in a copolymer, v/l_c increases while a_0 is not affected, thus p goes up and results in the transition from spherical to cylindrical to bilayer structure. For example, Bates *et al.* characterized several PEO-*b*-PB samples with different PB fractions in aqueous solution,

and a clear tendency of transition from spherical micelle to bilayer vesicle is observed as f_B increases.[50]

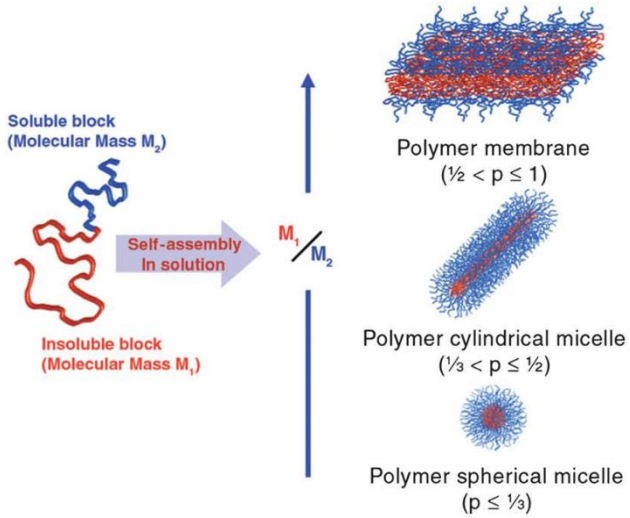

Figure 1.2. Schematic illustration of the effect of critical packing parameter (*p*) on the self-assembly of block copolymers (reproduced from Ref 60).

Solvent selectivity is another significant factor that determines micelle morphology. After the pioneering work of Eisenberg *et al.*, various other amphiphilic block copolymers are found to form micelles of different shapes as solvent selectivity changes.[61–63] Interfacial tension plays an important role in this process. By increasing the interfacial tension between solvent and the solvophobic core block, the total area of the core-corona interface has to decrease, which results in the decreasing curvature of the interface, as well as the transition from spherical micelles to cylindrical micelles to bilayer vesicles. For example, the Lodge group observed the morphology transition of one poly(styrene)-*block*-poly(dimethylsiloxane) (PS-*b*-PDMS) copolymer from spherical micelles to vesicles, simply by tuning the net selectivity of mixed solvents.[63]

Besides spheres, cylinders and bilayer structures which are commonly seen, diblock copolymers can also self-assemble into various other morphologies, including disk,[64] toroidal,[65] tubular micelles[66] and more complicated onion-like[67] and raspberry-like[68]

structures. It is noteworthy that the structures of block copolymer micelles are often highly path-dependent, due to the fact that some polymer/solvent systems are kinetically trapped in a metastable state immediately after the sample was prepared, especially when T_g of the core block is relatively high.

1.4. Block Copolymer Micelles: Kinetics

Like small surfactant micelles, block copolymer micelles have to go through some sort of chain redistribution in order to achieve thermodynamic equilibrium. Therefore, understanding the kinetics of block copolymer micelles is significant to the field of polymer physics. Multiple other topics, including the diffusion of polymer chains in ordered structures, and the formation mechanism of metastable states, are all closely related to the transport of polymer chains.

However, relatively few studies have so far been conducted on the equilibration mechanisms of block copolymer micelles. Compared with their small molecular weight counterparts, diblock copolymer micelles have much slower chain exchange dynamics for several reasons: (*i*) the high incompatibility between the core block and the solvent, embodied in the interaction parameter χ; (*ii*) large numbers of repeating units in the core block, N_{core}; (*iii*) crystallization and vitrification of the core block. All of the above factors contribute to the high activation barrier for the chain expulsion from the micelle and add to the difficulty of the experiments. Nevertheless, with the help of neutron scattering, a clearer, more general picture on micelle equilibration has emerged; a quantitative model has also been proposed and in part experimentally confirmed. In this section, a literature review on the recent development of block copolymer micelle kinetics will be provided. We will first discuss the difference between equilibration processes of small surfactant micelles and block copolymer micelles, then proceed with

the quantitative model developed by the Lodge and Bates groups, then discuss the problems that have not yet been fully resolved.

Equilibration of Small Surfactant and Block Copolymer Micelles

It is widely accepted that there are two separate relaxation processes in the formation of small surfactant micelles. The first is a fast process ($\tau_1 \sim 100\ \mu s$) that is attributed to the redistribution of surfactant micelles with different sizes; during this process, the total number of micelles does not change. The second process is relatively slower ($\tau_2 \sim 1 - 10$ *ms*), which is associated with the changes in both aggregation number and the total number of micelles (large micelles form and small "sub-micelles" dissolve).[69] The first quantitative analysis of the time constants of these two relaxation processes was given by Aniansson and Wall, in which they assumed that micelles can grow or diminish only by exchanging a single chain at a time (no fusion or fission). Based on the "stepwise" mechanism, they proposed that the rates of both processes are significantly affected by aggregation number and the distribution of aggregation number.[70–72]

Based on the Aniansson-Wall mechanism for small surfactant micelles, Halperin and Alexander proposed a similar scaling theory for block copolymers.[73] They pointed out that stepwise unimer exchange should be dominant, due to the high steric repulsion between coronas of two polymeric micelles, which hinders micelle fusion/fission. Dormidontova also proposed that the activation barrier of micelle fusion $U_{\text{fus}} \sim Q_1 Q_2^{1/2}$, where Q_1 and Q_2 are the aggregation numbers of the two micelles merged ($Q_1 \leq Q_2$).[74] This indicates that when the aggregation number is large, fusion/fission among micelles is not energetically favored.

As a complement of Halperin and Alexander's theory, Dormidontova calculated the activation barrier of unimer exchange and that of fusion/fission by a scaling approach,

and suggested that the fusion/fission pathway is only effective when the aggregation number of micelles is small, for example, at the early stage of micellization.[74] This calculation result has been supported by dissipative particle dynamics simulations.[75,76]

Before neutron scattering was used, a variety of other techniques have been utilized to study the kinetics of block copolymer micelles, which include stopped-flow method,[77] sedimentation,[78,79] temperature-jump (*T*-jump) light scattering,[80−84] non-radiative energy transfer and fluorescence-quenching,[85−91] and transmission electron microscopy.[92,93] Among the techniques above, *T*-jump light scattering and fluorescence quenching spectroscopy are most frequently used: the former mainly deals with the kinetics during micellization process, while the latter is mainly used to study the kinetics at or near equilibrium.

In a typical *T*-jump experiment, temperature is given an abrupt change across the critical micellization temperature (CMT), so that block copolymer unimers can form micelles, or micelles can dissolve; light scattering is used to monitor the change of micelle size as a function of time. By analyzing the scattering intensity, or the distribution of hydrodynamic radius of micelles, most authors observed two different stages in micellization process, as is predicted by Aniansson-Wall theory. As is shown in Figure 1.3a, the scattering intensity increases dramatically at the beginning of micellization (indicating the transformation from unimers to micelles), followed by a substantial decrease, owing to the reduction in the total number of micelles, according to Zana *et al.*[82] Honda and coworkers also observed a similar tendency, as shown in Figure 1.3b, in which a plateau exists, clearly indicating two relaxation processes.[80] Their results qualitatively agree with the assumption that micelle equilibration can be achieved via more than one pathway; however, there is still a lack of direct evidence of which mechanism actually governs the micellization process.

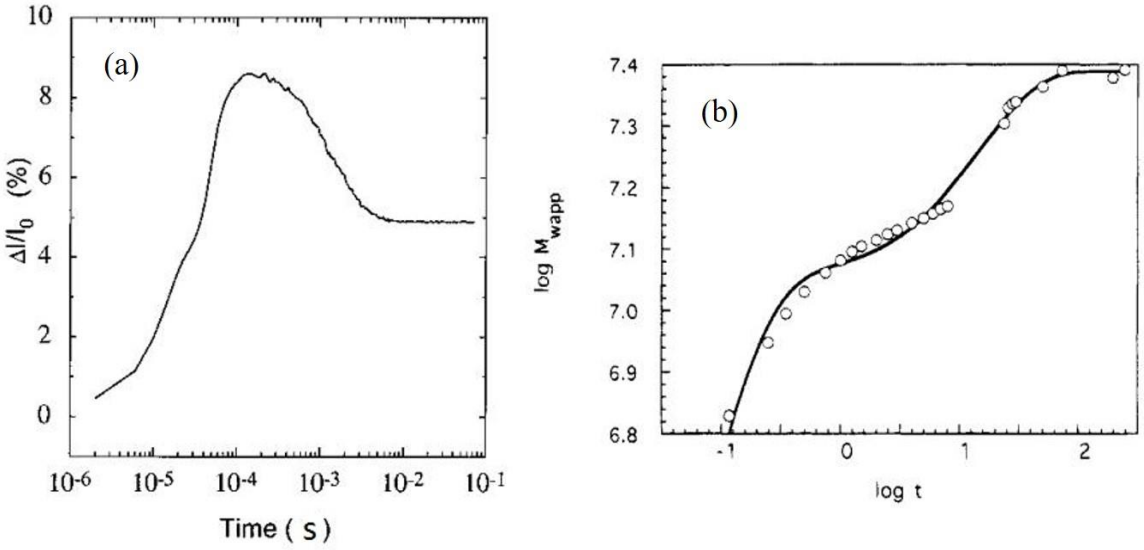

Figure 1.3. (a) Time dependence of the change in relative scattering intensity of PEO_{13}-*b*-PPO_{30}-*b*-PEO_{13} micelles in water after *T*-jump (final temperature = 40 °C, scattering angle = 90°, reproduced from Ref 82). (b) Time dependence of the apparent molecular weight ($M_{w,app}$) of PαMS-*b*-PVPA micelles in benzyl alcohol after *T*-jump (final temperature = 35 °C, reproduced from Ref 80).

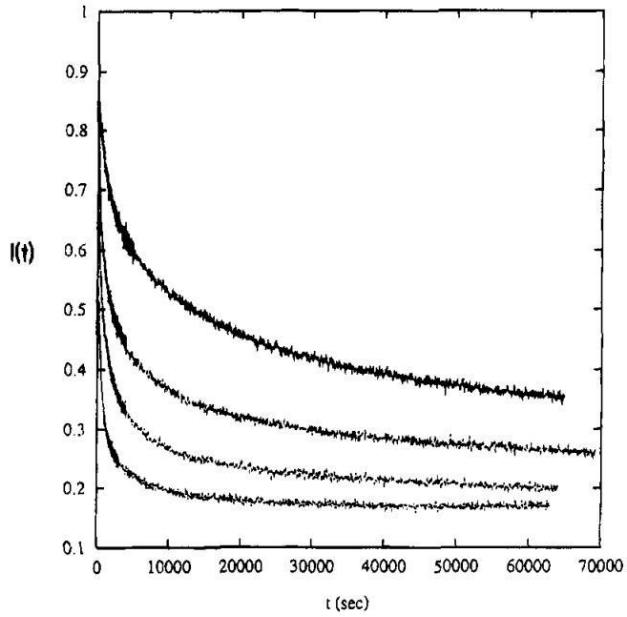

Figure 1.4. Normalized fluorescence emission of fluorophore-labeled PS-*b*-PEO at 338 nm in methanol/water = 9/1. The curves from top to bottom represent *T* = 25, 30, 35 and 40 °C, respectively (reproduced from Ref 87).

Fluorescence quenching spectroscopy, on the other hand, is typically used for investigating the chain redistribution among micelles near equilibrium. In a typical fluorescence quenching experiment, polymers are covalently labeled with donors (D) and acceptors (A). The micelles made up of D-chains and A-chains are mixed at $t = 0$, then the decrease in the donor fluorescence intensity is measured as a function of t. By fitting the donor fluorescence intensity, $I(t)$, against t, one can obtain a decay curve (in the form of exponential, double exponential, or others), which may shed light on how many pathways are present in the chain exchange process. A typical $I(t)$ plot is given in Figure 1.4.[87] The decay curves are fit to the following empirical equation:

$$\frac{I(t)}{I(0)} = 1 - \sum_{i=1}^{n} A_i \exp(-\frac{t}{\tau_i}) \qquad (1.1)$$

where n is the number of total possible pathways.

However, the fitting results from different authors are rather inconsistent. In fact, fluorescence methods have significant limitations: there are multiple quenching pathways other than non-radiative energy transfer from donors to acceptors. Therefore, more accurate methods are required to further investigate into chain exchange problems in block copolymer micelles.

TR-SANS and A Quantitative Model of Chain Exchange Kinetics

Small-angle neutron scattering (SANS) is a powerful tool for studying the structure and dynamics of systems at the nanometer scale. As the chain distribution among micelles can be reflected by the scattering intensity, neutron scattering works in a similar way to the fluorescence quenching spectroscopy mentioned above. A significant advantage for neutron scattering is that it does not require bulky fluorescence labels; the scattering intensity can be magnified by simply replacing some atoms with isotopes

(replacing hydrogen with deuterium, for example). The introduction of isotopes will not affect the chemical nature of the samples significantly.

In a typical time-resolved small-angle neutron scattering (TR-SANS) experiment, a contrast-matching strategy is used to study the chain distribution in micelles as a function of time. First, a pair of block copolymers — with protonated and (partially) deuterated core blocks — are synthesized. They are separately dissolved in the solvent in which they can form micelles; the solvent, water for example, is made up of a certain ratio of H_2O and D_2O in order to make its scattering length density exactly the same as the average of the protonated (H-) and deuterated (D-) core block (this isotopic mixture will be referred to as the "contrast-matched" solvent). Then, at $t = 0$, equal amounts of the H-micelle and D-micelle solutions (same concentration) are mixed, giving a 50-50 H- and D-micelle solution. Then as time passes, chain exchange takes place among the micelles, therefore, H- and D-chains tend to evenly distribute in all micelles. Finally, at $t = \infty$, all micelles will be composed of on average equal numbers of H- and D-chains, which has the same scattering length density as the contrast-matched solvent, thus making the coherent scattering intensity contributed by the micelle cores to be zero,. During the experiment, the observed scattering intensity should monotonically decrease with time, *i.e.*, $I_{max} = I(0)$ and $I_{min} = I(\infty)$. A relaxation function, $R(t)$, is then defined as:

$$R(t) = \sqrt{\frac{I(t) - I(\infty)}{I(0) - I(\infty)}} \tag{1.2}$$

which reflects the degree of chain exchange, with $0 \leq R(t) \leq 1$.[94]

It may not be straightforward to relate $R(t)$ to the degree of chain exchange; here we use a simple way to provide a brief derivation of $R(t)$. Imagine that there are only two micelles; at $t = 0$, one is completely protonated and the other is completely deuterated. Then we can define a degree of chain exchange, $x(t)$, which indicates the percentage of D-chains in the original H-micelle. Assuming no free chains in the solvent, then the

percentage of H-chains in the original D-micelle is also $x(t)$. Naturally, $x(t) = 0$ means that there is no exchange, and $x(t) = 0.5$ indicates complete exchange.

Now, we use ρ_H, ρ_D and ρ_{sol} for the scattering length density of the H-micelle core, D-micelle core, and the solvent. As the neutron scattering intensity is proportional to the square of the difference between the scattering length density (ρ) of micelle core and the surrounding (solvent), therefore we have:

$$I(t) = 2A[\rho(t) - \rho_{sol}]^2 = 2A\{[1 - x(t)]\rho_H + x(t)\rho_D - \rho_{sol}\}^2 \quad (1.3)$$

The "2" in coefficient indicates that there are two micelles in the system, and they contribute equally to the scattering intensity. As mentioned previously, the solvent is contrast-matched, which means

$$\rho_{sol} = \frac{\rho_H + \rho_D}{2} \quad (1.4)$$

Therefore, by combining eqs. 1.3 and 1.4, $I(t)$ can be expressed as

$$I(t) = 2A\{[x(t) - \frac{1}{2}](\rho_D - \rho_H)\}^2 \quad (1.5)$$

Specifically, at $t = 0$, $x(t) = 0$; at $t = \infty$, $x(t) = 1/2$. Therefore, it can be easily obtained that $I(0) = 0.5A(\rho_D - \rho_H)^2$, and $I(\infty) = 0$. As we already have all the three expressions — $I(t)$, $I(0)$ and $I(\infty)$, we can simplify the relaxation function, $R(t)$, as:

$$R(t) = \sqrt{\frac{I(t) - I(\infty)}{I(0) - I(\infty)}} = 2[\frac{1}{2} - x(t)] = 1 - 2x(t) \quad (1.6)$$

From eq. 1.6, we can easily see that the relaxation function $R(t)$ is related to the degree of chain exchange x(t), with a simple, linear dependence. The Richter group first used $R(t)$ to interpret their TR-SANS data,[94] and this method has been used in all related micelle equilibration studies henceforth.

As the typical block copolymer equilibration process is orders of magnitude slower than in small surfactant micelles, in some of the earlier studies, no chain exchange was observed with time-resolved small-angle neutron scattering (TR-SANS), even though the

samples were annealed for long periods of time.[95,96] It was not until 2001 that Richter *et al.* first observed chain exchange in PEP-*b*-PEO/DMF/H_2O system using TR-SANS.[97] According to Halperin and Alexander's theory, when the system is near equilibrium, *i.e.*, the aggregation number of micelles does not change with time, there should be only one process — single chain exchange, and $R(t)$ will follow a single exponential decay, represented by $R(t) \sim \exp(-t/\tau)$.[73] However, in Richter's studies, all $R(t)$'s are found to follow a quasi-logarithmic time dependence, *i.e.*, $R(t) \sim \ln(t)$.[94,97–100] At first, Richter *et al.* explained this dramatic difference in terms of an "unknown slower mechanism" that has not been predicted by previous theories.[97] Later on, after considering dispersity and ruling it out, the same authors concluded that the logarithmic time dependence is resulted from the coupling between the internal conformation dynamics of the chains and the chain expulsion process.[99,100]

In 2010, Choi and co-workers studied the micelle equilibration process of a series of PEP-*b*-PS diblock copolymers in squalane, and observed a similar logarithmic time dependence for $R(t)$.[101] This finding, together with previous results obtained by the Richter group, strongly suggests that this logarithmic time dependence should be a universal feature for all block copolymer micelles in dilute solution, regardless of the nature of the polymer and the solvent. Choi *et al.* established the first numerical model,[101] that not only successfully explains the apparent logarithmic time dependence, but also provides a clear physical picture to the micelle equilibration process:

$$R(t) = \int P(N_{core}) \exp[-t\frac{6\pi^2 kT}{N_{core}^2 b^2 \zeta} \exp(-\alpha\chi N_{core})]\mathrm{d}N_{core} \qquad (1.7)$$

where N_{core}, k, T, b, ζ, and α are the degree of polymerization of the core block, Boltzmann constant, temperature, statistical segment length of the core block, monomeric friction coefficient of the core block, and a dimensionless prefactor, respectively. $P(N_{\mathrm{core}})$ is the Schulz-Zimm distribution of the core block,[102] defined as:

$$P(N_i) = \frac{z^{z+1}}{\Gamma(z+1)} \frac{N_i^{z-1}}{N_n^z} \exp(-\frac{zN_i}{N_n}) \tag{1.8}$$

in which $z = [(N_w/N_n) - 1]^{-1}$, and Γ is the gamma function.

According to eq. 1.7, the core block length (N_{core}) has a remarkable effect on $R(t)$, because the dependence of $R(t)$ on N_{core} is an "exponential of exponential". Therefore, a small dispersity on N_{core} can result in a broad distribution of $R(t)$, which readily interprets why $R(t)$ has a much more stretched time dependence than the predicted single exponential decay. Within the outer exponential, the term can be seen as $(-t/\tau_{exp})$, where $\tau_{exp} = (N_{core}^2 b^2 \zeta / 6\pi^2 kT) \cdot \exp(\alpha\chi N_{core})$ is the chain expulsion time constant. The first part, $(N_{core}^2 b^2 \zeta / 6\pi^2 kT)$, is the Rouse relaxation time of the core block, and has unit of seconds; the dimensionless second part, $\exp(\alpha\chi N_{core})$, accounts for the activation barrier. For the first time, this model illustrated the role of Rouse relaxation in the micelle equilibration process, and it unambiguously pointed out that the "internal conformation dynamics" proposed by Richter *et al.* is essentially related to Rouse dynamics. Overall, this model gives satisfactory results in fitting the experimental data of TR-SANS (see Figure 1.5).

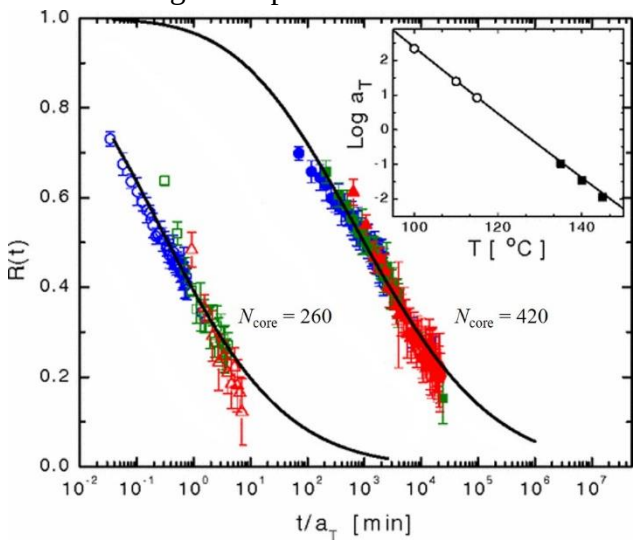

Figure 1.5. Fitting of TR-SANS data to eq. 1.7 (adapted from Ref 101).

With the advent of the new model, the Lodge and Bates groups and the Richter group successfully addressed some questions concerning the mechanism of micelle equilibration. In 2011, Choi *et al.* discovered that the chain exchange rate in ordered diblock copolymer micelles is almost 10 times slower than that in dilute solution, suggesting that $R(t)$ should have some concentration dependence.[103] In 2012, Zinn *et al.* observed that $R(t)$ goes back to an exponential time dependence, when polydispersity is eliminated from the system, *i.e.*, by using monodisperse oligomers as the core block.[104] In 2013, Lu *et al.* confirmed by a "long chain-short chain hybridized micelle" experiment that single chain exchange is the predominant mechanism in micelle equilibration process.[105,106] In 2015, Lu *et al.* investigated the effect of block copolymer architecture, and found that the chain exchange rate generally followed the order of PEP-*b*-PS-*b*-PEP > PEP-*b*-PS > PS-*b*-PEP-*b*-PS (PEP is the micelle corona and PS is the core). Notably, they also observed some cooperative effect in the two corona blocks (in the case of PEP-*b*-PS-*b*-PEP) and in the two core blocks (in the case of PS-*b*-PEP-*b*-PS), which indicates that the removal of covalently connected core blocks from micelle core is not an independent process.[107] In a more recent paper by Zinn *et al.*, the corona length dependence of the micelle chain exchange rate was also elaborated.[108] Significant experimental findings in this field up to 2015 are summarized in Table 1.1, listed in chronological order.

Table 1.1. Main achievements in the study of micelle chain exchange kinetics

Year	Systems studied	Conclusion	Ref.
2001	PEP-*b*-PEO in DMF	Chain exchange was observed by TR-SANS; there seemed to be more than one relaxation processes.	97
2004	PEP-*b*-PEO in DMF/H_2O	Lower interfacial tension between the core and the solvent can facilitate the chain exchange.	98, 99
2006	PEP-*b*-PEO in DMF/H_2O PS-*b*-PB in hexane	The relaxation function, R(t), followed a quasi-logarithmic time dependence, regardless of the system.	94, 100
2007	PS-*b*-PB and PB-*b*-PS-*b*-PB in *n*-alkanes	The triblock exchanges faster due to the cooperative effect of the two PB corona chains.	109
2010	PEP-*b*-PS in squalane	The first quantitative model with clear physical meaning was proposed.	101
2011	PEP-*b*-PS in squalane	Chain exchange in ordered micelles is significantly slower than that in dilute solution, possibly because high concentration of corona chains impose further barrier on chain expulsion.	103
2011	PEP-*b*-PEO in DMF/H_2O	The morphology of micelles does not play a significant role on chain exchange kinetics.	110
2012	PEO-*b*-C_n in H_2O [a]	The logarithmic time dependence of $R(t)$ originates from dispersity.	104
2013	PEP-*b*-PS in squalane	Single chain exchange is the predominant mechanism in micelle equilibration process.	105, 106
2015	PEP-*b*-PS-*b*-PEP and PS-*b*-PEP-*b*-PS in squalane	The triblock with two corona blocks has much faster kinetics than the diblock, while the triblock with two core blocks has much slower kinetics.	107

[a] C_n represents a monodisperse alkyl chain with n = 18 – 30.

Open Questions

In the last two decades, although the understanding of polymer micelle equilibration kinetics has been advanced considerably, there are still many questions that remain unsolved. Also, it is worth noticing that eq. 1.7 is not a panacea, since it does not include all the factors that can affect the chain exchange rate. For example, eq. 1.7 does not anticipate a concentration dependence on $R(t)$, which proves to be incorrect, since the ordered packing of the micelles will significantly slow down the chain exchange kinetics.[103] Besides concentration, there are various other factors on which the exact dependence of $R(t)$ is not completely understood. In this section, we will briefly discuss two of these factors: the activation barrier, and the corona block length.

The activation barrier reflects the enthalpic increment when a chain is pulled out from the micelle core and enters the solvent. According to eq. 1.7, this barrier is proportional to χN_{core}. In Halperin and Alexander's original theory, they made an educated guess of $\gamma a^2 N_{\text{core}}^{2/3}/kT$ as the activation barrier (in which γ and a are the interfacial tension between core and corona, and the statistical segment length of the core block), because they assumed that the core blocks adapted a rather collapsed conformation when exiting the core.[73] This apparent discrepancy requires further research into more systems, in order to determine which N_{core} dependence is correct. On the other hand, for the Flory-Huggins interaction parameter χ, both Halperin-Alexander theory and eq. 1.7 assumed a linear dependence. But if we take a further look into this issue, some unrealistic scenario will emerge — χN_{core} can only be zero when $\chi = 0$, which almost never happens. In fact, when χ is close to 0.5, there should be no activation barrier, since the solvent is already theta for the core block (and therefore, there are no micelles). Therefore, a system with tunable solvent selectivity is required for the purpose of

studying the χ dependence, and χ between the core and the solvent needs to be measured independently.

The effect of corona block length on the chain exchange rate is another topic of interest. Choi's model does not include any term of N_{corona}, since the effect of corona block is very little compared with that brought by N_{core}. But is this effect really negligible? Zinn *et al.* recently reported that the chain exchange kinetics slows down with the increase of corona block length, and the characteristic chain expulsion time, $\tau_0 \sim N_{corona}^{9/5}$; the authors attributed this effect to the increase of time consumed during the core block travelling through the thicker corona region.[108] Curiously, in the work done by Lu, Bates and Lodge on PEP-*b*-PS/squalane system, the opposite trend was observed.[111] Therefore, whether the corona block has a positive or negative effect on the chain pull-out process is still controversial, and thus will require further measurements to assess more fully.

1.5. Thesis Outline

In the previous sections, I have briefly summarized the background and history of the chain exchange study, as well as put forward some fundamental questions that need to be answered. Apart from the micelle equilibration kinetics, my thesis also covers other related topics of block copolymer micelles, such as micelle structure and the scaling relationship between the core radius, corona thickness and degree of polymerization of the core block.

In Chapter 2, synthesis of PMMA-*b*-PnBMA block copolymers is presented. In order to prepare block copolymers with narrowly distributed molecular weight, different polymerization methods and monomer addition orders were tried. By sequential radical addition-fragmentation chain-transfer (RAFT) polymerization starting from methyl

methacrylate, PMMA-*b*-PnBMA diblocks with dispersity ($Đ$) < 1.15 were synthesized, and characterized by nuclear magnetic resonance (NMR) spectroscopy, size exclusion chromatography (SEC) and matrix-assisted laser desorption/ionization mass spectroscopy (MALDI-MS).

Chapter 3 serves as an introduction part of the fundamentals of scattering techniques, including dynamic light scattering (DLS), small-angle X-ray scattering (SAXS) and small-angle neutron scattering (SANS).

In Chapter 4 and Chapter 5, DLS and SAXS are conducted on PMMA-*b*-PnBMA micelles in solvent mixtures of [EMIM][TFSI] and [BMIM][TFSI]. Specifically, Chapter 4 focuses on the scaling relationship between the micelle core radius, the corona thickness and the degree of polymerization of the core block; the micelle samples described in Chapter 4 are studied with the solvent composition being kept constant, *i.e.*, using only [EMIM][TFSI] as the solvent. In Chapter 5, the solvent composition becomes another variable, and the micelle core radius and hydrodynamic radius distribution are studied as a function of temperature as well as the weight percentage of [BMIM][TFSI].

In Chapter 6, the chain exchange kinetics of PMMA-*b*-PnBMA micelles in ionic liquids are investigated using TR-SANS. By carefully tuning the core block lengths and the solvent selectivity, the time scale of a typical chain exchange measurement is controlled within the range of tens of minutes to several hours. After data reduction, the time-temperature superposed $R(t)$ is fit to the aforementioned model, and the fitting results unambiguously illustrate the significant effect of the solvent selectivity on the chain exchange rate. Interestingly, the results show that the activation barrier is not simply proportional to χ. We propose a more elaborate function of χ for the activation barrier, which is rationalized by a calculation in the spirit of Flory-Huggins theory. In

addition, the effect of corona block length and micelle concentration on $R(t)$ is also investigated, and the results are compared with those obtained in other systems.

In Chapter 7, a summary of this dissertation is given, with suggestion for future work.

1.6. References

(1) Hashizume, J.; Teramoto, A.; Fujita, H. *J. Polym. Sci. Part B* **1981**, *19*, 1405-1422.

(2) Nakajima, A.; Hamada, F.; Hayashi, S. *J. Polym. Sci. Part C* **1966**, *15*, 285-294.

(3) Fox, T. G. *Polymer* **1962**, *3*, 111-128.

(4) Seuring, J.; Agarwal, S. *Macromolecules* **2012**, *45*, 3910−3918.

(5) Shimada, N.; Ino, H.; Maie, K.; Nakayama, M.; Kano, A.; Maruyama, A. *Biomacromolecules* **2011**, *12*, 3418−3422.

(6) Lee, H.-N.; Rosen, B. M.; Fenyvesi, G.; Sunkara, H. B. *J. Polym. Sci. Part A* **2012**, *50*, 4311-4315.

(7) Heskins, M.; Guillet, J. E. *J. Macromol. Sci. Part A* **1968**, *2*, 1441-1455.

(8) Ward, M. A.; Georgiou, T. K. *J. Polym. Sci. Part A* **2010**, *48*, 775–783.

(9) Maeda, Y.; Nakamura, T.; Ikeda, I. *Macromolecules* **2002**, *35*, 217-222.

(10) Schild, H. G.; Tirrell, D. A. *J. Phys. Chem.* **1990**, *94*, 4352-4356.

(11) Seno, K.; Kanaoka, S.; Aoshima, S. *J. Polym. Sci. Part A* **2008**, *46*, 5724-5733.

(12) Luan, C.-H.; Harris, R. D.; Prasad, K. U.; Urry, D. W. *Biopolymers* **1990**, *29*, 1699-1706.

(13) Luan, C.-H.; Urry, D. W. *J. Phys. Chem.* **1991**, *95*, 7896-7900.

(14) Luan, C.-H.; Parker, T. M.; Prasad, K. U.; Urry, D. W. *Biopolymers* **1991**, *31*, 465-475.

(15) Tanford, C. *The Hydrophobic Effect: Formation of Micelles and Biological Membranes, 2nd ed.*, John Wiley & Sons: New York, 1980.

(16) Otake, K.; Inomata, H.; Konno, M.; Saito, S. *Macromolecules* **1990**, *23*, 283-289.

(17) Inomata, H.; Goto, S.; Saito, S. *Macromolecules* **1990**, *23*, 4887-4888.

(18) Welton, T. *Chem. Rev.* **1999**, *99*, 2071-2083.

(19) Holbrey, J. D.; Seddon, K. R. *Clean Prod. Process* **1999**, *1*, 223-236.

(20) Wasserscheid, P.; Keim, W. *Angew. Chem. Int. Ed.* **2000**, *39*, 3772-3789.

(21) Susan, M. A. B. H.; Kaneko, T.; Noda, A.; Watanabe, M. *J. Am. Chem. Soc.* **2005**, *127*, 4976-4983.

(22) He, Y.; Boswell, P. G.; Bühlmann, P.; Lodge, T. P. *J. Phys. Chem. B* **2007**, *111*, 4645-4652.

(23) Lee, J.; Panzer, M. J.; He, Y.; Lodge, T. P.; Frisbie, C. D. *J. Am. Chem. Soc.* **2007**, *129*, 4532-4533.

(24) Mehnert, C. P. *Chem. Eur. J.* **2005**, *11*, 50-56.

(25) Riisager, A.; Fehrmann, R.; Haumann, M.; Wasserscheid, P. *Eur. J. Chem.* **2006**, *12*, 695-706.

(26) Phillips, D. M.; Drummy, L. F.; Conrady, D. G.; Fox, D. M.; Naik, R. R.; Stone, M. O.; Trulove, P. C.; De Long, H. C.; Mantz, R. A. *J. Am. Chem. Soc.* **2004**, *126*, 14350-14351.

(27) Xie, H. B.; Li, S. H.; Zhang, S. B. *Green Chem.* **2005**, *7*, 606-608.

(28) Forsyth, S. A.; MacFarlane, D. R.; Thomson, R. J.; Itzstein, M. *Chem. Commun.* **2002**, 714-715.

(29) Fukushima, T.; Kosaka, A.; Ishimura, Y.; Yamamoto, T.; Takigawa, T.; Ishii, N.; Aida, T. *Science* **2003**, *300*, 2072-2074.

(30) Costa, L. T.; Ribeiro, M. C. C. *J. Chem. Phys.* **2006**, *124*, 184902.

(31) Lee, H.-N.; Lodge, T. P. *J. Phys. Chem. Lett.* **2010**, *1*, 1962-1966.

(32) Winterton, N. *J. Mater. Chem.* **2006**, *16*, 4281-4293.

(33) Ueki, T.; Watanabe, M. *Macromolecules* **2008**, *41*, 3739-3749.

(34) Ueki, T.; Watanabe, M. *Bull. Chem. Soc. Jpn.* **2012**, *85*, 33-50.

(35) Batista, M. L. S.; Neves, C. M. S. S.; Carvalho, P. J.; Gani, R.; Coutinho, J. A. P. *J. Phys. Chem. B* **2011**, *115*, 12879-12888.

(36) Weerachanchai, P.; Wong, Y.; Lim, K. H.; Tan, T. T. Y.; Lee, J.-M. *Chem. Phys. Chem.* **2014**, *15*, 3580-3591.

(37) Swiderski, K.; McLean, A.; Gordon, C. M.; Vaughan, D. H. *Chem. Commun.* **2004**, 2178-2179.

(38) Brandrup, J.; Immergut, E. H.; Grulke, E. A. *Polymer Handbook*, 4th ed., Wiley-Interscience: New Jersey, 1999.

(39) Ueno, K.; Fukai, T.; Nagatsuka, T.; Yasuda, T.; Watanabe, M. *Langmuir* **2014**, *30*, 3228-3235.

(40) Miranda, D. F. *Interactions and Morphology of Triblock Copolymer - Ionic Liquid Mixtures and Applications for Gel Polymer Electrolytes*. PhD Dissertation, University of Minnesota, 2012.

(41) Ueno, K.; Inaba, A.; Kondoh, M.; Watanabe, M. *Langmuir* **2008**, *24*, 5253-5259.

(42) Lee, H.-N.; Lodge, T. P. *J. Phys. Chem. B* **2011**, *115*, 1971-1977.

(43) Ueki, T.; Watanabe, M. *Langmuir* **2007**, *23*, 988-990.

(44) Hoarfrost, M. L.; He, Y.; Lodge, T. P. *Macromolecules* **2013**, *46*, 9464-9472.

(45) Leibler, L. *Macromolecules* **1980**, *13*, 1602-1617.

(46) Bates, F. S. *Science* **1991**, *251*, 898-905.

(47) Bates, F. S.; Fredrickson, G. H. *Physics Today* **1999**, *52*, 32-38.

(48) Kataoka, K.; Harada, A.; Nagasaki, Y. *Adv. Drug Delivery Rev.* **2001**, *47*, 113-131.

(49) Schouten, M.; Dorrepaal, J.; Stassen, W. J. M.; Vlak, W. A. H. M.; Mortensen, K. *Polymer* **1989**, *30*, 2038–2046.

(50) Won, Y. Y.; Brannan, A. K.; Davis, H. T.; Bates, F. S. *J. Phys. Chem. B* **2002**, *106*, 3354-3364.

(51) Zheng, Y.; Won, Y. Y.; Bates, F. S.; Davis, H. T.; Scriven, L. E.; Talmon, Y. *J. Phys. Chem. B* **1999**, *103*, 10331-10334.

(52) Won, Y. Y.; Davis, H. T.; Bates, F. S. *Science* **1999**, *283*, 960-963.

(53) Zhang, L.; Eisenberg, A. *Science* **1995**, *268*, 1728-1731.

(54) Zhang, L.; Eisenberg A. *J. Am. Chem. Soc.* **1996**, *118*, 3168-3181.

(55) Zhang, L.; Shen, H.; Eisenberg, A. *Macromolecules* **1997**, *30*, 1001-1011.

(56) Shen, H.; Zhang, L.; Eisenberg, A. *J. Phys. Chem. B* **1997**, *101*, 4697-4708.

(57) LaRue, I.; Adam, M.; Zhulina, E. B.; Rubinstein, M.; Pitsikalis, M.; Hadjichristidis, N.; Ivanov, D. A.; Gearba, R. I.; Anokhin, D. V.; Sheiko, S. S. *Macromolecules* **2008**, *41*, 6555−6563.

(58) Israelachvili, J. N.; Mitchell, D. J.; Ninham, B. W. *J. Chem. Soc. Faraday Trans.* **1976**, *72*, 1525-1568.

(59) Zhulina, E. B.; Adam, M.; LaRue, I.; Sheiko, S. S.; Rubinstein, M. Macromolecules 2005, 38, 5330-5351.

(60) Holder, S. J.; Sommerdijk, N. A. J. M. *Polym. Chem.* **2011**, *2*, 1018-1028.

(61) Yu. Y.; Zhang, L.; Eisenberg, A. *Macromolecules* **1998**, *31*, 1144-1154.

(62) Zhu, J. T.; Yu, H. Z.; Jiang, W. *Polymer* **2005**, *46*, 11962-11968.

(63) Abbas, S.; Li, Z.; Hassan, H.; Lodge, T. P. *Macromolecules* **2007**, *40*, 4048-4052.

(64) Edmonds, W. F.; Li, Z.; Hillmyer, M. A.; Lodge, T. P. *Macromolecules* **2006**, *39*, 47, 4526-4530.

(65) LaRue, I.; Adam, M.; Pitsikalis, M.; Hadjichristidis, N.; Rubinstein, M.; Sheiko, S. S. *Macromolecules* **2006**, *39*, 309-314.

(66) Shen, H.; Eisenberg, A. *Macromolecules* **2000**, *33*, 2561-2572.

(67) Talingting, M. R.; Munk, P.; Webber, S. E. *Macromolecules* **1999**, *32*, 1593-1601.

(68) Jiang, X.; Wang, Y.; Zhang, W.; Zheng, P.; Shi, L. *Macromol. Rapid Commun.* **2006**, *27*, 1833-1837.

(69) Kahlweit, M. *J Colloid Interface Sci.* **1982**, *90*, 92-99.

(70) Aniansson, E. A. G.; Wall, S. N. *J. Phys. Chem.* **1974**, *78*, 1024-1030.

(71) Aniansson, E. A. G.; Wall, S. N. *J. Phys. Chem.* **1975**, *79*, 857-858.

(72) Aniansson, E. A. G.; Wall, S. N.; Almgren, M.; Hoffmann, H.; Kielmann, I.; Ulbricht, W.; Zana, R.; Lang, J.; Tondre, C. *J. Phys. Chem.* **1976**, *80*, 905-922.

(73) Halperin, A.; Alexander, S. *Macromolecules* **1989**, *22*, 2403-2412.

(74) Dormidontova, E. E. *Macromolecules* **1999**, *32*, 7630-7644.

(75) Li, Z.; Dormidontova, E. E. *Macromolecules* **2010**, *43*, 3521-3531.

(76) Li, Z.; Dormidontova, E. E. *Soft Matter* **2011**, *7*, 4179-4188.

(77) Bednáŕ, B.; Edwards, K.; Almgren, M.; Tormod, S.; Tuzar, Z. *Makromol. Chem. Rapid Commun.* **1988**, *9*, 785-790.

(78) Pacovská, M.; Procházka, K.; Tuzar, Z.; Munk, P. *Polymer* **1993**, *34*, 4585-4588.

(79) Tian, M.; Qin, A.; Ramireddy, C.; Webber, S. E.; Munk, P.; Tuzar, Z.; Procházka, K. *Langmuir* **1993**, *9*, 1741-1748.

(80) Honda, C.; Hasegawa, Y.; Hirunuma, R.; Nose, T. *Macromolecules* **1994**, *27*, 7660-7668.

(81) Honda, C.; Abe, Y.; Nose, T. *Macromolecules* **1996**, *29*, 6778-6785.

(82) Michels, B.; Waton, G.; Zana, R. *Langmuir* **1997**, *13*, 3111-3118.

(83) Goldmints, I.; Holzwarth, J. F.; Smith, K. A.; Hatton, T. A. *Langmuir* **1997**, *13*, 6130-6134.

(84) Kositza, M. J.; Rees, G. D.; Holzwarth, A.; Holzwarth, J. F. *Langmuir* **2000**, *16*, 9035-9041.

(85) Procházka, K.; Bednáŕ, B.; Mukhtar, E.; Svoboda, P.; Trnena, J.; Almgren, M. *J. Phys. Chem.* **1991**, *95*, 4563-4568.

(86) Wang, Y.; Balaji, R.; Quirk, R. P.; Mattice, W. L. *Polym. Bull.* **1992**, *28*, 333-338.

(87) Wang, Y.; Kausch, C. M.; Chun, M.; Quirk, R. P.; Mattice, W. L. *Macromolecules* **1995**, *28*, 904-911.

(88) Liu, G. *Can. J. Chem.* **1995**, *73*, 1995-2003.

(89) Smith, C. K.; Liu, G. *Macromolecules* **1996**, *29*, 2060-2067.

(90) Underhill, R. S.; Ding, J.; Birss, V. I.; Liu, G. *Macromolecules* **1997**, *30*, 8298-8303.

(91) van Stam, J.; Creutz, S.; Schryver, F. C. D.; Jérôme, R. *Macromolecules* **2000**, *33*, 6388-6395.

(92) Esselink, F. J.; Dormidontova, E.; Hadziioannou, G. *Macromolecules* **1998**, *31*, 2925-2932.

(93) Esselink, F. J.; Dormidontova, E.; Hadziioannou, G. *Macromolecules* **1998**, *31*, 4873-4878.

(94) Lund, R.; Willner, L.; Stellbrink, J.; Lindner, P.; Richter, D. *Phys. Rev. Lett.* **2006**, *96*, 068302.

(95) Won, Y. Y.; Davis, H. T.; Bates, F. S. *Macromolecules* **2003**, *36*, 953-955.

(96) Meli, L.; Santiago, J. M.; Lodge, T. P. *Macromolecules* **2010**, *43*, 2018-2027.

(97) Willner, L.; Poppe, A.; Allgaier, J.; Monkenbusch, M.; Richter, D. *Europhys. Lett.* **2001**, *55*, 667-673.

(98) Lund, R.; Willner, L.; Stellbrink, J.; Radulescu, A.; Richter, D. *Physica B* **2004**, *350*, 909-912.

(99) Lund, R.; Willner, L.; Richter, D.; Dormidontova, E. E. *Macromolecules* **2006**, *39*, 4566-4575.

(100) Lund, R.; Willner, L.; Stellbrink, J.; Richter, D. *Physica B* **2006**, *385*, 735-737.

(101) Choi, S.; Lodge, T. P.; Bates, F. S. *Phys. Rev. Lett.* **2010**, *104*, 047802.

(102) Zimm, B. H. *J. Chem. Phys.* **1948**, *16*, 1093-1099.

(103) Choi, S.; Lodge, T. P.; Bates, F. S. *Macromolecules* **2011**, *44*, 3594-3604.

(104) Zinn, T.; Willner, L.; Lund, R.; Pipich, V.; Richter, D. *Soft Matter* **2012**, *8*, 623-626.

(105) Lu, J.; Choi, S.; Lodge, T. P.; Bates, F. S. *ACS Macro Lett.* **2012**, *1*, 982-985.

(106) Lu, J.; Lodge, T. P.; Bates, F. S. *ACS Macro Lett.* **2013**, *2*, 451-455.

(107) Lu, J.; Bates, F. S.; Lodge, T. P. *Macromolecules* **2015**, *48*, 2667-2676.

(108) Zinn, T.; Willner, L.; Pipich, V.; Richter, D.; Lund, R. *ACS Macro Lett.* **2016**, *5*, 884-888.

(109) Lund, R.; Willner, L.; Richter, D.; Iatrou, H.; Hadjichristidis, N.; Lindner, P. *J. Appl. Cryst.* **2007**, *40*, 327-331.

(110) Lund, R.; Willner, L.; Pipich, V.; Grillo, I.; Lindner, P.; Colmenero, J.; Richter, D. *Macromolecules* **2011**, *44*, 6145-6154.

(111) Lu, J. *Mechanisms of Chain Exchange in Block Copolymer Micelles*. PhD Dissertation, University of Minnesota, 2015.

Chapter 2
Polymer Synthesis and Characterization

Most micelle equilibration studies have been conducted on upper critical micellization temperature (UCMT) systems, for example, PEP-*b*-PS in squalane. Therefore, it is interesting to examine whether the model proposed by Choi *et al.* can be equally applied to lower critical micellization temperature (LCMT) systems. In this study, a model polymer/solvent pair with LCST behavior was selected: PnBMA in [C_nMIM][TFSI], in which n = 2 and 4, representing [EMIM][TFSI] and [BMIM][TFSI], respectively. The phase diagrams of PnBMA in [EMIM][TFSI] and [BMIM][TFSI] have been thoroughly studied by Lee and Hoarfrost *et al.*,[1,2] and we already know that by tuning the solvent composition from 100% of [EMIM][TFSI] to 100% of [BMIM][TFSI], the LCST of a PnBMA homopolymer (*i.e.* molecular weight ≈ 40 kg/mol) can be tuned from below 0 to over 100 °C. This provides a very wide temperature window, within which the equilibration kinetics study can be conducted.

Specifically, in order to investigate the effect of solvent selectivity on the chain exchange rate, the model block copolymer/solvent system should meet the following three criteria:

(*i*) The LCST of the core block can be tuned continuously, so that χ between the solvent and the core block can be varied at a given temperature. More preferably, the χ values as a function of temperature and solvent composition should be available.

(*ii*) The glass transition temperature (T_g) of the core block should be lower than the experimental temperature to avoid kinetically frozen cores.

(*iii*) The block copolymer and the solvent should be stable at the experimental temperature.

The T_g of PnBMA is ~ 20 °C,[3] and the gap between the experimental temperature and the LCST of PnBMA in [C_nMIM][TFSI] mixtures can be easily tuned; therefore, this

core block/solvent combination ideally satisfies the above criteria. The corona block, on the other hand, does not require additional consideration other than its solubility in [C_nMIM][TFSI]. As has been mentioned in Chapter 1, PMMA is soluble in almost all imidazolium-based ionic liquids, and thereby is a good candidate for the corona block. Another reason for using PMMA-*b*-PnBMA as the model block copolymer is the versatility of the synthesis — because both blocks are methacrylates, and their radicals have similar reactivity, it is thus possible to tune the sequence of monomer addition, and prepare diblock and triblock copolymers with various architectures.

2.1. Synthetic Schemes of the Block Copolymer and Ionic Liquids

Synthetic Schemes of the Block Copolymer

There are multiple studies in which anionic polymerization was used to prepare poly(methacrylates),[4–7] however, due to the following two factors, low yield and poor molecular weight control were observed for the resulting polymers: (*i*) side reactions such as intramolecular Claisen condensation, which lead to the early termination of the propagating chains;[8,9] (*ii*) slow equilibria between aggregated and non-aggregated ion pairs, which lead to broad molecular weight distribution.[10,11] Compared with anionic polymerization, controlled radical polymerizations have better performance in synthesizing poly(methacrylate) homopolymers and copolymers. Among them, atom transfer radical polymerization (ATRP) and reversible addition-fragmentation chain-transfer polymerization (RAFT) are the two most widely used methods that allow precise control over the molecular weight of poly(methacrylates).

ATRP was independently discovered by Sawamoto *et al.*[12] and Matyjaszewski *et al.*[13] in 1995. It employs an alkyl halide (R-X) as the initiator, and a transition metal complex (M-X) as the catalyst. The transition metal that is most typically used in ATRP is copper. As the reaction R-X + M-X $\rightleftharpoons$ R$\cdot$ + M-X_2 is reversible and strongly favors the left side,

most of the chains tend to stay in the dormant species (R-X), with only a small fraction existing as free radicals (R·) and capable of propagating. This mechanism significantly reduces the free radical concentration in solution, and therefore reduces the chance of termination by radical coupling. ATRP has very good tolerance for many functional groups, such as amino, hydroxy, ester and amide, thus it is widely used in the polymerization of styrenes, (meth)acrylates and (meth)acrylamides.

RAFT was developed by Rizzardo *et al.*[14–16] of the Commonwealth Scientific and Industrial Research Organization (CSIRO) in 1996. It employs the concept of "dormant species" as in ATRP, but uses a different mechanism. In a typical RAFT polymerization, thiocarbonylthio-compounds are used as a chain-transfer agent (CTA). A propagating radical (R·) can reversibly react with this compound to form an adduct radical, which then releases a new radical (R'·). By rapid interchange between R· and R'·, all chains share equal opportunities to grow, leading to a narrow molecular weight distribution. Similarly, in RAFT polymerization, the concentration of the propagating species is low enough to suppress termination by radical coupling. RAFT polymerization is also amenable to various monomers, including styrenes, (meth)acrylates, (meth)acrylamides, and many vinyl monomers.

PMMA-*b*-PnBMA can be prepared *via* two sequential ATRP or RAFT polymerizations, as is shown in Figure 2.1. The reactivity ratios reported in the literature are $r_{n\text{-BMA}}$ =1.09 and r_{MMA} = 0.91;[17] both are fairly close to 1, suggesting that their radicals have similar reactivity to one another in statistical copolymerization. Therefore, in the ideal case, the order of polymerization can be either from MMA to *n*-BMA, or *vice versa*, without significantly affecting the molecular weight distribution of the final diblock. In Section 2.2 and 2.3, the results of both methods will be compared.

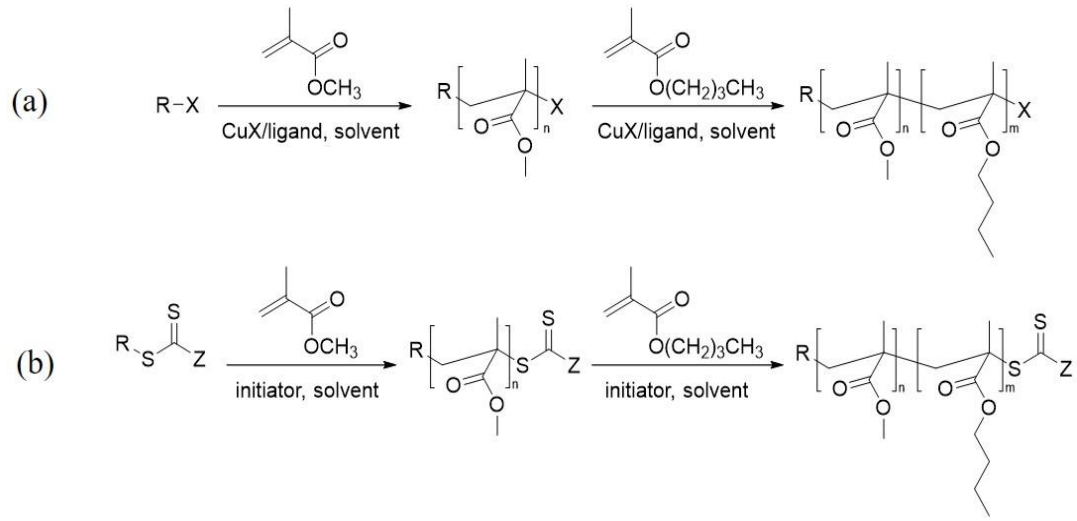

Figure 2.1. Synthetic schemes of PMMA-*b*-PnBMA by (a) ATRP and (b) RAFT, starting from methyl methacrylate.

Synthetic Schemes of Ionic Liquids

The protonated ionic liquids [EMIM][TFSI] and [BMIM][TFSI] were synthesized using a procedure adapted from the literature.[18] Typical reaction procedures are given as follows.

Synthesis of [EMIM][TFSI]. 1-Ethyl-3-methylimidazolium bromide ([EMIM]Br) and lithium bis(trifluorosulfonyl)imide (LiTFSI) were purchased from IoliTec Inc. and 3M, respectively; all materials and chemicals were used as received unless otherwise specified. In a 500 mL round bottom flask, [EMIM]Br (41.4 g, 0.217 mol) and LiTFSI (69.1 g, 0.241 mol) were combined, and mixed with about 200 mL of water. The reaction mixture was stirred for 36 hours at 70 °C. After cooling to room temperature, the mixture phase separated into two layers; the bottom layer (organic phase) was collected, and washed twice by deionized water. The organic phase was then dissolved in ~ 200 mL of dichloromethane (CH_2Cl_2), followed by filtration through an alumina column to remove the remaining water and salt. The final product (74.0 g) after vacuum drying is a colorless, clear and viscous liquid, with the yield of 87%. The ^{1}H-NMR spectrum is given in Figure 2.2a.

Synthesis of [BMIM][TFSI]. 1-Butyl-3-methylimidazolium chloride ([BMIM]Cl) was purchased from IoliTec Inc. In a 500 mL round bottom flask, [BMIM]Cl (40.8 g, 0.233 mol) and LiTFSI (69.4 g, 0.242 mol) were combined, and mixed with about 200 mL of water. The reaction mixture was stirred for 36 hours at 70 °C. The work-up procedures are the same as [EMIM][TFSI]. The final product (83.1 g) after vacuum drying is a colorless, clear and viscous liquid, with the yield of 85%. The ^{1}H-NMR spectrum is given in Figure 2.2b.

As the "contrast-matching" strategy in TR-SANS requires partial deuteration on the solvents, H-D exchange reactions were conducted on the two ionic liquids by reacting them with excess D_2O, according to an established method.[19] The three hydrogens on the imidazole ring in [EMIM][TFSI] and [BMIM][TFSI] are slight acidic, therefore, they can be extracted by base (such as potassium carbonate), which facilitates the H-D exchange process. Typical reaction procedures are as follows.

Synthesis of *d*$_3$-[EMIM][TFSI]. Deuterium oxide (D_2O) and potassium carbonate (K_2CO_3) were purchased from Cambridge Isotope Laboratories, Inc. and Fisher Chemicals, respectively. K_2CO_3 (41.2 g, 0.299 mol) was dissolved in D_2O (150 g, 7.5 mol), and the solution was combined with [EMIM][TFSI] (19.6g, 0.050 mol) in a 250 mL round bottom flask. The reaction mixture was stirred for 2 days at 100 °C. The work-up procedures are the same as [EMIM][TFSI]. The ^{1}H-NMR spectrum is given in Figure 2.2c. Notably, the three tiny peaks at 9.1 and 7.7 ppm correspond to the residual of H_a and H_b in Figure 2.2a, indicating a high conversion percentage of H to D.

Synthesis of *d*$_3$-[BMIM][TFSI]. K_2CO_3 (41.2 g, 0.299 mol) were dissolved in D_2O (150 g, 7.5 mol), and the solution was combined with [BMIM][TFSI] (19.6g, 0.468 mol) in a 250 mL round bottom flask. The reaction mixture was stirred for 2 days at 100 °C. The work-up procedures are the same as [EMIM][TFSI]. The ^{1}H-NMR result is given in Figure 2.2d. High conversion of H to D is also achieved as in the case of *d*$_3$-[EMIM][TFSI].

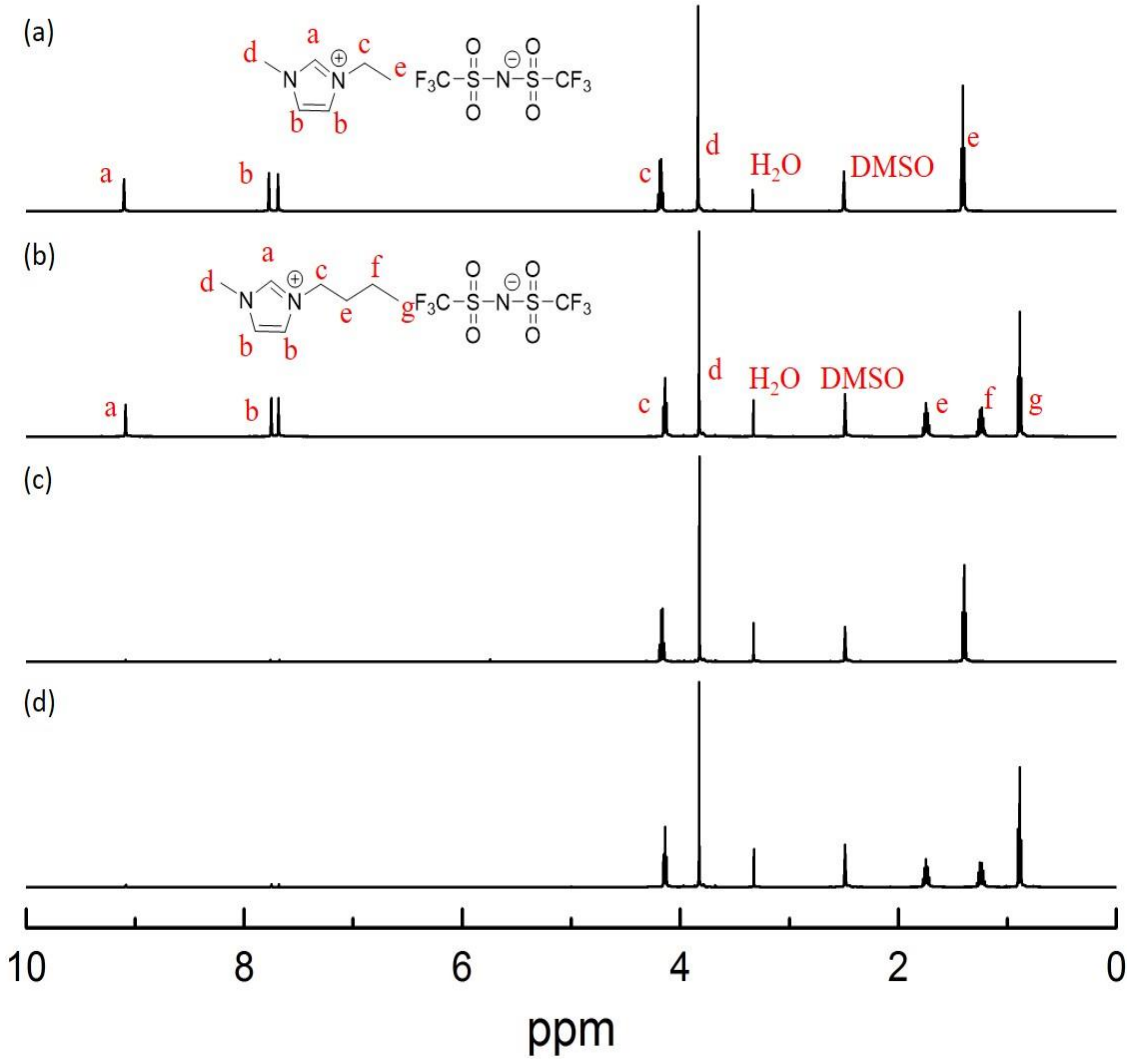

Figure 2.2. ^{1}H-NMR of (a) [EMIM][TFSI], (b) [BMIM][TFSI], (c) d_3-[EMIM][TFSI], and (d) d_3-[BMIM][TFSI]. (500 MHz, the solvent is DMSO-d_6.)

The ^{1}H-NMR spectroscopy of [EMIM][TFSI] and [BMIM][TFSI] are consistent with those reported in literature.[18] By comparing the three peaks in the range of 7.5 − 9.5 ppm in panel (a) and (c), as well as panel (b) and (d), it is clear that high deuteration level is achieved for the three hydrogens on the imidazole ring (D% > 95%), marked by the significant decrease in the integration area of the peaks.

2.2. Sequential Polymerization from MMA to *n*-BMA

Synthesis of PMMA-b-PnBMA

The PMMA-*b*-PnBMA diblock copolymers were synthesized through a two-step sequential RAFT polymerization, starting from MMA. A typical procedure is given as below.

Polymerization of MMA. All reagents were purchased from Sigma-Aldrich. Only methyl methacrylate (MMA) was purified by passing through an alumina column before use, in order to remove the inhibitor. 4-Cyano-4-[(dodecylsulfanylthiocarbonyl)-sulfanyl]pentanoic acid (CTAC12CN, 0.21 g, 0.52 mmol), methyl methacrylate (MMA, 21 g, 210 mmol) and 4,4'-azobis(4-cyanovaleric acid) (V501, 16.0 mg, 0.057 mmol) were combined with 60 mL of dioxane in a 250 mL Schlenk flask. The flask was sealed by a rubber septum and subsequently subjected to three freeze-pump-thaw cycles to remove oxygen. The flask was then filled with argon, and the reaction was allowed to proceed for 12 hours at 80 °C. The product was directly precipitated into hexanes and collected via filtration.

Polymerization of *n*-BMA. All reagents were purchased from Sigma-Aldrich. Only *n*-butyl methacrylate (*n*-BMA) was purified by passing through an alumina column before use, in order to remove the inhibitor. PMMA-CTAC12CN (0.70 g, 0.028 mmol), *n*-butyl methacrylate (*n*-BMA, 0.94 g, 6.6 mmol), and V501 (0.8 mg, 0.0028 mmol) were combined with 7 mL of dioxane in a 100 mL Schlenk flask. The reaction mixture went through three freeze−pump−thaw cycles and was then heated to 80 °C under argon. The reaction was allowed to proceed for 22 hours. The resulting copolymer was recovered by precipitation into cold methanol.

Size Exclusion Chromatography (SEC) Characterization. SEC was used to characterize the molecular weight and molecular weight distribution of the resulting

polymers. The essential part of the SEC used in this study is a series of three columns (Phenomenex Phenogel columns, with stationary phase pore sizes of 10^5, 10^4 and 10^3 Å, respectively, from upstream to downstream), which separate polymers with different molecular weights. Specifically, this SEC has a multi-angle laser light scattering (MALLS) detector (Wyatt DAWN DSP Laser Photometer) and a refractive index (RI) detector (Wyatt Optilab rEX Refractometer), which allows a direct measurement of the actual molecular weight of the macromolecules, without running calibration standards and constructing calibration curves. The determination of the actual molecular weight is based on the Zimm Equation:[20,21]

$$\frac{Kc}{R_\theta} = \frac{1}{M_w P(\theta)} + 2A_2 c \tag{2.1}$$

where c, R_θ, M_w, $P(\theta)$ and A_2 are the concentration of polymer, the Rayleigh ratio of the solution, weight-averaged molecular weight of the polymer, form factor of the polymer, and the second virial coefficient, respectively. K is the instrumental factor, defined by $K = 4\pi^2 n_0^2 (\mathrm{d}n/\mathrm{d}c)^2 \lambda^{-4} N_A^{-1}$, in which n_0, $\mathrm{d}n/\mathrm{d}c$, λ and N_A are the refractive index of the solvent, the refractive index increment, the wavelength of laser light, and Avogadro's number. In eq 2.1, $1/P(\theta)$ can be expanded to the first order:

$$\frac{1}{P(\theta)} = 1 + \frac{16\pi^2 R_g^2 \sin^2(\theta/2)}{3\lambda^2} \tag{2.2}$$

where R_g and θ are the mean square radius of the polymer and the scattering angle, respectively.

Because the polymer concentration used in SEC characterization is typically very small (~ 2 mg/mL), which is further spread along the column, therefore, $2A_2c$ is negligible compared to $1/M_w P(\theta)$. By combining eqs. 2.1 and 2.2, we can obtain:

$$\frac{Kc}{R_\theta} = \frac{1}{M_w}\left(1 + \frac{16\pi^2 R_g^2 \sin^2(\theta/2)}{3\lambda^2}\right) \tag{2.3}$$

According to eq. 2.3, M_w can be obtained by plotting Kc/R_θ versus $\sin^2(\theta/2)$.

In an SEC measurement, the disperse polymer chains are separated by their hydrodynamic volumes: longer polymer chains tend to elute from the column first. This leads to a distribution of different molecular weights. Software (Astra for Windows, v4.90) is used to split the peak into thousands of slices, and within each slice, the polymer concentration c is determined by $c = \Delta n/(\mathrm{d}n/\mathrm{d}c)$. By putting in the d$n$/d$c$ value of the polymer, the M_w of each slice can be calculated independently based on eq 2.3. As each slice is very thin, the polymers that elute within each slice can be taken as almost monodisperse, thus $M_w = M_n$ (M_n is the number-averaged molecular weight). Under such assumption, M_n, M_w and the dispersity ($Đ$) of the whole peak can be obtained.

The dn/dc values for PMMA and PnBMA are 0.084 and 0.068 mL/g, available in the literature.[22,23] The dn/dc of PMMA-*b*-PnBMA copolymers can be estimated by the following equation.

$$(\mathrm{d}n/\mathrm{d}c)_{\text{copolymer}} = w_{\text{PMMA}}(\mathrm{d}n/\mathrm{d}c)_{\text{PMMA}} + w_{\text{PnBMA}}(\mathrm{d}n/\mathrm{d}c)_{\text{PnBMA}} \qquad (2.4)$$

where w is the weight fraction of each block in the copolymer, which is determined by using ^{1}H-NMR spectroscopy.

In Figure 2.3, representative SEC traces of two series of PMMA-*b*-PnBMA copolymers — (*i*) PMMA-*b*-PnBMA (25-X) and (*ii*) PMMA-*b*-PnBMA (X-35) — are illustrated. All the traces indicate that these copolymers are monomodal, *i.e.*, without significant sign of homopolymers.

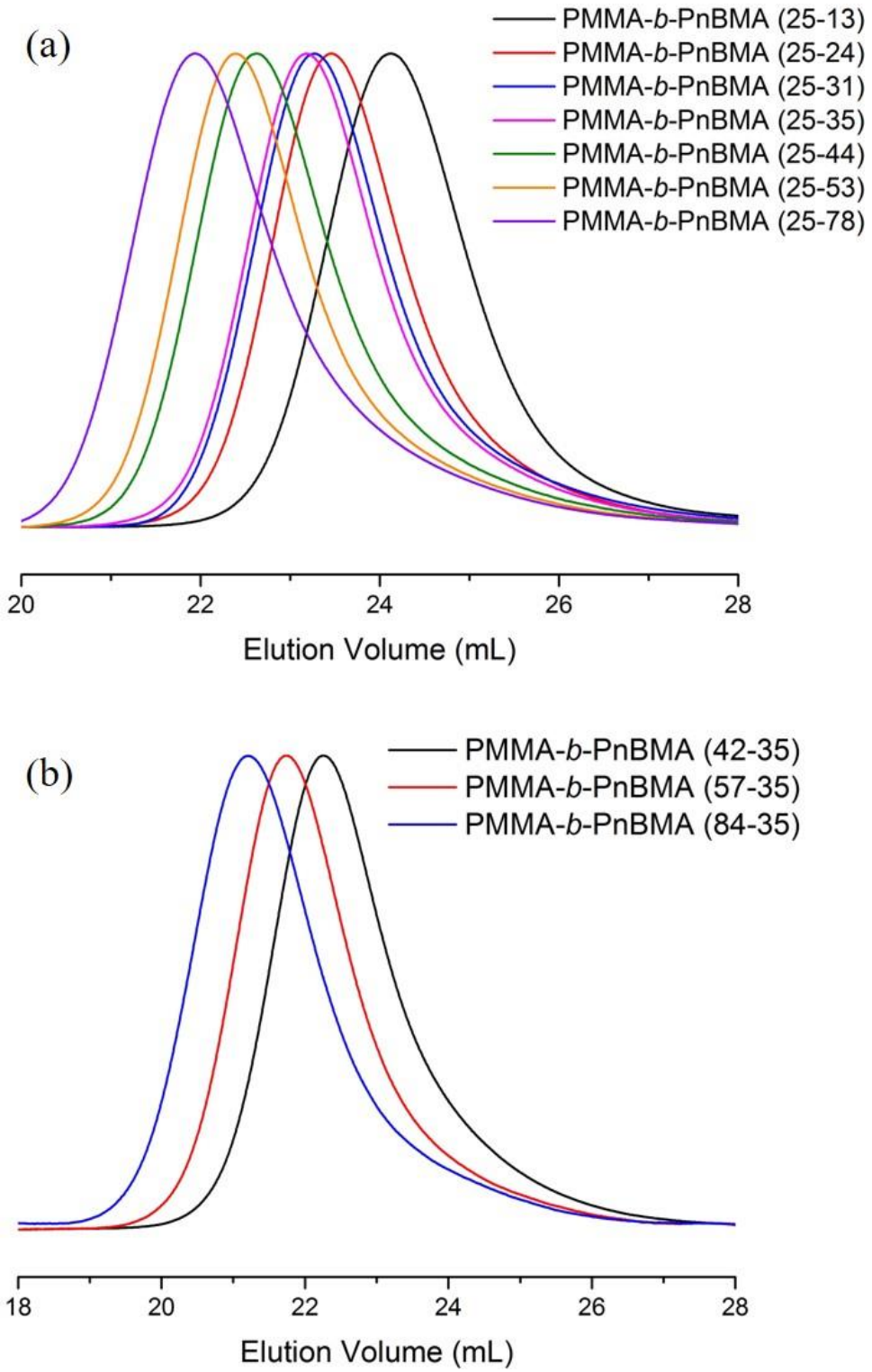

Figure 2.3. SEC traces (RI detector) of (a) PMMA-*b*-PnBMA (25-X), and (b) PMMA-*b*-PnBMA (X-35). The numbers in the brackets refer to the molecular weight of each block in kg/mol. THF is used as an eluent at a flow rate of 1.0 mL/min.

Nuclear Magnetic Resonance (NMR) Characterization. ^{1}H-NMR spectroscopy was used to confirm the identity of the copolymers, as well as calculate the ratio of PMMA and PnBMA monomers in each diblock copolymer. In this study, ^{1}H-NMR was conducted on a Varian Inova 500 MHz spectrometer. Additionally, for the synthesis of deuterated monomer and polymers, ^{2}H-NMR (deuterium-NMR) was used, which was conducted on a Bruker Ascend 500 MHz spectrometer equipped with a special probe.

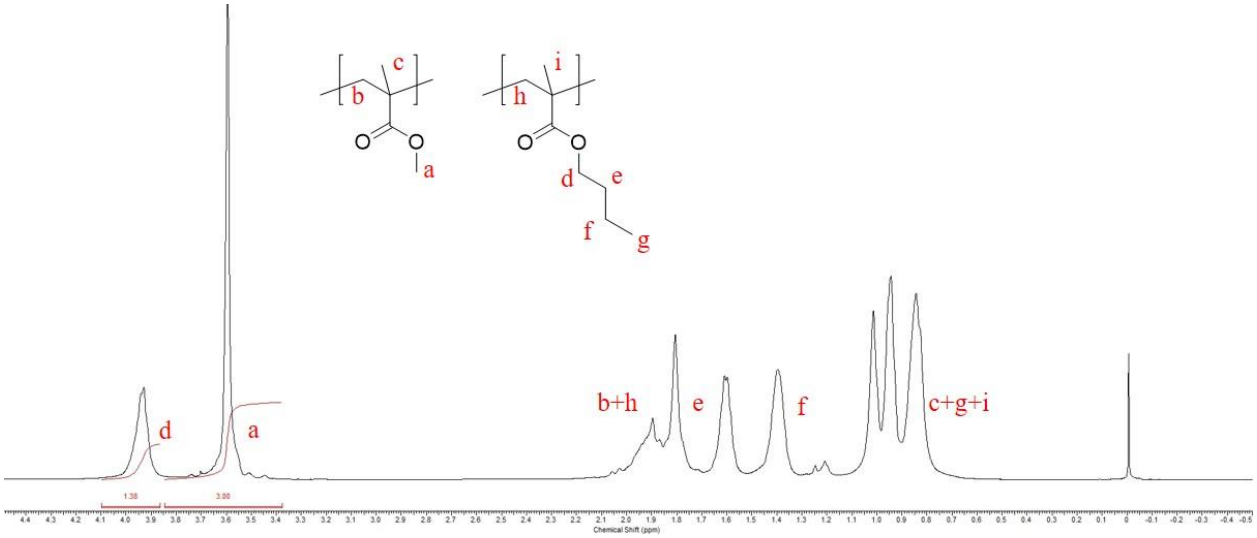

Figure 2.4. ^{1}H-NMR of PMMA-*b*-PnBMA (25-24). (The solvent is $CDCl_3$.)

In Figure 2.4, the ^{1}H-NMR spectrum of PMMA-*b*-PnBMA (25-24) is given as an example; all peaks in the figure are assigned to the corresponding hydrogens in the copolymer. As can be seen from Figure 2.4, the spectrum can be roughly divided into three parts: (*i*) 0.7 – 1.2 ppm, representing all the methyl groups except the one connected to the ester group of PMMA (c, g and i); (*ii*) 1.2 – 2.1 ppm, representing the methylene groups on the backbone, and the two methylene groups that are not directly connected to the ester group of PnBMA (b, e, f and h); (*iii*) 3.5 – 4.1 ppm, representing the $–OCH_3$ of PMMA and the $–OCH_2–$ of PnBMA (a and d). In part (*i*) and (*ii*), the peaks of PMMA and PnBMA are mostly overlapping, while in part (*iii*), the two peaks can be easily distinguished. Therefore, it is convenient to use the ratio of integration area between peak

a and d to determine the copolymer composition. An example of calculation is given as follows:

$$\frac{N_{\text{PnBMA}}}{N_{\text{PMMA}}} = \frac{S_{\text{d}}/2}{S_{\text{a}}/3} = \frac{1.38/2}{3.00/3} = 0.69$$

As M_{n} of the PMMA block is determined by SEC to be 25 kg/mol, therefore

$$N_{\text{PnBMA}} = 0.69 \times \frac{25000}{M_{\text{MMA}}} = 0.69 \times \frac{25000}{100} = 172.5$$

$$M_{\text{PnBMA}} = N_{\text{PnBMA}} \times M_{\text{n-BMA}} = 172.5 \times 142 \approx 24\,\text{kg/mol}$$

Table 2.1. Characteristics of PMMA-*b*-PnBMA Diblock Copolymers

Entry	**Sample**	$M_{\text{n,PMMA}}$ **(kg/mol)** [a]	$M_{\text{n,PnBMA}}$ **(kg/mol)** [b]	$M_{\text{n,total}}$ **(kg/mol)** [a]	$Đ$ [a]
1	PMMA-*b*-PnBMA (25-13)	25	13	40	1.04
2	PMMA-*b*-PnBMA (25-24)	25	24	52	1.05
3	PMMA-*b*-PnBMA (25-31)	25	31	57	1.05
4	PMMA-*b*-PnBMA (25-35)	25	35	61	1.05
5	PMMA-*b*-PnBMA (25-44)	25	44	68	1.07
6	PMMA-*b*-PnBMA (25-53)	25	53	76	1.08
7	PMMA-*b*-PnBMA (25-78)	25	78	97	1.11
8	PMMA-*b*-PnBMA (42-35)	42	35	72	1.10
9	PMMA-*b*-PnBMA (57-35)	57	35	89	1.09
10	PMMA-*b*-PnBMA (84-35)	84	35	114	1.11

[a] Determined by MALLS-SEC. [b] Determined by ^{1}H-NMR.

Apart from the molecular weight given by ^{1}H-NMR, another $M_{\text{n,total}}$ can be obtained from SEC measurement of the diblock copolymers. Theoretically, $M_{\text{n,total}}$ should be equal to the sum of M_{PMMA} and M_{PnBMA}; and the proximity of these two values can serve as a

criterion to judge whether or not the determined molecular weights of the two blocks are accurate. Table 2.1 summarizes the ^{1}H-NMR and SEC characterization results of the diblock copolymers used in this study. By comparing $M_{n,total}$ and ($M_{n,PMMA}$ + $M_{n,PnBMA}$) for each entry, we can see that their relative errors are less than 10% in all the cases, indicating reasonable accuracy in the molecular weight determination of these diblocks.

Synthesis of PMMA-b-dPnBMA

Compared with the protonated PMMA-*b*-PnBMA, the synthesis of its deuterated counterpart requires only one extra step: the synthesis of *n*-butyl methacrylate-d_9 (d_9-*n*-BMA). This material was prepared by a modified version of a documented method,[24] as briefly described below.

Synthesis of d_9-*n*-BMA. Methacryloyl chloride and 4-dimethylaminopyridine (DMAP) were purchased from Sigma-Aldrich; trimethylamine (TEA) was purchased from Fisher Chemicals; *n*-butanol-d_{10} was purchased from Cambridge Isotope Laboratories. All chemicals were used as received except for methacryloyl chloride, which requires distillation prior to use. TEA (2.02g, 20.0 mmol), *n*-butanol-d_{10} (1.147g, 13.7 mmol), and DMAP (0.33g, 2.7 mmol) were first combined with 100 mL methylene chloride in a 250 mL round-bottom flask. The mixture was cooled in an ice bath, and under stirring, pre-distilled methacryloyl chloride (1.405g, 13.4 mmol) was added dropwise to the mixture. The ice bath was then removed, and the reaction was run for 12 hours under room temperature. The resulting crude product was washed with 1 mol/L hydrochloric acid, 10% sodium bicarbonate aqueous solution, and then collected twice via extraction with methylene chloride. The crude product was then purified by flash column chromatography to give the pure product (eluent: hexanes/ethyl acetate = 10/1), which was characterized by ^{1}H-NMR and ^{2}H-NMR spectroscopy to confirm the chemical structure.

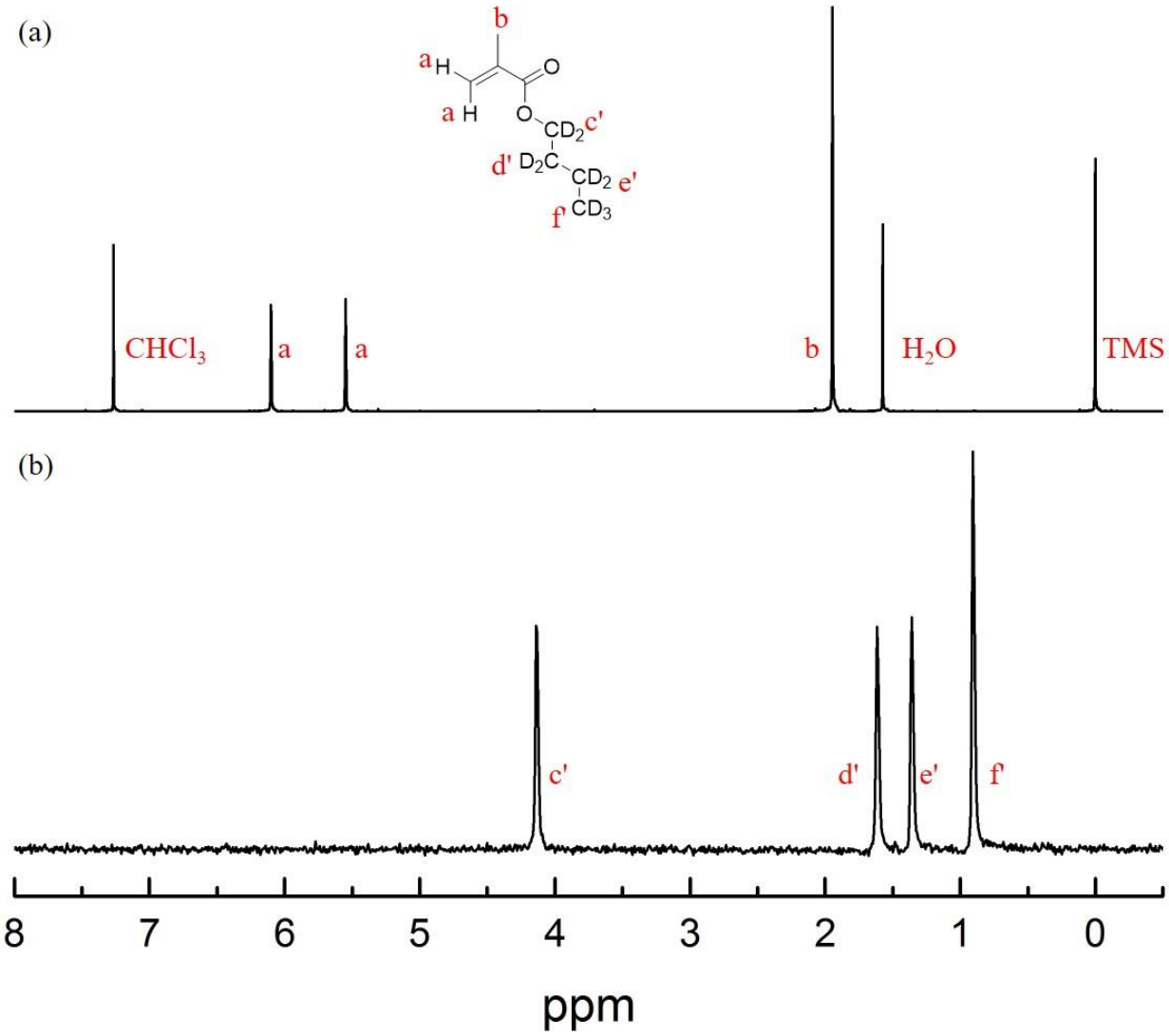

Figure 2.5. (a) ^{1}H-NMR and (b) ^{2}H-NMR of d_9-*n*-BMA. (The solvent is $CDCl_3$ for ^{1}H-NMR, and $CHCl_3$ for ^{2}H-NMR.)

As can be seen from the figure, the ^{1}H-NMR spectrum (Figure 2.5a) only displays three significant peaks, which can be assigned as the two vinyl hydrogens and the hydrogens of the methyl group; ^{2}H-NMR spectrum (Figure 2.5b) confirms the presence of the deuterated butyl group.

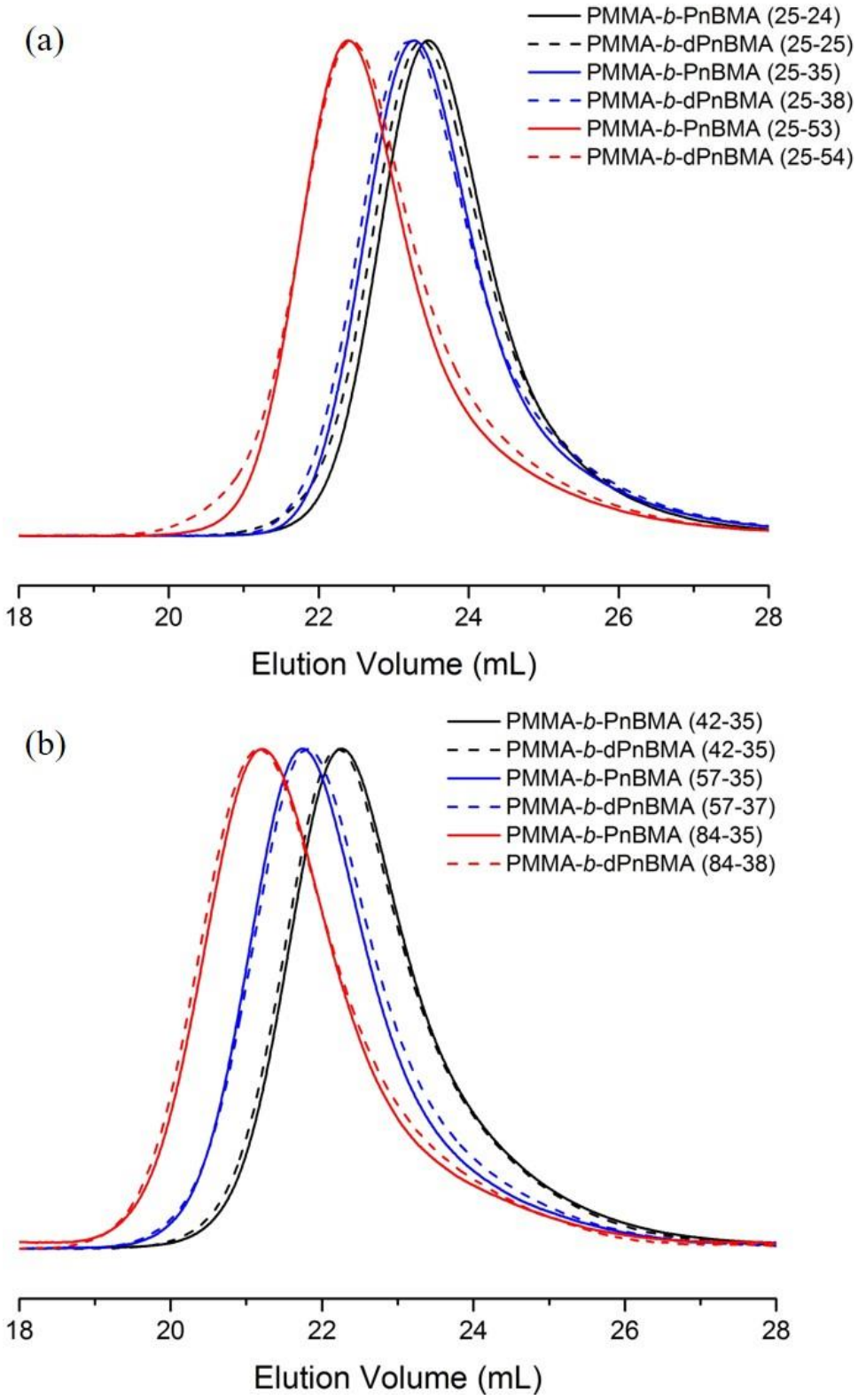

Figure 2.6. Comparison of SEC traces (RI detector) of (a) PMMA-*b*-(d)PnBMA (25-X), and (b) PMMA-*b*-(d)PnBMA (X-35). The numbers in the brackets refer to the molecular weight of each block in kg/mol. THF is used as an eluent at a flow rate of 1.0 mL/min.

Polymerization of d_9-*n*-BMA follows exactly the same procedure as that of *n*-BMA. The reagent ratio, reaction temperature and reaction time were also rigorously controlled to enable precise control over the monomer conversion. The SEC traces of the resulting PMMA-*b*-dPnBMA are compared with those of PMMA-*b*-PnBMA. As deuteration does not change the chemical nature of the molecules, therefore, in the same solvent, the hydrodynamic volumes of a PnBMA chain and a dPnBMA chain with identical degree of polymerization should be equal, which will make them elute at the same time. In Figure 2.6, the SEC traces of each pair of PMMA-*b*-(d)PnBMA almost overlap, clearly indicating similar degree of polymerization of the (d)PnBMA blocks, as well as similar dispersity.

^{1}H-NMR was also used to determine the chain composition in the case of PMMA-*b*-dPnBMA. ^{1}H-NMR spectroscopy of PMMA-*b*-dPnBMA (25-25) is given as an example; all peaks in Figure 2.7 are assigned to the corresponding hydrogens in the copolymer.

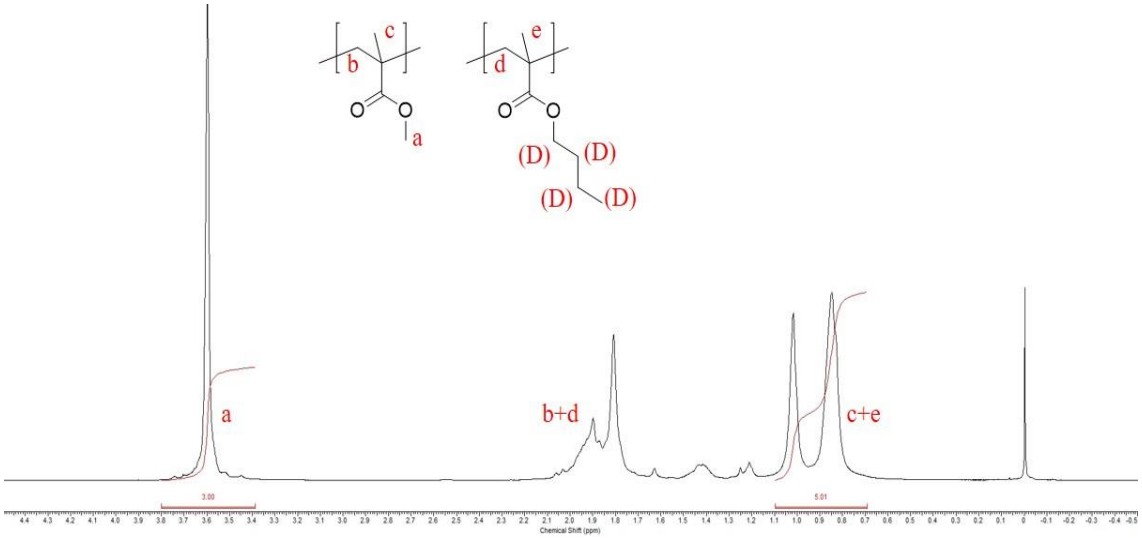

Figure 2.7. ^{1}H-NMR of PMMA-*b*-dPnBMA (25-25). (The solvent is $CDCl_3$.)

As is evidenced in Figure 2.7, due to deuterium substitution on the butyl chain, PMMA-*b*-dPnBMA lacks the peak at 3.95 ppm representing the $–OCH_2–$ group.

Therefore, the method to determine the monomer ratio in the case of PMMA-*b*-PnBMA can no longer be applied to the deuterated copolymers. Instead, the incremental integration area of the 0.7 – 1.2 ppm peaks is used. An example of calculation is given as follows:

$$\frac{N_{\mathrm{dPnBMA}}}{N_{\mathrm{PMMA}}} = \frac{(S_{\mathrm{c+e}} - S_{\mathrm{c}})/3}{S_{\mathrm{a}}/3} = \frac{(S_{\mathrm{c+e}} - S_{\mathrm{a}})/3}{S_{\mathrm{a}}/3} = \frac{(5.01-3.00)/3}{3.00/3} = 0.67$$

As M_{n} of the PMMA block is determined by SEC to be 25 kg/mol, therefore

$$N_{\mathrm{dPnBMA}} = 0.67 \times \frac{25000}{M_{\mathrm{MMA}}} = 0.67 \times \frac{25000}{100} = 167.5$$

$$M_{\mathrm{dPnBMA}} = N_{\mathrm{dPnBMA}} \times M_{\mathrm{d9\text{-}n\text{-}BMA}} = 167.5 \times 151 \approx 25 \text{ kg/mol}$$

Table 2.2 summarizes the ^{1}H-NMR and SEC characterization results of the deuterated diblock copolymers used in this study. Again, $M_{\mathrm{n,total}}$ and ($M_{\mathrm{n,PMMA}}$ + $M_{\mathrm{n,dPnBMA}}$) display relatively good agreement for all these diblocks.

Table 2.2. Characteristics of PMMA-*b*-dPnBMA Diblock Copolymers

Entry	**Sample**	$M_{\mathrm{n,PMMA}}$ **(kg/mol)** [a]	$M_{\mathrm{n,dPnBMA}}$ **(kg/mol)** [b]	$M_{\mathrm{n,total}}$ **(kg/mol)** [a]	$Đ$ [a]
1	PMMA-*b*-dPnBMA (25-25)	25	25	53	1.05
2	PMMA-*b*-dPnBMA (25-38)	25	38	60	1.05
3	PMMA-*b*-dPnBMA (25-54)	25	54	76	1.09
4	PMMA-*b*-dPnBMA (42-35)	42	35	71	1.10
5	PMMA-*b*-dPnBMA (57-37)	57	37	88	1.11
6	PMMA-*b*-dPnBMA (84-38)	84	38	111	1.14

[a] Determined by MALLS-SEC. [b] Determined by ^{1}H-NMR.

2.3. Sequential Polymerization from *n*-BMA to MMA

When the PnBMA block lengths need to be kept exactly constant for a series of block copolymers, it will then be desirable to do the sequential polymerization starting from *n*-BMA. Multiple attempts were made to reverse the order of polymerization in Section 2.2, both by RAFT and ATRP; nevertheless, only limited success was achieved.

Synthesis Attempts by RAFT.

Initially, the same reaction procedures and reagent ratio, *i.e.*, [CTA] : [Initiator] = 10 : 1, was applied, only with the order of polymerization reversed. After the first step of polymerization, the resulting PnBMA-CTAC12CN displayed a narrow, monomodal peak, as expected (the dashed line in Figure 2.8). However, after the second step, *i.e.*, the polymerization of MMA, the molecular weight distribution of the diblock copolymer became bimodal (the solid line in Figure 2.8), when the PMMA and PnBMA blocks have comparable lengths. This indicates that the diblock synthesized is contaminated with homopolymer, either PMMA or PnBMA, or both.

In RAFT, for a successful block copolymerization, the sequence of blocks should be carefully selected, so that the free radical of the preceding block (denoted as A·) should have higher stability than that of the succeeding block (denoted as B·).[25,26] Under such scenario, the B· initiated by the initiator will quickly combine with the macro-CTA of A block, and release the A· radicals, which will then start to grow B on their ends, resulting in block copolymerization. In the opposite case, if A· is less stable than B·, the equilibrium of "B· + CTA-A ⇌ CTA-B + A·" will favor the left side, resulting in more B· radicals initiating B monomer in the reaction. As a result, homopolymerization is predominant, which will give two homopolymers (CTA-A and B) as the final products. Therefore, a block of poly(methacrylate) should always precede a block of poly(styrene) or poly(acrylate), but not the other way around.

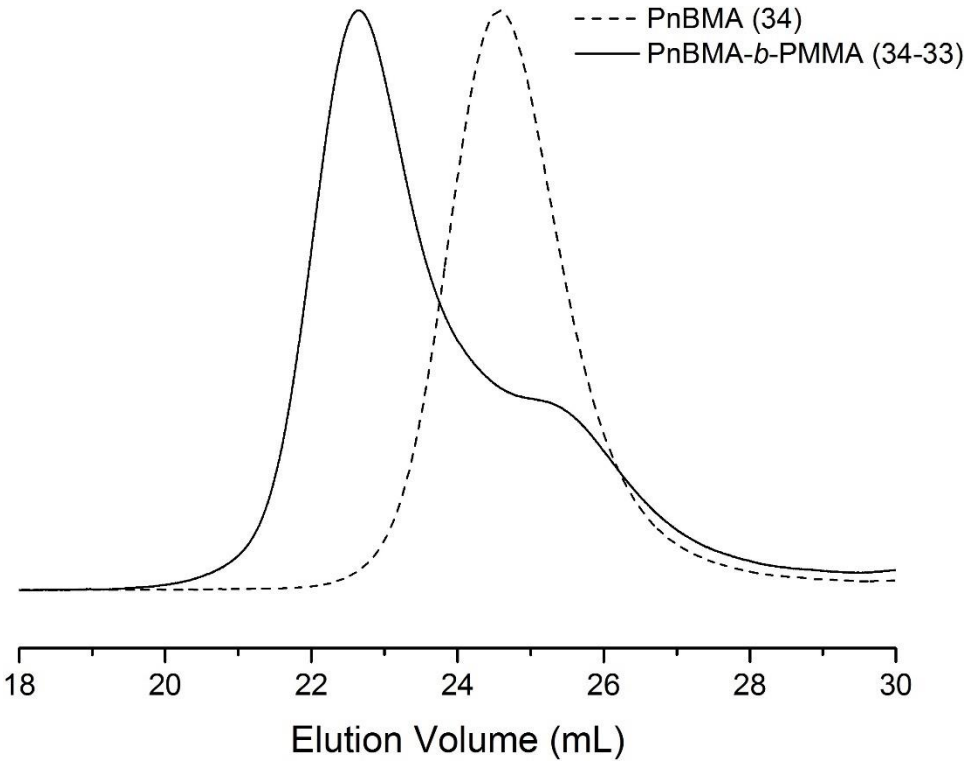

Figure 2.8. SEC traces (RI detector) of PnBMA (34) (dashed line) and PnBMA-*b*-PMMA (34-33) (solid line), synthesized by RAFT. The numbers in the brackets refer to the molecular weight of each block in kg/mol. THF is used as an eluent at a flow rate of 1.0 mL/min.

In the case of MMA and *n*-BMA, as has been discussed in Section 2.1, the free radical of the former is slightly more stable than the latter. Therefore, the more desirable polymerization sequence is from MMA to *n*-BMA in RAFT.

It is worth noticing that even in the RAFT synthesis of a homopolymer, there will always be some dead chains with no CTA connected to them, since the new chains in RAFT are introduced by the initiator at the early stage of polymerization. This is supported by simulation results that the percentage of the dead chains in the resulting polymer is determined by the [CTA]/[Initiator] ratio.[25,27] Therefore, a controlled study using a serial different [CTA]/[Initiator] ratios was done. Nevertheless, by varying the [CTA]/[Initiator] ratios in the first step (the polymerization of *n*-BMA) from 10/1 to 40/1,

the percentage of homopolymer in the resulting block copolymers does not differ very much, as summarized in Table 2.3.

Table 2.3. Characteristics of PnBMA-*b*-PMMA Diblock Copolymers Synthesized by RAFT under Different Conditions

Entry	[CTA]/[Initiator] in the first step[a]	[CTA]/[Initiator] in the second step[b]	$M_{n,PnBMA}$ (kg/mol)[c]	$M_{n,PMMA}$ (kg/mol)[d]	$Đ$ [c]	Homopolymer percent (%) [e]
1	10/1	10/1	34	33	1.14	27
2	20/1	10/1	34	54	1.15	23
3	40/1	10/1	31	51	1.21	23

[a] Reactions are conducted at 80 °C for 16 h; monomer conversion is ~ 65%. [b] Reactions are conducted at 80 °C for 26 h; monomer conversion is ~ 55%. [c] Determined by MALLS-SEC. [d] Determined by ^{1}H-NMR. [e] Determined by fitting the SEC traces to the sum of two Gaussian distributions, the results of which are given in the Appendices (Figure A.1.1).

Synthesis Attempts by ATRP.

ATRP is a possible substitute for RAFT that may afford PnBMA-*b*-PMMA copolymers with relatively good distribution. Because ATRP follows a different mechanism, *i.e.*, in the polymerization of the second block, the first block serves as the macro-initiator; therefore, no chain transfer will take place, thus the formation of homopolymer is hindered. A typical ATRP reaction procedure is given as follows.

Polymerization of *n*-BMA by ATRP. All reagents were purchased from Sigma-Aldrich. Only *n*-BMA was purified by passing through an alumina column before use, in order to remove the inhibitor. Ethyl α-bromoisobutyrate (EBiB, 0.023 g, 0.12 mmol), *n*-BMA (5.0 g, 35 mmol), and 4,4′-dinonyl-2,2′-bipyridine (dNbpy, 98 mg, 0.24 mmol)

were combined with 5 g of anhydrous anisole in a 100 mL Schlenk flask. The reaction mixture first went through three freeze−pump−thaw cycles, then CuCl (12 mg, 0.12 mmol) was added under nitrogen purge. The Schlenk flask was quickly re-capped with a septum and heated to 70 °C, and the reaction was allowed to proceed for 12 hours. The resulting polymer was recovered by precipitation into cold methanol.

Polymerization of MMA by ATRP. All reagents were purchased from Sigma-Aldrich. Only MMA was purified by passing through an alumina column before use, in order to remove the inhibitor. PnBMA-Cl (0.50 g, 0.014 mmol), MMA (2.5 g, 25 mmol), dNbpy (11 mg, 0.028 mmol), and Tin(II) 2-ethylhexanoate (2.9 mg, 0.007 mmol) were combined with 2.5 g of anhydrous anisole in a 100 mL Schlenk flask. The reaction mixture first went through three freeze−pump−thaw cycles, then CuCl (1.4 mg, 0.014 mmol) was added under nitrogen purge. The Schlenk flask was quickly re-capped with a septum and heated to 70 °C, and the reaction was allowed to proceed for 16 hours. The resulting copolymer was recovered by precipitation into cold methanol.

The SEC results of the homopolymer synthesized by step 1 and the copolymer synthesized by step 2 are given in Figure 2.9. As with RAFT, the peak representing the PnBMA homopolymer is narrow and symmetric, while the diblock copolymer peak has a shoulder at the low molecular weight side. This indicates that the diblock synthesized by ATRP still contains some homopolymer, although its percentage is much lower than that of RAFT. According to Figure 2.9, the shoulder on the SEC trace of the diblock almost falls on the same position as the homopolymer peak, indicating that part of the PnBMA macro-initiator does not initiate the polymerization of the second block.

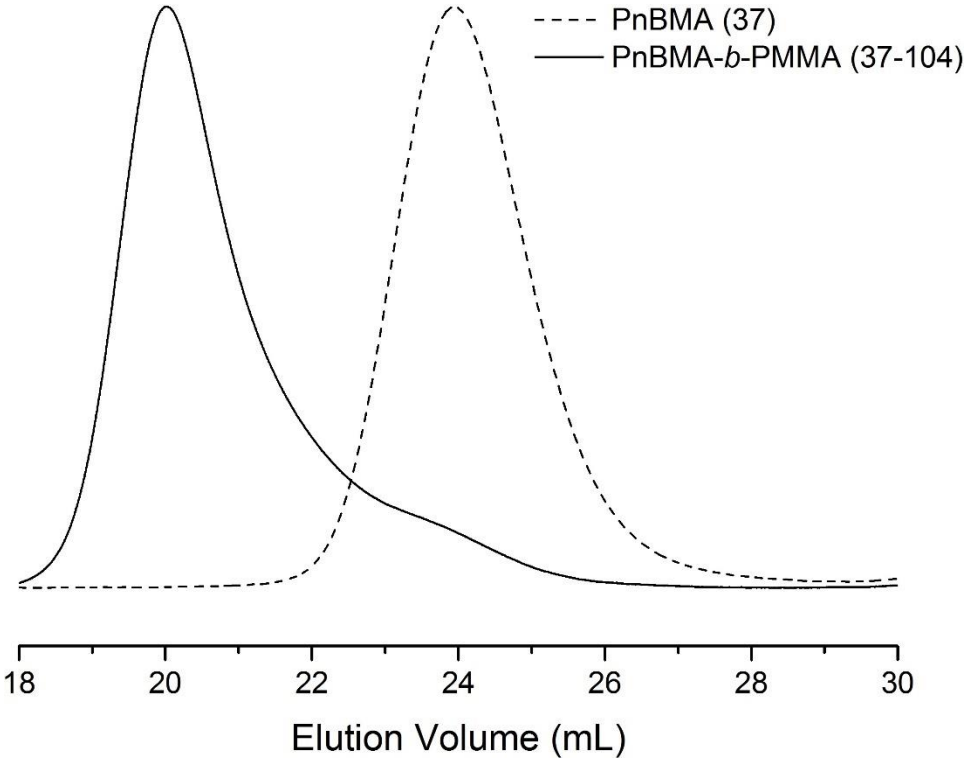

Figure 2.9. SEC traces (RI detector) of PnBMA (37) (dashed line) and PnBMA-*b*-PMMA (37-104) (solid line), synthesized by ATRP. The numbers in the brackets refer to the molecular weight of each block in kg/mol. THF is used as an eluent at a flow rate of 1.0 mL/min.

The loss of chain end functionality is an important issue in ATRP.[28] As ATRP requires that the chain propagation rate constant (k_p) is much lower than the deactivation and initiation rate constant (k_{deact} and k_i), therefore, if this ideal condition cannot be achieved, some chains will undergo coupling termination during the reaction, leading to the formation of dead chains. Therefore, for each monomer, it is crucial to find a proper initiator, a proper catalyst, and a proper ligand. In the literature, the typical ATRP recipes for poly(methacrylates) usually have EBiB or *p*-toluenesulfonyl chloride (*p*-TsCl) as the initiator, CuCl or CuBr as the catalyst, and dNbpy as the ligand.[29,30] Other ligands, such as 1,1,4,7,7-pentamethyldiethylenetriamine (PMDETA) and 1,1,4,7,10,10-hexamethyltriethylenetetramine (HMTETA), have also been reported.[31,32] Therefore, we conducted ATRP synthesis of PnBMA-*b*-PMMA using various conditions, in order to

Table 2.4 Characteristics of PnBMA-*b*-PMMA Diblock Copolymers Synthesized by ATRP under Different Conditions

Entry	First step: polymerization of *n*-BMA[a]		Second step: polymerization of MMA[b]		$M_{n,PnBMA}$ (kg/mol)[c]	$M_{n,PMMA}$ (kg/mol)[d]	$Đ$ [c]	Homopolymer percent (%) [e]
	[Intiator]:[CuX]:[Ligand]	Temp (°C)	[Intiator]:[CuX]:[Ligand]	Temp (°C)				
1	[EBiB]:[CuBr]:[HMTETA] = 1 : 0.5 : 0.5	70	[PnBMA-Br]:[CuBr]: [HMTETA] = 1 : 0.5 : 0.5	75	29	25	1.12	24
2	[EBiB]:[CuCl]:[dNbpy] = 1 : 1 : 2	70	[PnBMA-Cl]:[CuCl]: [dNbpy] = 1 : 1 : 2	75	37	56	1.11	14
3					37	104	1.24	10
4	[*p*-TsCl]:[CuBr]:[dNbpy] = 1 : 0.5 : 1	70	[PnBMA-Cl]:[CuBr]: [dNbpy] = 1 : 1 : 2	75	33	38	1.11	14
5					33	73	1.12	11
6	[*p*-TsCl]:[CuBr]:[dNbpy] = 1 : 0.5 : 1	60	[PnBMA-Cl]:[CuBr]: [dNbpy] = 1 : 1 : 2	75	29	58	1.06	10

[a] Reactions are conducted at 70 °C for 12 h, or at 60 °C for 24 h, with the monomer conversion of 50 – 70%. [b] Reactions are conducted at 75 °C for 16 h, with the monomer conversion of 40 – 60%. [c] Determined by MALLS-SEC. [d] Determined by ^{1}H-NMR. [e] Determined by fitting the SEC traces to the sum of two Gaussian distributions, the results of which are given in the Appendices (Figure A.1.2).

optimize the molecular weight distribution of the diblock. The results are listed in Table 2.4.

By comparing entries 2, 3 and 1, it is clear that the homopolymer percentage in the final diblock has a significant dependence on the ligand: using dNbpy as the ligand gives much lower dispersity than using HMTETA as the ligand. Compared with entries 2 and 3, in entries 4 and 5, the initiator and the catalyst were changed simultaneously in the first step, because *p*-TsCl/CuBr is reported to be a more efficient combination for the polymerization of methacrylates.[29,30] In entry 6, a lower temperature was used for the first step, because the chain propagation rate constant (k_p) is smaller at lower temperature, possibly resulting in a higher k_{deact}/k_p and k_i/k_p ratio. Nevertheless, entries 2 through 6 all have a homopolymer percentage of 10 – 14%, indicating that these condition changes (intiator, catalyst, and temperature) only have little impact on the dispersity of the final diblock copolymer.

2.4. Chapter Summary

This chapter summarizes the synthesis of H- and D- block copolymers and ionic liquids. Specifically, much effort was spent on the block copolymerization of MMA and *n*-BMA from both directions. By using RAFT polymerization starting with PMMA block, two series of PMMA-*b*-PnBMA diblock copolymers were successfully prepared with narrow dispersity, confirmed by SEC characterization. The molecular weight of each block of these copolymers were also determined, using SEC and ^{1}H-NMR spectroscopy. Additionally, six PMMA-*b*-dPnBMA copolymers were also synthesized, with their dPnBMA block lengths matching the length of PnBMA blocks in the protonated copolymers. RAFT polymerization from the other direction (*n*-BMA to MMA) proved to be problematic: the same reaction procedure gives much broader distribution for the resulting PnBMA-*b*-PMMA copolymers, with significant amount of

homopolymers; ATRP gives somewhat better results, but still cannot completely avoid the contamination by homopolymers.

2.5. References

(1) Lee, H.-N.; Lodge, T. P. *J. Phys. Chem. B* **2011**, *115*, 1971-1977.

(2) Hoarfrost, M. L.; He, Y.; Lodge, T. P. *Macromolecules* **2013**, *46*, 9464-9472.

(3) Wiley, R. H.; Brauer, G. M. *J. Polym. Sci.* **1948**, *3*, 455-461.

(4) Unger, R.; Beyer, D.; Donth, E. *Polymer* **1991**, *32*, 3305-3312.

(5) Varshney, S. K.; Jérôme, R.; Bayard, P.; Jacobs, C.; Fayt, R.; Teyssié, P. *Macromolecules* **1992**, *25*, 4457-4463.

(6) Reuter, H.; Berlinova, I.V.; Höring, S.; Ulbricht, J. *Eur. Polym. J.* **1991**, *27*, 673-680.

(7) Baskaran, D.; Chakrapani, S.; Sivaram, S. *Macromolecules* **1995**, *28*, 7315-7317.

(8) Schreiber, H. *Makromol. Chem.* **1960**, *36*, 86-88.

(9) Lochmann, L.; Rodová, M.; Petránek, J.; Lím, D. *J. Polym. Sci., Polym. Chem. Ed.* **1974**, *12*, 2295-2304.

(10) Kunkel, D.; Müller, A. H. E.; Lochmann, L.; Janata, M. *Makromol. Chem., Macromol. Symp.* **1992**, *60*, 315-326.

(11) Litvinenko, G.; Müller, A. H. E. *Macromolecules* **1997**, *30*, 1253-1266.

(12) Kato, M.; Kamigaito, M.; Sawamoto, M.; Higashimura, T. *Macromolecules* **1995**, *28*, 1721-1723.

(13) Wang, J.-S.; Matyjaszewski, K. *J. Am. Chem. Soc.* **1995**, *117*, 5614-5615.

(14) Rizzardo, E.; Meijs, G. F.; Thang, S. H. *Macromol. Symp.* **1995**, *98*, 101-123.

(15) Rizzardo, E; Chong, Y. K.; Evans, R. A.; Moad, G.; Thang, S. H. *Macromol. Symp.* **1996**, *111*, 1-12.

(16) Chiefari, J.; Chong, Y. K.; Ercole, F.; Krstina, J.; Jeffery, J.; Le, T. P. T.; Mayadunne, R. T. A.; Meijs, G. F.; Moad, C. L.; Moad, G.; Rizzardo, E.; Thang, S. H. *Macromolecules* **1998**, *31*, 5559-5562.

(17) Manders, B. G.; Smulders, W.; Aerdts, A. M.; van Herk, A. M. *Macromolecules* **1997**, *30*, 322-323.

(18) Bonhôte, P.; Dias, A.-P.; Papageorgiou, N.; Kalyanasundaram, K.; Grätzel, M. *Inorg. Chem.* **1996**, *35*, 1168-1178.

(19) Dzyuba, S. V.; Li, S.; Bartsch, R. A. *J. Heterocyclic Chem.* **2007**, *44*, 223-225.

(20) Zimm, B. H. *J. Chem. Phys.* **1948**, *16*, 1099-1116.

(21) Hiemenz, P. C.; Lodge, T. P. *Polymer Chemistry (2nd Ed.)*, CRC Press, Taylor & Francis Group: Boca Raton, FL, 2007.

(22) Numasawa, N.; Hamada, T.; Nose, T. *J. Polym. Sci., Polym. Lett. Ed.* **1985**, *23*, 1−4.

(23) Hoarfrost, M. L.; He, Y.; Lodge, T. P. *Macromolecules* **2013**, *46*, 9464-9472.

(24) Heyboer, J.; Staverman, A. J. *Rec. trav. chim.* **1950**, *69*, 787-798.

(25) Barner-Kowollik, C. *Handbook of RAFT Polymerization*, Wiley-VCH: Weinheim, 2008.

(26) Chong, B. Y. K.; Le, T. P. L.; Moad, G.; Rizzardo, E.; Thang, S. H. *Macromolecules* **1999**, *32*, 2071-2074.

(27) Vana, P.; Davis, T. P.; Barner-Kowollik, C. *Macromol. Theory Simul.* **2002**, *11*, 823-835.

(28) Matyjaszewski, K. *Controlled/Living Radical Polymerization: Progress in ATRP*. ACS Symposium Series, American Chemical Society, 2009.

(29) Grimaud, T.; Matyjaszewski, K. *Macromolecules* **1997**, *30*, 2216-2218.

(30) Wang, J.-L.; Grimaud, T.; Matyjaszewski, K. *Macromolecules* **1997**, *30*, 6507-6512.

(31) Karanam, S.; Goossens, H.; Klumperman, B.; Lemstra, P. *Macromolecules* **2003**, *36*, 3051-3060.

(32) Davis, K. A.; Matyjaszewski, K. *Chin. J. Polym. Sci.* **2004**, *22*, 195-204.

Chapter 3
Fundamentals of Scattering Techniques

In general, two methods are frequently used to study the size and morphology of block copolymer micelles: one is direct imaging with microscopy, and the other is indirect observation using scattering techniques. Both methods have their own advantages and disadvantages. TEM, for example, is an imaging technique with sub-nanometer resolution, typically used in the study of block copolymer micelles, as well as other block copolymer self-assembly structures. The most significant advantage for TEM is that it can provide direct visualization of nano-sized structures in the sample, and does not rely on any assumptions. Although one TEM picture can only reflect a small portion of the sample, nevertheless, the ensemble-averaged information can still be obtained by taking multiple pictures across the sample.

Scattering, on the other hand, can readily provide the averaged information of the whole specimen, embodied in the change of scattering intensity as a function of scattering angle. Compared with microscopic techniques such as TEM, they are indirect methods, because the translation from scattering intensity to structure is based on mathematics; most often than not, these “translations” require some understanding, or educated guess at least, on the systems studied. For example, in the case of SAXS, the morphology of the micelles has to be determined first based on the shape of the scattering profiles, before any fitting can be used to obtain the micelle radius. Despite such drawbacks, scattering techniques are still very powerful in the study of polymers, due to their extremely high versatility, as well as the relative ease of sample preparation. Here, consider a general case: most of the block copolymers and the solvents are composed of C, H, O and N. Under such a scenario, there will not be significant contrast between polymer and solvent in the case of TEM, since the contrast of TEM solely comes from the electron density

difference, which these light atoms lack. In comparison, scattering is more versatile: light scattering can be used when the refractive indices of the polymer and the solvent are different enough, and neutron scattering can be used when either of the two is fully or partially deuterated.

In this study, DLS, SAXS and SANS are used to provide insight into the thermodynamic and kinetic properties of the micelles. As Chapters 4, 5 and 6 will primarily deal with the scattering results, I find it appropriate to give a general introduction to these techniques.

3.1. General Theories of Scattering

Scattering Vector and Bragg Diffraction

A propagating wave will be deflected from its original trajectory when it encounters an object (scatterer), which is called scattering. More generally, scattering takes place whenever a beam of light, X-ray, or neutrons passes through a non-uniform medium. This is because the scattering waves emanated from a perfect array of atoms/particles will completely cancel out each other ("pairing-off"), leading to no net scattering. Non-uniformity, on the other hand, causes an extra scatterer to be present in, or a scatterer missing from such regular array of scatterers, which makes the "pairing-off" relationship fail, and thereby causing some net scattering.

Typically, the function of wave can be expressed as

$$\mathbf{E} = \mathbf{E_0}\cos(\omega t - \mathbf{k}\cdot\mathbf{r}) = \mathbf{E_0}\exp[\mathrm{i}(\omega t - \mathbf{k}\cdot\mathbf{r})] \qquad (3.1)$$

where $\mathbf{E_0}$ and ω are the amplitude and frequency of the wave, $\mathbf{k}$ is the wave vector, which represents the propagating direction of the wave, and $\mathbf{r}$ is the position. Note that all the variables in bold are vectors, and they have directions. The nature of the waves lies in the

cosine function, indicating that the amplitude of the waves is distributed in a cosine pattern over the time and space domains. It is worth pointing out that the other expression with the imaginary number i has the same meaning as the cosine function, but is mathematically more convenient when doing interference calculations.

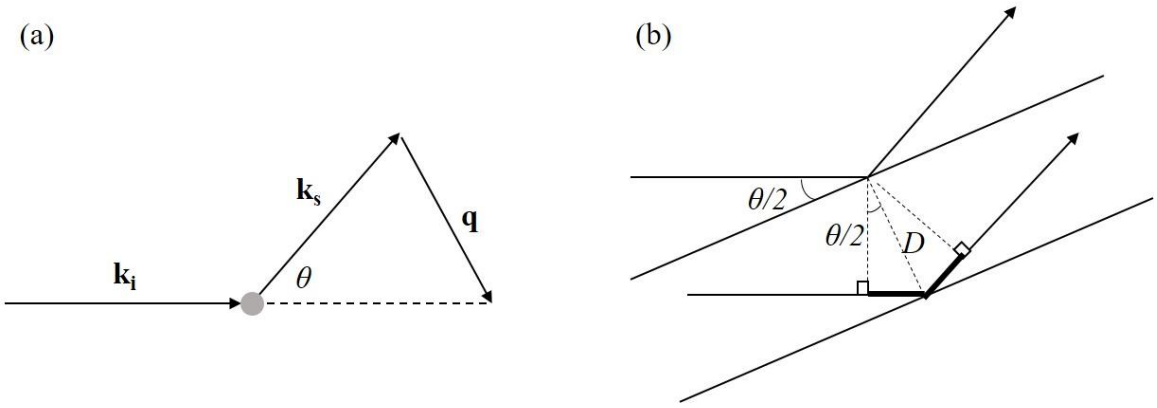

Figure 3.1. Schematic geometry of (a) scattering from a single scatterer, and (b) Bragg diffraction.

Now, we can consider the scattering from a single scatterer (with no actual size and shape), the geometry of which is displayed in Figure 3.1a. The subscripts "i" and "s" stand for "incident" and "scattering", respectively. The scattering vector **q** is defined as $\mathbf{k_i} - \mathbf{k_s}$, reflecting the momentum change before and after scattering. Based on the geometry, it is easy to obtain

$$q = |\mathbf{q}| = 2|\mathbf{k_i}|\sin(\frac{\theta}{2}) = \frac{4\pi}{\lambda}\sin(\frac{\theta}{2}) \qquad (3.2)$$

assuming $|\mathbf{k_i}| = |\mathbf{k_s}|$, where λ is the wavelength. In fact, this assumption may or may not be true: when $|\mathbf{k_i}| = |\mathbf{k_s}|$, *i.e.*, the wavelength does not change, there is no energy transfer between the wave and the scatterer, and this is called elastic scattering; its opposite case is known as inelastic scattering, in which eq 3.2 can no longer be applied. DLS, SAXS and SANS are all good examples of elastic scattering (or quasi-elastic scattering).[1,2]

The scattering vector q has fundamental significance in scattering, especially small-angle scattering techniques, because the scattering intensity $I(q)$ contains numerous useful information about the size, shape, and spatial distribution of the scatterers. The reason is briefly discussed as follows. By comparing eq 3.2 and the well-known Bragg equation: $m\lambda = 2D\sin(\theta/2)$, the following relationship between q and D can be obtained:

$$q = \frac{2\pi m}{D} \tag{3.3}$$

where D is the distance between the two neighboring planes (Figure 3.2b), and m is an integer. Therefore, according to eq 3.3, we know that when q coincides with $2\pi m/D$, there will be significant Bragg diffraction, indicated by a maximum on the $I(q)$ *vs* q plots. Based on this relation, q is also known as the "reciprocal lattice vector", which serves as the Fourier variable in reciprocal space conjugate to the positions of the scatters in real space. As $q \sim D^{-1}$, lower q is required to probe bigger objects/periodicity, whereas higher q is required to probe smaller objects/periodicity.[1,3]

Form Factor

To this end, the scattering from an infinitely small object (compared to the wavelength) has been discussed; now, consider the case where the size of the object is a significant fraction of the wavelength. This object can be a polymer chain, a micelle core, or something else, which is composed of many monomers. Under such scenario, the waves scattered from each monomer will have some destructive interference, thereby resulting in a net reduction in the scattering intensity. This part of reduction can be characterized by the form factor, $P(q)$ (or $P(\theta)$, commonly used in light scattering).

In light scattering, the form factor $P(q)$ is defined as the actual excess scattering intensity ($I_{ex,actual}(q)$) divided by Rayleigh excess scattering intensity ($I_{ex,Rayleigh}(q)$) at q.

According to the Zimm Equation (eq. 2.1), at infinite dilution, $2A_2c$ approaches zero; therefore, the following approximation can be achieved:

$$R_q = KcMP(q) \sim I_{\text{ex,actual}}(q) \tag{3.4}$$

Note that $I_{\text{ex,actual}}(q)$ is always smaller than $I_{\text{ex,Rayleigh}}(q)$ ($\sim KcM$); therefore, $0 \le \text{P(q)} \le 1$.[4]

In small-angle scattering, the definition of the form factor is similar to that in light scattering; although it takes a more general form, but the relation of $I(q) \sim P(q)$ still persists. Mathematically, for an object with n monomers, the absolute scattering intensity can be written as:

$$I(q) = \frac{\Delta\rho^2 V_{\text{P}}^2}{V} \sum_{i=1}^{n} \sum_{j=1}^{n} \left\langle \exp(-\text{i}\mathbf{q}\mathbf{r}_{\mathbf{ij}}) \right\rangle \tag{3.5}$$

in which $\Delta\rho$ is the contrast of the scattering length density between the object and the background, V_{p} and V are the volume of the object and the sample volume, respectively. The double summation in eq. 3.5 takes the interference between each pair of monomers in the object into consideration, and the angular bracket in the double summation term indicates the ensemble average.[5,6] Based on the equation above, $P(q)$ is defined as

$$P(q) = \frac{1}{n^2} \sum_{i=1}^{n} \sum_{j=1}^{n} \left\langle \exp(-\text{i}\mathbf{q}\mathbf{r}_{\mathbf{ij}}) \right\rangle \tag{3.6}$$

Therefore,

$$I(q) = \frac{\Delta\rho^2 V_{\text{P}}^2}{V} n^2 P(q) \tag{3.7}$$

Eq. 3.6 is the more general definition of the form factor, which is widely used in the small-angle scattering techniques. The exact form of eq. 3.6 depends on how to expand the double summation term mathematically, which is further determined by the geometry of the object. Table 3.1 lists some common form factors, and more can be found in the literature.[5–8]

Table 3.1. Form Factors of Some Common Geometry

Geometry	Parameters	Function
Gaussian chain	radius of gyration (R_g)	$P(q) = \frac{2}{(qR_g)^4}[\exp(-q^2R_g^2) + 1 - q^2R_g^2]$
Sphere	radius of gyration (R_g)	$P(q) = \left[\frac{3J_1(qR_g)}{qR_g}\right]^2$, $J_1(x) = \frac{\sin x - x\cos x}{x^2}$
Cylinder	radius (R), height (L), and an orientation parameter (α)	$P(q,\alpha) = \left[\frac{\sin(qL\cos\alpha/2)}{qL\cos\alpha/2}\right]^2\left[\frac{2J_1(qR\sin\alpha)}{qR\sin\alpha}\right]^2$, $J_1(x) = \frac{\sin x - x\cos x}{x^2}$

In Table 3.1, we can see that for Gaussian chain, when qR_g approaches zero, $P(q) \approx 1-q^2R_g^2/3$. In fact, $\lim_{qR_g \to 0} P(q) = 1 - q^2R_g^2/3$ is true no matter what the exact form factor is.[1] Therefore, the q range in scattering is typically divided into four regimes, each with its own characteristics:

(*i*) $qR_g << 1$, this regime is referred to as the Rayleigh limit. In this regime, $R_g << \lambda$, the interference among different parts of the object is insignificant, and the object can be taken as an isotropic scatterer.

(*ii*) $qR_g < 1$, this regime is referred to as the Guinier regime,[9] in which $I(q)$ always has a linear dependence with q^2 (with slope = $-R_g^2$), regardless of the geometry. This q range provides useful information on the size of the particle, however, no information about the shape can be obtained.

(*iii*) $qR_g \geq 1$, this regime is referred to as the fractal regime, in which the detailed structural information of the object can be reflected. The mass fractal regime will be first reached, which gives the shape information; as qR_g is further increased to much larger

than 1, the surface fractal regime is then attained, providing the information on surface roughness of the object.[10,11]

For a light scattering experiment, the wavelength of a red laser is 633 nm, and a polymer micelle, for example is on the order of 10 nm in radius; therefore, $qR_g \leq (4\pi/\lambda)R_g = 0.2 < 1$, thus the detection q range of light scattering falls in the Guinier regime. On the other hand, SAXS and SANS have the wavelength of one to several angstroms, and $(4\pi/\lambda)\, R_g \approx 1200 >> 1$ in the case of $\lambda = 0.1$ nm. This is the reason why SAXS and SANS typically use detectors with very small scattering angles ($\theta = 0.1 - 10°$) to probe the q ranges of interest.

Structure Factor

Eq. 3.5 neglects inter-particle contributions to the scattering intensity, which is justified by the assumption of infinite dilution: when the concentration of the objects is low enough, the average distance between any two objects are much bigger than the wavelength, therefore, the probability of constructive and destructive interference is equal. However, in real samples, this inter-particle contribution needs to be considered, which is characterized by the structure factor $S(q)$.

In a sample volume of V, assuming there are N identical objects, and each of them have n monomers, the scattering intensity can be written as:

$$I(q) = \frac{\Delta\rho^2 V_P^2}{V} \sum_{\alpha=1}^{N} \sum_{\beta=1}^{N} \sum_{j=1}^{n} \sum_{k=1}^{n} \left\langle \exp(-i\mathbf{q}\mathbf{r}_{\alpha j \beta k}) \right\rangle \tag{3.8}$$

This quadruple summation takes into consideration the interference between any two monomers on the same, or different objects, hence the total number of interferences is $nN(nN-1) \approx n^2N^2$. These n^2N^2 interferences can be further divided into the Nn^2 intra-particle, and the $N(N-1)n^2$ inter-particle terms:

$$I(q) = \frac{\Delta\rho^2 V_P^2}{V}\left\{\sum_{\alpha}^{N}\sum_{\beta=\alpha}^{N}\sum_{j=1}^{n}\sum_{k=1}^{n}\left\langle \exp(-i\mathbf{q}\mathbf{r}_{\alpha j\beta k})\right\rangle + \sum_{\alpha}^{N}\sum_{\beta\neq\alpha}^{N}\sum_{j=1}^{n}\sum_{k=1}^{n}\left\langle \exp(-i\mathbf{q}\mathbf{r}_{\alpha j\beta k})\right\rangle\right\}$$
$$= \frac{\Delta\rho^2 V_P^2}{V}\left\{N\sum_{j=1}^{n}\sum_{k=1}^{n}\left\langle \exp(-i\mathbf{q}\mathbf{r}_{1j1k})\right\rangle + N^2\sum_{j=1}^{n}\sum_{k=1}^{n}\left\langle \exp(-i\mathbf{q}\mathbf{r}_{1j2k})\right\rangle\right\} \quad (3.9)$$

In the curly bracket, the first term is essentially $Nn^2P(q)$, whereas the second term can be modified as

$$\sum_{j=1}^{n}\sum_{k=1}^{n}\left\langle \exp(-i\mathbf{q}\mathbf{r}_{1j2k})\right\rangle = \sum_{j=1}^{n}\sum_{k=1}^{n}\left\langle \exp(-i\mathbf{q}(-\mathbf{r}_{1j} + \mathbf{R}_{12} + \mathbf{r}_{2k})\right\rangle$$
$$= \sum_{j=1}^{n}\left\langle \exp(i\mathbf{q}\mathbf{r}_{1j})\right\rangle \cdot \left\langle \exp(-i\mathbf{q}\mathbf{R}_{12})\right\rangle \cdot \sum_{k=1}^{n}\left\langle \exp(-i\mathbf{q}\mathbf{r}_{2k})\right\rangle \quad (3.10)$$

by applying the vector operation shown in Figure 3.2.

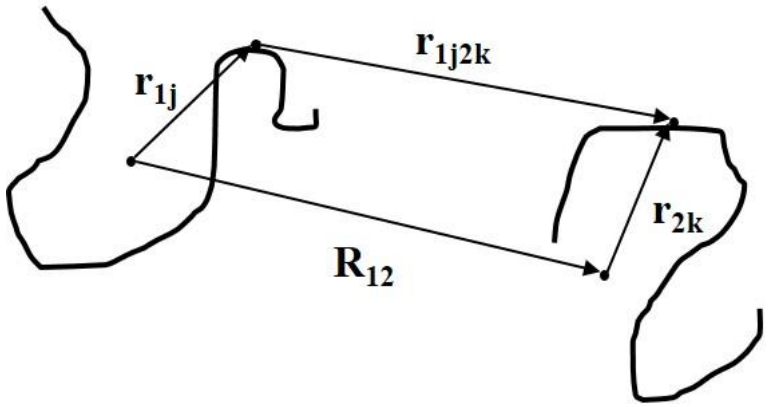

Figure 3.2. Schematic illustration of the vector relationship used in eq. 3.10 (adapted from Ref 5).

In eq. 3.10, the second summation is defined as *n*-fold of the form factor amplitude, $nF(q)$; then the first summation is obviously the conjugate of $nF(q)$, denoted as $nF^*(q)$. We then define the inter-particle structure factor, $S(q)$:

$$S(q) = \frac{1}{N}\sum_{\alpha,\beta}^{N}\left\langle \exp(-i\mathbf{q}\mathbf{R}_{\alpha\beta})\right\rangle = \frac{1}{N}\left[N + N^2\left\langle \exp(-i\mathbf{q}\mathbf{R}_{12})\right\rangle\right] \quad (3.11)$$

Therefore, we have

$$\left\langle \exp(-i\mathbf{qR}_{12}) \right\rangle = \frac{1}{N}\left[S(q)-1\right] \tag{3.12}$$

By introducing the results of eqs. 3.10 and 3.12, eq. 3.9 can be rewritten as

$$\begin{aligned} I(q) &= \frac{\Delta\rho^2 V_P^2}{V}\left\{Nn^2 P(q) + Nn^2\left|F(q)\right|^2\left[S(q)-1\right]\right\} \\ &= \frac{\Delta\rho^2 V_P^2}{V} Nn^2 P(q)\left\{1+\frac{\left|F(q)\right|^2}{P(q)}\left[S(q)-1\right]\right\} \end{aligned} \tag{3.13}$$

It is worth noticing that $|F(q)|^2 = P(q)$ when the particles are dense and isotropic; in this case, $I(q) \sim P(q)S(q)$ can be applied.[5]

Eq. 3.13 is widely used in small-angle scattering to fit the data from different systems, including homopolymer chains, micelles, nanoparticles, and many others. The specific $P(q)$ and $S(q)$ functions used for dilute micelle solutions will be further discussed in Chapter 4.

3.2. Small-Angle X-ray Scattering (SAXS)

SAXS is a powerful technique for investigating structures with various length scales, all the way from one to several hundreds of nanometers. With the advent of synchrotrons, SAXS can be performed with a higher beam flux as well as a better resolution (resulted from narrower wavelength distribution of the beam), and is now widely used in the field of colloids, polymers, proteins and pharmaceuticals. In this section, brief introduction will be given on the calculation of the scattering length density in SAXS, as well as its instrument setup.

Scattering Length Density in SAXS

X-ray is a form of high-energy electromagnetic radiation, which can be scattered when interacting with the electrons in atoms. In SAXS, the scattering length density (a measure of the strength of interaction between the beam and the scatterers) of a given material is proportional to its electron density:

$$\rho_{\mathrm{SAXS}} = d_{\mathrm{e}} r_{\mathrm{e}} = \frac{n_{\mathrm{e}}}{v} r_{\mathrm{e}} = \frac{n_{\mathrm{e}} \rho N_{\mathrm{A}}}{M} r_{\mathrm{e}} \tag{3.14}$$

where n_{e} and v are the total number of electrons in the molecule, and the volume of the molecule, respectively; $r_{\mathrm{e}} = 2.81 \times 10^{-13}$ cm is the classical radius of the electron.[12]

Table 3.2. Scattering Length Density of Some Common Polymers and Solvents

Material	Molecular Formula	Density (g/cm^3)	ρ_{SAXS} (10^{-6} Å^{-2})
Poly(styrene)	C_8H_8	1.04	9.52
Poly(ethylene oxide)	C_2H_4O	1.13	10.26
Poly(methyl methacrylate)	$C_5H_8O_2$	1.18	10.84
Poly(*n*-butyl methacrylate)	$C_8H_{14}O_2$	1.07	9.99
Water	H_2O	1.00	9.47
Squalane	$C_{30}H_{62}$	0.81	7.89
[EMIM][TFSI]	$C_8H_{11}F_6N_3O_4S_2$	1.52	13.16
[BMIM][TFSI]	$C_{10}H_{15}F_6N_3O_4S_2$	1.43	12.48

Note that in eq. 3.5, $I(q) \sim \Delta\rho^2 \sim (\rho_{\mathrm{SAXS,polymer}} - \rho_{\mathrm{SAXS,solvent}})^2$, *i.e.*, the scattering intensity from a given polymer/solvent system is very sensitive to their scattering length density difference; therefore, it will be desirable to have this contrast as large as possible.

According to eq. 3.14, r_e and the Avogadro number N_A are constants, and n_e/M are typically close to 1/2 for most of the molecules (remember that for most atoms, their number of electrons is half of their molar mass), therefore, the density of the material (ρ) is what really matters. Table 3.2 summarizes the SAXS scattering length density of some common polymers and solvents, as well as the ones that are used in this study. Among all, we can see that the scattering length density contrast between PMMA, PnBMA and the ionic liquids is quite large, because of this significant density difference.

Instrumentation of SAXS

Here, I will use the 5ID-D beamline of the DuPont−Northwestern−Dow Collaborative Access Team (DND-CAT) at the Advanced Photon Source, Argonne National Laboratory as an example. In this beamline, the X-ray has negligible wavelength spread ($\Delta\lambda/\lambda \sim 10^{-4}$) after passing through a series of monochromation, collimation and polarization devices. The scattered beam is detected by a two dimensional charge-coupled device (CCD) detector, which converts light signal to electric signal, and records the latter in a two dimensional pixel array. Because synchrotron SAXS has much larger beam flux then normal SAXS instruments, the collection time required for each sample is usually within several seconds.

Besides the small-angle detector, some SAXS instruments (5ID-D beamline, for example) are also equipped with medium-angle and wide-angle detectors, enabling the simultaneous collection of the scattering signal in a very broad q range.[13] As mentioned in the previous section, other ways to tune the q range include tuning the sample to detector distance (SDD) and tuning the wavelength.

3.3. Small-Angle Neutron Scattering (SANS)

SANS shares the same scattering theory as SAXS, and is also used to probe the internal structure of a variety of systems at nanometer scale. Compared with SAXS, SANS has both pros and cons, which will be discussed at the end of this section, following the introduction of scattering length density and instrument setup.

Scattering Length Density in SANS

Similar to eq. 3.14, in SANS, the scattering length density of a given material can be written as

$$\rho_{\mathrm{SANS}} = \frac{\sum b_i}{v} = \frac{\sum b_i}{M}\rho N_{\mathrm{A}} \tag{3.15}$$

where b_i is the scattering length of the i^{th} atom in the molecule; the other parameters have the same definition as in eq. 3.14. However, the scattering length of atoms in neutron scattering is not proportional to their atomic number; instead, it is isotope-dependent.

Table 3.3 lists the scattering lengths (b) of isotopes that are relevant to this study.[14] Most notably, hydrogen (H) and deuterium (D) have significantly different scattering lengths. (It is worth mentioning that H is among the few isotopes that have negative scattering length, because neutrons scattered by H are 180° out of phase compared to those scattered by other atoms.) Therefore, by substituting part of the H atoms in either solvent or polymer with D atoms, large contrast and decent scattering intensity can be achieved in SANS.

Table 3.3. Neutron Scattering Length of Some Common Isotopes

Isotope	**H (^{1}H)**	**D (^{2}H)**	**^{12}C**	**^{14}N**	**^{16}O**	**^{19}F**	**^{32}S**
***b* (10^{-15} m)**	−3.74	6.67	6.65	9.37	5.80	5.65	2.80

Instrumentation of SANS

Neutrons in SANS are generated by nuclear reactions; after going through monochromation and collimation processes, the neutron beam is scattered by the sample, and then reaches the detector. The details of SANS instruments can be found in Ref 5. Compared with X-ray, the neutron beam has the following two characteristics: (*i*) broader wavelength spread ($\Delta\lambda/\lambda \sim 0.1 - 0.2$), and (*ii*) much lower beam intensity. Therefore, the smearing of SANS signal is inevitable, and the collection time required for each SANS sample is typically on the order of several minutes to several hours, hundreds of times more than the time spent in SAXS experiments.

In sum, the pros of SAXS lie in the high beam flux and low smearing, which allows accurate measurement of scattering profiles with reasonable time cost. On the other hand, the pros of SANS include: (*i*) good contrast between particles and background (or between particles and particles, as in the case of this study) that can be readily achieved by isotopic substitution; (*ii*) friendliness to biomacromolecules, which are easily subject to beam damage in SAXS; and (*iii*) relative ease for absolute calibration. Therefore, in the study of micelle structures and sizes, SAXS is used as the primary technique, whereas in the study of micelle equilibration kinetics, SANS is the only option (because SAXS cannot tell the difference between a protonated micelle core and a deuterated micelle core).

3.4. Dynamic Light Scattering (DLS)

Static light scattering (SLS) and dynamic light scattering (DLS) are the two major classes of light scattering: in the former, the time-average scattering intensity is recorded and studied, whereas in the latter, information is extracted from the fluctuation of scattering intensity over time.

SLS has already been briefly discussed in Chapter 2, since the molecular weight determination by MALLS-SEC is essentially based on SLS (see eqs. 2.1 – 2.3 in Section 2.2); therefore, this section will mainly introduce the theories and instrument setup of DLS, which is the most frequently used method to investigate the hydrodynamic radius of particles in dilute solution.

The Autocorrelation Function in DLS

Although the excess scattering intensity $I_{ex,actual}$ can be calculated by eq. 3.4, nevertheless, this calculated scattering intensity is only the time-averaged intensity $\langle I(t) \rangle$. In fact, as can be seen in Figure 3.3, the real-time scattering intensity is constantly fluctuating around this average, due to concentration fluctuations in the solution, which arise from the motion of the particles. Empirically, we can imagine that the bigger the particles, the slower they move, and thus there will be less intensity fluctuation over a certain period of time. The working principle of DLS is indeed established on this relationship.

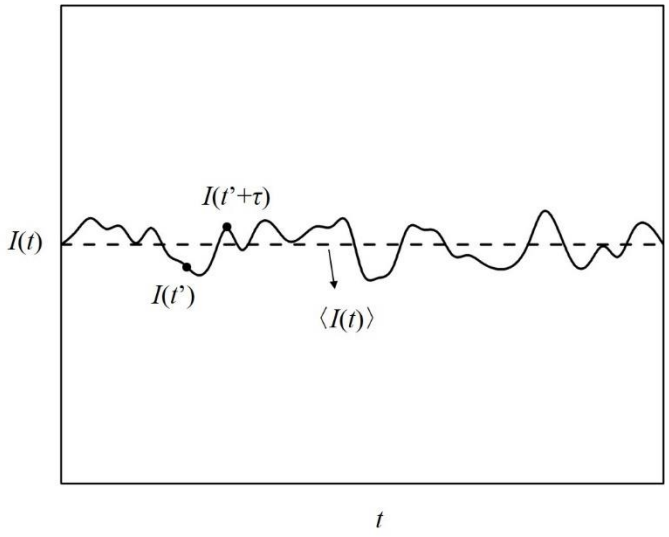

Figure 3.3. Schematic illustration of the scattering intensity fluctuation over time.

In DLS, the autocorrelation function $C(\tau)$ is defined as

$$C(\tau) = \lim_{t\to\infty} \frac{1}{t} \int_0^t I(t')I(t'+\tau)\mathrm{d}t' = \langle I(t')I(t'+\tau)\rangle \tag{3.16}$$

In eq. 3.16, the term with angular brackets represent the ensemble average of the product of the scattering intensities at two time points, which differ by τ seconds. Because the scattering intensity is phase dependent, when τ is close to zero, the $I(t')$ and $I(t'+\tau)$ will have exactly the same phase (in phase), and their product will be constructive. In the opposite scenario, when τ approaches infinity, the probability of whether $I(t')$ and $I(t'+\tau)$ are in phase or 180° out of phase will be 50-50, and their product will have no correlation. Therefore, as τ increases, $C(\tau)$ will monotonically decrease, and finally approaches $\left\langle \left| I(t') \right|^2 \right\rangle$.[15]

The autocorrelation function $C(\tau)$ can be normalized to give $g^{(2)}(\tau)$, and then converted to $g^{(1)}(\tau)$ by the Siegert relation:[16]

$$g^{(2)}(\tau) = \frac{C(\tau)}{\left\langle \left| I(t') \right|^2 \right\rangle} = 1 + \beta \left| g^{(1)}(\tau) \right|^2 \tag{3.17}$$

in which β is the coherence factor between 0 and 1.

For monodisperse particles, $g^{(1)}(\tau)$ takes the single exponential form of $g^{(1)}(\tau) = \exp(-\Gamma\tau) = \exp(-q^2 D\tau)$, where q is the scattering vector, and D is the mutual diffusion coefficient of the particles and the solvent, which is approximately equal to the tracer diffusion coefficient of the solvent at the limit of infinite dilution of the particles. According to Stokes-Einstein equation, the hydrodynamic radius (R_h) of the particles can be obtained by

$$R_h = \frac{kT}{6\pi\eta_s D} \tag{3.18}$$

assuming isotropic solution, where k, T and η_s are the Boltzmann constant, temperature, and the viscosity of the solvent, respectively.

Hydrodynamic Radius Distribution for Polydisperse Particles

For polydisperse particles, $g^{(1)}(\tau)$ can be expressed as

$$g^{(1)}(\tau) = \int G(\Gamma)\exp(-\Gamma\tau)\mathrm{d}\Gamma \tag{3.19}$$

where $G(\Gamma)$ is the distribution of the decay rates (equivalent to that of hydrodynamic radius, note that Γ and R_h are one-to-one correspondent). In order to mathematically solve the $G(\Gamma)$, two strategies are used. The first one is to perform inverse Laplace transform on the $g^{(1)}(\tau)$ function, using some algorithms, for example, CONTIN[17,18] and REPES.[19] The advantage for using inverse Laplace transform to analyze data is that it does not require any prior knowledge of what the particle R_h distribution is like. However, it is very likely that the $G(\Gamma)$ determined by these algorithms have multiple sets of solutions, and the noise in scattering signals further complicates the problem, which may cause the R_h distribution given by this method to significantly deviate from the real value.

The second strategy is to fit $g^{(1)}(\tau)$ to some model formula, such as the cumulant function (eq. 3.20),[20] and multimodal distribution function (eq. 3.21):

$$g^{(1)}(\tau) = \exp\left\{\left(-\bar{\Gamma}\tau\right)\left[1+\frac{1}{2!}\frac{\mu_2}{\bar{\Gamma}^2}\left(\bar{\Gamma}\tau\right)^2-\frac{1}{3!}\frac{\mu_3}{\bar{\Gamma}^3}\left(\bar{\Gamma}\tau\right)^3+\ldots\right]\right\} \tag{3.20}$$

$$g^{(1)}(\tau) = A_1\exp\left(-\bar{\Gamma}_1\tau\right)+A_2\exp\left(-\bar{\Gamma}_2\tau\right)+\ldots \tag{3.21}$$

The advantage of these fittings is that one can directly extract the information of the particle polydispersity (represented by $\mu_2/\bar{\Gamma}^2$ in eq. 3.20), or the relative number of particles in each population (represented by A_1/A_2 in eq. 3.21). Nevertheless, prior knowledge of the sample is required before performing the fitting.

Instrumentation of DLS

DLS instrument is commercially available; it is mainly composed of a laser source, a detector equipped on goniometer, an autocorrelator, and some supplementary parts. Different from SAXS and SANS, DLS does not require a two dimensional detector; instead, the detector (usually a photomultiplier) can be seen as a spot, and only collects the scattering intensity at a designated scattering angle at one time. The autocorrelator is the key part of a DLS instrument: it can save the digitized scattering intensity of $I(t'+\tau)$ at numerous τ's, and automatically calculates the instantaneous autrocorrelation functions instead of the discrete intensities.

3.5. References

(1) Hiemenz, P. C.; Lodge, T. P. *Polymer Chemistry (2nd Ed.)*, CRC Press, Taylor & Francis Group: Boca Raton, FL, 2007.

(2) Higgins, J. S.; Benoit, H. C. *Polymers and Neutron Scattering*, Oxford University Press: New York, 1994.

(3) Guinier, A.; Fournet, G. *Small-Angle Scattering of X-rays*, John Wiley & Sons: New York, 1955.

(4) Zimm, B. H. *J. Chem. Phys.* **1948**, *16*, 1099-1116.

(5) Hammouda, B. *Probing Nanoscale Structures – The SANS Toolbox*, 2009. (http://www.ncnr.nist.gov/staff/hammouda/the_SANS_toolbox.pdf)

(6) Hammouda, B. *A Tutorial on Small-Angle Neutron Scattering from Polymers*, 1995. (https://www.ncnr.nist.gov/programs/sans/pdf/polymer_tut.pdf)

(7) Burchard, W. *Adv. Polym. Sci.* **1983**, *48*, 1-124.

(8) Hammouda, B. *Adv. Polym. Sci.* **1993**, *106*, 87-133.

(9) Guinier, A. *Ann. Phys.* **1939**, *12*, 161-237.

(10) Roe, R. *Methods of X-ray and Neutron Scattering in Polymer Science*, Oxford University Press: New York, 2000.

(11) Rubinstein, M.; Colby, R. H. *Polymer Physics*, Oxford University Press: Oxford, 2003.

(12) Curtis, L. J. *Atomic Structure and Lifetimes: A Conceptual Approach*, Cambridge University Press: Cambridge, 2003.

(13) Weigand, S. J.; Keane, D. T. *Nucl. Instrum. Methods Phys. Res., Sect. A* **2001**, *649*, 61-63.

(14) *Neutron News* **1992**, *3*, 29-37.

(15) Brown, W. *Light Scattering: Principles and Development*, Clarendon Press: Oxford, 1996.

(16) Brown, W. *Dynamic Light Scattering: The Method and Some Applications*, Oxford University Press: New York, 1993.

(17) Provencher, S. W. *Comp. Phys. Commun.* **1982**, *27*, 213-227.

(18) Provencher, S. W. *Comp. Phys. Commun.* **1982**, *27*, 229-242.

(19) Jakeš, J. *Collect. Czech. Chem. Commun.* **1995**, *60*, 1781−1797.

(20) Koppel, D. E. *J. Chem. Phys.* **1972**, *57*, 4814−4820.

Chapter 4

Structure of Micelles in [EMIM][TFSI]

4.1. Introduction

Like small molecule surfactants, A-B diblock copolymers can self-assemble into micellar structures in a selective solvent, with the insoluble B blocks forming the core, surrounded by the solvophilic A blocks as the corona. The structure of spherical micelles can be characterized by the aggregation number (N_{agg}), core radius (R_c), and corona thickness (L_{corona}). A long-standing issue is whether or not there is a universal relationship between these parameters and the degrees of polymerization of the two blocks, N_A and N_B. In order to address this question, many theories have been proposed.[1–13] In the pioneering work of de Gennes,[1] Zhulina and Birshtein,[6] and Halperin and co-workers,[7, 8] scaling analysis was applied to a single micelle, in which the total free energy per chain, F, can be written as $F = F_{interface} + F_A + F_B$. The first term accounts for the free energy of the core-corona interface; the second and the third terms are the free energy contributions of the corona and the core blocks, respectively. Subsequently, the total F is minimized to give the dependence of R_c and N_{agg} on N_A and N_B. Notably, Halperin *et al.* divided micelles into two limiting cases: "hairy" micelles ($N_A >> N_B$) and "crew-cut" micelles ($N_A << N_B$). By omitting F_B in the former case and F_A in the latter, they found that $N_{agg} \sim N_B^{4/5}$ and $R_c \sim N_B^{3/5}$ in the case of hairy micelles, while $N_{agg} \sim N_B$ and $R_c \sim N_B^{2/3}$ in the case of crew-cut micelle.[8] In general, all scaling models suggested that $N_{agg} \sim N_B^{\nu}$ and $R_c \sim N_B^{(1+\nu)/3}$, with $\nu = 0.5 – 1$, under the assumption that the core is devoid of solvent.

Compared with scaling theory, mean-field theory enables a numerical approach, and can also take into account the three relevant Flory-Huggins parameters χ_{AB}, χ_{AS} and χ_{BS}, where the subscript S stands for solvent. Leibler, Orland and Wheeler,[3] and Noolandi and Hong[4,5] separately developed models, which were later elaborated by Nagarajan and Ganesh,[9,10] who provided a numerical dependence of N_{agg} on the corona block length, N_A, in contrast to prediction by scaling models that N_{agg} depends only on N_B. Other detailed approaches, such as Monte-Carlo simulations and other computational methods, are also available.[11,12,13] Extensive reviews in this field can be found elsewhere.[14,15]

In order to test aspects of these theories, many block copolymer/selective solvent systems have been studied using light (static and dynamic) and small-angle (X-ray and neutron) scattering techniques.[16–36] However, most of these studies are not completely quantitative, in terms of testing predictions. Several factors contribute to this. First, the core block should have a low glass transition temperature (T_g), to avoid forming kinetically frozen cores at the experimental temperature, thereby hindering access to thermodynamic equilibrium. Second, the Flory-Huggins parameter χ between the core block and the solvent should be large enough so that the core is not swollen appreciably. Third, the block copolymer should preferentially form simple spherical micelles, with no larger aggregates. Fourth, many studies use static light scattering to determine the molecular weight of the micelle, and thus to calculate N_{agg} and R_c; particularly for the core radius, this is an indirect method and may be less reliable compared with direct structural techniques, such as SAXS, SANS and transmission electron microscopy (TEM).

In this chapter, PMMA-*b*-PnBMA in the ionic liquid [EMIM][TFSI], which features a lower critical solution temperature (LCST), was selected as the model system, as it possesses particularly favorable attributes: (*i*) ease of synthesis and molecular weight control; (*ii*) low T_g of the core block (the T_g of PnBMA is ~ 20 °C),[37] which avoids the

kinetically trapped state of a frozen micelle core; (*iii*) reasonably strong segregation of PnBMA and [EMIM][TFSI]; (*iv*) no evidence of micelle clusters, in contrast to some systems.[20, 21] This choice of block copolymer and solvent also provides a wide composition window to study micelle structural parameters as a function of N_A and N_B. This study with seven samples, all with an identical corona-forming block, should serve as a rigorous test for theory.

4.2. Experimental Section

Materials

The synthetic procedures and characterization results of the PMMA-*b*-PnBMA diblock copolymers have been described in Chapter 2. Therefore, from this chapter on, only a table will be given, which summarizes the characteristics of the polymers used in the study, as can be seen in Table 4.1. The numbers in the brackets refer to the molecular weight of each block in kg/mol.

Preparation of Micelle Solutions

Methylene chloride was used as a cosolvent to dissolve PMMA-*b*-PnBMA; this solution was combined with [EMIM][TFSI] at room temperature in a predetermined ratio, and then purged with nitrogen overnight to slowly remove the cosolvent. The resulting solution was dried at 50 °C under vacuum (< 100 mTorr) for at least 12 h prior to use. The micelle solution had constant mass after vacuum drying, indicating no cosolvent remaining.

Table 4.1. Characteristics of PMMA-*b*-PnBMA Diblock Copolymers

Copolymers	PMMA block M_n (kg/mol)[a]	PnBMA block M_n (kg/mol)[b]	N_{PMMA}[c]	N_{PnBMA}[d]	$Đ$
PMMA-*b*-PnBMA (25-13)	25	13	250	92	1.04
PMMA-*b*-PnBMA (25-24)	25	24	250	169	1.04
PMMA-*b*-PnBMA (25-31)	25	31	250	218	1.05
PMMA-*b*-PnBMA (25-35)	25	35	250	246	1.05
PMMA-*b*-PnBMA (25-44)	25	44	250	310	1.07
PMMA-*b*-PnBMA (25-53)	25	53	250	373	1.07
PMMA-*b*-PnBMA (25-78)	25	78	250	549	1.11

[a] Number average molecular weight of the PMMA block was determined by light scattering detection during SEC, with 0.084 mL/g used as the d*n*/d*c* of PMMA.[38] [b] Number average molecular weight of PnBMA block determined by ^{1}H-NMR spectroscopy. [c] Degree of polymerization of PMMA block. [d] Degree of polymerization of PnBMA block.

Dynamic Light Scattering (DLS)

Dynamic light scattering was used to determine the mean and distribution of the hydrodynamic radius (R_h) of the micelles. The micelle solutions were filtered through 0.2 μm filters, and the DLS tubes were flame-sealed to avoid contact with moisture in air. The samples were measured on a home-built spectrometer, as described elsewhere.[34] The normalized intensity autocorrelation function, $g^{(2)}(t)$, was typically obtained at 90°, then treated by inverse Laplace transform using the Regularized Positive Exponential Sum (REPES) method to obtain the R_h distribution.[39] Most micelle solutions exhibited a monomodal distribution of R_h, and thus the cumulant fitting was used to determine the average decay rate ($\overline{\Gamma}$) and the second cumulant (μ_2), in which $\mu_2 / \overline{\Gamma}^2$ represents the width of distribution.[40] The method for converting $\overline{\Gamma}$ to R_h was described in Section 3.4.

Small-Angle X-ray Scattering (SAXS)

Small-angle X-ray scattering was conducted on the 5ID-D beamline of the DuPont-Northwestern-Dow Collaborative Access Team (DND-CAT) at the Advanced Photon Source, Argonne National Laboratory. The beam energy used was 9 keV, corresponding to a wavelength of 1.38 Å. 2D-SAXS images were collected using a MAR-CCD detector, with the sample-to-detector distance of 5.47 m. Temperature was controlled by an electric heater. Quartz capillary tubes were used for more dilute samples (< 10 wt%); aluminum pans were used for the samples with larger concentrations. The samples were annealed at the designated temperature for at least 5 min before exposure to the beam. A typical duration of beam exposure was 10 – 30 s. The 2D-SAXS images were averaged azimuthally to give one-dimensional $I(q)$ vs q profiles using the data reduction software provided by Argonne National Lab (FIT2D). Subsequently, the solvent background was subtracted from the 1D data, and the resulting intensity profiles were analyzed using a fitting model[41] built in Igor Pro.

Fitting Model for SAXS Data

The scattering form factor of a single micelle with a spherical core and Gaussian corona chains contains four terms: the self-correlation of the core, the self-correlation of the chains, the cross-term between the core and chains, and the cross-term between different chains.[41] The equation can be written as

$$\begin{aligned} P_{\text{mic}}(q) &= N_{\text{agg}}^2 \beta_{\text{core}}^2 A_{\text{core}}^2(q) + N_{\text{agg}} \beta_{\text{corona}}^2 P_{\text{chain}}(q) \\ &+ 2N_{\text{agg}}^2 \beta_{\text{core}} \beta_{\text{corona}} A_{\text{core}}(q) A_{\text{corona}}(q) + N_{\text{agg}}(N_{\text{agg}} - 1) \beta_{\text{corona}}^2 A_{\text{corona}}^2(q) \end{aligned} \tag{4.1}$$

in which q, N_{agg}, β_{core} and β_{corona} are the scattering vector, aggregation number, total excess scattering length of the core block, and total excess scattering length of the corona block, respectively. By definition, $\beta_{\text{core}} = (\rho_{\text{core}} - \rho_{\text{sol}})v_{\text{core-block}}$ and $\beta_{\text{corona}} = (\rho_{\text{corona}} -$

$\rho_{sol})v_{corona\text{-}block}$, where ρ_{core}, ρ_{corona} and ρ_{sol} are the scattering length densities of the core block, corona block and solvent, respectively; $v_{core\text{-}block}$ and $v_{corona\text{-}block}$ are the volumes of one core chain and one corona chain, respectively.

In the first term, for a spherical core with radius R_c and core-corona interface thickness σ_{int}, $A^2_{core}(q)$ can be written as

$$A^2_{core}(q) = \Phi^2(qR_c)\exp(-q^2\sigma^2_{int}) \tag{4.2}$$

where $\Phi(x) = 3(\sin x - x\cos x)/x^3$ is the form factor amplitude of a sphere with a sharp interface. The last exponential term takes into account the "fuzziness" of the interface between core and corona domains.

The second term reflects the correlation between two monomers in the same Gaussian chain, therefore, $P_{chain}(q)$ adapts the form of the Debye function:

$$P_{chain}(q) = \frac{2\left[\exp(-q^2R_g^2) - 1 + q^2R_g^2\right]}{q^4R_g^4} \tag{4.3}$$

where R_g is the radius of gyration of the corona chains. Although in most cases, corona chains of micelles adapt a rather stretched conformation, eq. 4.3 is still accurate enough to include this part of contribution to the form factor.

The last two terms both contain the contribution of corona scattering. The form factor of the corona chains is given as the normalized Fourier transform of the average radial density distribution of the micelle corona, $\rho_{corona}(r)$:

$$A_{corona}(q) = \frac{4\pi\int \rho_{corona}(r)\frac{\sin(qr)}{qr}r^2\mathrm{d}r}{4\pi\int \rho_{corona}(r)r^2\mathrm{d}r}\exp(-q^2\sigma^2_{int}/2) \tag{4.4}$$

In this work, a linear combination of 2 partial cubic *b* spline functions is used as the $\rho_{corona}(r)$, as has been described by Pedersen *et al*.[41,42]

In a real system, the dispersity of the micelle size also has to be taken into account, in which a Gaussian distribution is assumed for the core radius, while the corona chain size (R_g) and the thickness of core-corona interface (σ_{int}) are taken as constants. Under this assumption,

$$D(R_c) = \frac{1}{\sqrt{2\pi}\sigma_R} \exp\left[-\frac{\left(R_c - \langle R_c \rangle\right)^2}{2\sigma_R^2} \right] \tag{4.5}$$

in which $\langle R_c \rangle$ is the average core radius and σ_R is the standard deviation of the core radius. The total scattering intensity now can be written as the following equation:

$$I(q) = \int D(R_c) P_{mic}(q) \mathrm{d}R_c \tag{4.6}$$

Overall, there are seven adjustable parameters in this model: the average micelle core radius (R_c), the aggregation number (N_{agg}), the core-corona interface thickness (σ_{int}), radius of gyration of the corona chains (R_g), standard deviation of the core radius (σ_R), as well as the two fitting parameters (a_1, s) in the $\rho_{corona}(r)$ term. The other five parameters, the core block volume ($v_{core\text{-}block}$), the corona block volume ($v_{corona\text{-}block}$), and the scattering length density of the core (ρ_{core}), corona (ρ_{corona}) and solvent (ρ_{sol}), are fixed. Additionally, an arbitrary prefactor is multiplied to the total scattering intensity, $I(q)$, because the SAXS data were not reduced to an absolute scale. The complete Pedersen model with structure factor can be found in Refs 34 and 42.

4.3. Results and Discussion

DLS

The hydrodynamic radius distributions of the seven PMMA-*b*-PnBMA copolymers in [EMIM][TFSI] at 60 °C are shown in Figure 4.1. The copolymer micelle solutions were prepared with 1 wt% polymer, using the cosolvent method described in the previous

section. As can be seen in Figure 4.1, all the block copolymers form micelles with a very narrow R_h distribution, except for PMMA-*b*-PnBMA (25-13). This exception can be attributed to the short PnBMA block in PMMA-*b*-PnBMA (25-13), which inhibits complete micellization; as is evident in Figure 1a, there is a peak at $R_h \approx 3$ nm, indicating the coexistence of some PMMA-*b*-PnBMA (25-13) free chains at the experimental temperature. The results of the cumulant fitting are summarized in Table 4.2. These R_h distributions do not show appreciable temperature dependence from room temperature to 100 °C; the DLS results of PMMA-*b*-PnBMA (25-35) at different temperatures are given in the Appendices as an example (Figure A.3.1).

Table 4.2. Characteristics of PMMA-*b*-PnBMA Micelles in [EMIM][TFSI] by DLS

Polymer	Average R_h (nm)	$\mu_2/\bar{\Gamma}^2$
PMMA-*b*-PnBMA (25-13)	17.$_8$	0.18
PMMA-*b*-PnBMA (25-24)	22.$_1$	0.04
PMMA-*b*-PnBMA (25-31)	22.$_8$	≈ 0
PMMA-*b*-PnBMA (25-35)	24.$_0$	0.03
PMMA-*b*-PnBMA (25-44)	26.$_0$	0.04
PMMA-*b*-PnBMA (25-53)	27.$_9$	≈ 0
PMMA-*b*-PnBMA (25-78)	34.$_6$	≈ 0

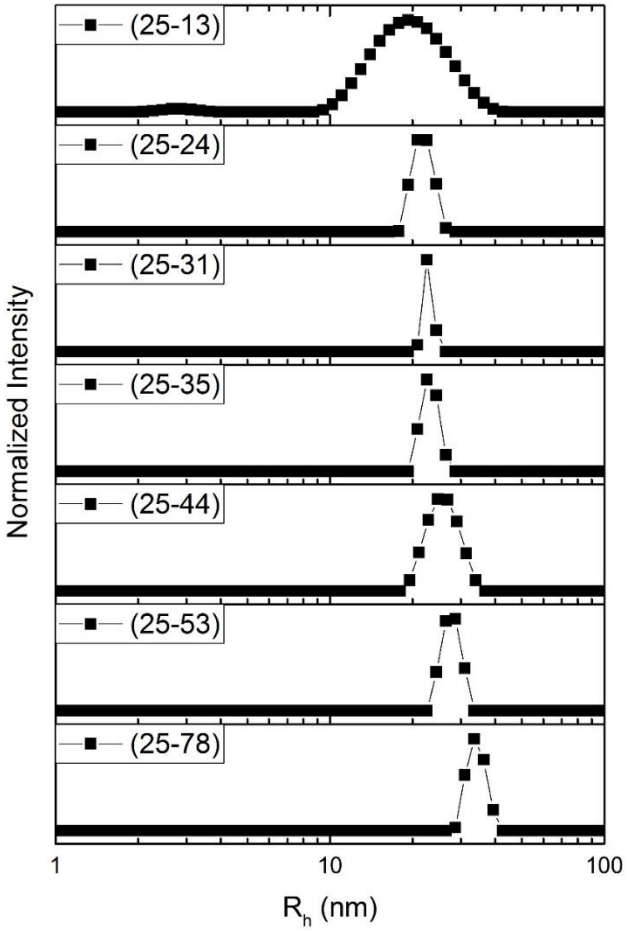

Figure 4.1. R_h distributions of PMMA-*b*-PnBMA copolymer micelles in [EMIM][TFSI] at 60 °C.

SAXS of Dilute Micelle Solutions

In order to determine the core radius (R_c) of the PMMA-*b*-PnBMA block copolymer micelles precisely, SAXS measurements were conducted on these micelle solutions and the scattering profiles fitted to the model developed by Pedersen *et al.*[41, 42] Figure 4.2 displays the SAXS patterns for all seven PMMA-*b*-PnBMA copolymers in 1 wt% solution at 60 °C. The SAXS data of these micelles also show little temperature dependence, consistent with the DLS results. The SAXS data of PMMA-*b*-PnBMA (25-35) at different temperatures are provided in the Appendices as an example (Figure A.3.2).

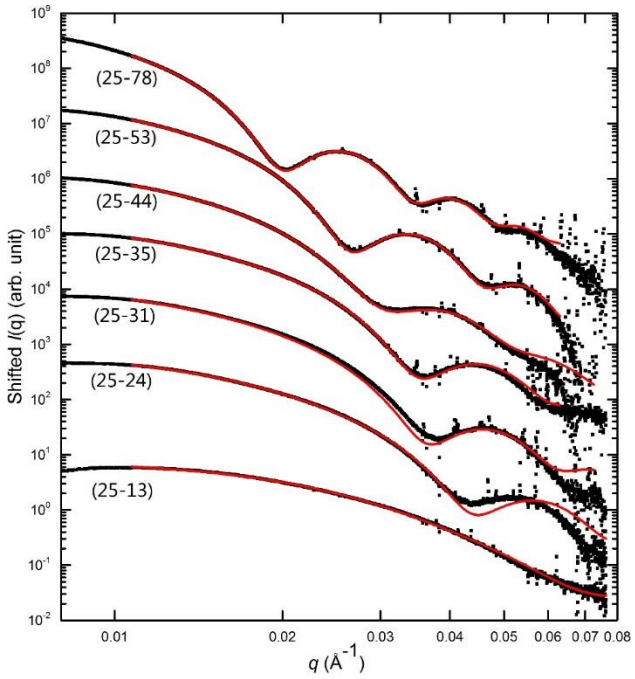

Figure 4.2. SAXS profiles of PMMA-*b*-PnBMA block copolymer micelles (1 wt%) in [EMIM][TFSI] at 60 °C. The solid lines are best fits to the Pedersen model. The profiles are shifted vertically by factors of 10 for clarity.

As can be seen in Figure 4.2, the scattering profiles for the six largest polymers show a clear first minimum, which progressively shifts towards lower q as the core block length increases. The only exception is PMMA-*b*-PnBMA(25-13), for which the first minimum approaches the upper limit of the q range used, and is also smeared by the broad R_c distribution as well. The solid curves in Figure 2 represent best fits to the Pedersen model. The total scattering intensity has contributions from both the core and the corona (as well as the cross-term) (eq. 4.1), but the scattering pattern is still dominated by the core. Consequently, the parameters related to the corona domain, *i.e.*, R_g, a_1 and s, are less reliable than those related to the core (R_c and σ_R). The aggregation number, N_{agg}, is defined as $N_{agg} = 4\pi R_c^3 / 3v_{core\text{-}block}$ assuming the core is devoid of solvent, as will be discussed subsequently. Furthermore, in dilute solution where the concentration of micelles is significantly smaller than the critical overlap concentration,

the structure factor can be neglected, *i.e.*, $S(q) \approx 1$; therefore, the independent parameters that can be accurately obtained from the fitting are the average core radius (R_c) and the standard deviation of the core radius (σ_R). The fitting results are summarized in Table 4.3. The error in R_c (and thus N_{agg}) for PMMA-*b*-PnBMA (25-13) is much larger than that of the other samples; this is a reflection of the fact that there is no clear first minimum in the scattering profile.

Table 4.3. Summary of SAXS Fitting

	R_c (Å)	σ_R (Å)	N_{agg}[a]
PMMA-*b*-PnBMA (25-13)	$58 \pm 2\times10^2$	$5 \pm 2\times10^2$	$41 \pm 4\times10^2$
PMMA-*b*-PnBMA (25-24)	100 ± 6	6 ± 5	112 ± 20
PMMA-*b*-PnBMA (25-31)	119 ± 2	9 ± 4	147 ± 7
PMMA-*b*-PnBMA (25-35)	128 ± 1	10 ± 2	162 ± 4
PMMA-*b*-PnBMA (25-44)	152 ± 1	18 ± 1	215 ± 1
PMMA-*b*-PnBMA (25-53)	171 ± 1	14 ± 1	255 ± 2
PMMA-*b*-PnBMA (25-78)	232 ± 1	22 ± 1	432 ± 2

[a] N_{agg} is calculated by $N_{agg} = 4\pi R_c^3 / 3v_{core\text{-}block}$, which represents the upper bound of the aggregation number as it assumes the core is only composed of polymer.

As mentioned above, one important assumption to obtain N_{agg} is that the micelle core is free of solvent. It was previously reported that the amount of solvent in the micelle core is mainly dictated by the distance of the experimental temperature to the critical micelle temperature (CMT);[43, 44] when this distance is sufficiently large, the solvent fraction in the core approaches zero. According to experimental results on PS-*b*-PI in

diethyl phthalate (DEP) and dibutyl phthalate (DBP), which are solvents selective to the polystyrene block, this temperature interval is approximately 40 – 70 °C. A similar conclusion was drawn by Liu *et al.* in a study of an LCST system, PEO-*b*-PPO-*b*-PEO in water, who noted that as the temperature was increased further above the CMT, the solvent fraction in the core became lower.[45] In the current study, the experimental temperature (60 °C) is ~ 80 °C above the highest CMT of all the seven copolymers (see Figure A.3.3 in the Appendices), and therefore the assumption of negligible solvent penetration is justified. We can also consider this issue in terms of χ. Seitz *et al.* have calculated by self-consistent field theory that when $\chi_{\text{solvent-core}}$ increases from 0.7 to 1.1, the solvent fraction in the micelle core (φ_s) decreases dramatically from 0.6 to 0.25.[46] Although the χ between PnBMA and [EMIM][TFSI] has not been measured directly, Hoarfrost *et al.* measured the χ between PnBMA and mixtures of [EMIM][TFSI] and [BMIM][TFSI].[47] By extrapolating the [BMIM][TFSI] wt% to zero, we estimated that $\chi_{\text{PnBMA/EMIM}} \approx 1.4$ at 60 °C. This is quite a large χ, under which the solvent fraction in micelle core should be almost nil.

Figure 4.3a shows the dependence of R_c on the number of repeat units in the core block, N_B, in which the slope for the six larger polymers is determined to be 0.71±0.01. This relationship is in rough agreement with Halperin's scaling theory, which predicts R_c to be proportional to $N_B^{0.60–0.67}$.[7] The exponent obtained from this experiment is slightly larger than that predicted for either the crew-cut or hairy limits. More elaborate theories have included an additional logarithmic term in the free energy of the corona block, which contributes to the size of the micelle core as well. Zhulina and coworkers proposed that in the hairy micelle limit, $R_c \sim N_B^{3/5}K^{-2/5}$, in which $K \sim \ln(N_B^{-11/15}N_A)$ when the solvent is good for the corona block (ν=3/5).[6, 48, 49] As $K^{-2/5}$ increases with N_B, therefore, the net scaling exponent between R_c and N_B should be greater than 3/5. Nagarajan and Ganesh found a relationship ($R_c \sim N_B^{0.70\text{-}0.73}$) by calculations for PS-*b*-PB/heptane and PEO-*b*-PPO/water systems using mean-field theory,[9] in excellent agreement with our

experimental result. In their calculation, the three essential parameters ($\chi_{solvent\text{-}core}$, $\chi_{solvent\text{-}corona}$ and $\sigma_{solvent\text{-}core}$) are rationalized based on literature data for real systems, and part of their predictions are corroborated by experimental data for PS-*b*-PI in heptane conducted by Bahadur *et al.*,[28] with reasonable comparison between theory and the experiment.

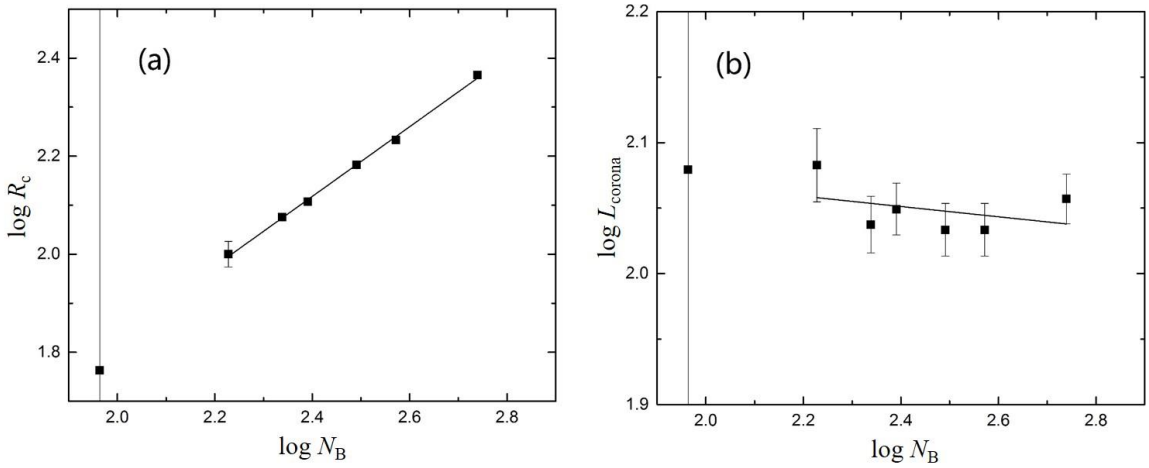

Figure 4.3. Dependence of (a) the core radius and (b) the corona thickness on the number of repeating units in the core block.

Based on our fitting, the interfacial widths in all the seven micelle specimens are below 1 nm, thus negligible compared to both R_c and L_{corona}; therefore, the corona thickness, L_{corona}, can be estimated as the difference between R_h obtained by DLS and R_c obtained by SAXS. Interestingly, for this system L_{corona} shows little dependence on N_B ($L_{corona} \sim N_B^{-0.04\pm0.05}$) as shown in Figure 4.3b, which deviates from the relationship $L_{corona} \sim N_B^{0.16–0.20}$ anticipated by the scaling theory. However, the scaling theory in the hairy limit assumes $R_c << L$, while in our experiments the micelles all have more comparable core and corona sizes, and which therefore fall between the two limiting cases. In fact, either limit is difficult to access experimentally, at least in uncharged systems. Zhulina *et al.* studied this intermediate case and found that $L_{corona} \sim N_A^{9/11} N_B^{0}$, assuming a good solvent for the corona, which indicates that L_{corona} is independent of N_B.[6, 49] Nagarajan and

Ganesh also gave $L_{corona} \sim N_B^{0.06\text{-}0.07} N_A^{0.68\text{-}0.74}$ in their mean-field study,[9] implying a much weaker dependence on N_B than the scaling theory, and very close to our result.

We can compare the mean square end-to-end distance of the core block $\sqrt{\langle R_0^2 \rangle}$ ($= (Nb^2)^{1/2}$) with the micelle core radius R_c. Since the statistical segment length (b) of PnBMA is 6.1 Å,[50] therefore, $\sqrt{\langle R_0^2 \rangle}$ of the PnBMA block of PMMA-*b*-PnBMA (25-13), (25-24), (25-31), (25-35), (25-44), (25-53) and (25-78) are estimated to be 59, 79, 90, 96, 107, 118 and 143 Å, respectively. Based on the results in Table 4.3, R_c of these micelles are approximately 1 – 1.5 times as large as $\sqrt{\langle R_0^2 \rangle}$, indicating significant stretching of the core block. This is not only due to the geometrical restriction, but also due to the crowding on the tethered interface. Note that in a sphere, only one chain needs to reach the center of the core, so to have the core radius significantly larger than the unperturbed end-to-end distance is proof of the importance of chain stretching. This reflects the fact that the micelles tend to increase N_{agg} in order to diminish the surface area per chain, and thus the interface free energy, which also agrees with the aforementioned theories.

An important question that needs to be addressed is whether or not these PMMA-*b*-PnBMA micelles are at equilibrium under the experimental conditions. It is well-known that non-ergodicity occurs widely in macromolecular micelle systems, which is not only attributed to the glassy cores, but also to geologically slow chain exchange caused by high incompatibility between the core and the solvent.[51 – 56] In our experiment, the micelles are at equilibrium when they are initially formed in the presence of cosolvent; however, as the methylene chloride is further evaporated, the interfacial tension between the solvent and the core increases, and thus the equilibrium aggregation number should also increase. Under such circumstances, the micelles may no longer be at equilibrium when in the pure ionic liquid, as the number of micelles has to decrease, either by chain exchange or by coalescence. According to our preliminary results on micelle chain

exchange in this system, only the two samples with the shortest PnBMA blocks have appreciable chain exchange rate at ~60 °C;[57] even this does not guarantee that these two micelle samples are fully equilibrated, since the rearrangement process requires a change in N_{agg}, which is a much slower process than single chain exchange according to Aniansson-Wall theory.[58, 59, 60] Accordingly, we infer that these micelles reflect the equilibrium state achieved when the micelles were first formed, and not the equilibrium state in the pure ionic liquid. However, the application of equilibrium theory is still justified, given that all the micelles were formed under equivalent conditions.

SAXS of Concentrated Micelle Solution

The scattering profiles of PMMA-*b*-PnBMA (25-35) micelles at higher concentration are shown in Figure 4.4. At 1 wt% concentration, the scattering profile does not show structure factor peaks; however, starting from 3 wt%, a structure peak emerges at low q, which progressively evolves into well-defined Bragg peaks at 15 wt% copolymer. The $q/q^* = 1 : 2^{1/2} : 3^{1/2} : 2$ pattern ($q^* \approx 0.017$ Å) strongly suggests a body-centered cubic (BCC) packing, as is often observed when the concentration of spherical micelles exceeds the critical overlap concentration.[34, 43, 61] However, due to the absence of characteristic peaks at higher q, the possibility of simple cubic packing cannot be ruled out. Nevertheless, assuming a BCC lattice, the nearest neighbor radius (R_{nn}) between the two micelles can be calculated from the BCC lattice parameter (a_{bcc}):

$$R_{nn} = \frac{\sqrt{6}}{4}\frac{2\pi}{q^*} = \frac{\sqrt{3}}{4}a_{bcc} \qquad (4.7)$$

At 15 wt% copolymer concentration, R_{nn} = 224 Å, slightly smaller than the R_h of the same micelle (240 Å) in 1 wt% solution. This presumably reflects some interpenetration of the corona chains at high concentration.

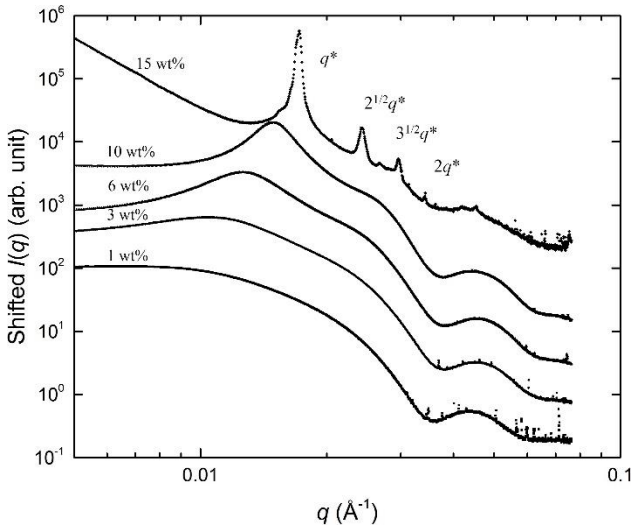

Figure 4.4. SAXS profiles of PMMA-*b*-PnBMA (25-35) in [EMIM][TFSI] at various concentrations at 60 °C. The profiles are shifted vertically by factors of 3 for clarity.

4.4. Summary

In this chapter, we quantified the structure of seven PMMA-*b*-PnBMA diblock copolymers in [EMIM][TFSI]; the corona block was fixed, and the core block length was varied. The micelle hydrodynamic radii R_h were determined by DLS using cumulant fitting, and the corresponding core radii R_c were extracted from SAXS data through fitting to the Pedersen model. This allowed for a precise determination of the dependence of R_c and L_{corona} on the degree of polymerization of the core block, N_B: $R_c \sim N_B^{0.71\pm0.01}$ and $L_{corona} \sim N_B^{-0.04\pm0.05}$. These results are in excellent agreement with the mean-field calculations of Nagarajan and Ganesh,[9,10] but are only approximately consistent with scaling theory in the hairy micelle limit ($L >> R_c$). This may be due in part to the comparable dimensions of the core and corona. The experimental results suggest that the core blocks are significantly stretched in the micelle. In addition, in the case of higher copolymer concentrations, micelles tend to pack onto a BCC lattice. Overall, this work provides a thorough and quantitative test of theories of micelle scaling, and will also aid

in the study of the kinetics of chain exchange between micelles, which will be discussed in detail in Chapter 7.

4.5. Acknowledgement

This work was supported by the National Science Foundation (NSF) through award DMR-1206459. The SAXS experiments were conducted on the DuPont-Northwestern-Dow Collaborative Access Team (DND-CAT) Synchrotron Research Center located at Sector 5 of the Advanced Photon Source. DND-CAT is supported by the E.I. DuPont de Nemours & Co., the Dow Chemical Company, the U.S. National Science Foundation through Grant DMR-9304725, and the State of Illinois through the Department of Commerce and the Board of Higher Education Grant IBHE HECA NWU 96. Use of the Advanced Photon Source was supported by the U.S. Department of Energy, Basic Energy Sciences, Office of Science, under Contract No. W-31-109-Eng-38.

4.6. References

(1) de Gennes, P.-G. Macromolecules and Liquid Crystals: Reflections on Certain Lines of Research. In *Solid State Physics*; Liebert, J., Ed.; Academic: New York, 1978; Suppl. 14; p 9-11.

(2) Daoud, M.; Cotton, J. P. *J. Phys. France* **1982**, *43*, 531-538.

(3) Leibler, L.; Orland, H.; Wheeler, J. C. *J. Chem. Phys.* **1983**, *79*, 3550-3557.

(4) Noolandi, J.; Hong, K. M. *Macromolecules* **1982**, *15*, 482-492.

(5) Noolandi, J.; Hong, K. M. *Macromolecules* **1983**, *16*, 1443-1448.

(6) Zhulina, E. B.; Birshtein, T. M. *Polym. Sci. USSR* **1985**, *27*, 570-578.

(7) Halperin, A. *Macromolecules* **1987**, *20*, 2943-2946.

(8) Halperin, A.; Tirrell, M.; Lodge, T. P. *Adv. Polym. Sci.* **1992**, *27*, 31-71.

(9) Nagarajan, R.; Ganesh, K. *J. Chem. Phys.* **1989**, *90*, 5843-5856.

(10) Nagarajan, R.; Ganesh, K. *J. Chem. Phys.* **1993**, *98*, 7440-7450.

(11) Binder, K. *Monte Carlo and molecular dynamics simulations in polymer science*, Oxford University Press: New York, 1995.

(12) Milchev, A.; Bhattacharya, A.; Binder, K. *Macromolecules* **2001**, *34*, 1881-1893.

(13) Kim, S. H.; Jo, W. H. *J. Chem. Phys.* **2002**, *117*, 8565-8572.

(14) Riess, G. *Prog. Polym. Sci.* **2003**, *28*, 1107-1170.

(15) Zhulina, E. B.; Borisov, O. V. *Macromolecules* **2012**, *45*, 4429-4440.

(16) Kotaka, T.; Tanaka, T.; Hattori, M.; Inagaki, H. *Macromolecules* **1978**, *11*, 138-145.

(17) Bluhm, T. L.; Whitmore, M. D. *Can. J. Chem.* **1985**, *63*, 249-252.

(18) Bluhm, T. L.; Malhotra, S. L. *Eur. Polym. J.* **1986**, *22*, 249-251.

(19) Oranli, L.; Bahadur, P.; Riess, G. *Can. J. Chem.* **1985**, *63*, 2691-2696.

(20) Xu, R.; Winnik, M. A.; Hallett, F. R.; Riess, G.; Croucher, M. D. *Macromolecules* **1991**, *24*, 87-93.

(21) Xu, R.; Winnik, M. A.; Riess, G.; Chu, B.; Croucher, M. D. *Macromolecules* **1992**, *25*, 644-652.

(22) Antonietti, M.; Heinz, S.; Schmidt, M.; Rosenauer, C. *Macromolecules* **1994**, *27*, 3276-3281.

(23) Calderara F.; Hruska, Z.; Hurtrez, G.; Lerch, J. P.; Nugay, T.; Riess, G. *Macromolecules* **1994**, *27*, 1210-1215.

(24) Jada, A.; Hurtrez, G.; Siffert, B.; Riess, G. *Macromol. Chem. Phys.* **1996**, *197*, 3697-3710.

(25) Förster, S.; Zisenis, M.; Wenz, E.; Antonietti, M. *J. Chem. Phys.* **1996**, *104*, 9956-9970.

(26) Tao, J.; Stewart, S.; Liu, G.; Yang, M. *Macromolecules* **1997**, *30*, 2738-2745.

(27) Pitsikalis, M.; Siakali-Kioulafa, E.; Hadjichristidis, N. *Macromolecules* **2000**, *33*, 5460-5469.

(28) Bahadur, P.; Sastry, N. V.; Marti, S.; Riess, G. *Colloids and Surfaces* **1985**, *16*, 337-346.

(29) Jada, A.; Siffert, B.; Riess, G. *Colloids and Surfaces A* **1993**, *75*, 203-209.

(30) Quintana, J. R.; Salazar, R. A.; Katime, I. *Macromol. Chem. Phys.* **1995**, *196*, 1625-1634.

(31) Pitsikalis, M.; Siakali-Kioulafa, E.; Hadjichristidis, N. *J. Polym. Sci. Part A* **2004**, *42*, 4177-4188.

(32) Guerrero-Sanchez, C.; Wouters, D.; Fustin, C.-A.; Gohy, J.-F.; Lohmeijer, B. G. G.; Schubert, U. S. *Macromolecules* **2005**, *38*, 10185-10191.

(33) LaRue, I.; Adam, M.; Zhulina, E. B.; Rubinstein, M.; Pitsikalis, M.; Hadjichristidis, N.; Ivanov, D. A.; Gearba, R. I.; Anokhin, D. V.; Sheiko, S. S. *Macromolecules* **2008**, *41*, 6555-6563.

(34) Choi, S.; Bates, F. S.; Lodge, T. P. *J. Phys. Chem. B* **2009**, *113*, 13840-13848.

(35) Jensen, G. V.; Shi, Q.; Deen, G. R.; Almdal, K.; Pedersen, J. S. *Macromolecules* **2012**, *45*, 430-440.

(36) Zinn, T.; Willner, L.; Lund, R.; Pipich, V.; Appavou, M.; Richter, D. *Soft Matter* **2014**, *10*, 5212-5220.

(37) Wiley, R. H.; Brauer, G. M. *J. Polym. Sci.* **1948**, *3*, 455.

(38) Numasawa, N.; Hamada, T.; Nose, T. *J. Polym. Sci., Polym. Lett. Ed.* **1985**, *23*, 1-4.

(39) Jakeš, J. *Collect. Czech. Chem. Commun.* **1995**, *60*, 1781-1797.

(40) Koppel, D. E. *J. Chem. Phys.* **1972**, *57*, 4814-4820.

(41) Pedersen, J. S.; Svaneborg, C.; Almdal, K.; Hamley, I. W.; Young, R. N. *Macromolecules* **2003**, *36*, 416-433.

(42) Castelletto, V.; Hamley, I. W.; Pedersen, J. S. *J. Chem. Phys.* **2002**, *117*, 8124-8129.

(43) Bang, J.; Viswanathan, K.; Lodge, T. P.; Park, M. J.; Char, K. *J. Chem. Phys.* **2004**, *121*, 11489-11500.

(44) Lodge, T. P.; Xu, X.; Ryu, C. Y.; Hamley, I. W.; Fairclough, J. P. A.; Ryan, A. J.; Pedersen, J. S. *Macromolecules* **1996**, *29*, 5955-5964.

(45) Liu, Y.; Chen, S.-H.; Huang, J. S. *Macromolecules* **1998**, *31*, 2236-2244.

(46) Seitz, M. E.; Burghardt, W. R.; Shull, K. R. *Macromolecules* **2009**, *42*, 9133-9140.

(47) Hoarfrost, M. L.; He, Y.; Lodge, T. P. *Macromolecules* **2013**, *46*, 9464-9472.

(48) Birshtein, T. M.; Zhulina, E. B. *Polymer* **1989**, *30*, 170-177.

(49) Zhulina, E. B.; Adam, M.; LaRue, I.; Sheiko, S. S.; Rubinstein, M. *Macromolecules* **2005**, *38*, 5330-5351.

(50) Helfand, E.; Sapse, A. M. *J. Chem. Phys.* **1975**, *62*, 1327-1331.

(51) Won, Y.-Y.; Davis, H. T.; Bates, F. S. *Macromolecules* **2003**, *36*, 953–955

(52) Lund, R.; Willner, L.; Stellbrink, J.; Lindner, P.; Richter, D. *Phys. Rev. Lett.* **2006**, *96*, 068302

(53) Lund, R.; Willner, L.; Lindner, P.; Richter, D. *Macromolecules* **2009**, *42*, 2686–2695.

(54) Choi, S.-H.; Bates, F. S.; Lodge, T. P. *Macromolecules* **2011**, *44*, 3594–3604.

(55) Lu, J.; Bates, F. S.; Lodge, T. P. *ACS Macro Lett.* **2013**, *2*, 451–455.

(56) Lu, J.; Bates, F. S.; Lodge, T. P. *Macromolecules* **2015**, 48, 2667–2676.

(57) Ma, Y.; Lodge, T. P. *Macromolecules* **2016**, *49*, 9542-9552.

(58) Aniansson, E. A. G.; Wall, S. N.; Almgren, M.; Hoffmann, H.; Kielmann, I.; Ulbricht, W.; Zana, R.; Lang, J.; Tondre, C. *J. Phys. Chem.* **1976**, *80*, 905-922.

(59) Cavicchi, K. A.; Lodge, T. P. *Macromolecules* **2003**, *36*, 7158-7164.

(60) Meli, L.; Santiago, J. M.; Lodge, T. P. *Macromolecules* **2010**, *43*, 2018-2027.

(61) McConnell, G. A.; Gast, A. P.; Huang, J. S.; Smith, S. D. *Phys. Rev. Lett.* **1993**, *71*, 2102-2105.

Chapter 5

Micelle Structures at Various Solvent Compositions

5.1. Introduction

In the case of polymer micelles, thermodynamically, there should always be a preferred size and aggregation number for a given set of micelle parameters (*i.e.*, N_A, N_B, χ_{AS}, χ_{BS}, and χ_{AB}, in which A and B stand for the corona and the core). This is because the micelle core has the tendency to expand, so that its surface area/volume ratio decreases, and thus the interfacial free energy of the system is minimized; however, the expansion of the core will inevitably result in the stretching of the core block, causing the chain conformational entropy to decrease as well. The balance between these two factors will favor an optimal micelle size, which gives a minimum total Gibbs free energy. At this point, the micelles are truly at equilibrium.

Nevertheless, non-ergodicity is prevalent in polymer systems.[1] As has previously been reported, the size, aggregation number and the morphology of micelles can be highly path-dependent.[2 – 4] For example, Bates and coworkers investigated the morphologies of poly(ethylene oxide)-*block*-poly(butadiene) (PEO-*b*-PB) micelles in water, and observed complicated topological structures with multiple Y-junctions and loops.[5,6] The authors attributed the origin of these non-classical structures to the ultra-slow inter-micellar chain exchange kinetics, due to the high hydrophobicity of the PB cores.[6, 7] Non-ergodicity is good in that it endows block copolymer micelles with robustness, and enables them to be used as building blocks and carriers; but its disadvantage is also obvious — it makes the micelle systems almost impossible to achieve the equilibrium state within a reasonable time frame.

An interesting question was proposed in the preceding chapter: whether or not these micelles in [EMIM][TFSI] are near equilibrium. This is actually a fundamental question, but hard to answer. According to multiple authors, the cosolvent method has better reproducibility in preparing stable, well-defined micelles, especially when the core block is long;[8–10] however, even the micelles prepared by this method can be affected by a variety of factors, such as cosolvent evaporation rate[11] and agitation. [5,6,12] Especially, in an LCST system, when the temperature is elevated farther above CMT, the solvent is less favorable to the core block, thereby imposing higher barriers to micelle equilibration. Under such a scenario, the micelles are more likely to be trapped in a kinetically metastable state.

One way to facilitate the micelle equilibration process is to first prepare the micelles under very slow cosolvent evaporation rate, and then anneal the sample at a moderate thermal distance,[11] *i.e.*, $T -$ CMT. In this case, χ is large enough to enable the formation of well-defined micelles, but is not too large to completely inhibit the inter-micellar chain exchange. Inspired by the scaling study in Chapter 4, the first half of this chapter features the SAXS characterization results of two similar series of micelle samples, each with identical CMT. Whether or not these two new series of micelles share the same scaling relationship will provide some insight into the equilibrium state of the micelles. In the second half of this chapter, the micelle sizes will be studied as a function of temperature in solvents with higher [BMIM][TFSI] compositions, in which other micelle morphologies can possibly be achieved.

5.2. Experimental Section

Materials

Six diblock copolymers, PMMA-*b*-PnBMA (25-24), (25-31), (25-35), (25-44), (25-53) and (25-78) were used in this study. Their characteristics have been summarized in Table 4.1 in Chapter 4.

Preparation of Micelle Solutions

The copolymer, [EMIM][TFSI], and [BMIM][TFSI] were mixed in a predetermined ratio at room temperature, and the cosolvent methylene chloride was added to make the mixture a homogeneous solution. The solution was purged with nitrogen overnight to slowly remove the cosolvent, and then was dried at 50 °C under vacuum (< 100 mTorr) for at least 12 h prior to use.

For the SAXS experiments, the polymer micelle solutions were transferred into quartz capillary tubes; the tubes were sealed with epoxy, followed by annealing at 60 °C for at least 30 h before data collection.

SAXS and DLS

The SAXS experiments were conducted on the 5ID-D beamline of the DuPont-Northwestern-Dow Collaborative Access Team (DND-CAT) at the Advanced Photon Source, Argonne National Laboratory. All instrumental configurations and data processing procedures are the same as introduced in Section 4.2, except that the beam energy used in this study was 17 keV instead of 9 keV, which corresponds to a wavelength of 0.73 Å. The collection time was 2 s for PMMA-*b*-PnBMA (25-78) micelles, and 5 s for the rest of the samples. Notably, changing the beam energy only makes the q range of detection slightly different. The same model (Pedersen model without structure factor) was used to fit the SAXS data as in Chapter 4.

The instrumental settings and procedures for the DLS experiments are exactly the same as introduced in Section 4.2.

5.3. Scaling of Micelles at Equal Thermal Distance from the CMT

Determination of CMT

Light scattering was used to determine the CMT of micelle solutions, across which the scattering intensity will have a significant change. Figure 5.1 illustrates the determination of the CMT, using PMMA-*b*-PnBMA (25-31) in the ionic liquid mixture with [BMIM] wt% = 80 as an example. In Figure 5.1, the scattering intensity as a function of temperature can be roughly described by two dash lines, the intersection of which is taken as the CMT.

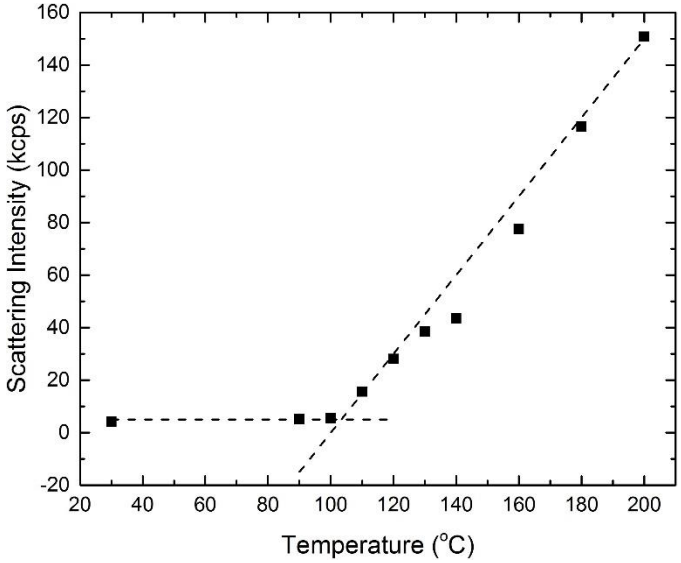

Figure 5.1. Scattering intensity of PMMA-*b*-PnBMA (25-31) in [EMIM][TFSI]:[BMIM][TFSI] = 20:80 as a function of temperature. The CMT is determined to be 103 °C.

Similarly, for each diblock copolymer, CMTs were measured at various solvent compositions, and the CMT of each copolymer was plotted against [BMIM] wt% in the solvent mixture, as displayed in Figure 5.2a. Note that the relationship between CMT and

[BMIM] wt% is almost linear, which is consistent with the experimental result of Lee *et al*.[13] It is not surprising that the CMT at a certain solvent composition decreases with the core block length in an LCST system. According to Flory-Huggins theory, the critical value of χ between PnBMA and ILs, χ_c, has the following relationship with the PnBMA block length:

$$\chi_c = A + \frac{B}{T_c} = \frac{1}{2N} + \frac{1}{\sqrt{N}} + \frac{1}{2} \tag{5.1}$$

where T_c is the critical temperature, and A and B are the two constants in the entropic and the enthalpic terms of χ. Although CMT is not equal to T_c, but we can use a similar strategy to plot 1/CMT at [BMIM] wt% = 0 (denoted as $1/CMT_0$ here, *i.e.*, the inverse intercept of each line in Figure 5.2a) against $\left(1/2N_{PnBMA} + 1/\sqrt{N_{PnBMA}}\right)$, which gives Figure 5.2b. As can be seen in Figure 5.2b, the four data points (black squares) are well-aligned; therefore, the CMT_0 of any other PMMA-*b*-PnBMA (25-X) copolymers with $24 \leq X \leq 78$ can also be calculated without doing further light scattering measurement (the red squares, for example). Assuming identical slope for each line in Figure 5.2a, then the complete CMT diagram with two variables — [BMIM] wt% and N_{PnBMA} — can be constructed with relatively high accuracy. The result is summarized in Table 5.1.

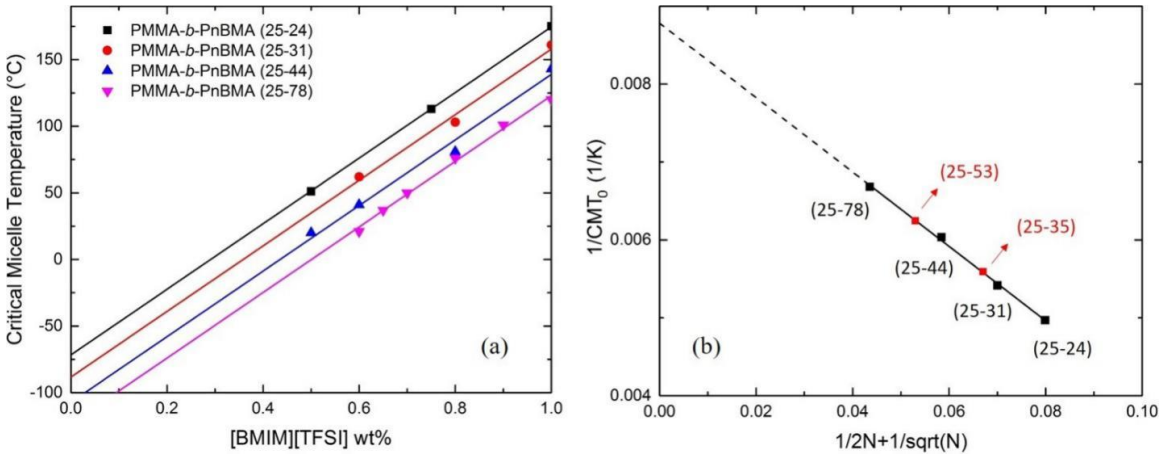

Figure 5.2. (a) CMT as a function of [BMIM] wt% in the solvent mixture for PMMA-*b*-PnBMA (25-24), (25-31), (25-44) and (25-78). (b) $1/CMT_0$ as a function of $\left(1/2N_{PnBMA} + 1/\sqrt{N_{PnBMA}}\right)$; the dash line represents extrapolation to infinite PnBMA molecular weight.

Table 5.1. Dependence of CMT on solvent composition and PnBMA block length

Block Copolymer	N_{PnBMA}	CMT_0 (°C)	CMT as a function w_B (°C) [a]	w_B when CMT = 0 °C [a]	w_B when CMT = −20 °C [a]
PMMA-*b*-PnBMA (25-24)	169	−72	CMT = −72 + 246w_{BMIM}	0.292	0.211
PMMA-*b*-PnBMA (25-31)	218	−88	CMT = −88 + 246w_{BMIM}	0.358	0.276
PMMA-*b*-PnBMA (25-35)	246	−96	CMT = −96 + 246w_{BMIM}	0.390	0.309
PMMA-*b*-PnBMA (25-44)	310	−107	CMT = −107 + 246w_{BMIM}	0.435	0.354
PMMA-*b*-PnBMA (25-53)	373	−113	CMT = −113 + 246w_{BMIM}	0.459	0.378
PMMA-*b*-PnBMA (25-78)	549	−123	CMT = −123 + 246w_{BMIM}	0.500	0.419

[a] w_B represents the weight fraction of [BMIM][TFSI] in the solvent mixture, and $0 \leq w_B \leq 1$.

SAXS

With the knowledge of CMT, two series of micelle solutions were prepared using mixtures of [EMIM][TFSI] and [BMIM][TFSI] as the solvent. In the first series, PMMA-*b*-PnBMA (25-24), (25-31), (25-35), (25-44), (25-53) and (25-78) were dispersed in [BMIM] wt% = 29.2, 35.8, 39.0, 43.5, 45.9 and 50.0, respectively. These micelles all have a CMT at 0 °C, so they will be referred to as the CMT = 0 °C series in this section. Similarly, the second series have CMT at −20 °C, and will be referred to as the CMT = −20 °C series. SAXS data were collected for the CMT = 0 °C series at 60, 80 and 100 °C,

whereas for the CMT = −20 °C series, SAXS data were performed at 40, 60 and 80 °C. In this case, the thermal distance between experimental temperature and CMT ($\Delta T = T$ – CMT) was kept the same between the two series, so we can say that the two series of micelles are equally far away from the CMT.

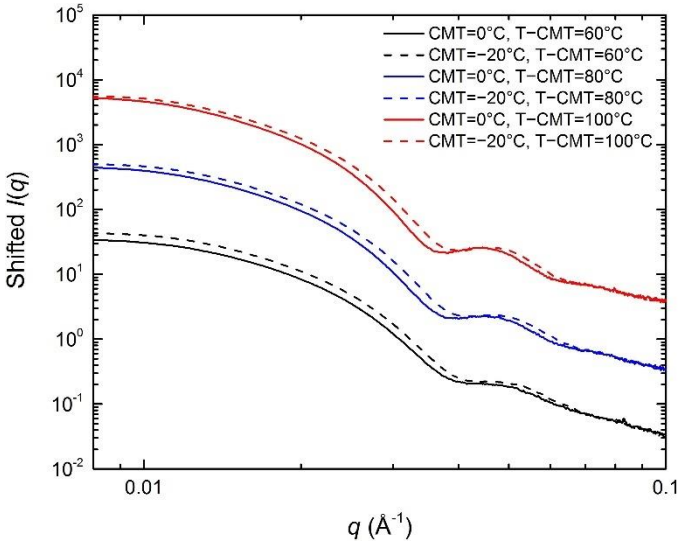

Figure 5.3. SAXS profiles of the two series of PMMA-*b*-PnBMA (25-35) micelles (1 wt%), with ΔT = 60, 80 and 100 °C. The blue and red curves are shifted vertically by factors of 10 and 100 from the black curves for clarity.

Figure 5.3 illustrates the SAXS profiles of PMMA-*b*-PnBMA (25-35) of the two series, with ΔT = 60, 80 and 100 °C. By comparing the solid curves and their nearest dashed curves, we can see that the curves are almost identical within each pair, with only a slight difference in the position of the first minimum (less than 10%). Meanwhile, if we look at the three solid curves only, it is clear that as ΔT increases from 60 to 100 °C, either the distribution of micelle core radii becomes narrower, or the core-corona interface becomes sharper, as indicated by the sharper first minimum at q = 0.035 – 0.04 $Å^{-1}$. These two findings both confirm that the thermal distance between experimental temperature and CMT (ΔT) plays a vital role in determining the micelle core size distribution, while the absolute T and CMT are comparatively less important.

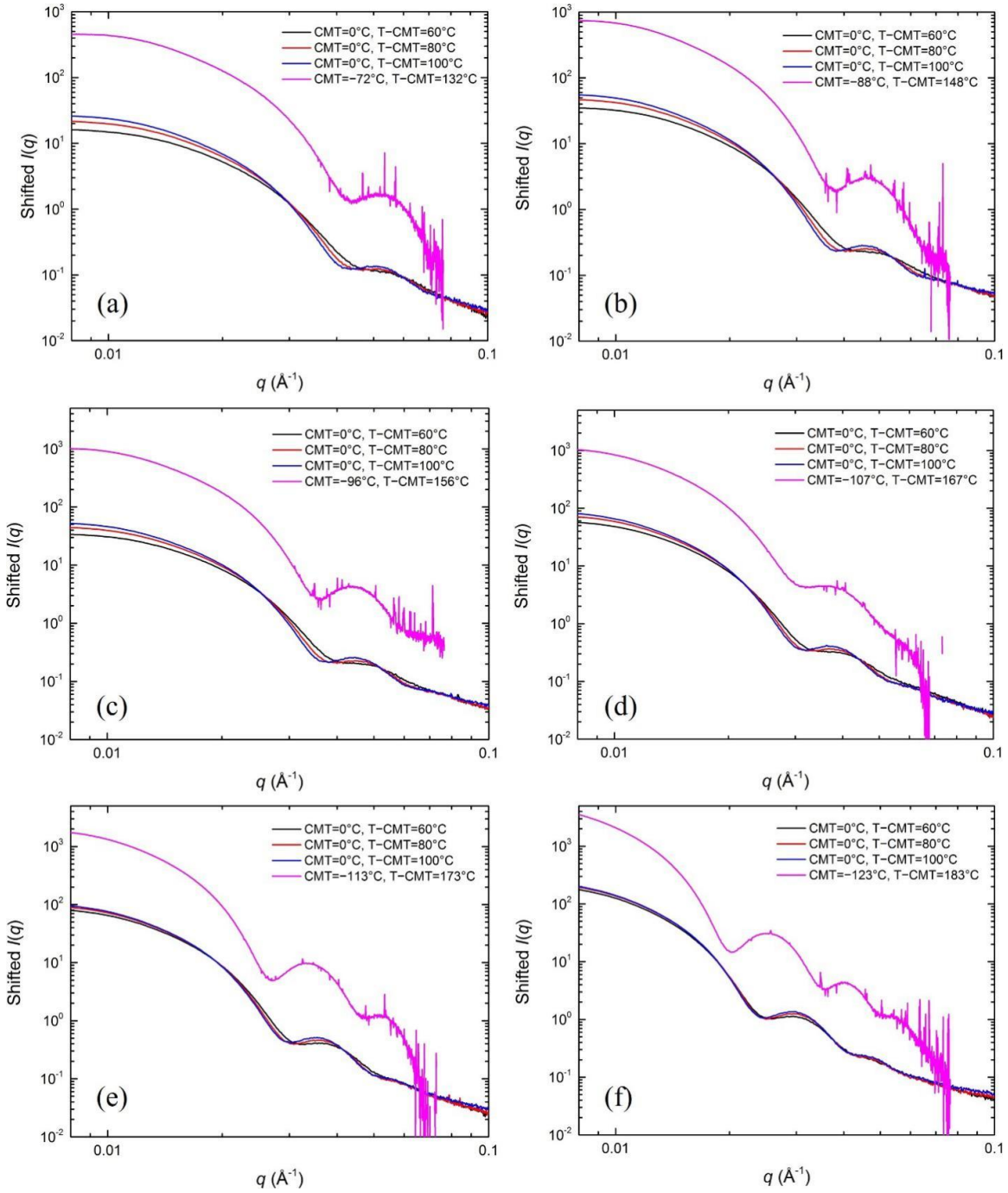

Figure 5.4. SAXS profiles of PMMA-*b*-PnBMA (a) (25-24), (b) (25-31), (c) (25-35), (d) (25-44), (e) (25-53), and (f) (25-78) micelles (1 wt%), in the CMT = 0 °C solvent (black, red and blue) and [EMIM][TFSI] (magenta). The magenta curves are shifted vertically by factors of 10 from the other curves for clarity.

Table 5.2. Summary of SAXS Fitting

Block Copolymer	CMT (°C)	ΔT (°C)	R_c (Å)	σ_R (Å)	σ_R/R_c
PMMA-*b*-PnBMA (25-24)	0	60	105±6	13±6	0.12
		80	105±5	11±6	0.11
		100	107±5	11±5	0.10
	–20	60	105±5	14±4	0.13
		80	106±4	12±4	0.11
		100	107±6	11±6	0.10
	–72	132	100±6	6±5	0.06
PMMA-*b*-PnBMA (25-31)	0	60	121±2	15±4	0.12
		80	120±2	13±3	0.11
		100	120±3	11±2	0.09
	–20	60	118±3	15±3	0.13
		80	115±3	13±3	0.11
		100	117±4	12±2	0.10
	–88	148	119±2	9±4	0.08
PMMA-*b*-PnBMA (25-35)	0	60	127±3	16±3	0.13
		80	125±2	14±2	0.11
		100	125±3	12±2	0.10
	–20	60	123±2	16±2	0.13
		80	122±3	14±1	0.11
		100	123±2	13±2	0.11
	–96	156	128±1	10±2	0.08

PMMA-*b*-PnBMA (25-44)	0	60	151±1	20±1	0.13
		80	147±1	16±1	0.11
		100	146±1	15±2	0.10
	–20	60	143±1	17±1	0.12
		80	145±1	16±1	0.11
		100	146±1	15±1	0.10
	–107	167	152±1	18±1	0.12
PMMA-*b*-PnBMA (25-53)	0	60	155±1	19±1	0.12
		80	158±1	17±1	0.11
		100	154±1	14±1	0.09
	–20	60	153±1	17±1	0.11
		80	155±1	16±1	0.10
		100	156±1	16±1	0.10
	–113	173	171±1	14±1	0.08
PMMA-*b*-PnBMA (25-78)	0	60	193±1	22±1	0.11
		80	193±1	20±1	0.10
		100	190±1	18±1	0.09
	–20	60	198±1	22±1	0.11
		80	194±1	19±1	0.10
		100	195±1	18±1	0.09
	–123	183	232±1	22±1	0.09

Now, we will primarily focus on the difference between the CMT = 0 °C series and the series with 100% [EMIM][TFSI] as the solvent (Figure 5.4). As is shown in Figure 5.4a – d, the first minima in the blue curves (CMT = 0 °C series, ΔT = 100 °C) and the magenta curves (100% [EMIM][TFSI] series, $\Delta T \geq 130$ °C) almost fall on the same q, indicating similar R_c values. However, in panels e and f, we can see a considerable difference between the blue and magenta curves in terms of first minimum position. This observation is supported by data fitting to the Pedersen model (see Appendices A.5),[14,15] the results of which are summarized in Table 5.2.

Dependence of R_c on ΔT

As can be seen in Table 5.2, for each polymer and each solvent composition, R_c is almost constant as ΔT changes from 60 to 100 °C. For example in rows 1 – 3, the maximum R_c difference of 2 Å is most probably the result of fitting error. Although both theoretical [16 – 18] and experimental [19 – 24] studies have suggested that N_{agg} (and/or R_c) increases as the solvent becomes more selective to the core block; nevertheless, this abrupt increase only persists for a small temperature range, *i.e.*, when T is slightly above CMT for LCST system, or slightly below CMT for UCST system, as summarized in Table 5.3. This can be attributed to the change in interfacial tension between the core and the solvent — when T just goes across the CMT, the core block becomes incompatible with the solvent, therefore, micelles tend to increase N_{agg} or R_c, in order to minimize their interfacial area per chain. Based on the pioneering work by de Gennes *et al.*, Halperin developed the scaling relationships for R_c and N_{agg} in the two limiting cases: when $N_A >> N_B$ (the corona block is much longer than the core block, or "hairy" micelles), $N_{agg} \sim \gamma^{6/5} N_B^{4/5}$, and $R_c \sim \gamma^{2/5} N_B^{3/5}$; when $N_A << N_B$ (the core block is much longer than the corona block, or "crew-cut" micelles), $N_{agg} \sim \gamma N_B$, and $R_c \sim \gamma^{1/3} N_B^{2/3}$ (γ denotes the

interfacial tension).[16,25] In both cases, N_{agg} and R_c increases with γ by a power law relationship, which readily explains why N_{agg} increases with $|T - \mathrm{CMT}|$.

However, there are two things in Table 5.3 that are worth attention: (*i*) in some cases, only N_{agg} increases with $|T - \mathrm{CMT}|$, while R_c keeps almost constant (entries 1, 2 and 7, for example); (*ii*) some systems clearly display a "level-off point", beyond which R_c and N_{agg} are no longer dependent on $|T - \mathrm{CMT}|$ (entries 4 and 5, for example). For the first statement, Halperin's scaling relationships fail in this case, because the scaling theory does not take the solvent penetration effect into consideration. In fact, one of the basic assumption in Halperin's theory is that micelle cores are free of solvent and only composed of core chains, therefore, $R_c \sim N_{agg}^{1/3} N_B^{1/3} a$ is valid geometrically, where a is the size of monomer in the core block. Nevertheless, as has been discussed in Chapter 4, solvent penetration is a significant issue when $T \approx \mathrm{CMT}$, therefore, $R_c \sim N_{agg}^{1/3} N_B^{1/3} a/\varphi_p^{1/3}$ when solvent penetration is considered, and φ_p is the polymer volume fraction in the micelle core, which is a function of $|T - \mathrm{CMT}|$ as well. Qualitatively, when $|T - \mathrm{CMT}|$ increases, both N_{agg} and φ_p will increase, so they may partially cancel out, thus making R_c a much weaker function of T than N_{agg}.

For the second statement, it can be rephrased as "N_{agg} and R_c cannot grow infinitely large when T is infinitely distant from CMT". This is widely accepted because from the geometric point of view, R_c cannot be larger than the contour length of the core block, otherwise there will be hollow space within the micelle core, which is impossible. In fact, this limit is almost never achieved in real systems, because the full extension of all core blocks will exert a high entropy penalty on the system, which will overweigh the enthalpic gain brought by the minimization of the surface area. Therefore, there should always be a balance point, above which further increase of γ will not result in the apparent change of R_c, or N_{agg}.

Table 5.3. Summary of Experimental Results on the Dependence of R_c and N_{agg} on $|T - CMT|$

Entry	System [a]	UCST/LCST	CMT (°C)	$\|T - CMT\|$ studied (°C)	N_{agg} change	R_c change	Ref.
1	PEO-*b*-PPO-*b*-PEO in water [b]	LCST	30	3.3 – 12.9	Increases linearly with $\|T - CMT\|$	Remains constant	19
2	PEO-*b*-PPO-*b*-PEO in water [b]	LCST	32	3 – 23	Increases by 50% from $\|T - CMT\|$ = 3 to 23 °C	Remains constant	20
3	PEO-*b*-PPO-*b*-PEO in water/formamide (60/40) [b]	LCST	25	5 – 35	Increases with $\|T - CMT\|$, then reaches a plateau.	Slightly increases.	21
4	PS-*b*-PI in diethyl phthalate [b]	UCST	76	6 – 46	Increases linearly with $\|T - CMT\|$	Increases linearly when $\|T - CMT\| \leq 36$ °C, then levels off	22
5	PS-*b*-PI in tetradecane [b]	UCST	87	7 – 57	Increases linearly when $\|T - CMT\| \leq 47$ °C, then levels off	Increases linearly when $\|T - CMT\| \leq 47$ °C, then levels off	22
6	PS-*b*-PI in heptane [b]	UCST	40	0 – 35	Increases linearly when $\|T - CMT\| \leq 15$ °C	Slightly decreases, then keeps constant.	23
7	PS-*b*-PI in squalane [b]	UCST	190	0 – 160	Remains almost constant	Remains constant	24

[a] Abbreviation used: PEO = poly(ethylene oxide), PPO = poly(propylene oxide), PS = poly(styrene), and PI = poly(isoprene). [b] The core blocks of the micelles are marked in red.

Now, after reviewing the previous studies on the $|T - \mathrm{CMT}|$ dependence of micelle R_c and N_{agg}, we can possibly attribute the temperature insensitivity of R_c in this PMMA-*b*-PnBMA/IL system to the relatively large gap between the experimental temperatures and CMT. That is to say, the "level-off point" for this system may lie somewhere between $|T - \mathrm{CMT}| = 0 - 60$ °C, which will be further illustrated in Section 5.4.

Dependence of σ_R on ΔT

σ_R/R_c is the coefficient of variation of the micelle core radius. It can be noted from Table 5.2 that except for PMMA-*b*-PnBMA (25-44), all other micelle samples display a clear tendency of decreasing σ_R/R_c as $|T - \mathrm{CMT}|$ increases, *i.e.*, when the gap between the experimental temperature and the CMT goes up, the micelle cores become more monodisperse. (Another explanation is that the core-corona interface becomes sharper.) This phenomenon is actually observed in almost all micelle systems so far,[22–24,26] but its reason has rarely been addressed.

If we consider the free energy diagram of the micelles as a function of R_c, there should be a global minimum at $R_{c,m}$, which represents the most probable core radius under a given set of parameters (T, $c_{polymer}$, N_A, N_B, χ_{AB}, χ_{AB}, and χ_{BS}), which is shown in Figure 5.5. This global minimum also corresponds to the equilibrium micelle core size.

Real systems always include a distribution of R_c, since not all the micelles necessarily have to be at the lowest free energy. In fact, the micelles with free energy values between G_m and ($G_m+\Delta G$) can be taken as stable, as is denoted by the shaded area in Figure 5.5; therefore, when the free energy "dip" is sharper, the corresponding R_c distribution will be narrower. This can be schematically reflected on the difference between the black ($|T - \mathrm{CMT}| \approx 0$) and the red ($|T - \mathrm{CMT}| >> 0$) curves in the figure, which provides a relatively satisfactory answer to why σ_R/R_c decreases as $|T - \mathrm{CMT}|$ increases.

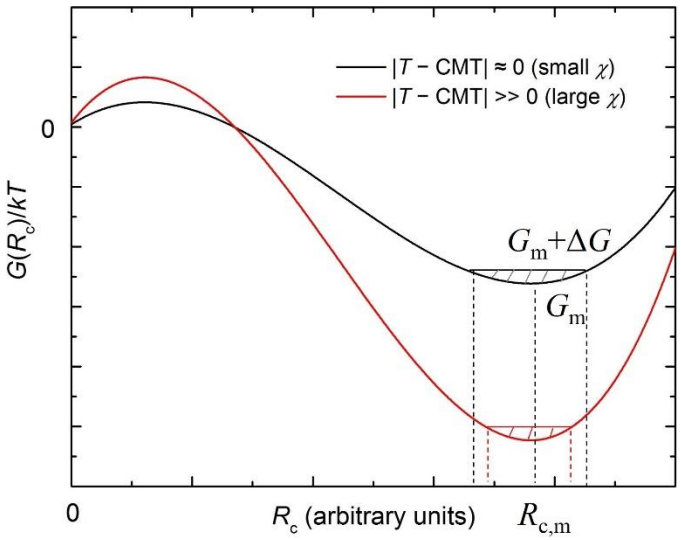

Figure 5.5. Schematic illustration of the free energy diagram of micelles as a function of R_c. The black and red curves represent the cases of $|T - \mathrm{CMT}| \approx 0$ and $|T - \mathrm{CMT}| >> 0$, respectively. (Inspired by Ref 18: Figure 6.3)

Whether Micelles Are Near Equilibrium

From Chapter 1, assuming monodisperse core block length in copolymer micelles, then relaxation function $R(t) = \exp(-t/\tau_{exp})$, where $\tau_{exp} = (N^2b^2\zeta/6\pi^2kT)\cdot\exp(\alpha\chi N)$.[27] Based on the chain exchange kinetic study on this PMMA-*b*-PnBMA/IL system, a rough estimate can be made for the τ_{exp} of a given combination of N_{PnBMA} and [BMIM] wt%. For example, in the CMT = 0 °C series, we let b = 6.1 Å, $\zeta = 7.1 \times 10^{-4}$ Ns/m, and $\alpha\chi$ = 0.012 at 35 °C;[28] then the characteristic time of micelle equilibration can be roughly estimated, as listed in Table 5.4.

Table 5.4. Estimate of the Characteristic Time of Micelle Equilibration

Block Polymer	[BMIM] wt%	N_{PnBMA}	τ_{exp} at 35 °C (s)	τ_{exp} at 55 °C (s)[a]	Estimated Time of Micelle Equilibration at 55 °C (s)[b]
PMMA-*b*-PnBMA (25-24)	0.292	169	2.3×10^{2}	3.6×10^{1}	1.7×10^{2}
PMMA-*b*-PnBMA (25-31)	0.358	218	6.8×10^{2}	1.1×10^{2}	5.0×10^{2}
PMMA-*b*-PnBMA (25-35)	0.390	246	1.2×10^{3}	2.0×10^{2}	9.0×10^{2}
PMMA-*b*-PnBMA (25-44)	0.435	310	4.2×10^{3}	6.7×10^{2}	3.1×10^{3}
PMMA-*b*-PnBMA (25-53)	0.459	373	1.3×10^{4}	2.1×10^{3}	9.5×10^{3}
PMMA-*b*-PnBMA (25-78)	0.500	549	2.3×10^{5}	3.7×10^{4}	1.7×10^{5}

[a] A factor of 0.16 is multiplied when converting the τ_{exp} at 35 °C to that at 55 °C, in the spirit of time-temperature superposition principle.[3] [b] The time of micelle equilibration is defined as the t at which $R(t) = 0.01$, indicating nearly complete rearrangement of chains among micelles.

Although Table 5.4 is only a rough estimate of micelle equilibration time, yet it can still be accurate within one order of magnitude; for example, it is clear that the copolymer with the longest PnBMA block, PMMA-*b*-PnBMA (25-78), has a characteristic equilibration time of ~ 50 hours, which is longer than the 30 hours of sample annealing time. From this sense, this sample is not likely to be ergodic.

Now, we can try to interpret the difference in R_c of PMMA-*b*-PnBMA (25-53) and (25-78) in the CMT = 0 °C and the 100% [EMIM][TFSI] series. A possible explanation

is that when the micelles are initially formed when most of the cosolvent is evaporated, the micelle core radii of the two series are different. However, after annealing, the micelles with shorter PnBMA blocks tend to equilibrate faster than the ones with longer PnBMA blocks. Therefore, for PMMA-*b*-PnBMA (25-24), (25-31), (25-35) and (25-44) micelles, the micelle cores have enough time to equilibrate to the same sizes (which are probably close to their respective equilibrium sizes), while for the PMMA-*b*-PnBMA (25-53) and (25-78) which are not fully equilibrated, R_c still have some difference after hours of annealing.

Similarly, we can extract the scaling relationship between R_c and the degree of polymerization of the core block, N_B, by doing linear fitting of logR_c vs logN_B, as shown in Figure 5.6. The slopes of the CMT = 0 °C series and the CMT = –20 °C series are determined to be 0.51±0.03 and 0.54±0.03, respectively. They both display a much weaker R_c – N_B dependence than the 100% [EMIM][TFSI] series (slope = 0.71±0.01). Additionally, this $R_c \sim N_B^{0.5}$ relationship was also observed in the PEP-*b*-PS micelles in squalane.[24]

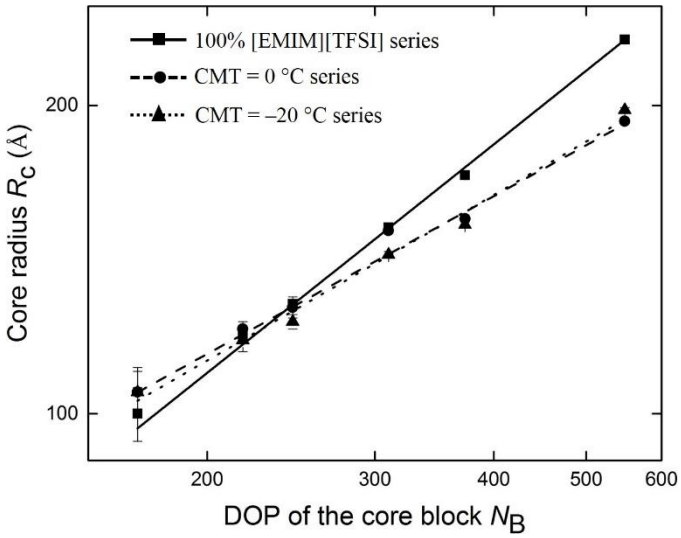

Figure 5.6. Dependence of the core radius on the number of repeating units in the core block for the 100% [EMIM][TFSI] series (filled squares, solid line), the CMT = 0 °C series (filled circles, dashed line), and the CMT = –20 °C series (filled triangles, dotted line).

5.4. Micelle Structures at Higher [BMIM][TFSI] Compositions

In this section, two copolymers, PMMA-*b*-PnBMA (25-78) and (25-44) were selected for the study of micelle structures at higher [BMIM][TFSI] compositions ([BMIM] wt% ≥ 50). In a typical DLS experiment, we collected R_h distribution of free chains/micelles every 10 °C, in order to fully understand the dependence of micelle structure on temperature. At each experimental temperature, the sample was annealed for at least 15 min prior to data collection.

R_h *Distribution of (25-78) Micelles*

The R_h distributions of PMMA-*b*-PnBMA (25-78) in [BMIM] wt% = 30, 65, 70, 80, 90 and 100 are shown in Figure 5.7a – f. Except for the sample with lowest [BMIM][TFSI] composition, all other samples have CMT higher than room temperature, therefore, a clear transition from free chains to micelles can be observed (for example in Figure 5.7b, between 30 and 40 °C).

As can be seen in Figure 5.7, when the temperature goes across the CMT, the average R_h abruptly increases from 7 – 8 nm to larger than 10 nm, indicating the conversion from free chains to micelles. The difference in peak widths of the free chains (top panels, Figure 5.7b – f) is probably owing to the low scattering intensity, which generates inaccuracy in the REPES method. By comparing the R_h distributions in the six solvent compositions, it is evident that (*i*) micelles shrink when *T* is farther removed from CMT; and (*ii*) when [BMIM] wt% exceeds 70, bimodal R_h distribution emerges. The decrease in micelle size is most likely to be the result of shrinkage of micelle cores. As has been mentioned in the previous section, $R_c \sim N_{agg}^{1/3} N_B^{1/3} a/\varphi_p^{1/3}$; therefore, when the increase in φ_p is larger than the increase in N_{agg}, *i.e.*, the loss of solvent predominates over the aggregation number increase, R_c will decrease as *T* is farther removed from CMT. In order to test whether this decrease in R_h is determined by R_c or L_{corona}, SAXS can be

conducted in this T range to separately measure R_c, which will be another topic of interest.

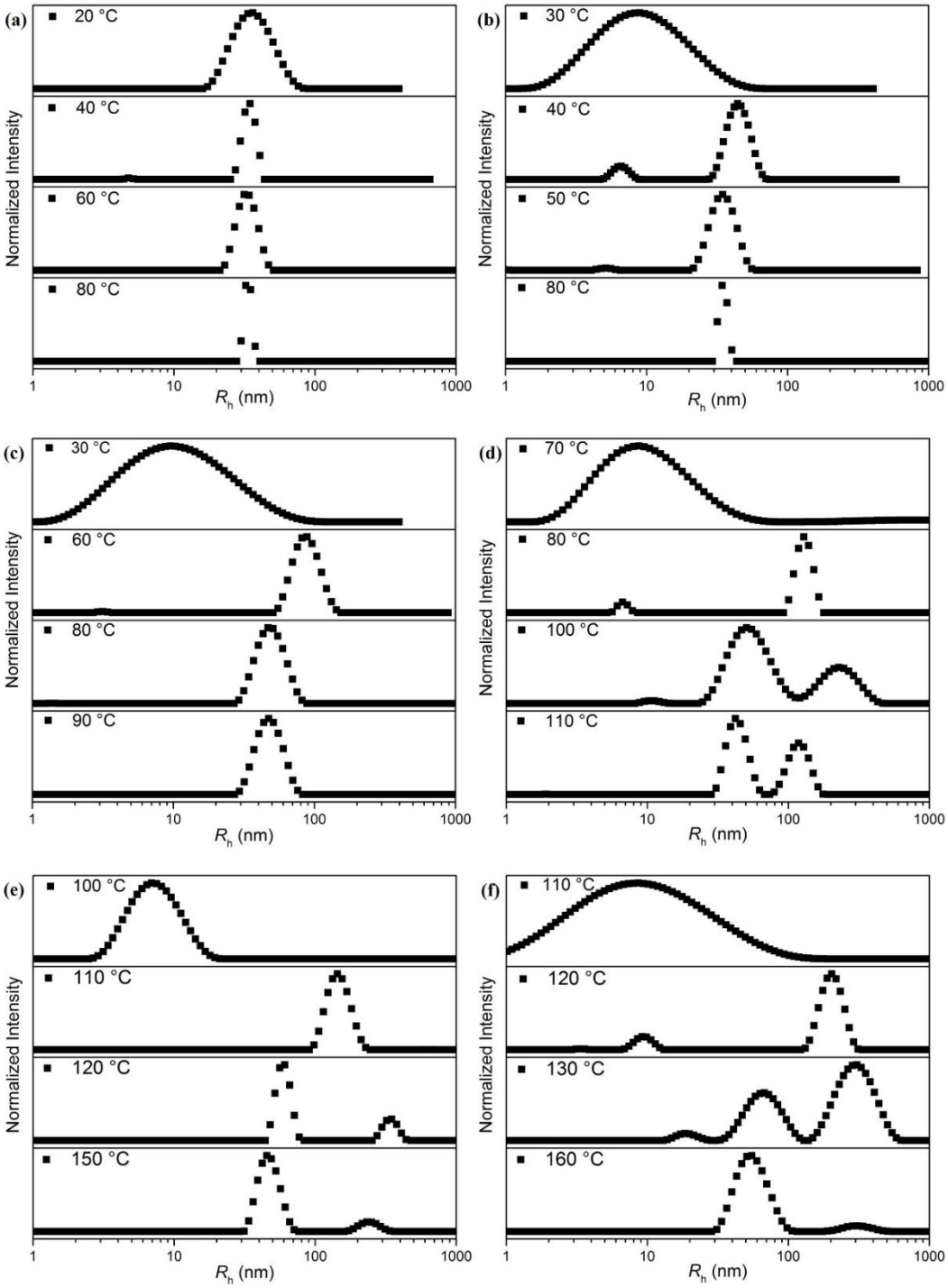

Figure 5.7 R_h distribution of PMMA-*b*-PnBMA (25-78) as a function of temperature in IL mixtures with (a) [BMIM] wt% = 30, (b) [BMIM] wt% = 65, (c) [BMIM] wt% = 70, (d) [BMIM] wt% = 80, (e) [BMIM] wt% = 90, and (f) [BMIM] wt% = 100.

Notably, when the [BMIM][TFSI] composition is increased to 80 wt%, more than one sizes of micelles appear. Although it is not clear whether the micelles with larger R_h represent another morphology, and whether these micelles are in a kinetically trapped state, it is speculated that their higher R_h (or N_{agg}) is attributed to the increase in the interfacial tension between the core and the solvent.

R_h Distribution of (25-44) Micelles

Similarly, the temperature-dependent R_h distributions of a copolymer with shorter core block length, PMMA-*b*-PnBMA (25-44), are also investigated by DLS. The solvent compositions used are [BMIM] wt% = 50, 60, 80 and 100 (Figure 5.8a – d).

In Figure 5.8, we can see that the R_h distributions of this (25-44) polymer in multiple solvent compositions generally follow the same tendency as (25-78): (*i*) at [BMIM] wt % $\leq$ 70, there is a decrease in R_h before approaching a stable value; and (*ii*) at [BMIM] wt % $\geq$ 80, bimodal distribution takes place. From this sense, the two polymers show almost identical behavior, and the existence of multiple micelle morphologies at higher [BMIM] wt% is less likely to be an artifact.

Despite the fact that R_h of the larger micelle species are not very consistent, we can still focus on R_h of the smaller micelles, and plot their stable values, $R_{h,stable}$, as a function of [BMIM] wt%, as can be seen in Figure 5.9. Curiously, it seems that $R_{h,stable}$ only starts to increase at [BMIM] wt% $\approx$ 70, which contradicts with the continuous change on the solvent quality assumed for this IL mixture. This effect may need to be assessed more fully in the future.

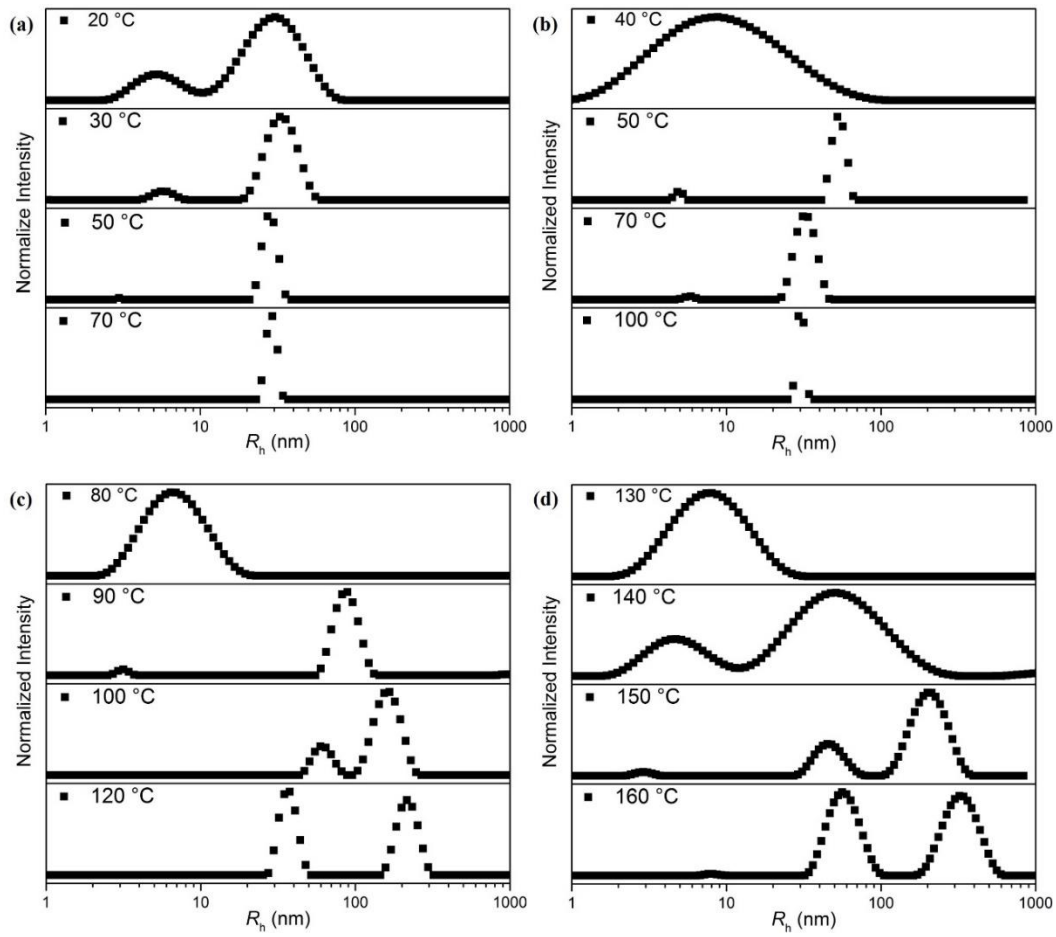

Figure 5.8 R_h distribution of PMMA-*b*-PnBMA (25-44) as a function of temperature in IL mixtures with (a) [BMIM] wt% = 50, (b) [BMIM] wt% = 60, (c) [BMIM] wt% = 80, and (d) [BMIM] wt% = 100.

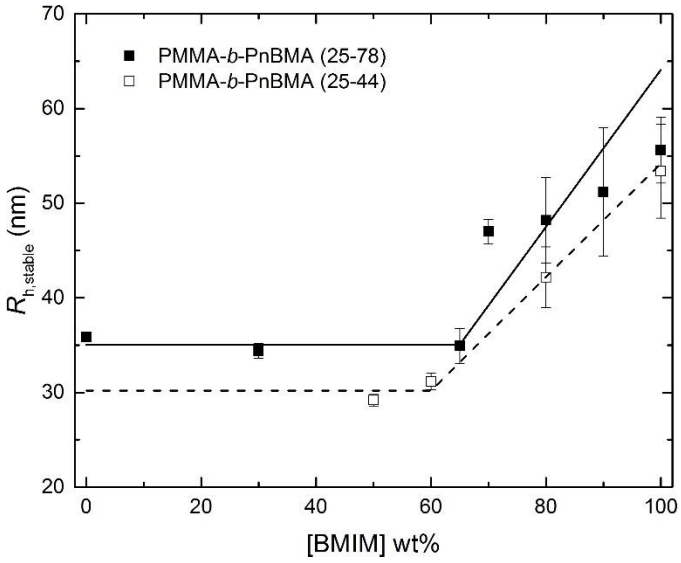

Figure 5.9 $R_{h,stable}$ of PMMA-*b*-PnBMA (25-78) and (25-44) as a function of [BMIM] wt%. The lines between the data points are only for visual aid.

5.5. Summary

In this chapter, we examined the effect of the solvent quality on micelle scaling. In the first part, six PMMA-*b*-PnBMA copolymers with different PnBMA (core block) lengths were dispersed in solvent mixtures with predetermined [BMIM] wt%, so that the resulting solutions all have identical CMT (0 and –20 °C). The core radii R_c of these micelle samples were then extracted from SAXS data fitting at temperatures which are 60, 80 and 100 °C above the CMT, respectively. It was observed that the thermal distance, T – CMT, has little effect on R_c, while the coefficient of variation of R_c (σ_R/R_c) monotonically decreases with T – CMT. Interestingly, the CMT = 0 °C and CMT = –20 °C series have different R_c–N_B relationships from that of 100% [EMIM][TFSI] series, which is speculated to result from the incomplete equilibration of the micelles with long core blocks.

In the second part, DLS was conducted on two of the copolymers in solvent mixtures with even higher [BMIM] wt% (50 – 100). In each solvent mixture, R_h distributions of the free chains/micelles were studied as the temperature rises above CMT. It was

observed that R_h first dramatically increases on the formation of micelles, then decreases within the next 10 or 20 °C, and finally approaches a stable value, $R_{h,stable}$, which is solvent quality-dependent. Most notably, above 70 [BMIM] wt%, bimodal distribution of micelles was observed, possibly indicating a different morphology, such as cylindrical micelles.

Overall, this chapter provides some interesting results of the solvent quality effect on the micelle structures, which may be worth probing into in the future. More conclusive results could be obtained if DLS and SAXS were used in combination for the same micelle samples.

5.6. Acknowledgement

This work was supported by the National Science Foundation (NSF) through award DMR-1206459. The SAXS experiments were conducted on the DuPont-Northwestern-Dow Collaborative Access Team (DND-CAT) Synchrotron Research Center located at Sector 5 of the Advanced Photon Source. DND-CAT is supported by the E.I. DuPont de Nemours & Co., the Dow Chemical Company, the U.S. National Science Foundation through Grant DMR-9304725, and the State of Illinois through the Department of Commerce and the Board of Higher Education Grant IBHE HECA NWU 96. Use of the Advanced Photon Source was supported by the U.S. Department of Energy, Basic Energy Sciences, Office of Science, under Contract No. W-31-109-Eng-38.

5.7. References

(1) Strobl, G. R. *The Physics of Polymers: Concepts for Understanding Their Structures and Behavior*, Springer-Verlag: Berlin Heidelberg, 1996.

(2) Choucair, A.; Eisenberg, A. *Eur. Phys. J. E* **2003**, *10*, 37-44.

(3) Gohy, J. *Adv. Polym. Sci.* **2005**, *190*, 65-136.

(4) Hayward, R. C.; Pochan, D. J. *Macromolecules* **2010**, *43*, 3577-3584.

(5) Jain, S.; Bates, F. S. *Science* **2003**, *300*, 460-464.

(6) Jain, S.; Bates, F. S. *Macromolecules* **2004**, *37*, 1511-1523.

(7) Won, Y.-Y.; Davis, H. T.; Bates, F. S. *Macromolecules* **2003**, *36*, 953-955.

(8) Chen, L.; Shen, H. W.; Eisenberg, A. *J. Phys. Chem. B* **1999**, *103*, 9488-9497.

(9) Meli, L.; Lodge, T. P. *Macromolecules* **2009**, *42*, 580-583.

(10) Meli, L.; Santiago, J. M.; Lodge, T. P. *Macromolecules* **2010**, *43*, 2018-2027.

(11) He, Y.; Li, Z.; Simone, P.; Lodge, T. P. *J. Am. Chem. Soc.* **2006**, *128*, 2745-2750.

(12) Kelly, E. G.; Murphy, R. P.; Seppala, J. E.; Smart, T. P.; Hann, S. D.; Sullivan, M. O.; Epps, T. H., III *Nat. Commun.* **2014**, *5*, 3599.

(13) Lee, H.-N.; Lodge, T. P. *J. Phys. Chem. B* **2011**, *115*, 1971-1977.

(14) Pedersen, J. S.; Svaneborg, C.; Almdal, K.; Hamley, I. W.; Young, R. N. *Macromolecules* **2003**, *36*, 416-433.

(15) Castelletto, V.; Hamley, I. W.; Pedersen, J. S. *J. Chem. Phys.* **2002**, *117*, 8124-8129.

(16) Halperin, A. *Macromolecules* **1987**, *20*, 2943-2946.

(17) Zhulina, E. B.; Adam, M.; LaRue, I.; Sheiko, S. S.; Rubinstein, M. *Macromolecules*, **2005**, *38*, 5330-5351.

(18) Thiagarajan, R. *Modeling of Diblock Copolymers in Selective Solvents*. PhD Dissertation, University of Minnesota, 2012.

(19) Goldmints, I.; von Gottberg, F. K.; Smith, K. A.; Hatton, T. A. *Langmuir* **1997**, *13*, 3659-3664.

(20) Yang, L.; Alexandridis, P; Steytler, D. C.; Kositza, M. J.; Holzwarth, J. F. *Langmuir* **2000**, *16*, 8555-8561.

(21) Alexandridis, P.; Yang, L. *Macromolecules* **2000**, *33*, 5574-5587.

(22) Bang, J.; Viswanathan, K.; Lodge, T. P.; Park, M. J.; Char, K. *J. Chem. Phys.* **2004**, *121*, 11489-11500.

(23) LaRue, I.; Adam, M.; Zhulina, E. B.; Rubinstein, M.; Pitsikalis, M.; Hadjichristidis, N.; Ivanov, D. A.; Gearba, R. I.; Anokhin, D. V.; Sheiko, S. S. *Macromolecules* **2008**, *41*, 6555-6563.

(24) Choi, S.; Bates, F. S.; Lodge, T. P. *J. Phys. Chem. B* **2009**, *113*, 13840-13848.

(25) de Gennes, P.-G. In *Solid State Physics*; Liebert, L., Ed.; Academic: New York, 1978; *Suppl*. 14.

(26) Lu, J.; Bates, F. S.; Lodge, T. P. *Macromolecules* **2015**, *48*, 2667-2676.

(27) Choi, S.; Lodge, T. P.; Bates, F. S. *Phys. Rev. Lett.* **2010**, *104*, 047802.

(28) Ma, Y.; Lodge, T. P. *Macromolecules* **2016**, *49*, 9542-9552.

Chapter 6
Micelle Chain Exchange Kinetics

6.1. Introduction

Block copolymers can self-assemble into various structures in selective solvents, such as spherical micelles, cylindrical micelles, and vesicles, of which the thermodynamic properties have been extensively studied.[1–6] Despite this, relatively few studies have been conducted on the kinetics of molecular exchange among these micelles. Compared with their small molecular weight counterparts, diblock copolymer micelles have much slower chain exchange dynamics for two reasons: (*i*) the high incompatibility between the core block and the solvent, embodied in the interaction parameter χ; (*ii*) large numbers of repeating units in the core block, N_{core}. Both factors contribute to the high activation barrier for the chain expulsion from the micelle, and add to the difficulty of the experiments. Chain exchange kinetics between micelles have been studied using T-jump light scattering,[7–11] non-radiative energy transfer spectroscopy and fluorescence quenching spectroscopy,[12–18] and transmission electron microscopy;[19,20,21] however, a general, quantitative picture has not emerged. Richter and coworkers[22–28] used small-angle neutron scattering (SANS) to investigate chain exchange for poly(ethylene oxide)-*block*-poly(ethylene-*alt*-propylene) (PEO-*b*-PEP) in water/N,N-dimethylformamide (DMF) mixtures, and later reported a quasi-logarithmic time dependence for the overall chain exchange rate.[23,24,25] Lodge, Bates, and coworkers systematically studied chain exchange of a series of poly(ethylene-*alt*-propylene)-*block*-poly(styrene) (PEP-*b*-PS) diblocks in squalane, and elucidated the effect of N_{core} [29,30] and its dispersity ($Đ$),[31] temperature,[29–33] concentration,[32] as well as polymer architecture (using PS-*b*-PEP-*b*-PS

and PEP-*b*-PS-*b*-PEP)[33] on the micelle chain exchange kinetics. A numerical model[29] was established that quantitatively explained the remarkably strong dependence on core block length and the apparent logarithmic decay, which was also consistent with previous analyses of chain diffusion in bulk sphere-forming block copolymers.[34–37]

Both experiment and simulation[38,39] results on chain exchange kinetics in block copolymer micelles are still scarce, and mainly focus on the two model systems mentioned above. In particular, the dependence of the barrier to chain extraction on χ has not been fully elucidated. Here, we report a TR-SANS study on a lower critical micellization temperature (LCMT) system: PMMA-*b*-PnBMA in mixtures of the ionic liquids [EMIM][TFSI] and [BMIM][TFSI]. PMMA is well soluble in both ILs, while PnBMA has lower critical solution temperature (LCST) behavior, where the critical solution temperature increases almost linearly with the [BMIM] wt% in the solvent.[40,41,42] To the best of our knowledge, this is the first study that quantifies chain exchange kinetics in ILs, although Meli, *et al*. examined equilibration of micelle size using dynamic light scattering for diblocks in ILs, and used TR-SANS to confirm that there was no chain exchange during that process.[43,46] Another virtue of this system is that the glass transition temperature (T_g) of the core block, PnBMA, is about 20 °C,[44] which avoids the "glassy core" problem that can also hinder chain exchange.[45,46]

In this chapter, we report TR-SANS measurements of chain exchange kinetics for two series of PMMA-*b*-PnBMA copolymers, one with identical PMMA blocks, and the other with identical PnBMA blocks. In Section 6.3, the series with identical PMMA blocks, PMMA-*b*-PnBMA (25-X), were used as the model copolymers, and the solvent composition is changed systematically, which gives access to a range of the Flory-Huggins interaction parameter χ between the solvent and the core block. A quantitative expression for χ as a function of solvent composition and temperature was obtained from prior measurements.[41,42] The results are compared with the model proposed by Choi *et*

al.,[29,30,31] and particular emphasis is placed on the effect of χ on the overall chain exchange rate. In particular, we show that the previous assumption of a barrier simply proportional to χ is incorrect, and offer a more elaborate expression, developed in the spirit of Flory-Huggins theory. Following the study of χ-dependence, Section 6.4 features the role of corona block on the chain exchange kinetics, in which the series with identical PnBMA blocks, PMMA-*b*-PnBMA (X-35), were used in the TR-SANS study. The preliminary results indicate that the micelles with longer corona blocks exhibit slower kinetics than their counterparts with shorter corona blocks, which is consistent with the recent results published by Zinn *et al.*,[56] but apparently contradicts the previous observation by Lu *et al.* in the PEP-*b*-PS/squalane system.[55] Last, in Section 6.5, the concentration effect on chain exchange kinetics is investigated; the results show that $R(t)$ is almost independent of concentration, when the corona concentration is below its critical overlap concentration.

6.2. Experimental Section

Materials

The two series of copolymers used in this chapter are PMMA-*b*-(*d*)PnBMA (25-X) and (X-35), as has been described in Chapter 2. The (25-X) copolymers have exactly the same PMMA block length of 25 kg/mol, while their PnBMA block lengths vary from 24 to 54 kg/mol. The (X-35) copolymers, on the other hand, do not have any blocks with identical lengths (because the PMMA block is always the first block synthesized in RAFT polymerization), but their (*d*)PnBMA blocks are all close to 35 kg/mol. The characterization results of the six pairs of *h*- and *d*- PMMA-*b*-PnBMA copolymers are listed in Table 6.1. The numbers in the brackets refer to the molecular weight of each block in kg/mol.

Table 6.1. Characterization of PMMA-*b*-PnBMA Diblock Copolymers

	PMMA block M_n (kg/mol)[a]	**(*d*)PnBMA block M_n (kg/mol)[b]**	N_{PMMA}[c]	$N_{(d)PnBMA}$[d]	$Đ$
PMMA-*b*-PnBMA (25-24)	25	24	250	169	1.05
PMMA-*b*-*d*PnBMA (25-25)	25	25	250	166	1.05
PMMA-*b*-PnBMA (25-35)	25	35	250	246	1.05
PMMA-*b*-*d*PnBMA (25-38)	25	38	250	252	1.05
PMMA-*b*-PnBMA (25-53)	25	53	250	373	1.08
PMMA-*b*-*d*PnBMA (25-54)	25	54	250	354	1.09
PMMA-*b*-PnBMA (42-35)	42	35	420	246	1.10
PMMA-*b*-*d*PnBMA (42-35)	42	35	420	232	1.10
PMMA-*b*-PnBMA (57-35)	57	35	570	246	1.09
PMMA-*b*-*d*PnBMA (57-37)	57	37	570	245	1.11
PMMA-*b*-PnBMA (84-35)	84	35	840	246	1.11
PMMA-*b*-*d*PnBMA (84-38)	84	38	840	252	1.14

[a]Number average molecular weight of the PMMA block was determined by light scattering detection during SEC, with 0.084 mL/g used as the d*n*/d*c* of PMMA.[47] [b]Number average molecular weight of (*d*)PnBMA block determined by ^{1}H-NMR spectroscopy. [c]Degree of polymerization of PMMA block. [d]Degree of polymerization of (*d*)PnBMA block.

Sample preparation

Isotopic solvent mixtures of protonated ionic liquid and d_3-ionic liquid were used in the contrast-matching method, the ratio of which was selected so that the average neutron scattering length density (SLD) of the solvent mixture ρ_{sol} is equal to that of a 50/50 PnBMA/dPnBMA micelle core, *i.e.*, $\rho_{sol} = \Phi_{h\text{-}IL}\,\rho_{h\text{-}IL} + (1 - \Phi_{h\text{-}IL})\,\rho_{d\text{-}IL} = (\rho_{PnBMA} + \rho_{dPnBMA})/2$, where $\Phi_{h\text{-}IL}$ is the volume fraction of the protonated ionic liquid in the solvent

mixture. In this work, the $\Phi_{h\text{-}IL}$ for [EMIM][TFSI] and [BMIM][TFSI] are calculated to be 0.62 and 0.08, respectively. The calculated SLD results are listed in Table 6.2.

Table 6.2. Scattering Length Densities and Volume Fractions for Contrast-Matching

Material	Molecular weight of repeat unit (g/mol)	Density[a] (g/cm^3)	Coherent scattering length (10^{-12} cm)	Scattering length density (10^{10} cm^{-2})	Volume fraction[b]
PMMA	100	1.18	1.491	1.06	–
PnBMA	142	1.07	1.244	0.564	0.5
dPnBMA	151	1.14	10.61	4.82	0.5
50/50 *h*-/*d*-PnBMA	–	–	–	2.69	–
[EMIM][TFSI]	391	1.52	10.29	2.41	0.62
d_3-[EMIM][TFSI]	394	1.53	13.42	3.14	0.38
[BMIM][TFSI]	419	1.44	10.13	2.10	0.08
d_3-[BMIM][TFSI]	422	1.45	13.25	2.74	0.92

[a] Density of deuterated material was calculated assuming that the molar volume is identical to that of the protonated material. [b] Volume fraction under which the contrast-matching condition is achieved.

In the preparation of the micelle specimens, methylene chloride was used as a cosolvent to dissolve the PMMA-*b*-PnBMA and PMMA-*b*-*d*PnBMA separately. These solutions were then combined with a predetermined ratio of contrast-matched [EMIM][TFSI] and [BMIM][TFSI] mixture at room temperature, and then purged with nitrogen overnight to slowly remove the cosolvent. The resulting solutions were dried at 50 °C under vacuum (< 100 mTorr) for at least 12 h prior to use.

Time-Resolved Small-Angle Neutron Scattering (TR-SANS)

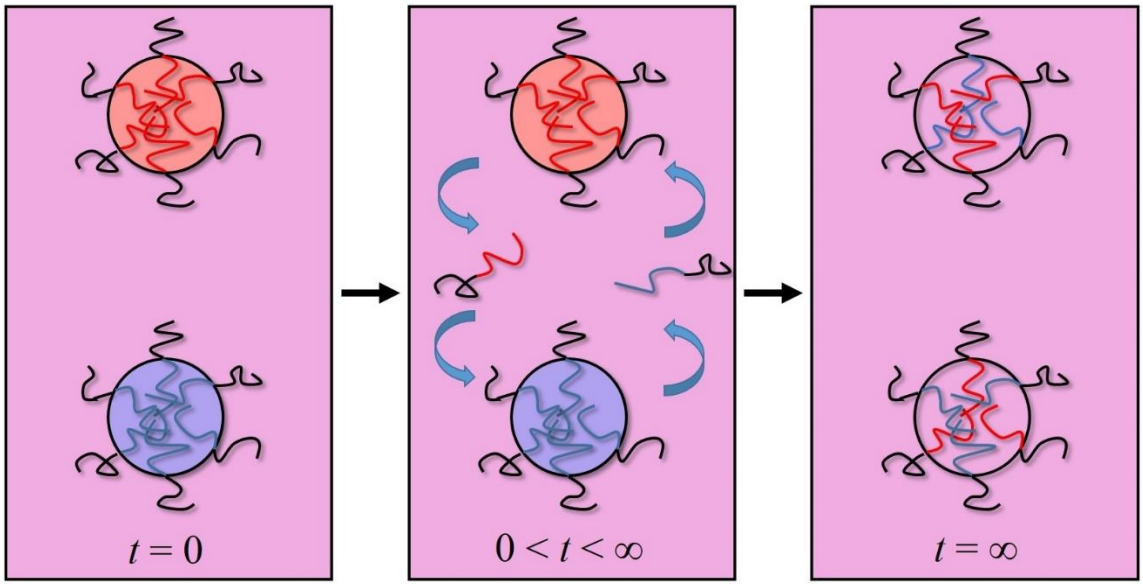

Figure 6.1. Schematic illustration of chain exchange process among block copolymer micelles.

In a typical TR-SANS measurement, *h*- and *d*-micelle solutions were first mixed at the designated temperature, and then quickly transferred into a 1 mm thickness demountable titanium cell, which was then placed on the neutron beamline. At t = 0, the micelle cores in solution (denoted as "post-mixed" solution) are uniformly composed of isotopically pure PnBMA chains, which gives maximum contrast; as chain exchange takes place between micelles, the contrast between the micelle cores and the solvent diminishes with time, and finally decays to zero at $t = \infty$ (Figure 6.1). As the coherent scattering intensity of the core, $I_{\text{coh, core}} \sim (\rho_{\text{core}} - \rho_{\text{sol}})^2$, therefore, the total scattering intensity also monotonically decreases with time, as the corona scattering remains the same during the whole process. In order to quantitatively reflect the extent of chain exchange, the normalized relaxation function, $R(t)$, is defined as follows:

$$R(t) = \sqrt{\frac{I(t) - I(\infty)}{I(0) - I(\infty)}} \tag{6.1}$$

in which $I(t)$, $I(0)$ and $I(\infty)$ are the scattering intensity at time = t, 0 ("post-mixed"[24]), and infinity. Since it is sometimes not practical to obtain the experimental data at infinitely long time, *i.e*. a fully equilibrated sample, a "pre-mixed" sample is used instead, which is prepared by co-dissolving 50/50 *h*-/*d*-copolymers with contrast-matched ILs and the cosolvent, followed by the removal of cosolvent. Notably in this work, the chain exchange rate for some copolymer samples is relatively fast, making the measurement at t = 0 not feasible, and therefore the scattering intensities of the separate *h*- and *d*-micelle solutions are averaged to give $I(0)$ in eq. 6.1. Further discussion of $R(t)$ can be found in previous papers.[29,32]

The TR-SANS experiments in Sections 6.3 and 6.4 were conducted on the NG-7 30m SANS beamline at the Center for Neutron Research of the National Institute of Standards and Technology (NIST), Gaithersburg, MD. Data were acquired using an instrument configuration with a wavelength of 6.0 Å, a wavelength spread ($\Delta\lambda/\lambda$) of 0.22, and a sample-to-detector distance of 4.70 m, thereby providing a q range of 0.007–0.07 $Å^{-1}$ (q is the scattering wave vector, defined as $q = 4\pi\sin(\theta/2)/\lambda$). The 1 mm demountable cells containing the samples were placed and heated on a 7-position temperature-controlled heating block provided by NIST, which was capable of maintaining the temperature within ±1 °C. A calibrated thermocouple was used to monitor the actual temperature within the cell by inserting the tip into a reference cell filled with [EMIM][TFSI]. In each group of measurements, the scattering intensities of the *h*-, *d*-, and pre-mixed micelle solutions were first collected for 5 minutes each; then the post-mixed micelle solution was measured and its scattering pattern was recorded for 5 minute intervals, which lasted for 2 – 3 hours in total. The 2-D scattering patterns were first reduced to absolute intensity using the transmittance of the sample, the scattering of the empty cell, and the transmittance of the empty cell, then converted to 1-D data using the Igor Pro package developed by the NIST.[48]

The TR-SANS experiments in Section 6.5 were conducted on the CG-2 GP-SANS at Oak Ridge National Laboratory (ORNL), Oak Ridge, TN. Data were acquired using an instrument configuration with a wavelength of 4.75 Å, a wavelength spread ($\Delta\lambda/\lambda$) of 0.13, and a sample-to-detector distance of 10 m. The valid q range of this configuration is 0.007–0.1 $Å^{-1}$. All the other conditions are the same as described above. The data reduction follows a similar protocol also by using Igor Pro.

6.3. Micelle Chain Exchange Kinetics: Dependence on χ

TR-SANS Results

Figure 6.2 displays representative 1-D SANS profiles of the post-mixed PMMA-*b*-PnBMA micelle specimens (1 wt% copolymer) as a function of time. Each panel illustrates a different combination of core block length and IL composition, which are the two main variables. In each example, the t = 0 data reflect the scattering of the micelle cores with isotopically pure *h*- and *d*- chains (with the chain exchange not yet taking place). The scattering intensity for t = 0 is calculated by taking the average of the scattering intensities of the *h*- and *d*- micelle solutions of the same concentration, because the polymer concentration (1 wt%) is below the concentration at which any structure factor peaks start to emerge. The $t = \infty$ data reflect the completion of the chain exchange between micelles, which is marked by the random distribution of the *h*- and *d*- chains in each core. As can be seen from all the panels in Figure 6.2, the scattering intensities approach the $t = \infty$ curve as t increases, which establishes that chain exchange takes place. It is worth noticing that the $t = \infty$ curves deviate slightly from the baseline (pure solvent) at low q; this can be attributed to the corona scattering, as the PMMA corona blocks are not contrast-matched. Nevertheless, this does not affect the data analysis, because this part of the scattering is included in all the three terms: $I(0)$, $I(t)$ and $I(\infty)$, and

is cancelled out according to eq. 6.1. For each combination of core block lengths and solvent compositions, at least two temperatures were used to test whether chain exchange occurred, and the results were used to construct master curves by time-temperature superposition, which will be discussed subsequently.

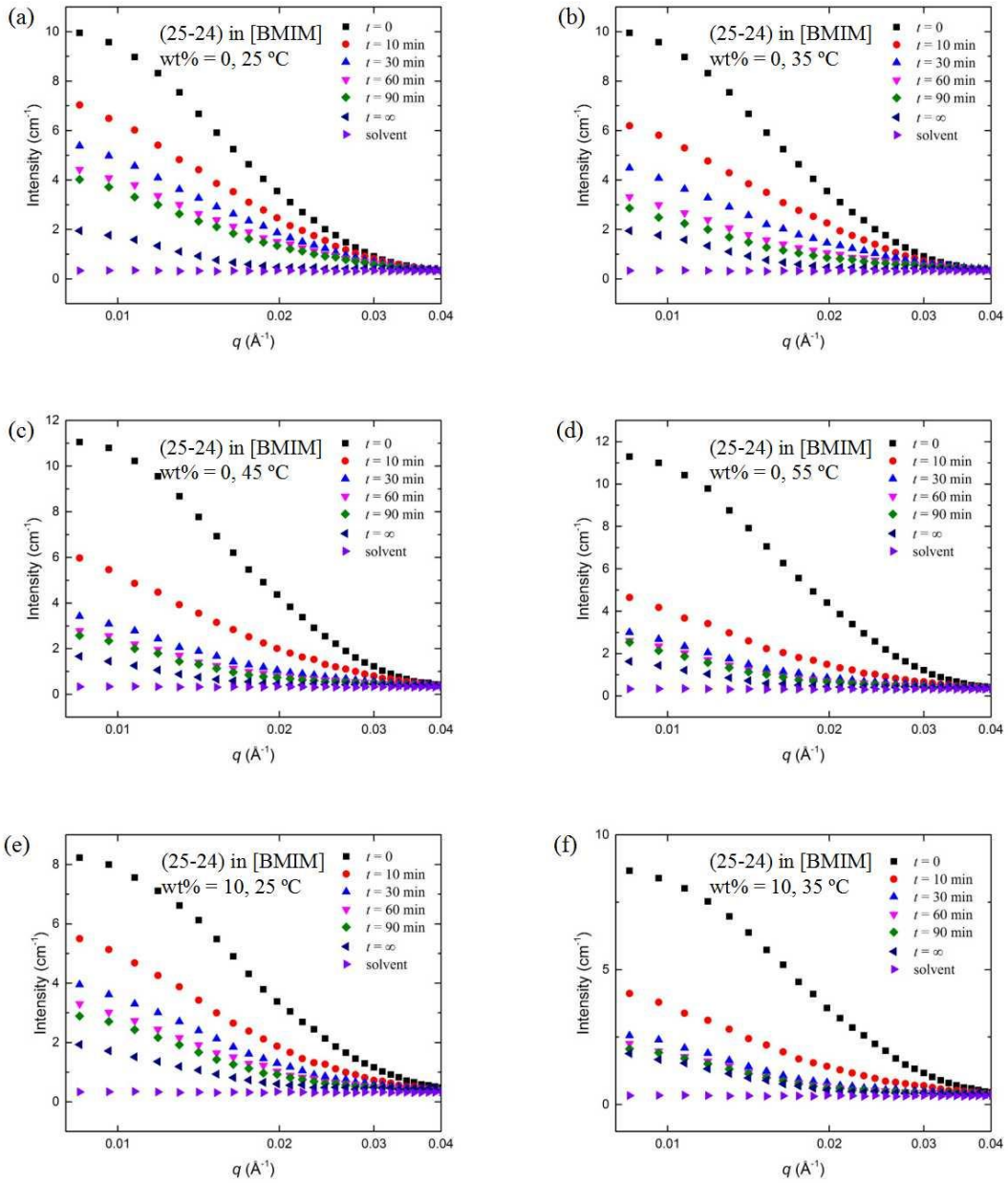

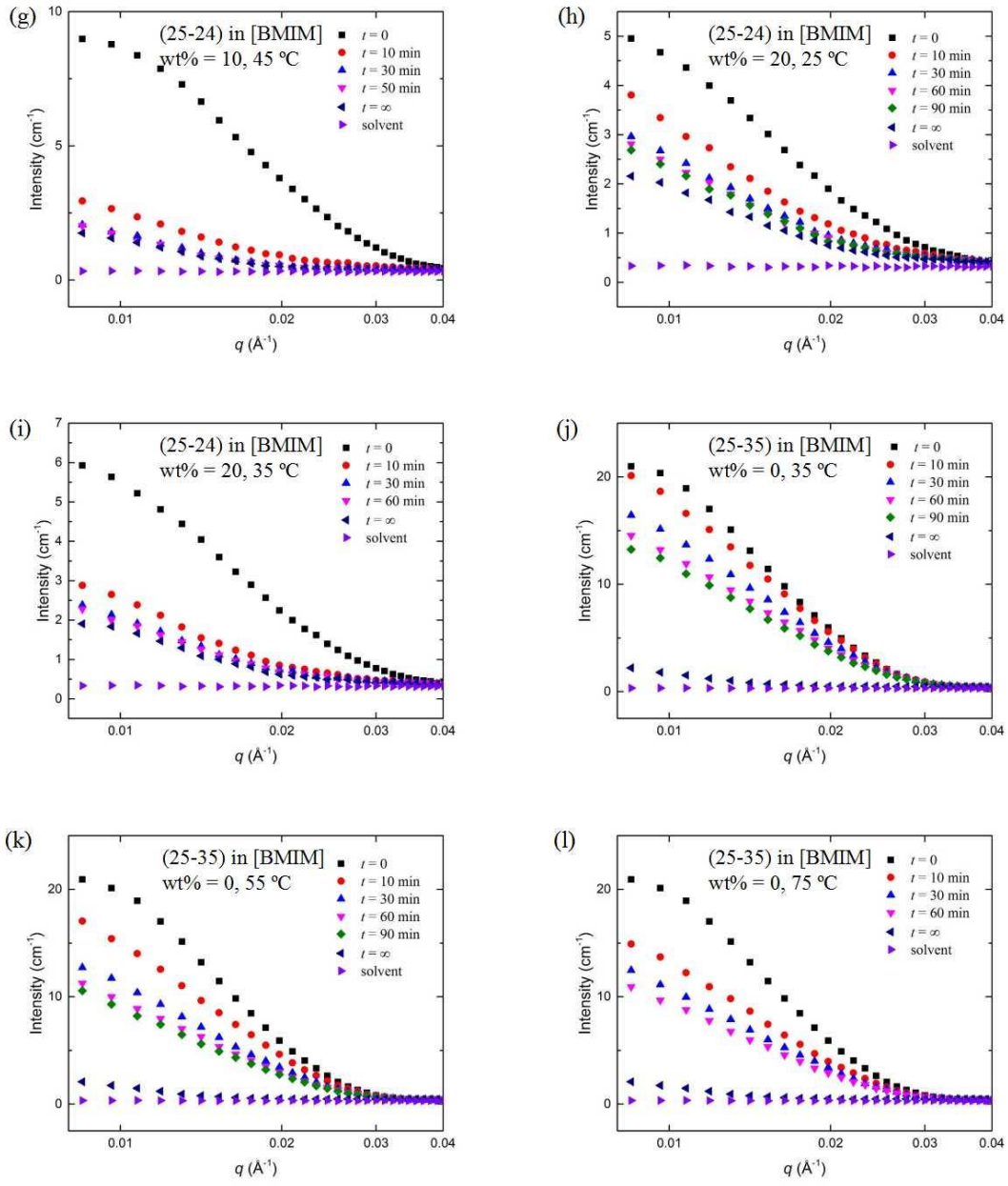
(g)
(25-24) in [BMIM]
wt% = 10, 45 ℃
t = 0
t = 10 min
t = 30 min
t = 50 min
t = ∞
solvent
Intensity (cm-1)
q (Å-1)
(h)
(25-24) in [BMIM]
wt% = 20, 25 ℃
t = 0
t = 10 min
t = 30 min
t = 60 min
t = 90 min
t = ∞
solvent
Intensity (cm-1)
q (Å-1)
(i)
(25-24) in [BMIM]
wt% = 20, 35 ℃
t = 0
t = 10 min
t = 30 min
t = 60 min
t = ∞
solvent
Intensity (cm-1)
q (Å-1)
(j)
(25-35) in [BMIM]
wt% = 0, 35 ℃
t = 0
t = 10 min
t = 30 min
t = 60 min
t = 90 min
t = ∞
solvent
Intensity (cm-1)
q (Å-1)
(k)
(25-35) in [BMIM]
wt% = 0, 55 ℃
t = 0
t = 10 min
t = 30 min
t = 60 min
t = 90 min
t = ∞
solvent
Intensity (cm-1)
q (Å-1)
(l)
(25-35) in [BMIM]
wt% = 0, 75 ℃
t = 0
t = 10 min
t = 30 min
t = 60 min
t = ∞
solvent
Intensity (cm-1)
q (Å-1)

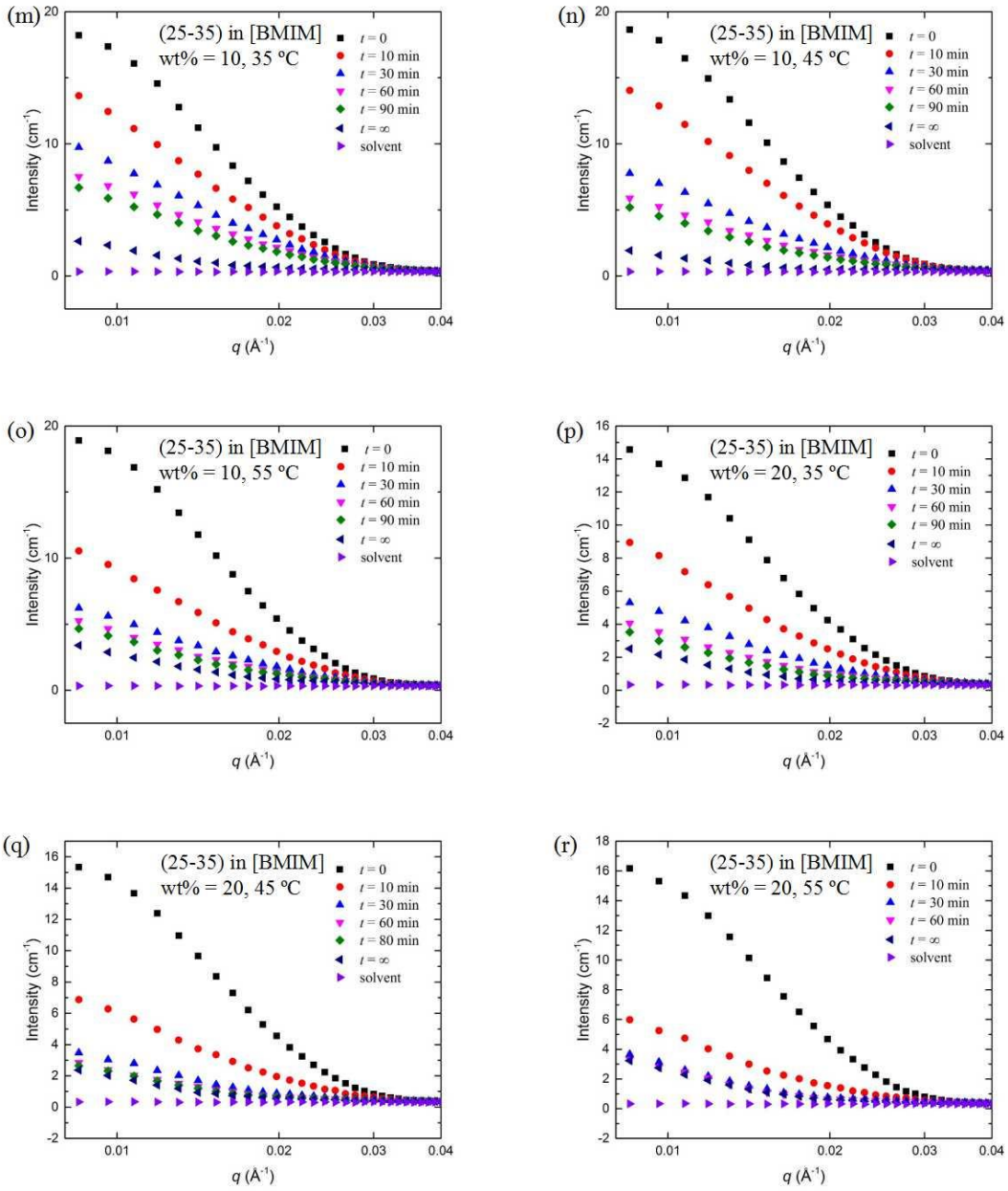
(m)
(25-35) in [BMIM]
wt% = 10, 35 °C
(n)
(25-35) in [BMIM]
wt% = 10, 45 °C
(o)
(25-35) in [BMIM]
wt% = 10, 55 °C
(p)
(25-35) in [BMIM]
wt% = 20, 35 °C
(q)
(25-35) in [BMIM]
wt% = 20, 45 °C
(r)
(25-35) in [BMIM]
wt% = 20, 55 °C
t = 0
t = 10 min
t = 30 min
t = 60 min
t = 90 min
t = 80 min
t = ∞
solvent
Intensity (cm-1)
q (Å-1)

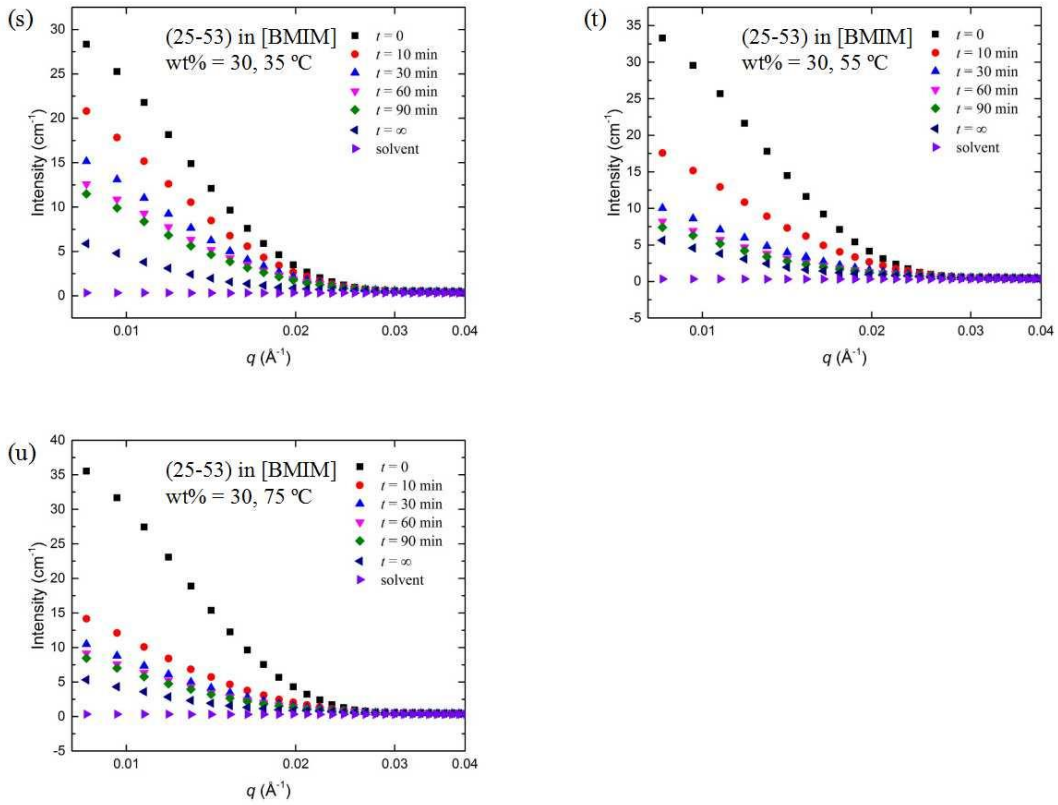

Figure 6.2. Representative TR-SANS profiles over 5-minute intervals for PMMA-*b*-PnBMA (25-24) in [BMIM] wt% = 0 at (a) 25 ºC, (b) 35 ºC, (c) 45 ºC, and (d) 55 ºC; PMMA-*b*-PnBMA (25-24) in [BMIM] wt% = 10 at (e) 25 ºC, (f) 35 ºC, and (g) 45 ºC; PMMA-*b*-PnBMA (25-24) in [BMIM] wt% = 20 at (h) 25 ºC, and (i) 35 ºC; PMMA-*b*-PnBMA (25-35) in [BMIM] wt% = 0 at (j) 35 ºC, (k) 55 ºC, and (l) 75 ºC; PMMA-*b*-PnBMA (25-35) in [BMIM] wt% = 10 at (m) 35 ºC, (n) 45 ºC, and (o) 55 ºC; PMMA-*b*-PnBMA (25-35) in [BMIM] wt% = 20 at (p) 35 ºC, (q) 45 ºC, and (r) 55 ºC; PMMA-*b*-PnBMA (25-53) in [BMIM] wt% = 30 at (s) 35 ºC, (t) 55 ºC, and (u) 75 ºC.

On the basis of eq. 6.1, $I(t)$ in Figures 6.2a–u are converted to $R(t)$, which are displayed in Figure 6.3. Here we use the integrated intensity over the q range of $0.008 < q < 0.040$, $0.008 < q < 0.035$ and $0.008 < q < 0.030$ ($Å^{-1}$) for PMMA-*b*-PnBMA (25-24), (25-35) and (25-53), respectively. This is based on the consideration of minimizing the error caused by baseline difference, while still including sufficient data.

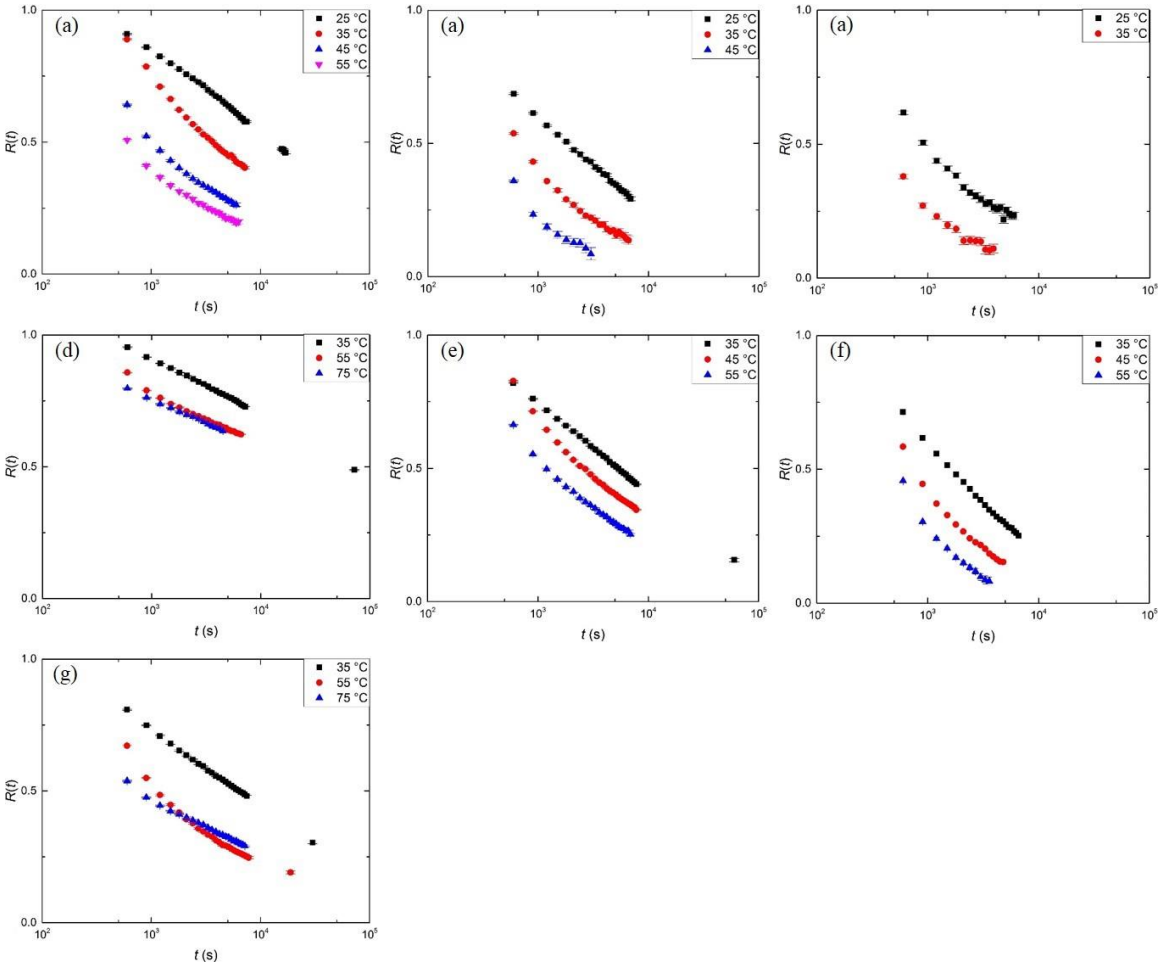

Figure 6.3. *R*(*t*) of the post-mixed solutions at various temperatures for (a) PMMA-*b*-PnBMA (25-24) in [BMIM] wt% = 0%, (b) PMMA-*b*-PnBMA (25-24) in [BMIM] wt% = 10%, (c) PMMA-*b*-PnBMA (25-24) in [BMIM] wt% = 20%, (d) PMMA-*b*-PnBMA (25-35) in [BMIM] wt% = 0%, (e) PMMA-*b*-PnBMA (25-35) in [BMIM] wt% = 10%, (f) PMMA-*b*-PnBMA (25-35) in [BMIM] wt% = 20%, and (g) PMMA-*b*-PnBMA (25-53) in [BMIM] wt% = 30%.

The time-temperature superposition (tTS) principle has been consistently applied to the micelle chain exchange problem in the previous work from our group.[29,30,31,32,33] The key underlying point is that the chain exchange kinetics are mainly dictated by two factors: chain relaxation in the core block, and the activation barrier that a core block has to overcome when it moves into the solvent. Both factors depend on temperature in a molecular weight independent way, and thus a master curve can be constructed by shifting individual *R*(*t*) curves horizontally along the time axis onto the *R*(*t*) at the

reference temperature (T_{ref}). In this study, T_{ref} is selected as 35 °C, and the $R(t)$ curves are shifted empirically by a factor of a_T towards the $R(t)$ of 35 °C so that the maximum overlap can be achieved, where a_T is the temperature-dependent shift factor. The time-temperature superposed $R(t)$ are shown in Figure 6.4, and the data are fit to the model proposed by Choi *et al.*:[29]

$$R(t) = \int P(N_{core}) \exp[-t \frac{6\pi^2 kT}{N_{core}^2 b^2 \zeta} \exp(-\alpha \chi N_{core})] dN_{core} \quad (6.2)$$

where k, T, b, ζ, and α are the Boltzmann constant, temperature, statistical segment length of the core block, monomeric friction coefficient of the core block, and a dimensionless prefactor, respectively. $P(N_{core})$ is the Schulz-Zimm distribution of the degree of polymerization of the core block,[49] defined as:

$$P(N_i) = \frac{z^{z+1}}{\Gamma(z+1)} \frac{N_i^{z-1}}{N_n^z} \exp(-\frac{zN_i}{N_n}) \quad (6.3)$$

in which $z = [(N_w/N_n) - 1]^{-1}$, and Γ is the gamma function.

In the PMMA-*b*-PnBMA/IL system, the statistical segment length (b) of PnBMA is 6.1 Å,[50] and its monomeric friction coefficient (ζ) can be calculated using zero-shear viscosity data (see Figure A.6.1 and Table A.6.1 in the Appendices), which generally agree with the ζ values reported by Ferry *et al.*[51,52] Assuming modest solvent penetration into the micellar core, we use ζ at 65 °C instead of ζ at 35 °C as the monomeric friction coefficient at T_{ref}, in order to account for the depression in the T_g of PnBMA. This empiricism is reasonable, since it is clear from Figure 6.2 that the chain exchange can still take place at 25 °C, which is only slightly higher than the literature T_g of PnBMA at 20 °C. Such a negligible temperature interval would normally strongly hinder the chain movement in the core and thereby slow down the overall chain exchange rate dramatically, given that the T_g of PnBMA is the same in the micelle core as in bulk. However, it is not the case here. This indicates that the T_g in PnBMA core is lower than

that in bulk, although the selection of a 30 °C interval is an educated guess based on the previous study of the PEP-*b*-PS/squalane system.[29,32]

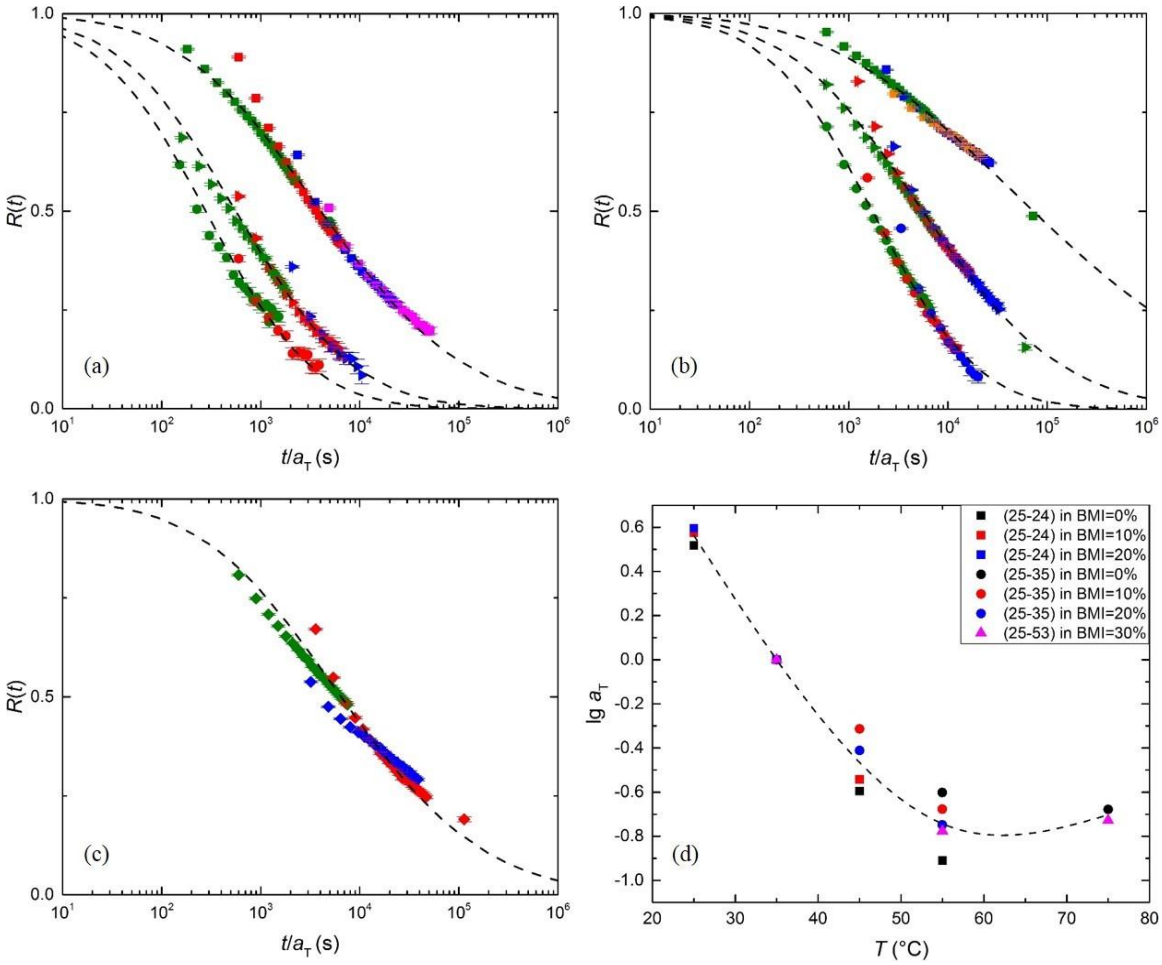

Figure 6.4. Time-temperature superposed $R(t)$ for (a) PMMA-*b*-PnBMA (25-24), (b) PMMA-*b*-PnBMA (25-35), and (c) PMMA-*b*-PnBMA (25-53). The filled square (■), triangle (►), circle (●) and diamond (♦) represent [BMIM] wt% = 0, 10, 20 and 30%, respectively. The dashed lines are best fit to the model proposed by Choi *et al*. (d) Shift factor a_T as a function of temperature (dashed line drawn as a visual aid).

The $\alpha\chi$ and N_w/N_n values obtained from the fitting to eqs. 6.2 and 6.3 are listed in Table 6.3. Notably, the $\alpha\chi$ values of PMMA-*b*-PnBMA (25-24) in [BMIM] wt% = 0, 10 and 20% are in very good agreement with those of PMMA-*b*-PnBMA (25-35) for identical solvent compositions. This is expected since under the assumption that α is a

constant in this system, χ should not depend strongly on the core block length, as predicted by Flory-Huggins theory.[53] Since the monomeric friction coefficient (ζ) estimated by different methods can differ by as much as a factor of five,[51] therefore, the errors introduced via the statistical segment length (b) and core block length (N_{core}) are negligible. If we use a factor of 5 as the estimate for the error margin of ζ, then the relative error it will bring to the determination of $\alpha\chi$ is $\pm(\ln 5/N_{core})$, as given in Table 6.3. We will go further into detail about the χ dependence of the chain exchange rate in the Discussion. The values of dispersity obtained from the fits are also eminently reasonable.

Table 6.3. Fitting Results for Chain Exchange Kinetics of PMMA-*b*-PnBMA (25-X)

Copolymer	N_n input	[BMIM] wt%	N_w/N_n	$\alpha\chi$
PMMA-*b*-PnBMA (25-24)	169	0	1.10	0.033±0.009
		10	1.11	0.021±0.009
		20	1.11	0.017±0.009
PMMA-*b*-PnBMA (25-35)	246	0	1.14	0.032±0.006
		10	1.10	0.021±0.006
		20	1.07	0.016±0.006
PMMA-*b*-PnBMA (25-53)	373	30	1.13	0.012±0.004

Discussion

In 2010, Choi, *et al*. proposed the first successful quantitative model that can effectively predict the chain exchange behavior, based on knowledge of the Rouse dynamics of the core block, the length of the core block, and the interaction parameter between core and solvent, in an upper critical micelle temperature (UCMT) system (PEP-*b*-PS/squalane).[29,32] Therefore, the following discussion will be primarily based on this

model (eq. 2). However, it will emerge that the dependence on χ in this equation is not correct. (Note that equation 6.2 also does not explicitly consider the dependence on the corona block length, which is a separate topic of interest).[54, 55, 56]

The Effect of Temperature. As can be seen from eq. 6.2, the effect of temperature (T) enters mainly through ζ and χ. Both parameters can be strong functions of temperature: the monomeric friction coefficient, $\zeta(T)$, decreases monotonically with temperature following a WLF-type relationship for all polymers above T_g; $\chi(T)$, on the other hand, may increase or decrease. For UCMT systems, $\chi(T)$ decreases, while for LCMT systems, $\chi(T)$ increases with temperature. Therefore, unlike the UCMT systems where $\zeta(T)$ and $\chi(T)$ change in the same direction, LCMT systems have the two varying in the opposite way; therefore changes in the two factors partially cancel, and $R(t)$ of LCMT systems may be relatively less sensitive to T. This is apparent in Figure 6.4d, in which $log\ a_T$ only changes by about 0.4 units when T changes by 10 °C, whereas in the PEP-*b*-PS/squalane system, $log\ a_T$ changes by about 1 unit over the same interval.[32] This significant difference further corroborates that both relaxation of the core block and the thermodynamic barrier of chain expulsion contribute to the chain exchange process. Nevertheless, the overall chain exchange rate still increases with T as in the case of UCMT systems, indicating that the decrease in Rouse relaxation time ($N_{core}^2 b^2 \zeta / 6\pi^2 kT$) predominates over the increase in the enthalpy penalty term [$\exp(\alpha\chi N_{core})$]. Interestingly, for T = 55 and 75 °C, the shift factors are almost identical, which has not been observed previously in UCMT systems. This may indicate that at some point between these two temperatures, there is a crossover where the decrease in the Rouse relaxation time is cancelling the increase in energy penalty. This is reasonable, because the Rouse relaxation time follows a WLF-relationship with temperature, thus its temperature dependence becomes weaker when the temperature is further removed from T_g.

The Effect of χ. It is quite clear in Figures 6.4a and 6.4b that the solvent composition plays a vital role in determining the chain exchange rate between micelles: when the [BMIM] wt% increases from 0 to 10, the chain exchange dynamics accelerates by almost one order of magnitude. This is because in eq. 6.2, $R(t)$ has a "exponential of an exponential" relationship with χ; therefore, it is reasonable that by changing the [BMIM] wt% in the solvent, χ is changed as well, which leads to a dramatic change in $R(t)$. In Table 6.3, the extracted values of $\alpha\chi$ decrease systematically with the increase of [BMIM] wt%. This reflects the fact that the LCST of PnBMA increases with the [BMIM] wt%.[40,41]

The Effect of Core Block Dispersity. From eq. 6.2, N_w/N_n is another important parameter in the fitting, which dictates the apparent slope of the time-temperature superposed $R(t)$ curve.[29] This N_w/N_n represents the combined core block dispersity of the *h*- and *d*-PnBMA (which does not have to be identical to $Đ$ measured by SEC, since SEC gives $Đ$ of the whole diblock copolymer). By comparing the N_w/N_n obtained from the fitting (Table 6.3) and the $Đ$ measured by SEC (Table 1), it can be seen that the dispersities obtained by the fitting are slightly larger than those obtained by SEC in all cases. Nevertheless, the difference is within experimental error, which might be due to the fact that the TR-SANS technique is more sensitive to the core block chains with lower molecular weight, while SEC is not.

Improved Model. So far, the model has assumed that the activation barrier for single chain expulsion is proportional to χN. In fact, when first looking into this issue, Halperin and Alexander proposed that the core block forms a collapsed globule when going through the corona, thus the activation barrier should scale with $\chi N^{2/3}$.[57] To test whether this approach can be successful, we fit some of our data with respect to both χN and $\chi N^{2/3}$ for comparison; the results are given in Table 6.4. From these data, it is apparent that the $\alpha\chi$ values of the same [BMIM] wt% are more consistent when fitting to χN; moreover,

this fitting gives more reasonable dispersities (N_w/N_n). Therefore, these data favor the linear dependence on N, as do all the data on PS-PEP in squalane.[29, 58]

The most important unresolved issue is the exact dependence on χ. When the experimental temperature approaches the LCST of the core block, the theta condition is achieved, thus there should be no barrier for chain expulsion (and, in fact, there will be no micelles). However at theta condition, $\chi \approx 0.5$, so χN cannot be zero. In order to resolve this discrepancy, the exponential term in eq. 2 could be modified empirically to $\exp[\alpha(\chi–0.5)N]$, or more generally $\exp[\alpha f(\chi)N]$. Based on Flory-Huggins theory, $f(\chi)$ should be asymptotically proportional to $(\chi–1)$ in the limit of a non-solvent ($\chi >> 1$) and large N_{core} (see Appendices A.7); near the LCST of the core block, there will be appreciable solvent in the core, and the dependence could be more complicated.[59]

Table 6.4. Comparison Between Fitting of Two Models

Copolymer	[BMIM] wt%	Fit to χN		Fit to $\chi N^{2/3}$	
		N_w/N_n	$\alpha\chi$	N_w/N_n	$\alpha\chi$
PMMA-*b*-PnBMA (25-24)	0	1.10	0.033	1.17	0.186
	10	1.11	0.021	1.21	0.118
	20	1.11	0.017	1.24	0.093
PMMA-*b*-PnBMA (25-35)	0	1.14	0.032	1.22	0.204
	10	1.10	0.021	1.16	0.133
	20	1.07	0.016	1.11	0.100

First, we consider the more general case, where the molar volume of the solvent (v_1) and the polymer repeat unit (v_2) do not have to be equal. The previous determination of χ for this system used the solvent molar volume as the reference, but then N_{core}, b, and ζ would all need to be renormalized. Therefore we will use v_2 as the reference, and we will

need to adjust χ from the literature. As a result, the form of $f(\chi)$ slightly deviates from that in ref 59, and is given in eq. 6.4:

$$f(\chi) = \frac{v_2}{v_1}(\chi - \frac{v_2}{v_1}) + \frac{1}{a\chi^2 + b\chi + c} \tag{6.4}$$

The first term is the new asymptote, and the second term serves as an empirical offset when the solvent is poor enough to enable the formation of micelles, but not large enough to make $\chi >> 1$. The derivation of eq. 6.4 is summarized in Appendices A.7.

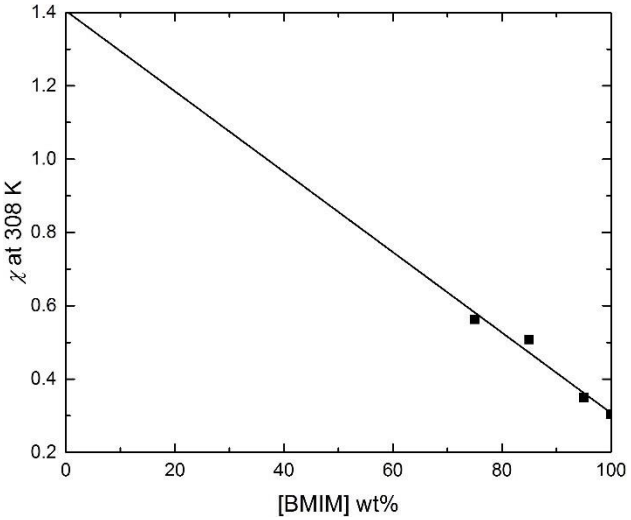

Figure 6.5. Linear extrapolation of $\chi_{PnBMA/IL}$ based on Ref 41.

The interaction parameter χ was determined independently by SANS measurements of PnBMA homopolymer/ionic liquid solutions, following the random phase approximation (RPA).[60] Hoarfrost, *et al*. measured χ between PnBMA and mixtures of [EMIM][TFSI] and [BMIM][TFSI], and obtained values for the entropic (*A*) and the enthalpic (*B*) parts for [BMIM] wt% = 75, 85, 95 and 100, based on the empirical equation $\chi = A + B/T$.[41] On the basis of these results, we can estimate the χ for our system by linear extrapolation of these χ values to [BMIM] wt% = 0, 10, 20 and 30 at 35 °C (308 K). Here we assume a linear relationship between $\chi_{PnBMA/IL}$ and [BMIM] wt%, because the two ILs used are homologous solvents, and should mix randomly at all length scales. As can be seen in Figure 6.5, the $\chi_{PnBMA/IL}$ values for [BMIM] wt% = 0, 10, 20 and 30 are

determined to be 1.40, 1.29, 1.18 and 1.07, respectively, using the molar volume of IL as the reference volume. As noted above, in order to make the χ and N consistent, we convert these χ values using the molar volume of *n*-BMA repeating unit as the reference volume. This is done by having the original χ values multiplied by a factor of (v_2/v_1), which gives new χ values of 0.73, 0.66, 0.60 and 0.53 for [BMIM] wt% = 0, 10, 20 and 30.

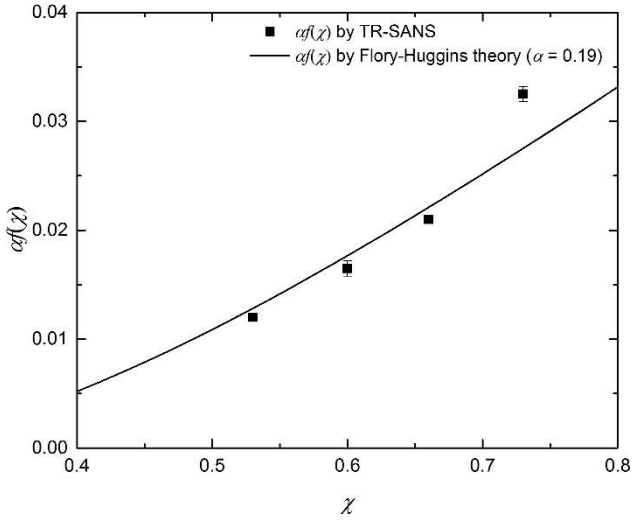

Figure 6.6. Dependence of $\alpha f(\chi)$ on χ.

Now, we can plot $\alpha f(\chi)$ obtained from fitting $R(t)$ to eq. 6.2 against χ, as shown in Figure 6.6. Assuming that the $f(\chi)$ adapts the form of eq. 6.4, and α does not change in these experiments, then we have a reasonable agreement between the experimental data and the theory (solid line), with $\alpha = 0.19$. The fact that the prefactor $\alpha < 1$ implies that the actual barrier for chain pull-out is smaller than predicted by Flory-Huggins theory, which can be partially interpreted by the effect of corona block. As the corona blocks are tethered on the micelle interface, they are expected to adapt a rather stretched conformation in order to minimize the monomer-monomer interaction. This causes the entropy to decrease. When one of the chains is released from the micelle and moves into

the solvent, its corona block can adopt a coil conformation, so that the entropic gain for the corona block partially offsets the enthalpic increase of the core block.

6.4. Micelle Chain Exchange Kinetics: Dependence on N_{corona}.

TR-SANS Results

In this section, the chain exchange rates of PMMA-*b*-(*d*)PnBMA (42-35), (57-35) and (84-35) micelles were measured in [EMIM][TFSI]; as the core block lengths of these micelles are nearly identical, their $R(t)$ data will shed light on the role of corona block length on the chain exchange kinetics. In Figure 6.7, representative 1-D SANS profiles of the post-mixed PMMA-*b*-PnBMA micelles are given at various times at 35 °C, which are then converted to $R(t)$ following eq. 6.1, as shown in Figure 6.8. When calculating $I(0)$, $I(\infty)$ and $I(t)$, we use the integrated intensity over the q range of 0.008 – 0.040 $Å^{-1}$ for all the three copolymer micelles, due to their similar first minimum positions.

Figure 6.9 shows the time-temperature superposed $R(t)$ of PMMA-*b*-PnBMA (25-35), (42-35), (57-35) and (84-35) micelles, which are subsequently fit to eq. 6.2 and 6.3. The statistical segment length (b) and the monomeric friction coefficient (ζ) used here are the same as in Section 6.3. The fitting result is summarized in Table 6.5. It is clear that both Figure 6.9 and the $\alpha\chi$ obtained from the fitting indicate that longer PMMA (corona) block makes the chain exchange kinetics slower, although its effect is not as remarkable as the change in N_{core}.

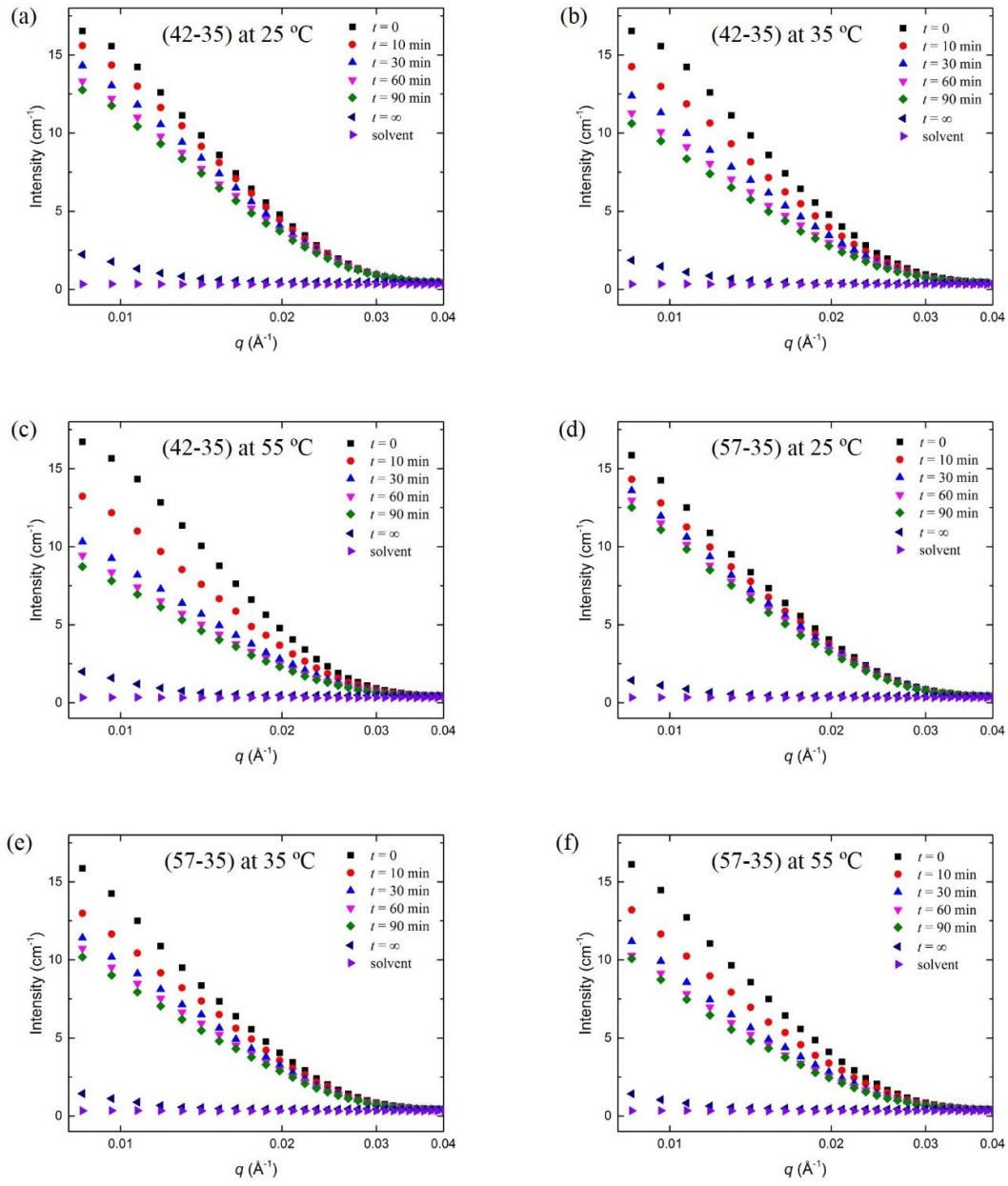
(a)
(42-35) at 25 °C
(b)
(42-35) at 35 °C
(c)
(42-35) at 55 °C
(d)
(57-35) at 25 °C
(e)
(57-35) at 35 °C
(f)
(57-35) at 55 °C
t = 0
t = 10 min
t = 30 min
t = 60 min
t = 90 min
t = ∞
solvent
Intensity (cm-1)
q (Å-1)
0
5
10
15
0.01
0.02
0.03
0.04

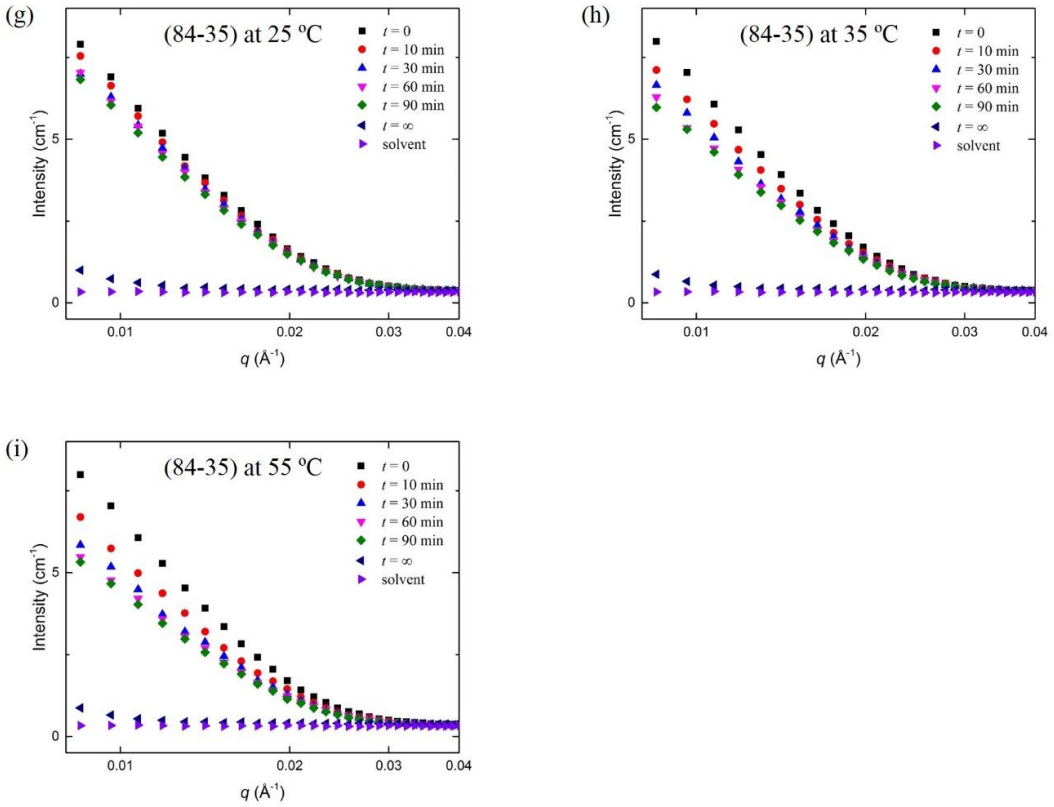

Figure 6.7. Representative TR-SANS profiles over 5-minute intervals for PMMA-*b*-PnBMA (42-35), 1 wt% in [EMIM][TFSI] at (a) 25 ºC, (b) 35 ºC, and (c) 55 ºC; PMMA-*b*-PnBMA (57-35), 1 wt% in [EMIM][TFSI] at (d) 25 ºC, (e) 35 ºC, and (f) 55 ºC; PMMA-*b*-PnBMA (84-35), 0.5 wt% in [EMIM][TFSI] at (g) 25 ºC, (h) 35 ºC, and (i) 55 ºC.

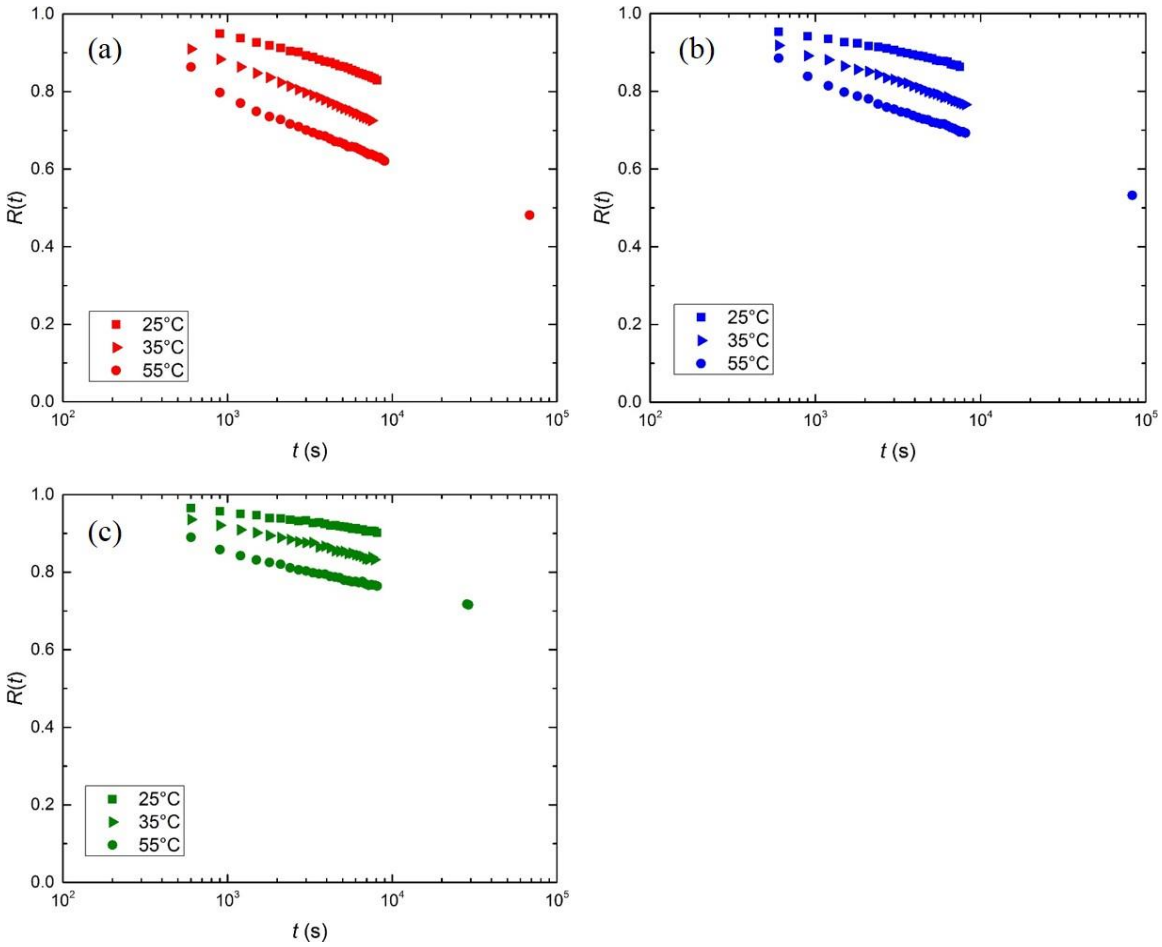

Figure 6.8. *R*(*t*) of the post-mixed solutions at various temperatures for (a) PMMA-*b*-PnBMA (42-35) in [EMIM][TFSI], (b) PMMA-*b*-PnBMA (57-35) in [EMIM][TFSI], and (c) PMMA-*b*-PnBMA (84-35) in [EMIM][TFSI].

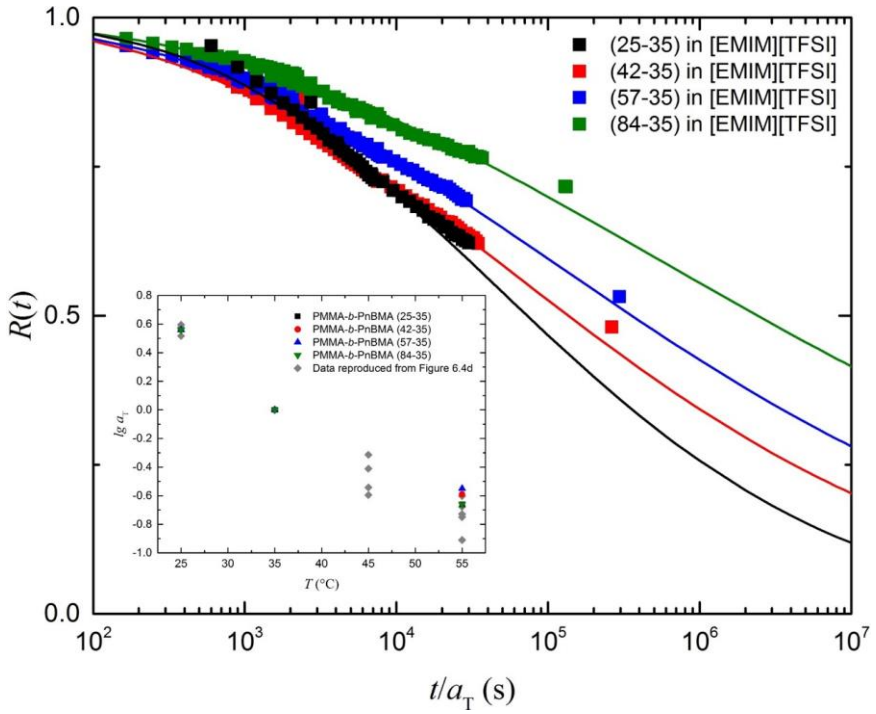

Figure 6.9. Time-temperature superposed $R(t)$ for PMMA-*b*-PnBMA (X-35) micelles. The solid lines are best fit to the model proposed by Choi *et al*. The shift factor a_T as a function of temperature is displayed in the inset.

Table 6.5. Fitting Results for Chain Exchange Kinetics of PMMA-*b*-PnBMA (X-35)

Copolymer	N_n input	N_w/N_n	$\alpha\chi$
PMMA-*b*-PnBMA (25-35)	246	1.14	0.032
PMMA-*b*-PnBMA (42-35)		1.19	0.036
PMMA-*b*-PnBMA (57-35)		1.21	0.040
PMMA-*b*-PnBMA (84-35)		1.22	0.049

Discussion

Remember in eq. 6.2, there is no term related to N_{corona}. In fact, the role of the corona block in the chain exchange process is still controversial. In the original Halperin-Alexander theory, it was proposed that longer corona blocks will slow down the chain exchange, as it takes more time for the core blocks to go through the corona domain

during the chain expulsion process.[57] However, Li and Dormidontova studied this issue by dissipative particle dynamics (DPD) simulations, and reached the opposite conclusion: chain exchange rate increases with the corona block length. Two reasons were provided by the authors: (*i*) longer corona block lengths result in higher critical micelle concentration (CMC),[61–65] which lowers the activation barrier of chain expulsion; and (*ii*) under the same N_{core}, both R_c and the grafting density of the corona chains decrease with N_{corona}, thereby making the chain expulsion easier.[39] The first reason may not seem too obvious, but if we think about the micelles as being in equilibrium with a pool of free chains, and assume that the number of micelles in the solution does not change, then we have:

$$r_{exp} = k_{exp} c_{mic} \tag{6.5}$$

and

$$r_{ins} = k_{ins} c_{mic} c_{free-chain} \tag{6.6}$$

where r and k are the rate and the rate constant; the subscripts "exp" and "ins" denote expulsion and insertion, respectively. Since the concentration of free chains and micelles does not change with time, therefore we have $r_{exp} = r_{ins}$. By combining eqs. 6.5 and 6.6, $k_{exp} = k_{ins} c_{free\text{-}chain} = k_{ins} \cdot \text{CMC}$. If we treat k_{ins} as a constant, then the rate constant of chain expulsion, k_{exp}, has a linear relationship with CMC.

Interestingly, both Halperin-Alexander theory and Li-Dormidontova simulations are supported by some experimental results. Lu *et al.* compared the chain exchange rates of PEP-*b*-PS (70-26) and (40-28) in squalane (the numbers in brackets are the molecular weight of each block in kg/mol), and observed that the chain exchange kinetics of (70-26) is 4 – 5 times faster than (40-28), even when the slight difference of N_{core} between the two copolymers is taken into consideration.[55] This finding favors Li and Dormidontova's simulations. Nevertheless, in a more recent study conducted on PEO-*b*-*n*-alkane micelles

in aqueous solution, Zinn *et al.* observed that the chain exchange kinetics slow down dramatically as PEO (corona) block molecular weight increases from 4 to 36 kg/mol, which favors Halperin and Alexander's theory.[56]

At this point, no explicit dependence of $R(t)$ on N_{corona} can be derived, but we know that at least two competing factors come into play, and the net effect of whether chain exchange kinetics becomes faster of slower may vary from case to case. In this study, the PMMA-*b*-PnBMA micelles in IL demonstrate the same tendency as has been predicted by Halperin and Alexander: longer corona blocks hinder the chain expulsion process. Here, I will mainly focus on the qualitative interpretation of the data, before more experimental results are obtained.

Scaling of Chain Expulsion Time on N_{corona}. As has been discussed in the previous section, the characteristic chain expulsion time, $\tau_{exp} = (N_{core}^2 b^2 \zeta / 6\pi^2 kT) \cdot \exp(\alpha\chi N_{core})$. Therefore, with identical N_{core} and all other conditions being equal, $\tau_{exp} \sim \exp(\alpha\chi N_{core})$. In Figure 6.10, the $\alpha\chi N_{core}$ values in Table 6.5 are plotted against N_{corona} with a linear-log relationship, and the linear regression of the data gives a slope of 3.4±0.7, *i.e.*, $\tau_{exp} \sim N_{corona}^{3.4\pm0.7}$. This τ_{exp} dependence on N_{corona} is somewhat stronger than that predicted by Halperin, which is $\tau_{exp} \sim N_{corona}^{9/5}$;[57] but it should be noted that in the fitting to eqs. 6.2 and 6.3, N_w/N_n is actually coupled with $\alpha\chi$, which brings more complexity to the interpretation of the result.

Abnormally High Dispersity. It is noteworthy that in Table 6.5, the N_w/N_n values obtained from the fitting are much larger than the dispersity given by SEC (Table 6.1). This is probably a result of overestimation, because $R(t)$ of these micelles measured by TR-SANS are all above 0.5, which can cause inaccuracy in the fitting. In order to understand the chain exchange kinetics of these micelle samples better, solvents with higher [BMIM][TFSI] compositions can be used, for example, [BMIM] wt% = 10 or 20, so that $R(t)$ can cover a broader range between 0 and 1.

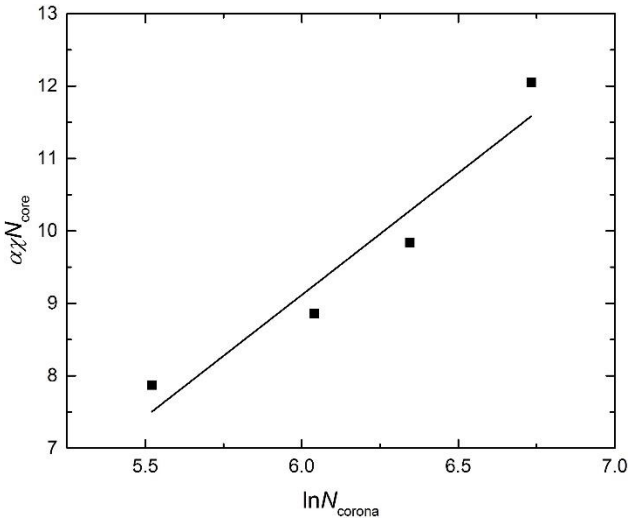

Figure 6.10. Dependence of the activation barrier, $\alpha\chi N_{core}$, on the natural logarithm of the corona block degree of polymerization, $\ln N_{corona}$. The solid line represents the linear fit to the data, which gives $\alpha\chi N_{core} = 3.4\ln N_{corona} - 11.1$.

6.5. Micelle Chain Exchange Kinetics: Dependence on concentration.

TR-SANS Results

The concentration dependence of micelle chain exchange kinetics was studied using PMMA-*b*-PnBMA (25-24) micelles in [EMIM][TFSI], with polymer concentration varying from 0.5 to 6 wt%. Representative 1-D SANS profiles of 0.5, 3 and 6 wt% post-mixed (25-24) micelles are displayed in Figure 6.11a – k, which are then converted to $R(t)$ following eq. 6.1 (Figure 6.12a – c). Notably, $I(0)$ of 3 wt% and 6 wt% post-mixed micelles cannot simply be calculated by averaging the scattering profiles of *h*- and *d*-micelles, because structure factor starts to emerge in these higher concentration micelle solutions. Instead, $I(0)$ of these samples are obtained by extrapolating $I(t)$ to $t = 0$, using linear extrapolation of the first two data points, *i.e.*, $I(t)$ at $t = 10$ and 15 min. A typical example of extrapolation is given in Figure 6.12d.

The time-temperature superposed $R(t)$ of 0.5, 3 and 6 wt% micelles are shown in Figure 6.13. Except for the 6 wt% data (olive squares), reasonably good superposition is

achieved for the other two concentrations, indicating that these experimental data share the same set of a_T's as in Sections 6.3 and 6.4. The poor alignment in 6 wt% data is probably owing to the inaccuracy in the determination of $I(0)$, which is an inherent disadvantage in LCST systems. Overall, all the three sets of superposed $R(t)$ data nearly fall on the same master curve as the 1 wt% data (solid line in Figure 6.13) within experimental error, which suggests that the micelle concentration has at most very slight effect on the chain exchange rate, when the concentration is below 6 wt%.

Discussion

Micelle chain exchange kinetics were once assumed to be independent of concentration. [39,57] However, Choi *et al.* studied the chain exchange of 15 wt% PEP-*b*-PS micelles in squalane in comparison with the 1 wt% micelles, and observed a significant decrease (about one order of magnitude) in exchange rate for the former.[32] The authors attributed this slowdown to a further chain expulsion barrier imposed by crowding of the corona chains. Later on, Halperin calculated this extra barrier using scaling theory, and proposed two critical volume fractions for the corona block, φ^* and φ^{**}: the former is the critical volume fraction at which corona starts to overlap, and the latter is the critical volume fraction at which screening effect is so large that the whole coronal star structure disappears. According to Halperin, when $\varphi^* < \varphi_{corona} < \varphi^{**}$, the slowdown in chain exchange kinetics originates from an extra free energy term in the activation barrier, which is closely related to the screening-induced R_c increase; when $\varphi_{corona} > \varphi^{**}$, chain exchange is further suppressed due to the significant increase in the difficulty of chain insertion. Moreover, Halperin predicted that the addition of corona block homopolymer will have the same effect as increasing micelle concentration.[54]

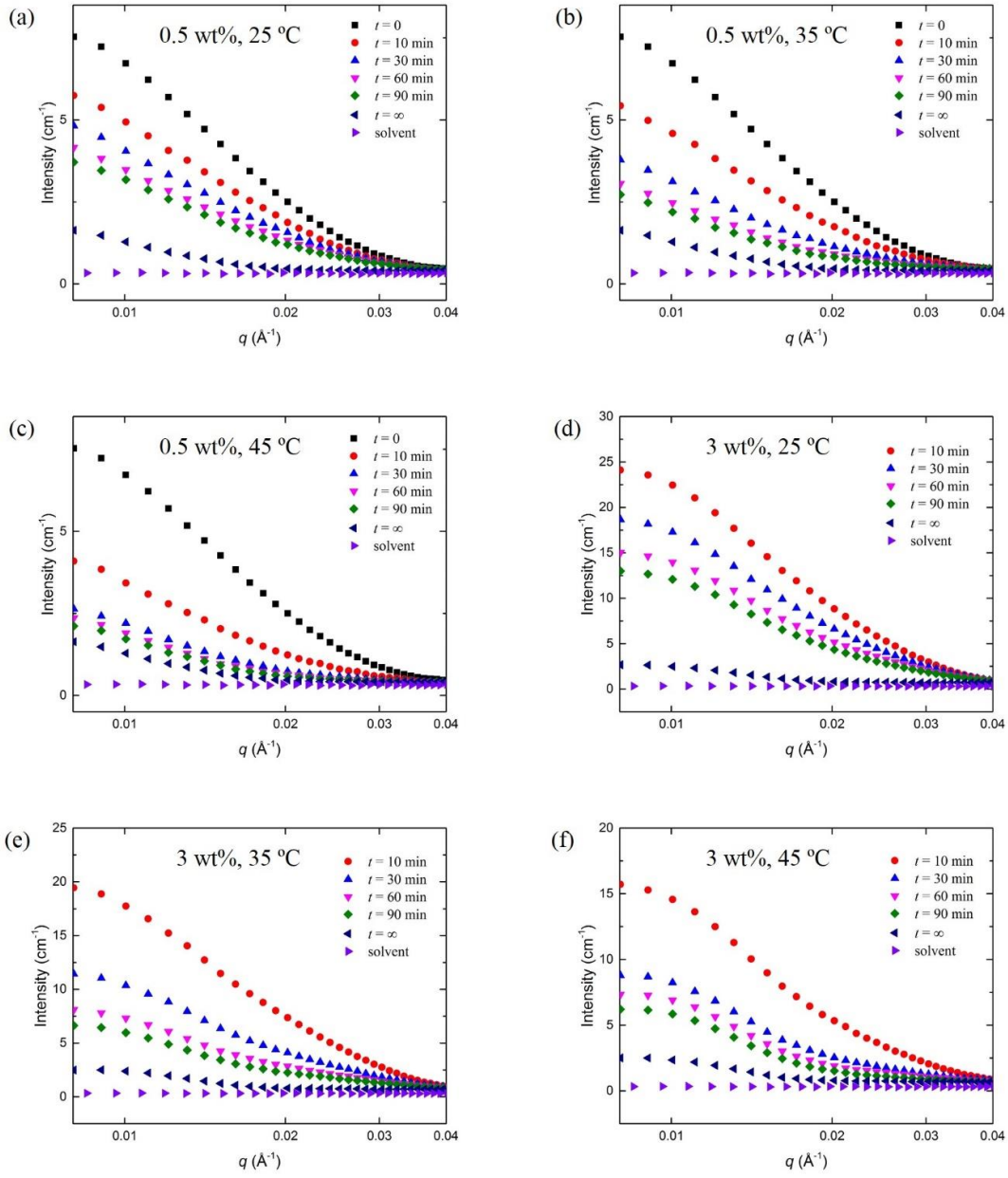
(a)
0.5 wt%, 25 ºC
(b)
0.5 wt%, 35 ºC
(c)
0.5 wt%, 45 ºC
(d)
3 wt%, 25 ºC
(e)
3 wt%, 35 ºC
(f)
3 wt%, 45 ºC
t = 0
t = 10 min
t = 30 min
t = 60 min
t = 90 min
t = ∞
solvent
Intensity (cm-1)
q (Å-1)

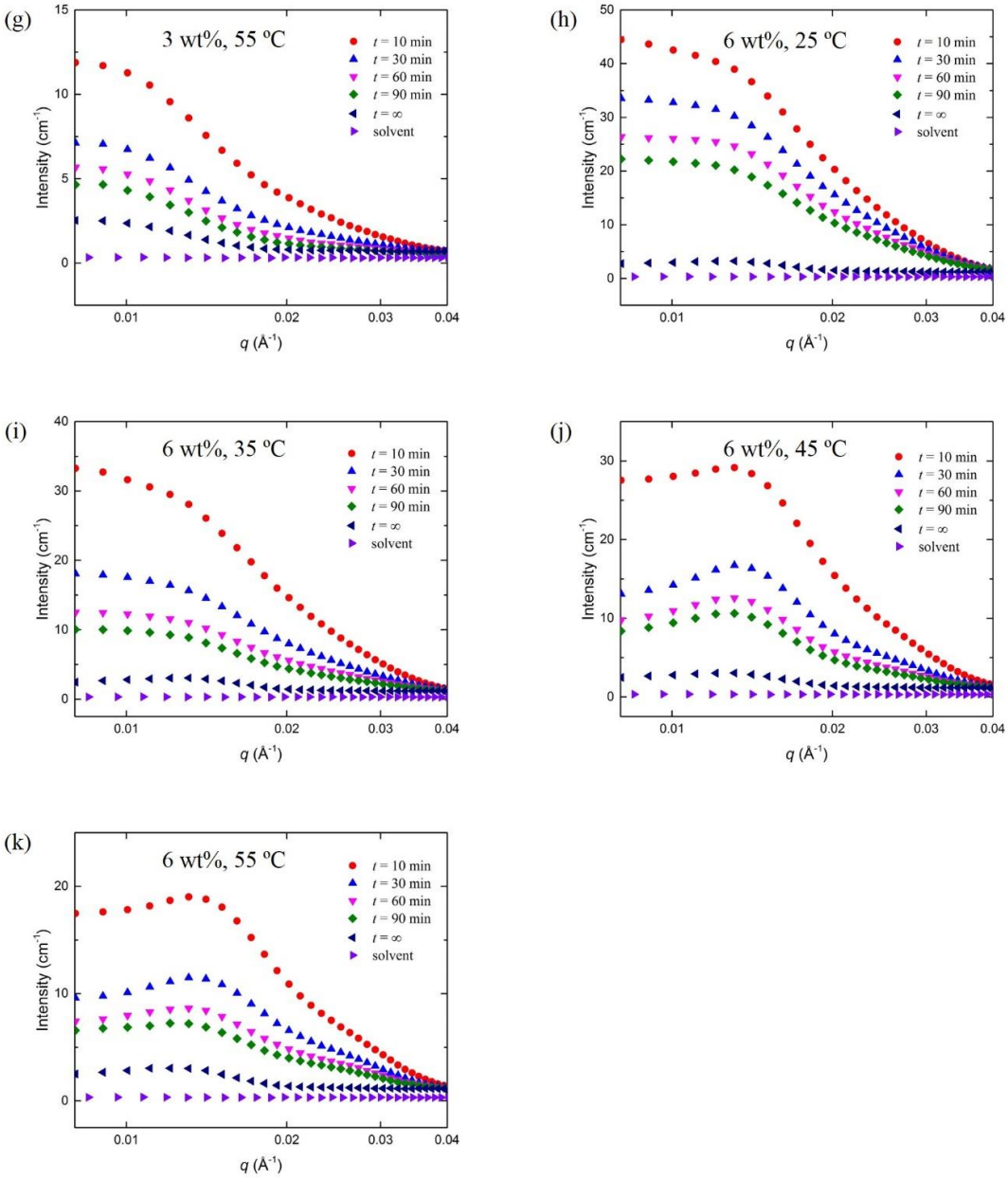

Figure 6.11. Representative TR-SANS profiles over 5-minute intervals for PMMA-*b*-PnBMA (25-24) in [EMIM][TFSI]: (a) 0.5 wt% at 25 ºC, (b) 0.5 wt% at 35 ºC, (c) 0.5 wt% at 45 ºC, (d) 3 wt% at 25 ºC, (e) 3 wt% at 35 ºC, (f) 3 wt% at 45 ºC, (g) 3 wt% at 55 ºC, (h) 6 wt% at 25 ºC, (i) 6 wt% at 35 ºC, (j) 6 wt% at 45 ºC, and (k) 6 wt% at 55 ºC.

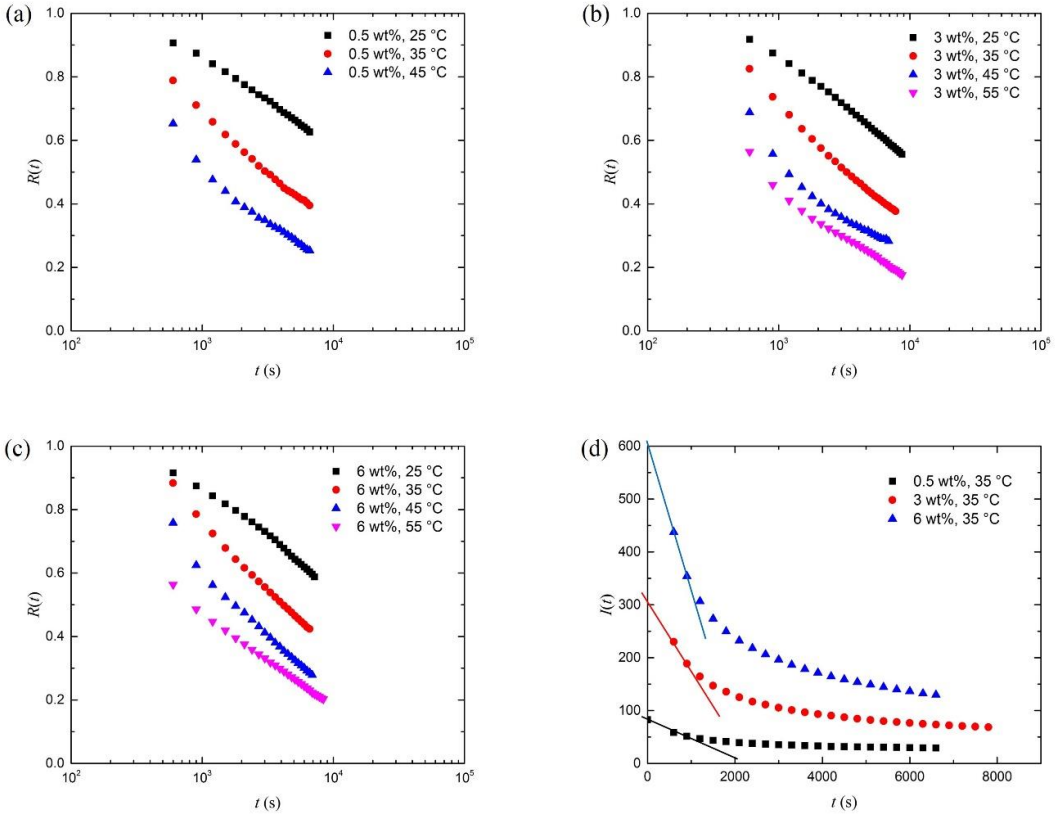

Figure 6.12. $R(t)$ of the post-mixed solutions at various temperatures for PMMA-*b*-PnBMA (25-24) in [EMIM][TFSI]: (a) 0.5 wt%, (b) 3 wt%, and (c) 6 wt%. (d) Schematic illustration of linear extrapolation to obtain $I(0)$ for 3 wt% and 6 wt% post-mixed micelles. $I(0)$ of 3 wt% and 6 wt% micelles at 35 ºC are marked by the intercepts of the red and blue lines, respectively.

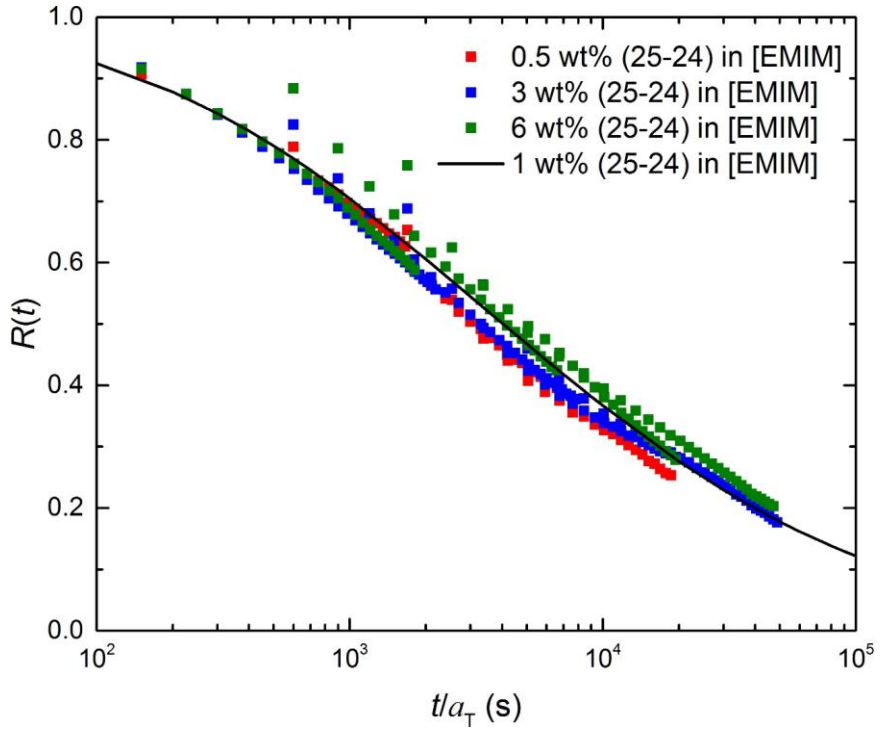

Figure 6.13. Time-temperature superposed $R(t)$ of 0.5, 3 and 6 wt% PMMA-*b*-PnBMA (25-24) micelles in [EMIM][TFSI]. The solid line represents the $R(t)$ of 1 wt% micelle, reproduced from Figure 6.4a. The shift factors a_T used here are 3.98, 0.355 and 0.178 at 25, 45 and 55 ºC, which are the averaged a_T's in Figure 6.4d at each temperature.

Halperin's slowdown mechanism was supported by a series of experiments conducted by Lu *et al.*, in which various vol% of PEP homopolymer was mixed with the PEP-*b*-PS/squalane solution, and significant reduction in chain exchange rate was observed for 7 vol% PEP homopolymer and beyond.[55,66] Nevertheless, Lu *et al.* provided a slightly different reason for the case of $\varphi^* < \varphi_{corona} < \varphi^{**}$: the change in R_c is not the main reason for the slowdown; instead, because of the screening effect of the added homopolymer, the entropic driving force is reduced for the corona blocks to enter the solvent, leading to slower kinetics.

Despite the origin of the slowdown in kinetics, both theoretical and experimental studies have agreed on that the significant reduction in chain exchange rate can be observed only when φ_{corona} exceeds a certain threshold. In the system composed of only

block copolymer chains and solvent molecules, the critical corona overlap concentration c^* (in wt%) can be estimated by

$$c^* = \frac{MN_{agg}}{\frac{4}{3}\pi R_h^3 N_{av} \rho_{solv}} \quad (6.7)$$

in which M, N_{av} and ρ_{solv} are the average molecular weight of the block copolymer, Avogadro's number and the density of the solvent. In this study, for PMMA-*b*-PnBMA (25-24) in [EMIM][TFSI], M = 49000 g/mol, ρ_{solv} = 1.52 g/cm^3; and based on the DLS and SAXS characterization result in Table 4.2 and 4.3, R_h = 22.1 nm and N_{agg} = 112 at 1 wt% polymer concentration. With these data, eq. 6.7 gives $c^* \approx 0.13$ g polymer/1 g solution, *i.e.*, the micelle chain exchange rate will not significantly decrease unless the polymer concentration approaches somewhere around 13 wt%. Therefore, it can be justified that 0.5, 1, 3 and 6 wt% PMMA-*b*-PnBMA (25-35) micelles all show similar $R(t)$. This is consistent with the observation of Lu *et al.* that the chain exchange kinetics of PEP-*b*-PS (40-28) micelles only experiences a slight slowdown, when the polymer concentration is increased from 1 vol% to 6 vol%.[55]

6.6. Summary

In this chapter, we studied the chain exchange kinetics of two series of PMMA-*b*-PnBMA copolymers, (25-X) and (X-35), in the mixtures of [EMIM][TFSI] and [BMIM][TFSI]. The effect of core block length, corona block length, the Flory-Huggins interaction parameter χ, and polymer concentration on the chain exchange rate was thoroughly investigated. Notably, the χ between the core block and the solvent is tuned by varying the [BMIM] wt% in the solvent mixture. The relaxation function $R(t)$ obtained by TR-SANS experiments demonstrate that the micelle chain exchange rate is

hypersensitive to core block length and the $\chi_{PnBMA/IL}$, somewhat sensitive to the corona block length, while almost independent of polymer concentration (below 6 wt%).

In particular, $R(t)$ of the PMMA-*b*-PnBMA (25-X) micelles are fit to the model previously established by Choi, *et al.*, and the results show that the $\alpha\chi$ values obtained from the fitting are consistent for different core block lengths with the same χ. This finding, together with the fact that the shift factor (a_T) for this system is less sensitive to the temperature, shows that both the Rouse relaxation and the enthalpy penalty for chain expulsion have significant effect on the chain exchange kinetics. Then, a more elaborate χ-function is proposed for the barrier, with $f(\chi) = (v_2/v_1)(\chi - v_2/v_1)+1/(a\chi^2+b\chi+c)$ replacing χ; this helps solve the discrepancy between the model and the Flory-Huggins theory, while still maintaining a quasi-linear relationship between $f(\chi)$ in the energy barrier term and χ. This dependence has not been tested before, and thus will require further measurements to assess more fully.

On the other hand, the role of corona block on chain exchange is still less clear. $R(t)$ fitting of the PMMA-*b*-PnBMA (X-35) micelles can only give apparent $\alpha\chi$ values in this case, which monotonically increase with corona block lengths, suggesting that the chains with longer corona blocks exchange more slowly. We speculate that at least two competing factors come into play, and the fact that it takes more time for core blocks to penetrate a thicker corona is the predominant mechanism for the slower dynamics

6.7. Acknowledgement

This work was supported by the National Science Foundation (NSF) through award DMR-1206459. The TR-SANS experiments were conducted on NG-7 30m SANS instrument in NIST Center for Neutron Research (NCNR), and CG-2 GP-SANS at High Flux Isotope Reactor (HFIR) in ORNL. We acknowledge the support of NIST, ORNL,

U.S. Department of Commerce and U.S. Department of Energy in providing the neutron research facilities used in this work. We thank Dr. Paul Butler and Dr. Yimin Mao at NIST, as well as Dr. Lilin He at ORNL for assistance with SANS measurements. We are also grateful to Professor David Morse, Dr. Andrew Peters and Dr. Jennifer Laaser for helpful discussions.

6.8. References

(1) Tuzar, Z.; Kratochvil, P. *Adv. Colloid Interface Sci.* **1976**, *6*, 201-232.

(2) Halperin, A.; Tirrell, M.; Lodge, T. P. *Adv. Polym. Sci.* **1992**, *27*, 31-71.

(3) Hamley, I. W. *The Physics of Block Copolymers*, Oxford University: New York, 1998.

(4) Riess, G. *Prog. Polym. Sci.* **2003**, *28*, 1107-1170.

(5) Gohy, J. -F. *Adv. Polym. Sci.* **2005**, *190*, 65-136.

(6) Zhulina, E. B.; Adam, M.; LaRue, I.; Sheiko, S. S.; Rubinstein, M. *Macromolecules* **2005**, *38*, 5330-5351.

(7) Honda, C.; Hasegawa, Y.; Hirunuma, R.; Nose, T. *Macromolecules* **1994**, *27*, 7660-7668.

(8) Honda, C.; Abe, Y.; Nose, T. *Macromolecules* **1996**, *29*, 6778-6785.

(9) Michels, B.; Waton, G.; Zana, R. *Langmuir* **1997**, *13*, 3111-3118.

(10) Goldmints, I.; Holzwarth, J. F.; Smith, K. A.; Hatton, T. A. *Langmuir* **1997**, *13*, 6130-6134.

(11) Kositza, M. J.; Rees, G. D.; Holzwarth, A.; Holzwarth, J. F. *Langmuir* **2000**, *16*, 9035-9041.

(12) Procházka, K.; Bednar, B.; Mukhtar, E.; Svoboda, P.; Trnena, J.; Almgren, M. *J. Phys. Chem.* **1991**, *95*, 4563-4568.

(13) Wang, Y.; Balaji, R.; Quirk, R. P.; Mattice, W. L. *Polym. Bull.* **1992**, *28*, 333-338.

(14) Wang, Y.; Kausch, C. M.; Chun, M.; Quirk, R. P.; Mattice, W. L. *Macromolecules* **1995**, *28*, 904-911.

(15) Liu, G. *Can. J. Chem.* **1995**, *73*, 1995-2003.

(16) Smith, C. K.; Liu, G. *Macromolecules* **1996**, *29*, 2060-2067.

(17) Underhill, R. S.; Ding, J.; Birss, V. I.; Liu, G. *Macromolecules* **1997**, *30*, 8298-8303.

(18) Stam, J.; Creutz, S.; Schryver, F. C. D.; Jérôme, R. *Macromolecules* **2000**, *33*, 6388-6395.

(19) Zhang, L.; Shen, H.; Eisenberg, A. *Macromolecules* **1997**, *30*, 1001-1011.

(20) Esselink, F. J.; Dormidontova, E. E.; Hadziioannou, G. *Macromolecules* **1998**, *31*, 2925-2932.

(21) Esselink, F. J.; Dormidontova, E. E.; Hadziioannou, G. *Macromolecules* **1998**, *31*, 4873-4878.

(22) Willner, L.; Poppe, A.; Allgaier, J.; Monkenbusch, M.; Richter, D. *Europhys. Lett.* **2001**, *55*, 667-673.

(23) Lund, R.; Willner, L.; Stellbrink, J.; Radulescu, A.; Richter, D. *Physica B* **2004**, *350*, 909-912.

(24) Lund, R.; Willner, L.; Stellbrink, J.; Lindner, P.; Richter, D. *Phys. Rev. Lett.* **2006**, *96*, 068302.

(25) Lund, R.; Willner, L.; Richter, D.; Dormidontova, E. E. *Macromolecules* **2006**, *39*, 4566-4575.

(26) Lund, R.; Willner, L.; Stellbrink, J.; Richter, D. *Physica B* **2006**, *385-386*, 735-737.

(27) Lund, R.; Willner, L.; Richter, D.; Iatrou, H.; Hadjichristidis, N.; Lindner, P. *J. Appl. Cryst.* **2007**, *40*, 327-331.

(28) Lund, R.; Willner, L.; Pipich, V.; Grillo, I.; Lindner, P.; Colmenero, J.; Richter, D. *Macromolecules* **2011**, *44*, 6145-6154.

(29) Choi, S.; Lodge, T. P.; Bates, F. S. *Phys. Rev. Lett.* **2010**, *104*, 047802.

(30) Lu, J.; Lodge, T. P.; Bates, F. S. *ACS Macro Lett.* **2013**, *2*, 451-455.

(31) Lu, J.; Choi, S.; Lodge, T. P.; Bates, F. S. *ACS Macro Lett.* **2012**, *1*, 982-985.

(32) Choi, S.; Lodge, T. P.; Bates, F. S. *Macromolecules* **2011**, *44*, 3594-3604.

(33) Lu, J.; Bates, F. S.; Lodge, T. P. *Macromolecules* **2015**, *48*, 2667-2676.

(34) Barrat, J. L.; Fredrickson, G. H. *Macromolecules* **1991**, *24*, 6378-6383.

(35) Dalvi, M. C.; Lodge, T. P. *Macromolecules* **1993**, *26*, 859-861.

(36) Yokoyama, H.; Kramer, E. J. *Macromolecules* **1998**, *31*, 7871-7876.

(37) Cavicchi, K. A.; Lodge, T. P. *Macromolecules* **2003**, *36*, 7158-7164.

(38) Li, Z.; Dormidontova, E. E. *Macromolecules* **2010**, *43*, 3521-3531.

(39) Li, Z.; Dormidontova, E. E. *Soft Matter* **2011**, *7*, 4179-4188.

(40) Lee, H.-N.; Lodge, T. P. *J. Phys. Chem. B* **2011**, *115*, 1971-1977.

(41) Hoarfrost, M. L.; He, Y; Lodge, T. P. *Macromolecules* **2013**, *46*, 9464-9472.

(42) Hoarfrost, M. L.; Lodge, T. P. *Macromolecules* **2014**, *47*, 1455-1461.

(43) Meli, L.; Lodge, T. P. *Macromolecules* **2009**, *42*, 580-583.

(44) Wiley, R. H.; Brauer, G. M. *J. Polym. Sci.* **1948**, *3*, 455.

(45) Won, Y. Y.; Davis, H. T.; Bates, F. S. *Macromolecules* **2003**, *36*, 953-955.

(46) Meli, L.; Santiago, J. M.; Lodge, T. P. *Macromolecules* **2010**, *43*, 2018-2027.

(47) Numasawa, N.; Hamada, T.; Nose, T. *J. Polym. Sci., Polym. Lett. Ed.* **1985**, *23*, 1-4.

(48) Kline, S. R. *J. Appl. Crystallogr.* **2006**, *39*, 895-900.

(49) Zimm, B. H. *J. Chem. Phys.* **1948**, *16*, 1093-1099.

(50) Helfand, E.; Sapse, A. M. *J. Chem. Phys.* **1975**, *62*, 1327-1331.

(51) Ferry, J. D. *Viscoelastic Properties of Polymers (3rd Ed)*, Wiley: New York, 1980; pp 328-343.

(52) Ferry, J. D.; Landel, R. F. *Kolloid-Zeitschrift* **1956**, 148, 1-6.

(53) Flory, P. J. *J. Chem. Phys.* **1942**, *10*, 51-61.

(54) Halperin, A. *Macromolecules* **2011**, *44*, 5072-5074.

(55) Lu, J. Mechanisms of Chain Exchange in Block Copolymer Micelles. PhD Dissertation, University of Minnesota, 2015.

(56) Zinn, T.; Willner, L.; Pipich, V.; Richter, D.; Lund, R. *ACS Macro Lett.* **2016**, *5*, 884-888.

(57) Halperin, A.; Alexander, S. *Macromolecules* **1989**, *22*, 2403-2412.

(58) Zinn, T.; Willner, L.; Pipich, V.; Richter, D.; Lund, R. *ACS Macro Lett.* **2015**, *4*, 651-655.

(59) Thiagarajan, R. Modeling of Diblock Copolymers in Selective Solvents. PhD Dissertation, University of Minnesota, 2012.

(60) de Gennes, P. G. *J. Chem. Phys.* **1980**, *72*, 4756-4763.

(61) Nagarajan, R.; Ganesh, K. *J. Chem. Phys.* **1989**, *90*, 5843-5856.

(62) Whitmore, M. D.; Noolandi, J. *Macromolecules* **1985**, *18*, 657-665.

(63) Stauffer, D.; Woermann, D. *J. Phys. II* **1995**, *5*, 1-3.

(64) Anghel, D. F.; Winnik, F. M.; Galatanu, N. *Colloids Surf. A* **1999**, *149*, 339-345.

(65) Kenward, M.; Whitmore, M. D. *J. Chem. Phys.* **2002**, *116*, 3455-3470.

(66) Lu, J.; Bates, F. S.; Lodge, T. P. *Macromolecules* **2016**, *49*, 1405-1413.

Chapter 7

Summary and Outlook

7.1. Thesis Summary

In this thesis, the structure and equilibration kinetics of PMMA-*b*-PnBMA micelles in IL mixtures of [EMIM][TFSI] and [BMIM][TFSI] were systematically studied. This system is of particular interest because the solvent selectivity to the core block, PnBMA, can be tuned on a broad range by mixing the two ILs in different ratios, which can potentially give access to a variety of states of micelles from near equilibrium to far away from equilibrium.

The structures of micelles were mainly characterized by dynamic light scattering (DLS) and small-angle X-ray scattering (SAXS). The dependences of micelle core radius (R_c) and hydrodynamic radius (R_h) were investigated as a function of both temperature (T) and [BMIM] wt% in the solvent mixture. Specifically, in a given solvent composition, when T rises above the critical micelle temperature (CMT), R_h initially increases abruptly due to micelle formation, then gradually decreases to a stable value, $R_{h,stable}$, within 30 – 40 °C. When T is further increased above (CMT+40) °C, both R_h and R_c are insensitive to T. By comparing the R_h distributions of the same copolymer in various solvent compositions, we observed a peculiar transition point at [BMIM] wt% ≈ 70, above which multimodal distribution of R_h occurs, signaled by a concurrent increase in $R_{h,stable}$.

Another part of the micelle structure study is the scaling relationship between R_c and the degree of polymerization of the core block, N_B. In general, they follow the relationship of $R_c \sim N_B^a$; the exponent, a, varies with solvent compositions, which possibly reflects the prohibitive effect of the thermal distance ($|T - CMT|$) on micelle equilibration, especially for micelles with long core blocks.

In order to quantify the equilibration kinetics of block copolymer micelles, time-resolved small-angle neutron scattering (TR-SANS) was used to investigate their chain exchange rate, which is defined by the relaxation function, $R(t)$. Following a model proposed by Choi *et al.*,[1,2] $R(t)$ were extracted from the TR-SANS data of a variety of copolymer-solvent combinations, and its dependence was elaborated in terms of the core block length (N_{core}) and the Flory-Huggins interaction parameter (χ). As predicted, $R(t)$ is hypersensitive to both N_{core} and χ, and a more sophisticated function of χ for the activation barrier term was proposed, which is rationalized by a calculation in the spirit of Flory-Huggins theory. In general, the experiments directly shed light on the role of χ on the chain exchange rate between micelles, which is the first systematic study of this issue.

7.2. Outlook

For this PMMA-*b*-PnBMA/ILs system, there are some future directions for both the structure and the chain exchange kinetics study. In Chapter 5, we have demonstrated by DLS that this system has some interesting features when [BMIM] wt% exceeds 70, therefore, it would be desirable to use some imaging techniques, such as cryo-TEM, to provide direct evidence on the existence of other micelle morphologies. Since SAXS has proved that there is decent electron density contrast between the micelle core and the solvent, therefore, the feasibility of using TEM to visualize these micelles is almost warranted.

In terms of the chain exchange kinetics, previous studies tend to neglect the effect of corona block length (N_{corona}). In Section 6.4, we presented some preliminary results on the kinetics of PMMA-*b*-PnBMA (X-35) micelles, which suggested that their chain exchange rate decreases with the increase of N_{corona}. This finding, together with the recent results of Lu et al.[3,4] and Zinn et al.,[5] implied that there may not be a universal

relationship between $R(t)$ and N_{corona}. Nevertheless, more TR-SANS experiments are required on the PMMA-*b*-PnBMA (X-35) micelles in solutions with higher [BMIM] wt%, before any final conclusions can be drawn.

Another topic of interest is whether the morphology of micelles affects the chain exchange rate. So far, there is only one research in this field conducted by Lund *et al.*, which suggested that cylindrical micelles have almost the same $R(t)$ as spherical micelles, when all other conditions are kept identical.[6] This topic is worthy of revisiting using our system of PMMA-*b*-PnBMA/ILs, if cylindrical micelles do exist in the solvent mixtures with [BMIM] wt% > 70. From a broader perspective, $R(t)$ can be studied for micelles which are deliberately prepared out of equilibrium (by direct dissolution of polymer in ILs, for example),[7,8] and the result can be compared with that of micelles prepared by cosolvent method.

7.3. References

(1) Choi, S.; Lodge, T. P.; Bates, F. S. *Phys. Rev. Lett.* **2010**, *104*, 047802.

(2) Choi, S. Block Copolymer Self-Assembly in Solution: Structure and Dynamics. PhD Dissertation, University of Minnesota, 2010.

(3) Lu, J. Mechanisms of Chain Exchange in Block Copolymer Micelles. PhD Dissertation, University of Minnesota, 2015.

(4) Wang, E.; Bates, F. S.; Lodge, T. P. Unpublished results.

(5) Zinn, T.; Willner, L.; Pipich, V.; Richter, D.; Lund, R. *ACS Macro Lett.* **2016**, *5*, 884-888.

(6) Lund, R.; Willner, L.; Pipich, V.; Grillo, I.; Lindner, P.; Colmenero, J.; Richter, D. *Macromolecules* **2011**, *44*, 6145-6154.

(7) Meli, L.; Lodge, T. P. *Macromolecules* **2009**, *42*, 580-583.

(8) Meli, L.; Santiago, J. M.; Lodge, T. P. *Macromolecules* **2010**, *43*, 2018-2027.

Bibliography

(1) Hashizume, J.; Teramoto, A.; Fujita, H. *J. Polym. Sci. Part B* **1981**, *19*, 1405-1422.

(2) Nakajima, A.; Hamada, F.; Hayashi, S. *J. Polym. Sci. Part C* **1966**, *15*, 285-294.

(3) Fox, T. G. *Polymer* **1962**, *3*, 111-128.

(4) Seuring, J.; Agarwal, S. *Macromolecules* **2012**, *45*, 3910−3918.

(5) Shimada, N.; Ino, H.; Maie, K.; Nakayama, M.; Kano, A.; Maruyama, A. *Biomacromolecules* **2011**, *12*, 3418−3422.

(6) Lee, H.-N.; Rosen, B. M.; Fenyvesi, G.; Sunkara, H. B. *J. Polym. Sci. Part A* **2012**, *50*, 4311-4315.

(7) Heskins, M.; Guillet, J. E. *J. Macromol. Sci. Part A* **1968**, *2*, 1441-1455.

(8) Ward, M. A.; Georgiou, T. K. *J. Polym. Sci. Part A* **2010**, *48*, 775–783.

(9) Maeda, Y.; Nakamura, T.; Ikeda, I. *Macromolecules* **2002**, *35*, 217-222.

(10) Schild, H. G.; Tirrell, D. A. *J. Phys. Chem.* **1990**, *94*, 4352-4356.

(11) Seno, K.; Kanaoka, S.; Aoshima, S. *J. Polym. Sci. Part A* **2008**, *46*, 5724-5733.

(12) Luan, C.-H.; Harris, R. D.; Prasad, K. U.; Urry, D. W. *Biopolymers* **1990**, *29*, 1699-1706.

(13) Luan, C.-H.; Urry, D. W. *J. Phys. Chem.* **1991**, *95*, 7896-7900.

(14) Luan, C.-H.; Parker, T. M.; Prasad, K. U.; Urry, D. W. *Biopolymers* **1991**, *31*, 465-475.

(15) Tanford, C. *The Hydrophobic Effect: Formation of Micelles and Biological Membranes, 2nd ed.*, John Wiley & Sons: New York, 1980.

(16) Otake, K.; Inomata, H.; Konno, M.; Saito, S. *Macromolecules* **1990**, *23*, 283-289.

(17) Inomata, H.; Goto, S.; Saito, S. *Macromolecules* **1990**, *23*, 4887-4888.

(18) Welton, T. *Chem. Rev.* **1999**, *99*, 2071-2083.

(19) Holbrey, J. D.; Seddon, K. R. *Clean Prod. Process* **1999**, *1*, 223-236.

(20) Wasserscheid, P.; Keim, W. *Angew. Chem. Int. Ed.* **2000**, *39*, 3772-3789.

(21) Susan, M. A. B. H.; Kaneko, T.; Noda, A.; Watanabe, M. *J. Am. Chem. Soc.* **2005**, *127*, 4976-4983.

(22) He, Y.; Boswell, P. G.; Bühlmann, P.; Lodge, T. P. *J. Phys. Chem. B* **2007**, *111*, 4645-4652.

(23) Lee, J.; Panzer, M. J.; He, Y.; Lodge, T. P.; Frisbie, C. D. *J. Am. Chem. Soc.* **2007**, *129*, 4532-4533.

(24) Mehnert, C. P. *Chem. Eur. J.* **2005**, *11*, 50-56.

(25) Riisager, A.; Fehrmann, R.; Haumann, M.; Wasserscheid, P. *Eur. J. Chem.* **2006**, *12*, 695-706.

(26) Phillips, D. M.; Drummy, L. F.; Conrady, D. G.; Fox, D. M.; Naik, R. R.; Stone, M. O.; Trulove, P. C.; De Long, H. C.; Mantz, R. A. *J. Am. Chem. Soc.* **2004**, *126*, 14350-14351.

(27) Xie, H. B.; Li, S. H.; Zhang, S. B. *Green Chem.* **2005**, *7*, 606-608.

(28) Forsyth, S. A.; MacFarlane, D. R.; Thomson, R. J.; Itzstein, M. *Chem. Commun.* **2002**, 714-715.

(29) Fukushima, T.; Kosaka, A.; Ishimura, Y.; Yamamoto, T.; Takigawa, T.; Ishii, N.; Aida, T. *Science* **2003**, *300*, 2072-2074.

(30) Costa, L. T.; Ribeiro, M. C. C. *J. Chem. Phys.* **2006**, *124*, 184902.

(31) Lee, H.-N.; Lodge, T. P. *J. Phys. Chem. Lett.* **2010**, *1*, 1962-1966.

(32) Winterton, N. *J. Mater. Chem.* **2006**, *16*, 4281-4293.

(33) Ueki, T.; Watanabe, M. *Macromolecules* **2008**, *41*, 3739-3749.

(34) Ueki, T.; Watanabe, M. *Bull. Chem. Soc. Jpn.* **2012**, *85*, 33-50.

(35) Batista, M. L. S.; Neves, C. M. S. S.; Carvalho, P. J.; Gani, R.; Coutinho, J. A. P. *J. Phys. Chem. B* **2011**, *115*, 12879-12888.

(36) Weerachanchai, P.; Wong, Y.; Lim, K. H.; Tan, T. T. Y.; Lee, J.-M. *Chem. Phys. Chem.* **2014**, *15*, 3580-3591.

(37) Swiderski, K.; McLean, A.; Gordon, C. M.; Vaughan, D. H. *Chem. Commun.* **2004**, 2178-2179.

(38) Brandrup, J.; Immergut, E. H.; Grulke, E. A. *Polymer Handbook*, 4th ed., Wiley-Interscience: New Jersey, 1999.

(39) Ueno, K.; Fukai, T.; Nagatsuka, T.; Yasuda, T.; Watanabe, M. *Langmuir* **2014**, *30*, 3228-3235.

(40) Miranda, D. F. *Interactions and Morphology of Triblock Copolymer - Ionic Liquid Mixtures and Applications for Gel Polymer Electrolytes*. PhD Dissertation, University of Minnesota, 2012.

(41) Ueno, K.; Inaba, A.; Kondoh, M.; Watanabe, M. *Langmuir* **2008**, *24*, 5253-5259.

(42) Lee, H.-N.; Lodge, T. P. *J. Phys. Chem. B* **2011**, *115*, 1971-1977.

(43) Ueki, T.; Watanabe, M. *Langmuir* **2007**, *23*, 988-990.

(44) Hoarfrost, M. L.; He, Y.; Lodge, T. P. *Macromolecules* **2013**, *46*, 9464-9472.

(45) Leibler, L. *Macromolecules* **1980**, *13*, 1602-1617.

(46) Bates, F. S. *Science* **1991**, *251*, 898-905.

(47) Bates, F. S.; Fredrickson, G. H. *Physics Today* **1999**, *52*, 32-38.

(48) Kataoka, K.; Harada, A.; Nagasaki, Y. *Adv. Drug Delivery Rev.* **2001**, *47*, 113-131.

(49) Schouten, M.; Dorrepaal, J.; Stassen, W. J. M.; Vlak, W. A. H. M.; Mortensen, K. *Polymer* **1989**, *30*, 2038–2046.

(50) Won, Y. Y.; Brannan, A. K.; Davis, H. T.; Bates, F. S. *J. Phys. Chem. B* **2002**, *106*, 3354-3364.

(51) Zheng, Y.; Won, Y. Y.; Bates, F. S.; Davis, H. T.; Scriven, L. E.; Talmon, Y. *J. Phys. Chem. B* **1999**, *103*, 10331-10334.

(52) Won, Y. Y.; Davis, H. T.; Bates, F. S. *Science* **1999**, *283*, 960-963.

(53) Zhang, L.; Eisenberg, A. *Science* **1995**, *268*, 1728-1731.

(54) Zhang, L.; Eisenberg A. *J. Am. Chem. Soc.* **1996**, *118*, 3168-3181.

(55) Zhang, L.; Shen, H.; Eisenberg, A. *Macromolecules* **1997**, *30*, 1001-1011.

(56) Shen, H.; Zhang, L.; Eisenberg, A. *J. Phys. Chem. B* **1997**, *101*, 4697-4708.

(57) LaRue, I.; Adam, M.; Zhulina, E. B.; Rubinstein, M.; Pitsikalis, M.; Hadjichristidis, N.; Ivanov, D. A.; Gearba, R. I.; Anokhin, D. V.; Sheiko, S. S. *Macromolecules* **2008**, *41*, 6555−6563.

(58) Israelachvili, J. N.; Mitchell, D. J.; Ninham, B. W. *J. Chem. Soc. Faraday Trans.* **1976**, *72*, 1525-1568.

(59) Zhulina, E. B.; Adam, M.; LaRue, I.; Sheiko, S. S.; Rubinstein, M. Macromolecules 2005, 38, 5330-5351.

(60) Holder, S. J.; Sommerdijk, N. A. J. M. *Polym. Chem.* **2011**, *2*, 1018-1028.

(61) Yu. Y.; Zhang, L.; Eisenberg, A. *Macromolecules* **1998**, *31*, 1144-1154.

(62) Zhu, J. T.; Yu, H. Z.; Jiang, W. *Polymer* **2005**, *46*, 11962-11968.

(63) Abbas, S.; Li, Z.; Hassan, H.; Lodge, T. P. *Macromolecules* **2007**, *40*, 4048-4052.

(64) Edmonds, W. F.; Li, Z.; Hillmyer, M. A.; Lodge, T. P. *Macromolecules* **2006**, *39*, 47, 4526-4530.

(65) LaRue, I.; Adam, M.; Pitsikalis, M.; Hadjichristidis, N.; Rubinstein, M.; Sheiko, S. S. *Macromolecules* **2006**, *39*, 309-314.

(66) Shen, H.; Eisenberg, A. *Macromolecules* **2000**, *33*, 2561-2572.

(67) Talingting, M. R.; Munk, P.; Webber, S. E. *Macromolecules* **1999**, *32*, 1593-1601.

(68) Jiang, X.; Wang, Y.; Zhang, W.; Zheng, P.; Shi, L. *Macromol. Rapid Commun.* **2006**, *27*, 1833-1837.

(69) Kahlweit, M. *J Colloid Interface Sci.* **1982**, *90*, 92-99.

(70) Aniansson, E. A. G.; Wall, S. N. *J. Phys. Chem.* **1974**, *78*, 1024-1030.

(71) Aniansson, E. A. G.; Wall, S. N. *J. Phys. Chem.* **1975**, *79*, 857-858.

(72) Aniansson, E. A. G.; Wall, S. N.; Almgren, M.; Hoffmann, H.; Kielmann, I.; Ulbricht, W.; Zana, R.; Lang, J.; Tondre, C. *J. Phys. Chem.* **1976**, *80*, 905-922.

(73) Halperin, A.; Alexander, S. *Macromolecules* **1989**, *22*, 2403-2412.

(74) Dormidontova, E. E. *Macromolecules* **1999**, *32*, 7630-7644.

(75) Li, Z.; Dormidontova, E. E. *Macromolecules* **2010**, *43*, 3521-3531.

(76) Li, Z.; Dormidontova, E. E. *Soft Matter* **2011**, *7*, 4179-4188.

(77) Bednáŕ, B.; Edwards, K.; Almgren, M.; Tormod, S.; Tuzar, Z. *Makromol. Chem. Rapid Commun.* **1988**, *9*, 785-790.

(78) Pacovská, M.; Procházka, K.; Tuzar, Z.; Munk, P. *Polymer* **1993**, *34*, 4585-4588.

(79) Tian, M.; Qin, A.; Ramireddy, C.; Webber, S. E.; Munk, P.; Tuzar, Z.; Procházka, K. *Langmuir* **1993**, *9*, 1741-1748.

(80) Honda, C.; Hasegawa, Y.; Hirunuma, R.; Nose, T. *Macromolecules* **1994**, *27*, 7660-7668.

(81) Honda, C.; Abe, Y.; Nose, T. *Macromolecules* **1996**, *29*, 6778-6785.

(82) Michels, B.; Waton, G.; Zana, R. *Langmuir* **1997**, *13*, 3111-3118.

(83) Goldmints, I.; Holzwarth, J. F.; Smith, K. A.; Hatton, T. A. *Langmuir* **1997**, *13*, 6130-6134.

(84) Kositza, M. J.; Rees, G. D.; Holzwarth, A.; Holzwarth, J. F. *Langmuir* **2000**, *16*, 9035-9041.

(85) Procházka, K.; Bednáŕ, B.; Mukhtar, E.; Svoboda, P.; Trnena, J.; Almgren, M. *J. Phys. Chem.* **1991**, *95*, 4563-4568.

(86) Wang, Y.; Balaji, R.; Quirk, R. P.; Mattice, W. L. *Polym. Bull.* **1992**, *28*, 333-338.

(87) Wang, Y.; Kausch, C. M.; Chun, M.; Quirk, R. P.; Mattice, W. L. *Macromolecules* **1995**, *28*, 904-911.

(88) Liu, G. *Can. J. Chem.* **1995**, *73*, 1995-2003.

(89) Smith, C. K.; Liu, G. *Macromolecules* **1996**, *29*, 2060-2067.

(90) Underhill, R. S.; Ding, J.; Birss, V. I.; Liu, G. *Macromolecules* **1997**, *30*, 8298-8303.

(91) van Stam, J.; Creutz, S.; Schryver, F. C. D.; Jérôme, R. *Macromolecules* **2000**, *33*, 6388-6395.

(92) Esselink, F. J.; Dormidontova, E.; Hadziioannou, G. *Macromolecules* **1998**, *31*, 2925-2932.

(93) Esselink, F. J.; Dormidontova, E.; Hadziioannou, G. *Macromolecules* **1998**, *31*, 4873-4878.

(94) Lund, R.; Willner, L.; Stellbrink, J.; Lindner, P.; Richter, D. *Phys. Rev. Lett.* **2006**, *96*, 068302.

(95) Won, Y. Y.; Davis, H. T.; Bates, F. S. *Macromolecules* **2003**, *36*, 953-955.

(96) Meli, L.; Santiago, J. M.; Lodge, T. P. *Macromolecules* **2010**, *43*, 2018-2027.

(97) Willner, L.; Poppe, A.; Allgaier, J.; Monkenbusch, M.; Richter, D. *Europhys. Lett.* **2001**, *55*, 667-673.

(98) Lund, R.; Willner, L.; Stellbrink, J.; Radulescu, A.; Richter, D. *Physica B* **2004**, *350*, 909-912.

(99) Lund, R.; Willner, L.; Richter, D.; Dormidontova, E. E. *Macromolecules* **2006**, *39*, 4566-4575.

(100) Lund, R.; Willner, L.; Stellbrink, J.; Richter, D. *Physica B* **2006**, *385*, 735-737.

(101) Choi, S.; Lodge, T. P.; Bates, F. S. *Phys. Rev. Lett.* **2010**, *104*, 047802.

(102) Zimm, B. H. *J. Chem. Phys.* **1948**, *16*, 1093-1099.

(103) Choi, S.; Lodge, T. P.; Bates, F. S. *Macromolecules* **2011**, *44*, 3594-3604.

(104) Zinn, T.; Willner, L.; Lund, R.; Pipich, V.; Richter, D. *Soft Matter* **2012**, *8*, 623-626.

(105) Lu, J.; Choi, S.; Lodge, T. P.; Bates, F. S. *ACS Macro Lett.* **2012**, *1*, 982-985.

(106) Lu, J.; Lodge, T. P.; Bates, F. S. *ACS Macro Lett.* **2013**, *2*, 451-455.

(107) Lu, J.; Bates, F. S.; Lodge, T. P. *Macromolecules* **2015**, *48*, 2667-2676.

(108) Zinn, T.; Willner, L.; Pipich, V.; Richter, D.; Lund, R. *ACS Macro Lett.* **2016**, *5*, 884-888.

(109) Lund, R.; Willner, L.; Richter, D.; Iatrou, H.; Hadjichristidis, N.; Lindner, P. *J. Appl. Cryst.* **2007**, *40*, 327-331.

(110) Lund, R.; Willner, L.; Pipich, V.; Grillo, I.; Lindner, P.; Colmenero, J.; Richter, D. *Macromolecules* **2011**, *44*, 6145-6154.

(111) Lu, J. *Mechanisms of Chain Exchange in Block Copolymer Micelles*. PhD Dissertation, University of Minnesota, 2015.

(112) Wiley, R. H.; Brauer, G. M. *J. Polym. Sci.* **1948**, *3*, 455-461.

(113) Unger, R.; Beyer, D.; Donth, E. *Polymer* **1991**, *32*, 3305-3312.

(114) Varshney, S. K.; Jérôme, R.; Bayard, P.; Jacobs, C.; Fayt, R.; Teyssié, P. *Macromolecules* **1992**, *25*, 4457-4463.

(115) Reuter, H.; Berlinova, I.V.; Höring, S.; Ulbricht, J. *Eur. Polym. J.* **1991**, *27*, 673-680.

(116) Baskaran, D.; Chakrapani, S.; Sivaram, S. *Macromolecules* **1995**, *28*, 7315-7317.

(117) Schreiber, H. *Makromol. Chem.* **1960**, *36*, 86-88.

(118) Lochmann, L.; Rodová, M.; Petránek, J.; Lím, D. *J. Polym. Sci., Polym. Chem. Ed.* **1974**, *12*, 2295-2304.

(119) Kunkel, D.; Müller, A. H. E.; Lochmann, L.; Janata, M. *Makromol. Chem., Macromol. Symp.* **1992**, *60*, 315-326.

(120) Litvinenko, G.; Müller, A. H. E. *Macromolecules* **1997**, *30*, 1253-1266.

(121) Kato, M.; Kamigaito, M.; Sawamoto, M.; Higashimura, T. *Macromolecules* **1995**, *28*, 1721-1723.

(122) Wang, J.-S.; Matyjaszewski, K. *J. Am. Chem. Soc.* **1995**, *117*, 5614-5615.

(123) Rizzardo, E.; Meijs, G. F.; Thang, S. H. *Macromol. Symp.* **1995**, *98*, 101-123.

(124) Rizzardo, E; Chong, Y. K.; Evans, R. A.; Moad, G.; Thang, S. H. *Macromol. Symp.* **1996**, *111*, 1-12.

(125) Chiefari, J.; Chong, Y. K.; Ercole, F.; Krstina, J.; Jeffery, J.; Le, T. P. T.; Mayadunne, R. T. A.; Meijs, G. F.; Moad, C. L.; Moad, G.; Rizzardo, E.; Thang, S. H. *Macromolecules* **1998**, *31*, 5559-5562.

(126) Manders, B. G.; Smulders, W.; Aerdts, A. M.; van Herk, A. M. *Macromolecules* **1997**, *30*, 322-323.

(127) Bonhôte, P.; Dias, A.-P.; Papageorgiou, N.; Kalyanasundaram, K.; Grätzel, M. *Inorg. Chem.* **1996**, *35*, 1168-1178.

(128) Dzyuba, S. V.; Li, S.; Bartsch, R. A. *J. Heterocyclic Chem.* **2007**, *44*, 223-225.

(129) Zimm, B. H. *J. Chem. Phys.* **1948**, *16*, 1099-1116.

(130) Hiemenz, P. C.; Lodge, T. P. *Polymer Chemistry (2nd Ed.)*, CRC Press, Taylor & Francis Group: Boca Raton, FL, 2007.

(131) Numasawa, N.; Hamada, T.; Nose, T. *J. Polym. Sci., Polym. Lett. Ed.* **1985**, *23*, 1−4.

(132) Heyboer, J.; Staverman, A. J. *Rec. trav. chim.* **1950**, *69*, 787-798.

(133) Barner-Kowollik, C. *Handbook of RAFT Polymerization*, Wiley-VCH: Weinheim, 2008.

(134) Chong, B. Y. K.; Le, T. P. L.; Moad, G.; Rizzardo, E.; Thang, S. H. *Macromolecules* **1999**, *32*, 2071-2074.

(135) Vana, P.; Davis, T. P.; Barner-Kowollik, C. *Macromol. Theory Simul.* **2002**, *11*, 823-835.

(136) Matyjaszewski, K. *Controlled/Living Radical Polymerization: Progress in ATRP*. ACS Symposium Series, American Chemical Society, 2009.

(137) Grimaud, T.; Matyjaszewski, K. *Macromolecules* **1997**, *30*, 2216-2218.

(138) Wang, J.-L.; Grimaud, T.; Matyjaszewski, K. *Macromolecules* **1997**, *30*, 6507-6512.

(139) Karanam, S.; Goossens, H.; Klumperman, B.; Lemstra, P. *Macromolecules* **2003**, *36*, 3051-3060.

(140) Davis, K. A.; Matyjaszewski, K. *Chin. J. Polym. Sci.* **2004**, *22*, 195-204.

(141) Elias, H.-G.; Bareiss, R.; Watterson, J. G. *Adv. Polym. Sci.* **1973**, *11*, 111-204.

(142) Tanaka, K.; Waki, H.; Ido, Y.; Akita, S.; Yoshida, Y.; Yoshida, T.; Matsuo, T. *Rapid Commun. Mass Spectrom.* **1988**, *2*, 151-153.

(143) Karas, M.; Bahr, U. *Trends in Analytical Chemistry* **1990**, *9*, 321-325.

(144) Schrepp, W.; Pasch, H. *MALDI-TOF Mass Spectrometry of Synthetic Polymers*, Springer-Verlag: Berlin Heidelberg, 2003.

(145) Knochenmuss, R. *Analyst* **2006**, *131*, 966-986.

(146) Nielen, M. W. F. *Mass Spectrom. Rev.* **1999**, *18*, 309-344.

(147) Hilker, B.; Clifford, K. J.; Sauter, A. D., Jr.; Sauter, A. D., III; Gauthier, T.; Harmon, J. P. *Polymer* **2009**, *50*, 1015-1024.

(148) Kavitha, A. A.; Singha, N. K. *Macromol. Chem. Phys.* **2009**, *210*, 1536-1543.

(149) Watanabe, T.; Nakanishi, K.; Ozawa, T.; Kawasaki, H.; Ute, K.; Arakawa, R. *Rapid Commun. Mass Spectrom.* **2010**, *24*, 1835-1841.

(150) Wyzgoski, F. J.; Polce, M. J.; Wesdemiotis, C.; Arnould, M. A. *J. Polym. Sci.: Part A* **2007**, *45*, 2161-2171.

(151) Nakamura, Y.; Kitada, Y.; Kobayashi, Y.; Ray, B.; Yamago, S. *Macromolecules* **2011**, *44*, 8388-8397.

(152) Karas, M.; Bachmann, D.; Bahr, U.; Hillenkamp, F. *Int. J. Mass Spectrom. Ion Proc.* **1987**, *78*, 53-68.

(153) Schnöll-Bitai, I.; Hrebicek, T.; Rizzi, A. *Macromol. Chem. Phys.* **2007**, *208*, 485-495.

(154) Schriemer, D. C.; Li, L. *Anal. Chem.* **1997**, *69*, 4169-4175.

(155) Higgins, J. S.; Benoit, H. C. *Polymers and Neutron Scattering*, Oxford University Press: New York, 1994.

(156) Guinier, A.; Fournet, G. *Small-Angle Scattering of X-rays*, John Wiley & Sons: New York, 1955.

(157) Hammouda, B. *Probing Nanoscale Structures – The SANS Toolbox*, 2009. (http://www.ncnr.nist.gov/staff/hammouda/the_SANS_toolbox.pdf)

(158) Hammouda, B. *A Tutorial on Small-Angle Neutron Scattering from Polymers*, 1995. (https://www.ncnr.nist.gov/programs/sans/pdf/polymer_tut.pdf)

(159) Burchard, W. *Adv. Polym. Sci.* **1983**, *48*, 1-124.

(160) Hammouda, B. *Adv. Polym. Sci.* **1993**, *106*, 87-133.

(161) Guinier, A. *Ann. Phys.* **1939**, *12*, 161-237.

(162) Roe, R. *Methods of X-ray and Neutron Scattering in Polymer Science*, Oxford University Press: New York, 2000.

(163) Rubinstein, M.; Colby, R. H. *Polymer Physics*, Oxford University Press: Oxford, 2003.

(164) Curtis, L. J. *Atomic Structure and Lifetimes: A Conceptual Approach*, Cambridge University Press: Cambridge, 2003.

(165) Weigand, S. J.; Keane, D. T. *Nucl. Instrum. Methods Phys. Res., Sect. A* **2001**, *649*, 61-63.

(166) *Neutron News* **1992**, *3*, 29-37.

(167) Brown, W. *Light Scattering: Principles and Development*, Clarendon Press: Oxford, 1996.

(168) Brown, W. *Dynamic Light Scattering: The Method and Some Applications*, Oxford University Press: New York, 1993.

(169) Provencher, S. W. *Comp. Phys. Commun.* **1982**, *27*, 213-227.

(170) Provencher, S. W. *Comp. Phys. Commun.* **1982**, *27*, 229-242.

(171) Jakeš, J. *Collect. Czech. Chem. Commun.* **1995**, *60*, 1781−1797.

(172) Koppel, D. E. *J. Chem. Phys.* **1972**, *57*, 4814−4820.

(173) Daoud, M.; Cotton, J. P. *J. Phys. France* **1982**, *43*, 531-538.

(174) Leibler, L.; Orland, H.; Wheeler, J. C. *J. Chem. Phys.* **1983**, *79*, 3550-3557.

(175) Noolandi, J.; Hong, K. M. *Macromolecules* **1982**, *15*, 482-492.

(176) Noolandi, J.; Hong, K. M. *Macromolecules* **1983**, *16*, 1443-1448.

(177) Zhulina, E. B.; Birshtein, T. M. *Polym. Sci. USSR* **1985**, *27*, 570-578.

(178) Halperin, A. *Macromolecules* **1987**, *20*, 2943-2946.

(179) Halperin, A.; Tirrell, M.; Lodge, T. P. *Adv. Polym. Sci.* **1992**, *100*, 31-71.

(180) Nagarajan, R.; Ganesh, K. *J. Chem. Phys.* **1989**, *90*, 5843-5856.

(181) Nagarajan, R.; Ganesh, K. *J. Chem. Phys.* **1993**, *98*, 7440-7450.

(182) Binder, K. *Monte Carlo and molecular dynamics simulations in polymer science*, Oxford University Press: New York, 1995.

(183) Milchev, A.; Bhattacharya, A.; Binder, K. *Macromolecules* **2001**, *34*, 1881-1893.

(184) Kim, S. H.; Jo, W. H. *J. Chem. Phys.* **2002**, *117*, 8565-8572.

(185) Riess, G. *Prog. Polym. Sci.* **2003**, *28*, 1107-1170.

(186) Zhulina, E. B.; Borisov, O. V. *Macromolecules* **2012**, *45*, 4429-4440.

(187) Kotaka, T.; Tanaka, T.; Hattori, M.; Inagaki, H. *Macromolecules* **1978**, *11*, 138-145.

(188) Bluhm, T. L.; Whitmore, M. D. *Can. J. Chem.* **1985**, *63*, 249-252.

(189) Bluhm, T. L.; Malhotra, S. L. *Eur. Polym. J.* **1986**, *22*, 249-251.

(190) Oranli, L.; Bahadur, P.; Riess, G. *Can. J. Chem.* **1985**, *63*, 2691-2696.

(191) Xu, R.; Winnik, M. A.; Hallett, F. R.; Riess, G.; Croucher, M. D. *Macromolecules* **1991**, *24*, 87-93.

(192) Xu, R.; Winnik, M. A.; Riess, G.; Chu, B.; Croucher, M. D. *Macromolecules* **1992**, *25*, 644-652.

(193) Antonietti, M.; Heinz, S.; Schmidt, M.; Rosenauer, C. *Macromolecules* **1994**, *27*, 3276-3281.

(194) Calderara F.; Hruska, Z.; Hurtrez, G.; Lerch, J. P.; Nugay, T.; Riess, G. *Macromolecules* **1994**, *27*, 1210-1215.

(195) Jada, A.; Hurtrez, G.; Siffert, B.; Riess, G. *Macromol. Chem. Phys.* **1996**, *197*, 3697-3710.

(196) Förster, S.; Zisenis, M.; Wenz, E.; Antonietti, M. *J. Chem. Phys.* **1996**, *104*, 9956-9970.

(197) Tao, J.; Stewart, S.; Liu, G.; Yang, M. *Macromolecules* **1997**, *30*, 2738-2745.

(198) Pitsikalis, M.; Siakali-Kioulafa, E.; Hadjichristidis, N. *Macromolecules* **2000**, *33*, 5460-5469.

(199) Bahadur, P.; Sastry, N. V.; Marti, S.; Riess, G. *Colloids and Surfaces* **1985**, *16*, 337-346.

(200) Jada, A.; Siffert, B.; Riess, G. *Colloids and Surfaces A* **1993**, *75*, 203-209.

(201) Quintana, J. R.; Salazar, R. A.; Katime, I. *Macromol. Chem. Phys.* **1995**, *196*, 1625-1634.

(202) Pitsikalis, M.; Siakali-Kioulafa, E.; Hadjichristidis, N. *J. Polym. Sci. Part A* **2004**, *42*, 4177-4188.

(203) Guerrero-Sanchez, C.; Wouters, D.; Fustin, C.-A.; Gohy, J.-F.; Lohmeijer, B. G. G.; Schubert, U. S. *Macromolecules* **2005**, *38*, 10185-10191.

(204) LaRue, I.; Adam, M.; Zhulina, E. B.; Rubinstein, M.; Pitsikalis, M.; Hadjichristidis, N.; Ivanov, D. A.; Gearba, R. I.; Anokhin, D. V.; Sheiko, S. S. *Macromolecules* **2008**, *41*, 6555-6563.

(205) Choi, S.; Bates, F. S.; Lodge, T. P. *J. Phys. Chem. B* **2009**, *113*, 13840-13848.

(206) Jensen, G. V.; Shi, Q.; Deen, G. R.; Almdal, K.; Pedersen, J. S. *Macromolecules* **2012**, *45*, 430-440.

(207) Zinn, T.; Willner, L.; Lund, R.; Pipich, V.; Appavou, M.; Richter, D. *Soft Matter* **2014**, *10*, 5212-5220.

(208) Pedersen, J. S.; Svaneborg, C.; Almdal, K.; Hamley, I. W.; Young, R. N. *Macromolecules* **2003**, *36*, 416-433.

(209) Castelletto, V.; Hamley, I. W.; Pedersen, J. S. *J. Chem. Phys.* **2002**, *117*, 8124-8129.

(210) Bang, J.; Viswanathan, K.; Lodge, T. P.; Park, M. J.; Char, K. *J. Chem. Phys.* **2004**, *121*, 11489-11500.

(211) Lodge, T. P.; Xu, X.; Ryu, C. Y.; Hamley, I. W.; Fairclough, J. P. A.; Ryan, A. J.; Pedersen, J. S. *Macromolecules* **1996**, *29*, 5955-5964.

(212) Liu, Y.; Chen, S.-H.; Huang, J. S. *Macromolecules* **1998**, *31*, 2236-2244.

(213) Seitz, M. E.; Burghardt, W. R.; Shull, K. R. *Macromolecules* **2009**, *42*, 9133-9140.

(214) Birshtein, T. M.; Zhulina, E. B. *Polymer* **1989**, *30*, 170-177.

(215) Helfand, E.; Sapse, A. M. *J. Chem. Phys.* **1975**, *62*, 1327-1331.

(216) Lund, R.; Willner, L.; Lindner, P.; Richter, D. *Macromolecules* **2009**, *42*, 2686–2695.

(217) Ma, Y.; Lodge, T. P. *Macromolecules* **2016**, *49*, 9542-9552.

(218) Cavicchi, K. A.; Lodge, T. P. *Macromolecules* **2003**, *36*, 7158-7164.

(219) McConnell, G. A.; Gast, A. P.; Huang, J. S.; Smith, S. D. *Phys. Rev. Lett.* **1993**, *71*, 2102-2105.

(220) Strobl, G. R. *The Physics of Polymers: Concepts for Understanding Their Structures and Behavior*, Springer-Verlag: Berlin Heidelberg, 1996.

(221) Choucair, A.; Eisenberg, A. *Eur. Phys. J. E* **2003**, *10*, 37-44.

(222) Gohy, J. *Adv. Polym. Sci.* **2005**, *190*, 65-136.

(223) Hayward, R. C.; Pochan, D. J. *Macromolecules* **2010**, *43*, 3577-3584.

(224) Jain, S.; Bates, F. S. *Science* **2003**, *300*, 460-464.

(225) Jain, S.; Bates, F. S. *Macromolecules* **2004**, *37*, 1511-1523.

(226) Chen, L.; Shen, H. W.; Eisenberg, A. *J. Phys. Chem. B* **1999**, *103*, 9488-9497.

(227) He, Y.; Li, Z.; Simone, P.; Lodge, T. P. *J. Am. Chem. Soc.* **2006**, *128*, 2745-2750.

(228) Thiagarajan, R. *Modeling of Diblock Copolymers in Selective Solvents*. PhD Dissertation, University of Minnesota, 2012.

(229) Goldmints, I.; von Gottberg, F. K.; Smith, K. A.; Hatton, T. A. *Langmuir* **1997**, *13*, 3659-3664.

(230) Yang, L.; Alexandridis, P; Steytler, D. C.; Kositza, M. J.; Holzwarth, J. F. *Langmuir* **2000**, *16*, 8555-8561.

(231) Alexandridis, P.; Yang, L. *Macromolecules* **2000**, *33*, 5574-5587.

(232) de Gennes, P.-G. In *Solid State Physics*; Liebert, L., Ed.; Academic: New York, 1978; *Suppl*. 14.

(233) Tuzar, Z.; Kratochvil, P. *Adv. Colloid Interface Sci.* **1976**, *6*, 201-232.

(234) Hamley, I. W. *The Physics of Block Copolymers*, Oxford University: New York, 1998.

(235) Barrat, J. L.; Fredrickson, G. H. *Macromolecules* **1991**, *24*, 6378-6383.

(236) Dalvi, M. C.; Lodge, T. P. *Macromolecules* **1993**, *26*, 859-861.

(237) Yokoyama, H.; Kramer, E. J. *Macromolecules* **1998**, *31*, 7871-7876.

(238) Hoarfrost, M. L.; Lodge, T. P. *Macromolecules* **2014**, *47*, 1455-1461.

(239) Meli, L.; Lodge, T. P. *Macromolecules* **2009**, *42*, 580-583.

(240) Kline, S. R. *J. Appl. Crystallogr.* **2006**, *39*, 895-900.

(241) Ferry, J. D. *Viscoelastic Properties of Polymers (3rd Ed)*, Wiley: New York, 1980.

(242) Ferry, J. D.; Landel, R. F. *Kolloid-Zeitschrift* **1956**, 148, 1-6.

(243) Flory, P. J. *J. Chem. Phys.* **1942**, *10*, 51-61.

(244) Halperin, A. *Macromolecules* **2011**, *44*, 5072-5074.

(245) de Gennes, P. G. *J. Chem. Phys.* **1980**, *72*, 4756-4763.

(246) Whitmore, M. D.; Noolandi, J. *Macromolecules* **1985**, *18*, 657-665.

(247) Stauffer, D.; Woermann, D. *J. Phys. II* **1995**, *5*, 1-3.

(248) Anghel, D. F.; Winnik, F. M.; Galatanu, N. *Colloids Surf. A* **1999**, *149*, 339-345.

(249) Kenward, M.; Whitmore, M. D. *J. Chem. Phys.* **2002**, *116*, 3455-3470.

(250) Lu, J.; Bates, F. S.; Lodge, T. P. *Macromolecules* **2016**, *49*, 1405-1413.

(251) Choi, S. Block Copolymer Self-Assembly in Solution: Structure and Dynamics. PhD Dissertation, University of Minnesota, 2010.

Appendices

A.1. Fitting of SEC Traces in Section 2.3

The SEC traces of entries 1 – 3 in Table 2.3 and entries 1 – 6 in Table 2.4 are fit to the sum of two Gaussian distributions:

$$y = A_1 \frac{1}{\sqrt{2\pi}\sigma_1} \exp[-\frac{(x-\mu_1)^2}{2\sigma_1^2}] + A_2 \frac{1}{\sqrt{2\pi}\sigma_2} \exp[-\frac{(x-\mu_2)^2}{2\sigma_2^2}] \quad \text{(A.1.1)}$$

in which x is the elution volume, and y is the normalized RI signal. For controlled radical polymerization, the Schulz-Zimm distribution is an accurate function for describing the molecular weight distribution in the resulting polymers; however, a Gaussian distribution is used here for simplicity. Additionally, the σ_1 and σ_2 were fixed as identical in the fitting, which proves to be more reasonable, and avoids overestimation of the homopolymer percentage.

Based on eq A.1.2, the peak areas have the ratio of

$$S_1 / S_2 = A_1\sigma_1 / A_2\sigma_2 \quad \text{(A.1.2)}$$

To convert this peak area ratio to the mass ratio of the two species, the numerator and the denominator in eq A.1.2 should be divided by their dn/dc, which gives

$$\frac{w_1}{w_2} = \frac{S_1/(dn/dc)_1}{S_2/(dn/dc)_2} = \frac{A_1\sigma_1(dn/dc)_2}{A_2\sigma_2(dn/dc)_1} \quad \text{(A.1.3)}$$

Because the *dn*/*dc* of PMMA (0.084 mL/g) and PnBMA (0.068 mL/g) are quite similar, the ratio between the two *dn*/*dc*'s in eq A.1.3 can be taken as 1. Therefore, the homopolymer (denoted as the subscript 2) weight fraction can be simplified as $w_2 = A_2\sigma_2/(A_1\sigma_1+A_2\sigma_2)$, in which all parameters can be directly obtained from the fitting.

The fitting results of Table 2.3 and Table 2.4 are given in Figures A.1.1 and A.1.2, respectively.

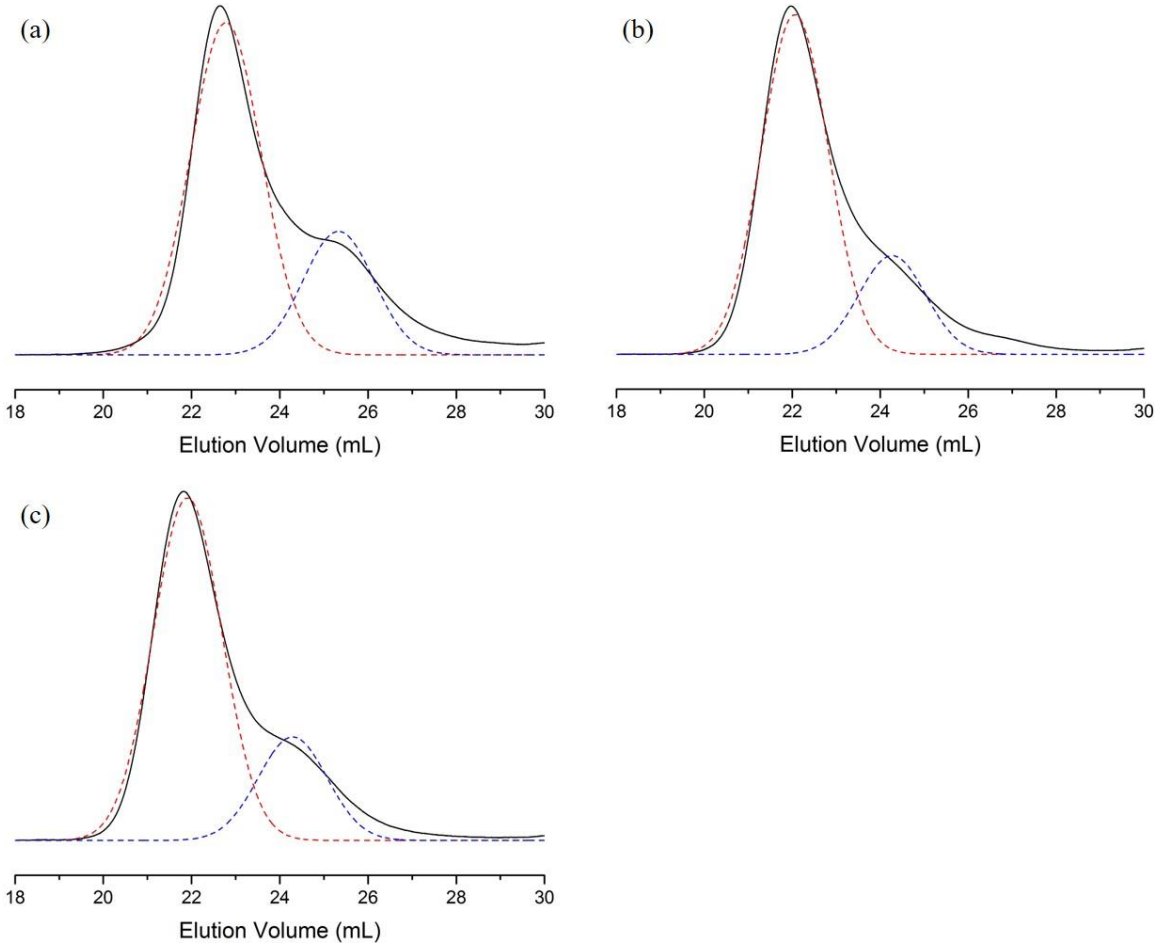

Figure A.1.1. Fitting of SEC traces (Table 2.3, entries 1 – 3) to the sum of two Gaussian distributions: (a) entry 1: PnBMA-*b*-PMMA (34-33); (b) entry 2: PnBMA-*b*-PMMA (34-54); (c) entry 3: PnBMA-*b*-PMMA (31-51).

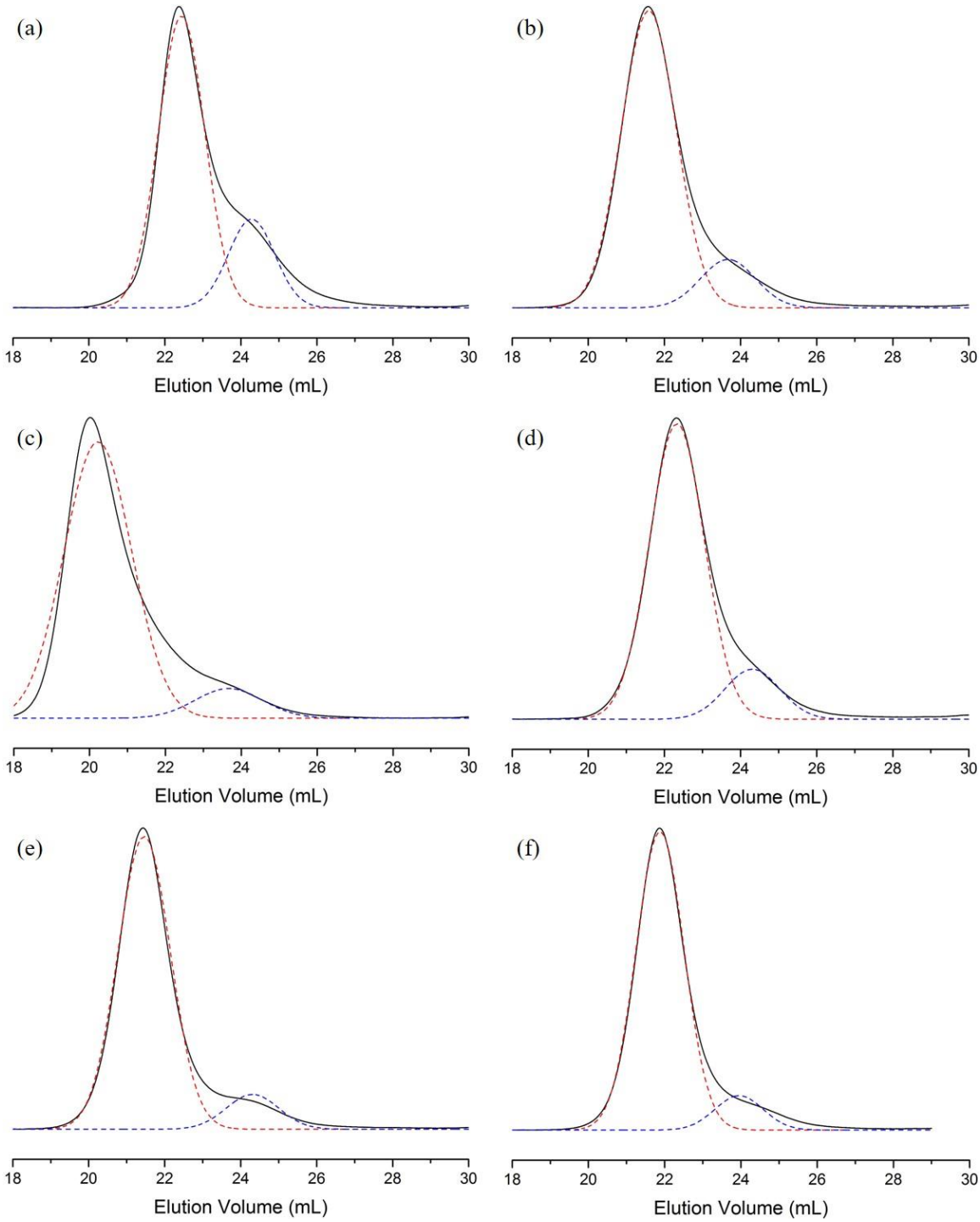

Figure A.1.2. Fitting of SEC traces (Table 2.4, entries 1 – 6) to the sum of two Gaussian distributions: (a) entry 1: PnBMA-*b*-PMMA (29-25); (b) entry 2: PnBMA-*b*-PMMA (37-56); (c) entry 3: PnBMA-*b*-PMMA (37-104); (d) entry 4: PnBMA-*b*-PMMA (33-38); (e) entry 5: PnBMA-*b*-PMMA (33-73); (f) entry 6: PnBMA-*b*-PMMA (29-58).

A.2. Polymer Characterization: Matrix-assisted Laser Desorption/ Ionization Mass Spectroscopy (MALDI-MS)

The absolute molecular weight of homopolymers can be determined by various methods, such as static light scattering (MALLS-SEC), end-group analysis (^{1}H-NMR), and the measurement of colligative properties of polymer solutions (boiling point elevation, freezing point depression, and osmotic pressure).[1] Among the above, end-group analysis is not so reliable for polymers with more than 100 repeating units, as accurate integrations are not easy to achieve in that case. On the other hand, static light scattering measurement in SEC requires accurate measurement of *dn*/*dc* as well as careful calibration of the instrument, thus 10% of error is often observed for the same polymer measured at multiple SECs.

Matrix-assisted laser desorption/ionization mass spectroscopy (MALDI-MS) is a novel technique that enables the accurate measurement of the molecular weight and molecular weight distribution of macromolecules.[2–4] MALDI-MS employs the strategy of using small organic molecules as matrix to "transfer" the laser energy to the macromolecules, avoiding their fragmentation, which will otherwise take place in conventional ionization methods. Generally, it is believed that the mechanism of ionization follows two steps: (*i*) matrix molecules absorb laser energy, they are then desorbed and ionized, forming a hot plume. (*ii*) The ablated matrix molecules in the hot plume transfer the energy and charges to the neutral macromolecules (denoted as M) via complicated reactions, causing them to form $[M\text{-}H]^+$ and other possible adducts, such as $[M\text{-}Na]^+$ and $[M\text{-}K]^+$.[5]

Up to now, the MALDI-MS analyses of synthetic polymers are still based on a highly empirical approach: matrices, cationaztion salts and sample preparation methods have to be carefully selected for each specific polymer, which requires a lot of trial and error. Furthermore, adequate laser intensity should be applied, so as to make the macromolecules just able to "fly" while not be broken apart.[6] Typically, for analyzing

PMMA, 2,5-dihydroxybenzoic acid (DHB)[7,8] and 1,8,9-anthracenetriol (dithanol)[9–11] are often used as the matrix; some sodium or silver salts are also added to facilitate the formation of polymer-ion adducts. Following the reported procedures, we found that by mixing polymer, DHB and silver acetylacetonate (Ag(acac)) in 1:10:1 ratio, the optimal result is achieved for PMMA with molecular weight of 15 – 30 kg/mol. When the molecular weight of PMMA is further increased to over 40 kg/mol, MALDI-MS only gives very poor signal, which can hardly be distinguished from the baseline.

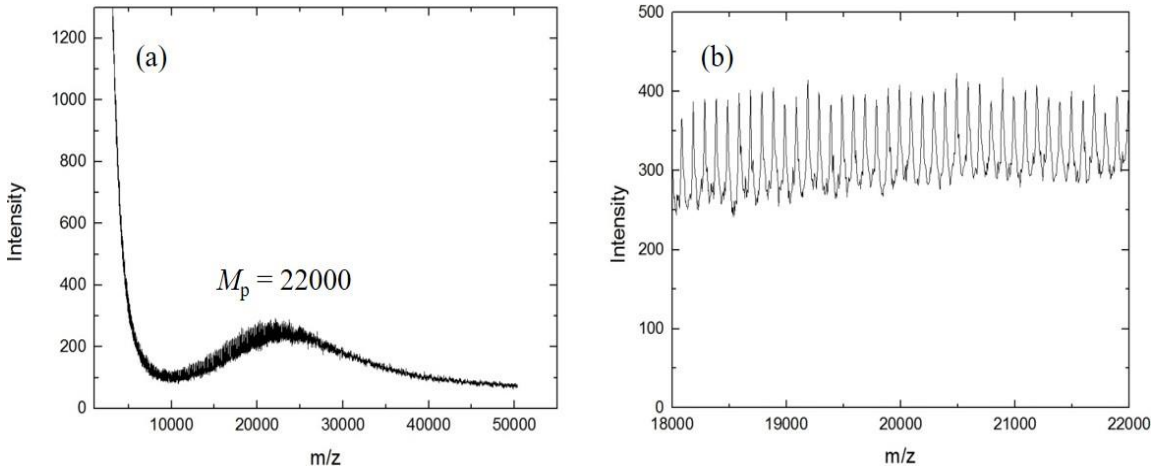

Figure A.2.1. (a) MALDI-MS of PMMA (25). The experiment was conducted on an AB Sciex 5800 TOF/TOF Mass Spectrometer. (b) Zoom-in of (a).

A typical MALDI spectroscopy of PMMA (25) is given in Figure A.2.1a. As can be seen from the spectrum, in the region of m/z < 10000, the intensity dramatically increases as m/z approaches zero. This baseline decay is actually an artifact due to the convolution of matrix ions, which has also been observed in various other cases.[12,13] Therefore, the bump at m/z ≈ 22000 is actually representative of PMMA, which slightly deviates from the M_n value of 25 kg/mol given by the SEC characterization. A zoom-in version of the mass spectrum is given in Figure A.2.1b. Clearly, the m/z difference between each peak is exactly 100, identical to the molar mass of MMA monomer. This is a clear evidence that confirms the identity of the bump.

It is worth noticing that the molecular weight distribution given by MALDI-MS does not necessarily represent the absolute molecular weight distribution of the polymer. In fact, MALDI-MS tends to underestimate the M_n of a synthetic polymer, due to the discrimination effect against high molecular weight species, *i.e.*, heavier polymer chains have less probability to be ionized and "fly".[6,14] With such underestimation accounted for, the discrepancy between the molecular weights given by MALDI-MS and SEC can now be justified; and MALDI-MS further supports the accuracy of the molecular weight determined by SEC.

A.3. DLS and SAXS Data at Different Temperatures

Besides 60 °C, DLS and SAXS data for the seven diblock copolymer micelles were collected at other temperatures, such as 40 and 100 °C. Here, PMMA-*b*-PnBMA (25-35) is used as an example. As can be seen from Figure A.3.1, the R_h peak positions of PMMA-*b*-PnBMA (25-35) micelles are all around 24±2 nm, regardless of temperature; such difference is within experimental error. The SAXS patterns in Figure A.3.2 also indicate that the micelle sizes (both R_c and R_h) are almost independent of temperature in the range of 40 – 100 °C.

This weak temperature dependence of micelle size is probably due to the relatively big gap between the experimental temperature and the CMTs, which are given in Figure A.3.3. It is worth mentioning that the CMTs of these copolymers in [EMIM][TFSI] were not measured directly. Instead, they were obtained by measuring the CMTs of each polymer in a series of mixed solvents of [BMIM][TFSI] and [EMIM][TFSI] with various [BMIM] wt%, then linearly extrapolating to [BMIM] wt% = 0. The linear relationship between CMT and [BMIM] wt% has been observed previously by Lee *et al.*[15]

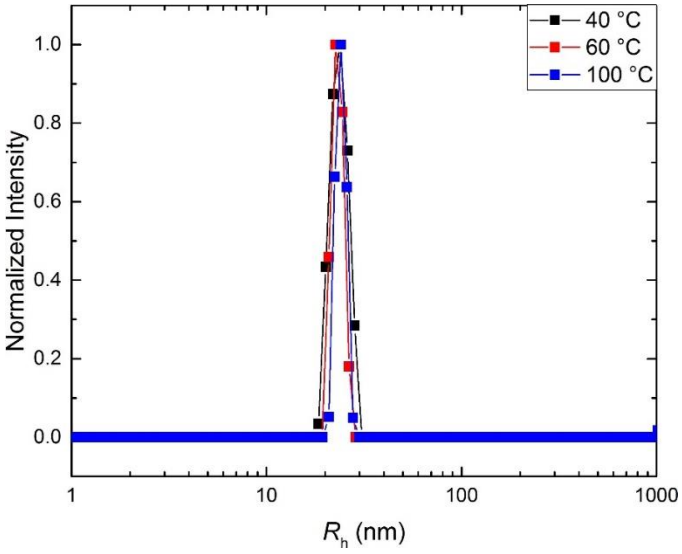

Figure A.3.1. R_h distribution of PMMA-*b*-PnBMA (25-35) in [EMIM][TFSI] at 40, 60 and 100 °C.

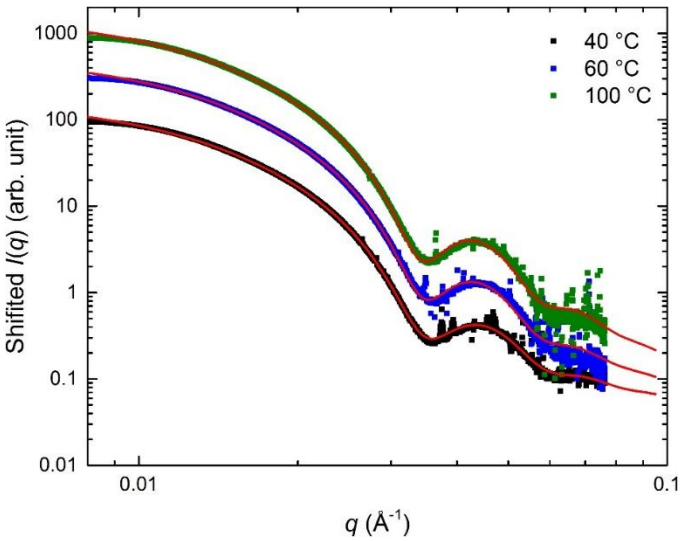

Figure A.3.2. SAXS data of PMMA-*b*-PnBMA (25-35) in [EMIM][TFSI] at 40, 60 and 100 °C. The data are shifted vertically for clarity. The solid lines are best fits to Pedersen model.

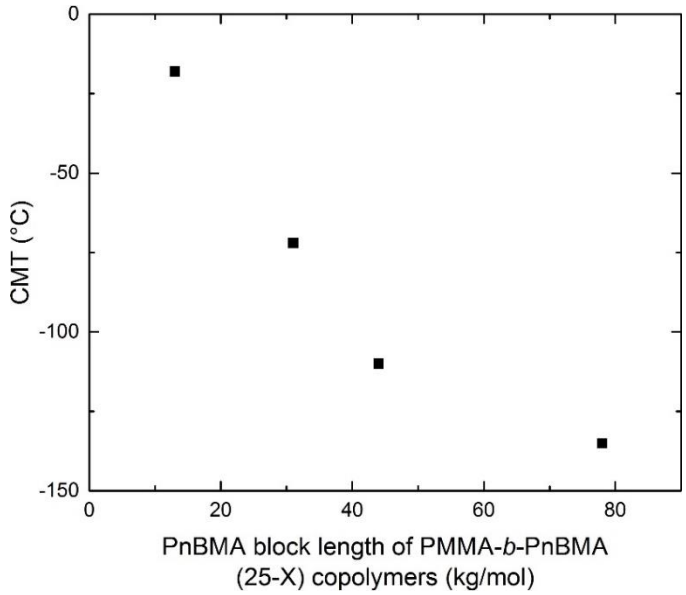

Figure A.3.3. CMT of PMMA-*b*-PnBMA (25-X) in [EMIM][TFSI] as a function of PnBMA block lengths (in the unit of kg/mol).

A.4. Comparison Between Two Fitting Methods

In the original Pedersen model, the hard sphere potential is used to derive the structure factor, $S(q)$, based on the Percus-Yevick closure.[16] This structure factor plays a vital role when the micelle concentration is sufficiently large. Nevertheless, the boundary between dilute and concentrated solution is rather vague. Therefore, the SAXS data for the seven 1 wt% micelle solutions are also fit to the original Pedersen model (with structure factor) for comparison, the results of which are summarized in Table A.4.1.

Similarly, we can plot the R_c obtained from the fitting to the original Pedersen model against the degree of polymerization of the core block, N_B, which yields the red line in Figure A.4.1. The slope of the new $\log R_c$ – $\log N_B$ plot is determined to be 0.68, very close to the one we obtained previously (the black line in Figure A.4.1). In sum, the two fitting methods do not display any significant difference.

Table A.4.1. Summary of the results obtained from the two fitting methods (with structure factor and without structure factor)

	Fitting without structure factor		**Fitting with structure factor**	
	R_c **(Å)**	σ_R **(Å)**	R_c **(Å)**	σ_R **(Å)**
PMMA-*b*-PnBMA (25-13)	$58 \pm 2\times10^2$	$5 \pm 2\times10^2$	$62 \pm 6\times10^2$	$5 \pm 5\times10^2$
PMMA-*b*-PnBMA (25-24)	100 ± 6	6 ± 5	106 ± 9	8 ± 10
PMMA-*b*-PnBMA (25-31)	119 ± 2	9 ± 4	123 ± 4	10 ± 4
PMMA-*b*-PnBMA (25-35)	128 ± 1	10 ± 2	132 ± 3	10 ± 3
PMMA-*b*-PnBMA (25-44)	152 ± 0.2	18 ± 0.1	156 ± 7	18 ± 5
PMMA-*b*-PnBMA (25-53)	171 ± 0.5	14 ± 0.7	173 ± 2	13 ± 0.5
PMMA-*b*-PnBMA (25-78)	232 ± 0.3	22 ± 0.2	238 ± 2	22 ± 0.5

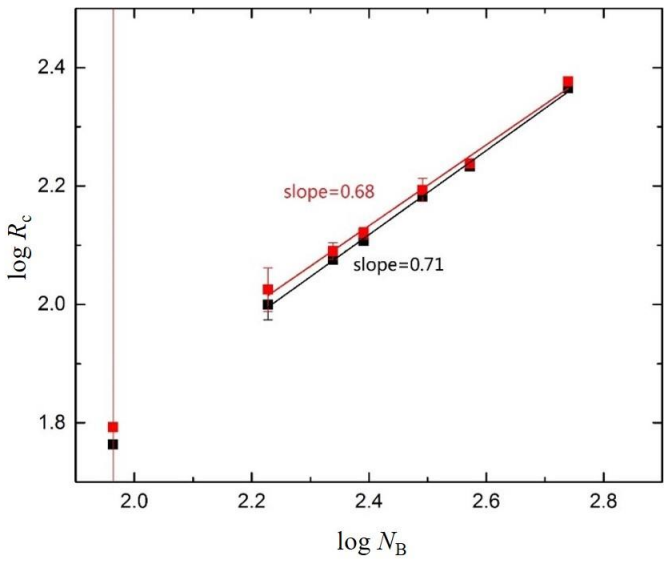

Figure A.4.1. Relationship of R_c and N_B for the two fitting methods. The lowest N sample data are not used in the fittings due to large uncertainty.

A.5. Fitting Results of the SAXS Data in Figure 5.4

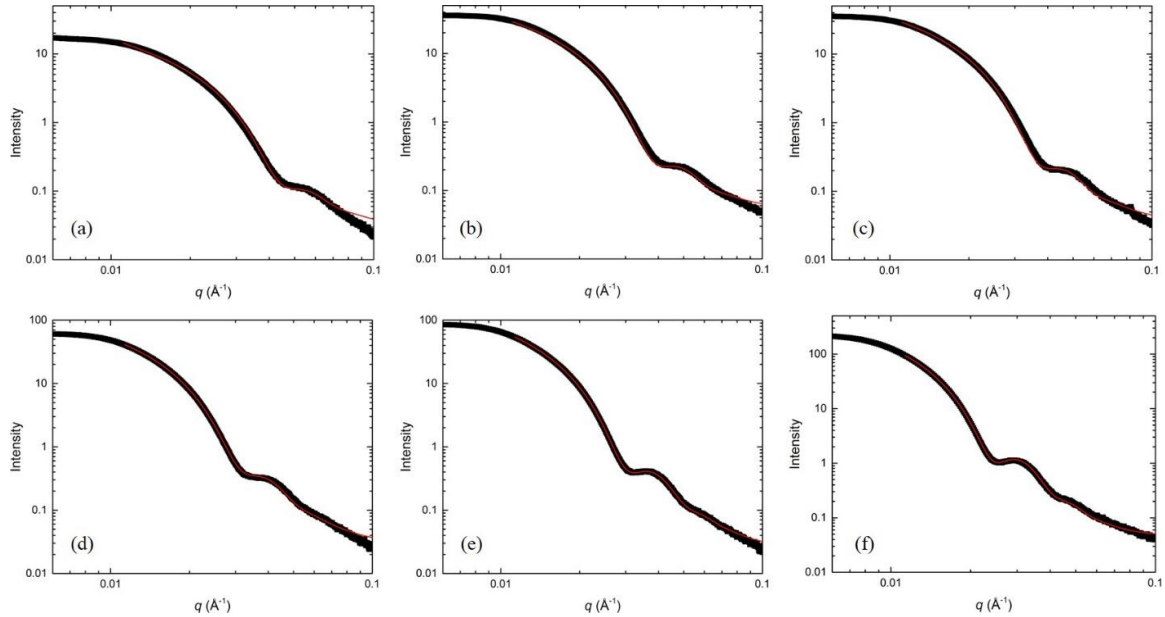

Figure A.5.1 Fitting of SAXS profiles of PMMA-*b*-PnBMA (a) (25-24), (b) (25-31), (c) (25-35), (d) (25-44), (e) (25-53), and (f) (25-78) with the condition of CMT = 0 °C, *T* – CMT = 60 °C.

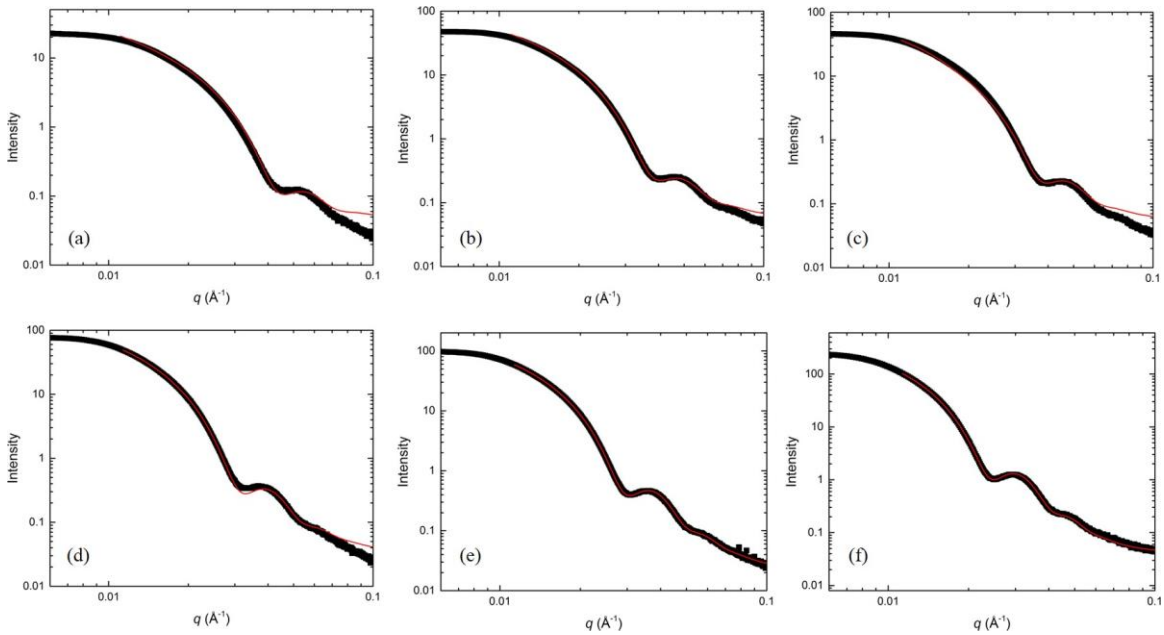

Figure A.5.2 Fitting of SAXS profiles of PMMA-*b*-PnBMA (a) (25-24), (b) (25-31), (c) (25-35), (d) (25-44), (e) (25-53), and (f) (25-78) with the condition of CMT = 0 °C, *T* – CMT = 80 °C.

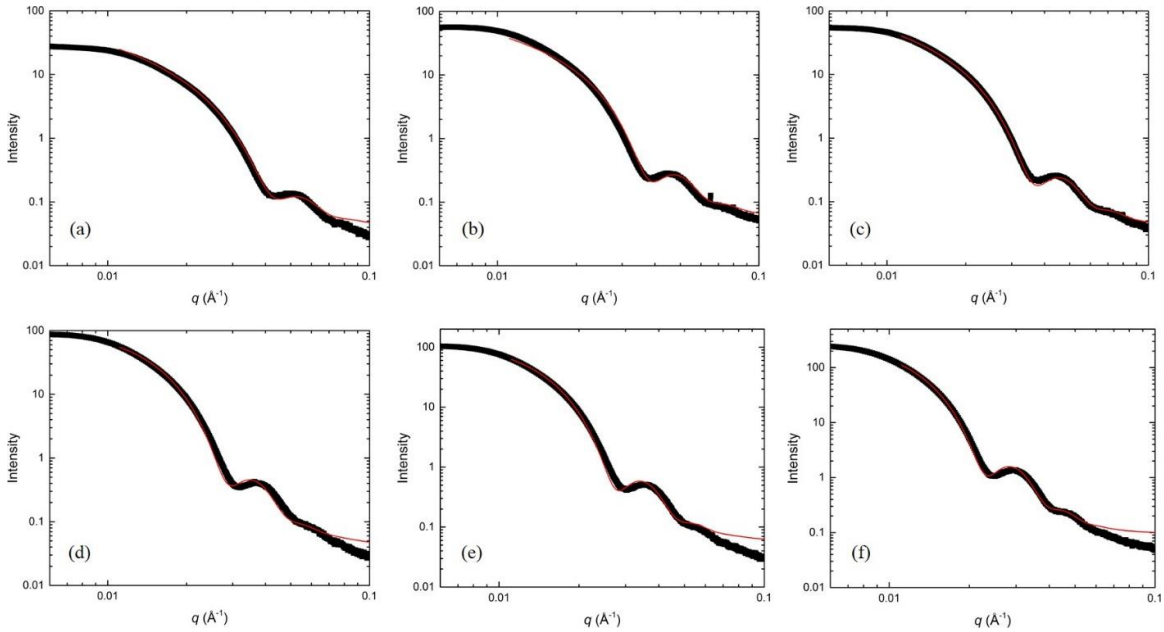

Figure A.5.3 Fitting of SAXS profiles of PMMA-*b*-PnBMA (a) (25-24), (b) (25-31), (c) (25-35), (d) (25-44), (e) (25-53), and (f) (25-78) with the condition of CMT = 0 °C, *T* – CMT = 100 °C.

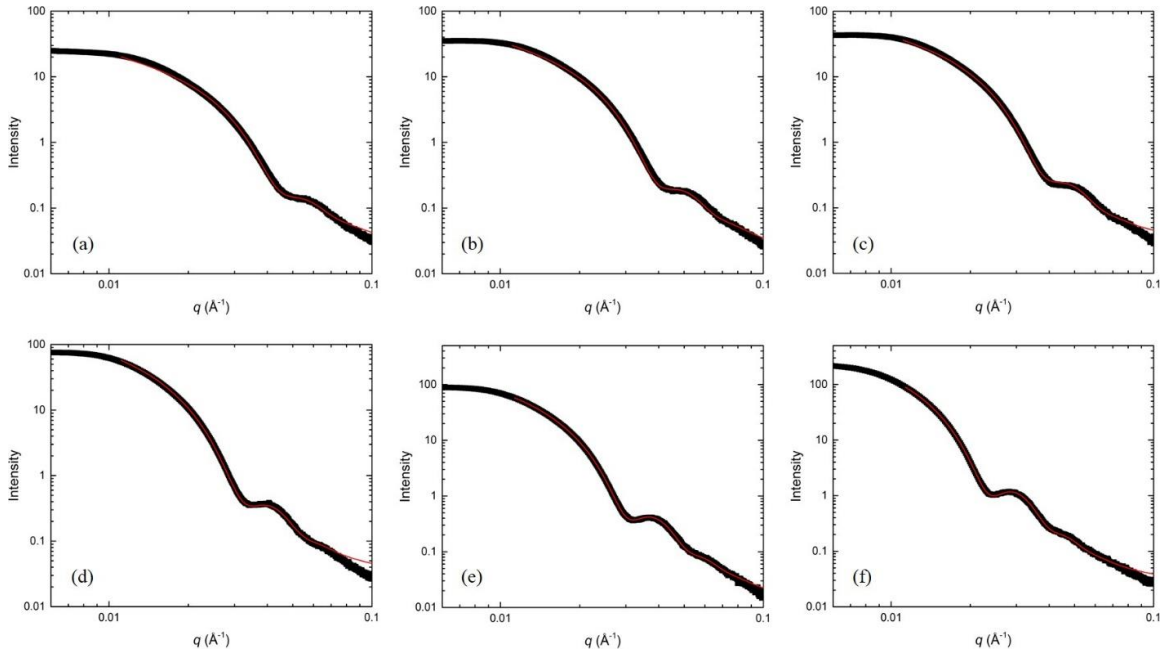

Figure A.5.4 Fitting of SAXS profiles of PMMA-*b*-PnBMA (a) (25-24), (b) (25-31), (c) (25-35), (d) (25-44), (e) (25-53), and (f) (25-78) with the condition of CMT = –20 °C, *T* – CMT = 60 °C.

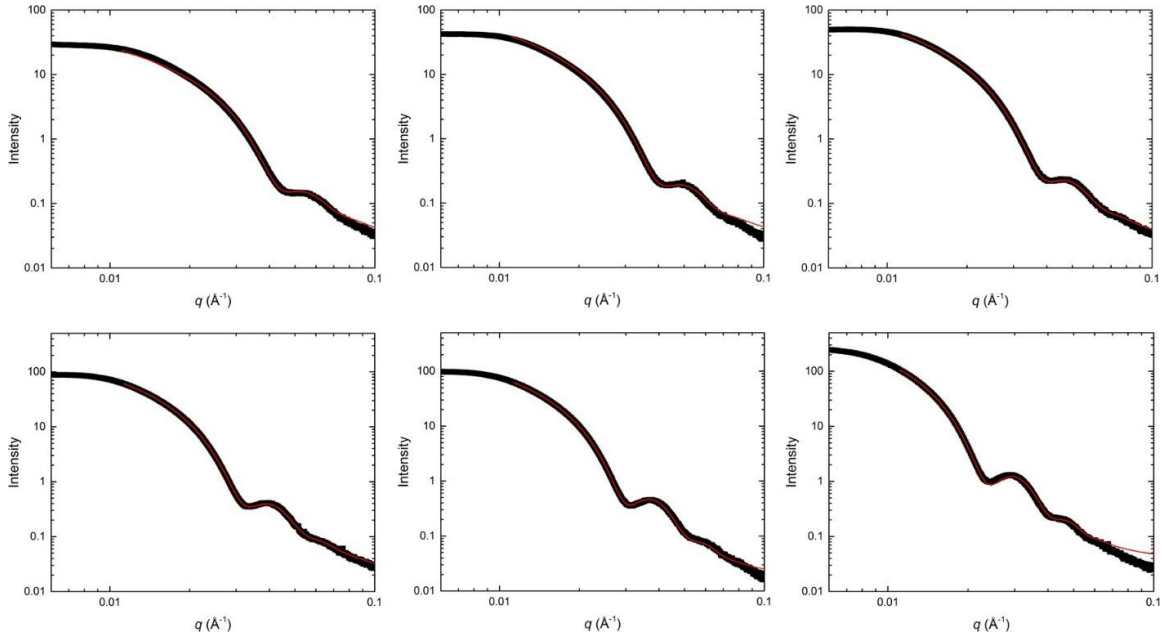

Figure A.5.5 Fitting of SAXS profiles of PMMA-*b*-PnBMA (a) (25-24), (b) (25-31), (c) (25-35), (d) (25-44), (e) (25-53), and (f) (25-78) with the condition of CMT = –20 °C, *T* – CMT = 80 °C.

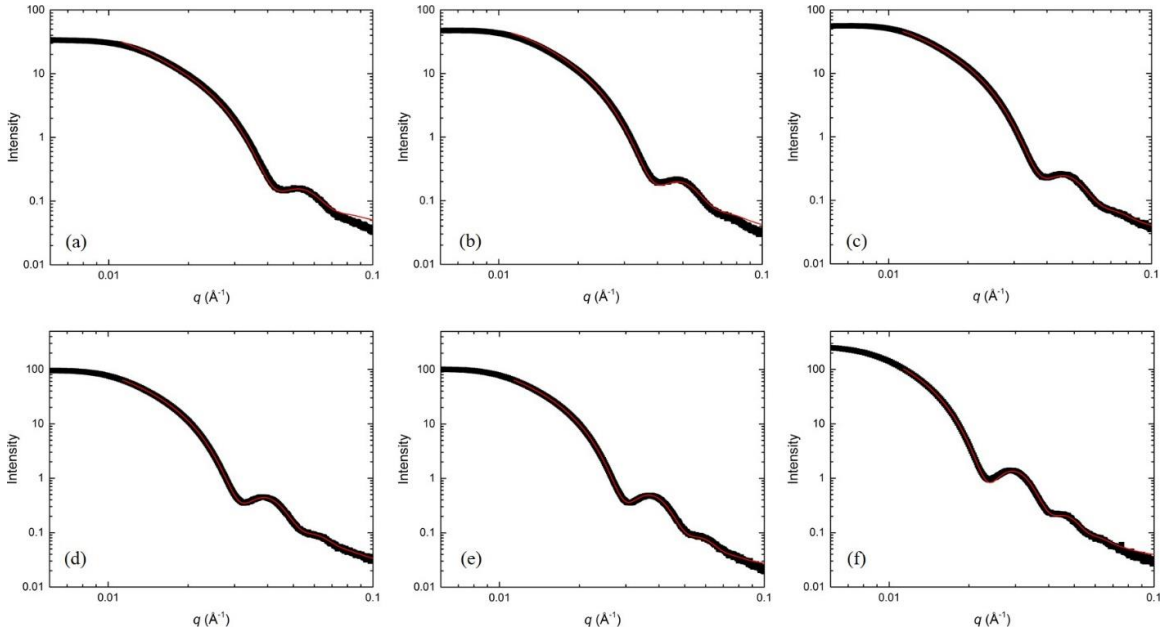

Figure A.5.6 Fitting of SAXS profiles of PMMA-*b*-PnBMA (a) (25-24), (b) (25-31), (c) (25-35), (d) (25-44), (e) (25-53), and (f) (25-78) with the condition of CMT = –20 °C, *T* – CMT = 100 °C.

A.6. Determination of Monomeric Friction Coefficient for PnBMA

According to the Rouse model, the monomeric friction coefficient (ζ) can be estimated by

$$\zeta = \frac{36 M_0 \eta_0}{\rho N_A N b^2} \tag{A.6.1}$$

in which M_0, η_0, ρ, N_A, N and b are the molar mass of the monomer, zero-shear viscosity of an unentangled polymer, density, Avogadro number, degree of polymerization, and the statistical segment length, respectively. For PnBMA, M_0 = 142 g/mol, ρ = 1.07 g/cm^3 and b = 6.1 Å. Therefore, by measuring the zero-shear viscosity of PnBMA at different temperatures, we are able to calculate the monomeric friction coefficient at these temperatures, and thereby obtain a WLF-type relationship for ζ and temperature. The WLF equation is given below:

$$\lg(\zeta / \zeta_{ref}) = -\frac{C_1 (T - T_{ref})}{C_2 + (T - T_{ref})} \tag{A.6.2}$$

We conducted dynamic viscosity measurements on a 45 kg/mol PnBMA homopolymer, using an ARES rheometer. As can be seen from Figure A.6.1a, the G' and G'' indicate that there is at most weak entanglement in this sample, therefore, PnBMA has a Rouse-like rheological behavior even at a rather high molecular weight. In Figure A.6.1b, the zero-shear viscosity, η_0, is obtained by extrapolating these dynamic viscosity data to ω = 0; then ζ at 90, 100, 110, 120 and 150 °C are calculated on the basis of eq. A.6.1 (the result is given in Table A.6.1). We select 110 °C (383K) as the reference temperature (T_{ref}), and fit the log(ζ/ζ_{ref}) to eq. A.6.2. The fitting gives C_1 = 10.1 and C_2 = 191 K (Figure A.6.1c).

In the study of chain exchange kinetics, we are interested in ζ at 65 °C. With the C_1 and C_2 obtained from fitting, ζ (65°C) = 7.1×10^{-4} N-s/m, which has the same magnitude as the value reported by Ferry *et al*. (ζ = 1.4×10^{-4} N-s/m at T = 65 °C)[17,18]

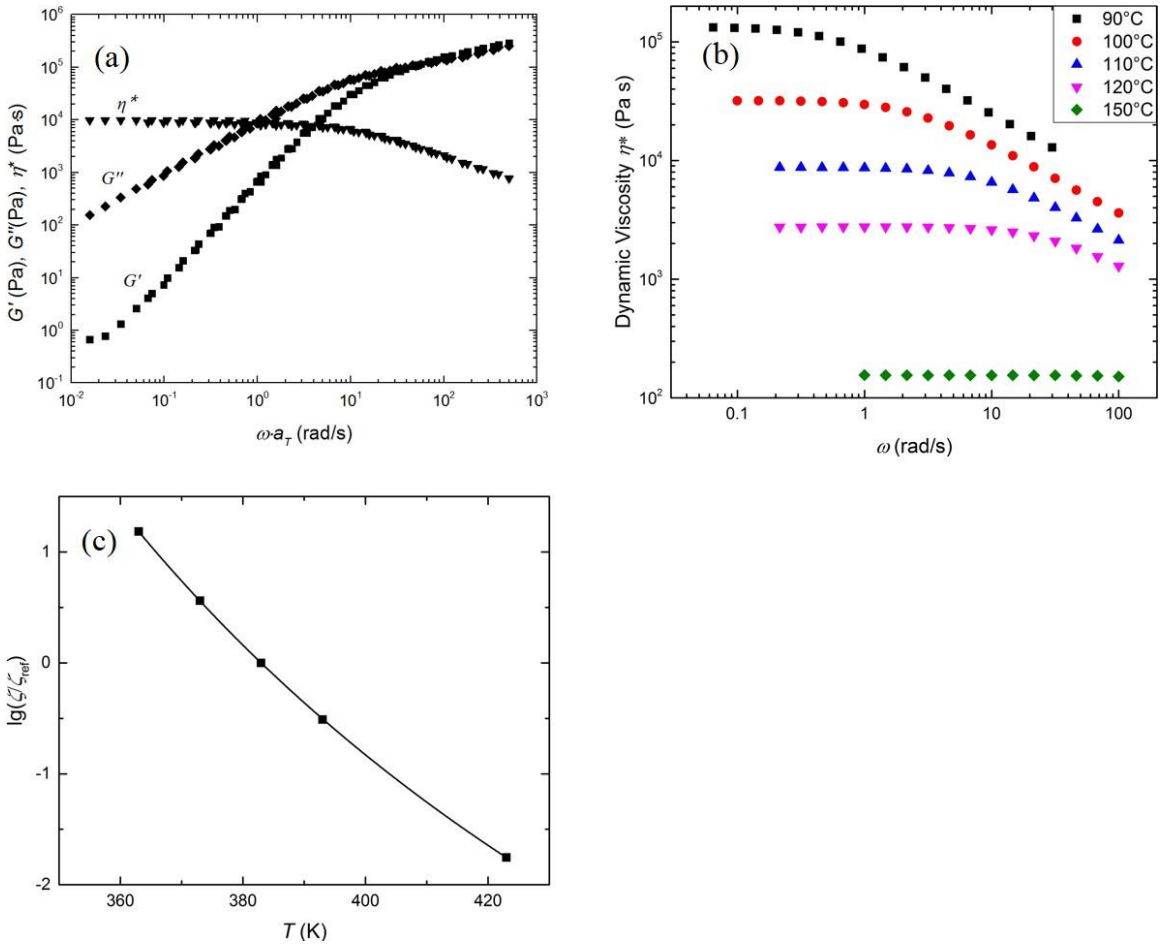

Figure A.6.1. (a) Storage modulus (G'), loss modulus (G''), and dynamic viscosity (η*) after time-temperature superposition, with T_{ref} = 383K. (b) Dynamic viscosity (η*) of PnBMA (45K) as a function of frequency at various temperatures. (c) The monomeric friction coefficient (ζ) relative to the one at reference temperature (ζ_{ref}) for PnBMA as a function of temperature. T_{ref} = 383 K, and the solid line is the best fit to WLF equation.

Table A.6.1. Zero-shear viscosity and monomeric friction coefficient of PnBMA (45K) at different temperatures.

T (K)	η_0 (Pa-s)	ζ (N-s/m)	ζ/ζ_{ref}
363	1.33×10^{5}	8.4×10^{-6}	1.5×10^{1}
373	3.19×10^{4}	2.0×10^{-6}	3.6
383	8.74×10^{3}	5.5×10^{-7}	1
393	2.76×10^{3}	1.7×10^{-7}	3.1×10^{-1}
423	1.55×10^{2}	9.7×10^{-9}	1.8×10^{-2}

A.7. Derivation of Energy Barrier from Flory-Huggins Theory

In Flory-Huggins theory, the free energy density of mixing (Δg_{mix}) between solvent (component 1) and polymer (component 2) can be written as

$$\frac{\Delta g_{mix}}{RT} = \frac{n_1 \ln \varphi_1}{v_1} + \frac{n_2 \ln \varphi_2}{v_2} + \frac{n_1 \varphi_2 \chi}{v_0} \tag{A.7.1}$$

where n and φ are the number of moles and volume fraction for the corresponding components. In this equation, v_1 and v_2 are the molar volumes of the solvent and the repeating unit of the polymer, while v_0 is the reference volume. In Flory-Huggins theory, the solvent is typically treated as a small molecule, with 1 repeating unit; however, when considering a more general case, we use N_1 and N_2 to represent the number of repeating units for the solvent and the polymer, respectively. For the reference volume v_0, we let $v_0 = v_2$ in the following calculations for consistency. Under such scenario, we have:

$$\varphi_1 = \frac{N_1 v_1 n_1}{N_1 v_1 n_1 + N_2 v_2 n_2} \tag{A.7.2}$$

$$\varphi_2 = \frac{N_2 v_2 n_2}{N_1 v_1 n_1 + N_2 v_2 n_2} \tag{A.7.3}$$

By taking partial derivatives with respect to n_1 and n_2 in eq. A.7.1, we obtain expressions for the chemical potential of solvent and polymer, respectively, as given in eqs. A.7.4 and A.7.5.

$$\mu_1 - \mu_1^{\,0} = \frac{\chi \varphi_2^{\,2}}{v_2} + \left(\frac{1}{v_1} - \frac{N_1 v_1}{N_2 v_2^{\,2}}\right)\varphi_2 + \frac{\ln \varphi_1}{v_1} \tag{A.7.4}$$

$$\mu_2 - \mu_2^{\,0} = \frac{\chi}{v_1}\frac{N_2}{N_1}\varphi_1^{\,2} + \left(\frac{1}{v_2} - \frac{N_2 v_2}{N_1 v_1^{\,2}}\right)\varphi_1 + \frac{\ln \varphi_2}{v_2} \tag{A.7.5}$$

Here we assume that the micelle solution is a two-phase system (*i.e.*, micelle cores and solvent) that is under equilibrium, and thus neglect the effect of the corona for simplicity; therefore, in order to achieve a polymer-rich (core) and a solvent-rich (solvent) phase

with composition not changing with time, the following coexistence conditions need to be met:

$$\frac{\chi\phi_2^{\,2}}{v_2}+(\frac{1}{v_1}-\frac{N_1v_1}{N_2v_2^{\,2}})\phi_2+\frac{\ln\phi_1}{v_1}=\frac{\chi\psi_2^{\,2}}{v_2}+(\frac{1}{v_1}-\frac{N_1v_1}{N_2v_2^{\,2}})\psi_2+\frac{\ln\psi_1}{v_1} \qquad \text{(A.7.6)}$$

$$\frac{\chi}{v_1}\frac{N_2}{N_1}\phi_1^{\,2}+(\frac{1}{v_2}-\frac{N_2v_2}{N_1v_1^{\,2}})\phi_1+\frac{\ln\phi_2}{v_2}=\frac{\chi}{v_1}\frac{N_2}{N_1}\psi_1^{\,2}+(\frac{1}{v_2}-\frac{N_2v_2}{N_1v_1^{\,2}})\psi_1+\frac{\ln\psi_2}{v_2} \qquad \text{(A.7.7)}$$

where $\phi_{1(2)}$ and $\psi_{1(2)}$ represent the volume fraction of solvent (polymer) in the solvent and the micelle core, respectively; we also have $\phi_2 = 1-\phi_1$, and $\psi_2 = 1 - \psi_1$.

From eq. A.7.7 we can obtain:

$$\frac{1}{v_2}(\ln\phi_2-\ln\psi_2)=\frac{\chi}{v_1}\frac{N_2}{N_1}(\psi_1^{\,2}-\phi_1^{\,2})+(\frac{1}{v_2}-\frac{N_2v_2}{N_1v_1^{\,2}})(\psi_1-\phi_1) \qquad \text{(A.7.8)}$$

Due to the strong asymmetry between the polymer and the solvent, the volume fraction of polymer in the solvent phase (ϕ_2) is always close to zero, while the volume fraction of solvent in the polymer phase (ψ_1) cannot be neglected (unless χ >> 1). Therefore, it is safe to let $\phi_1 = 1$ when χ is moderate, and thus we obtain:

$$\ln\phi_2-\ln\psi_2=\chi\frac{N_2v_2}{N_1v_1}(\psi_1^{\,2}-1)+(1-\frac{N_2v_2^{\,2}}{N_1v_1^{\,2}})(\psi_1-1) \qquad \text{(A.7.9)}$$

In the limit of χ >> 1, there is virtually no solvent in the core, thus ψ_1 = 0. For polymer/solvent system, N_2 >> N_1, thus $N_2v_2^2/N_1v_1^2$ >> 1 is valid in most cases. Therefore, eq. A.7.9 can be further simplified as

$$\ln\phi_2-\ln\psi_2=\ln(\frac{\phi_2}{\psi_2})\approx-\chi\frac{N_2v_2}{N_1v_1}+\frac{N_2v_2^{\,2}}{N_1v_1^{\,2}}=-\frac{N_2v_2}{N_1v_1}(\chi-\frac{v_2}{v_1}) \qquad \text{(A.7.10)}$$

and

$$\phi_2=\psi_2\exp[-\frac{N_2v_2}{N_1v_1}(\chi-\frac{v_2}{v_1})]=\psi_2\exp(-\frac{\Delta E}{RT}) \qquad \text{(A.7.11)}$$

This result is a Boltzmann distribution of the polymer in the solvent versus in the core, and the difference in probability of distribution is dictated by the difference in the energy, $\Delta E/RT$, which is essentially the "energy barrier". Therefore, neglecting the prefactor α, $f(\chi N) = (N_2 v_2/N_1 v_1)(\chi - v_2/v_1)$ should be a better substitute for χN in the limit of $\chi >> 1$. Specifically, when $N_2 = N$, $N_1 = 1$, and $v_2 = v_1$, this energy barrier term is essentially equal to $N(\chi - 1)$, as predicted by ref 19.

In fact, as long as we know the exact values of ϕ_2 and ψ_2, then the relationship of $\phi_2 = \psi_2 \exp[-f(\chi)(N_2/N_1)]$ can be used to calculate any $f(\chi)$ at a given χ. The only problem is that $f(\chi)$ may not have an analytical expression, because there is no analytical solution for ϕ_2 and ψ_2 in the context of Flory-Huggins theory. We hereafter assume $N_2/N_1 = 200$. In the PnBMA/IL system, the molar volumes for PnBMA, [EMIM][TFSI] and [BMIM][TFSI] are 133, 256 and 293 cm^3/mol, respectively. As v_1 is only weakly dependent on the solvent composition, we can use the molar volume of 20/80 (v/v) of [BMIM][TFSI]/[EMIM][TFSI] as v_1, then $v_2/v_1 = 0.50$. Based on eq. A.7.6 and A.7.7, the numerical solutions of ϕ_2 and ψ_2 can be determined, which can be used to calculate the value of $f(\chi)$. The result is shown in Figure A.7.1a.

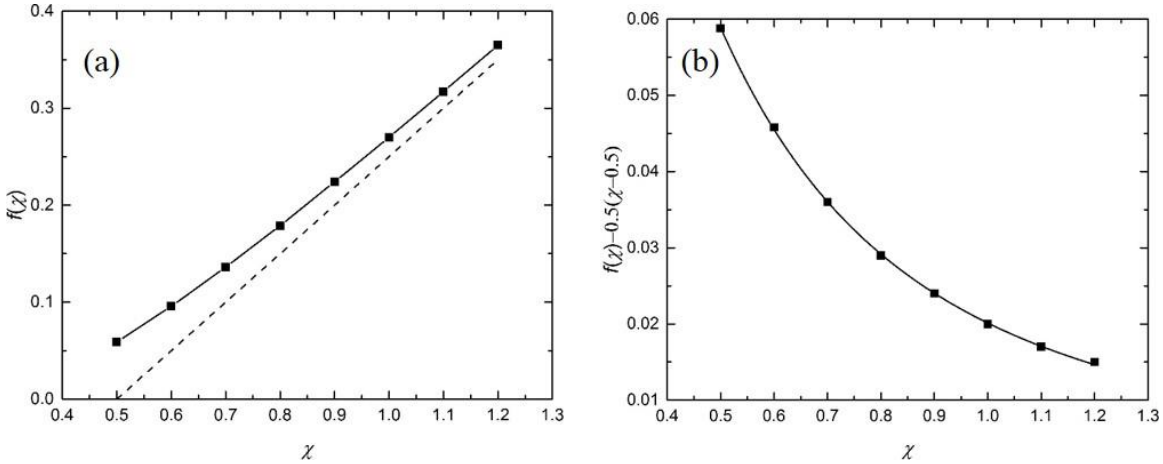

Figure A.7.1. (a) Numerical solution of $f(\chi)$ based on Flory-Huggins theory (the solid line is only for visual aid). The dashed line represents $f(\chi) = 0.5(\chi - 0.5)$, which is the asymptote to the solid line when χ approaches infinity. (b) $f(\chi) - 0.5(\chi - 0.5)$ as a function of χ. The solid line is best fit to eq. 6.4.

Then, the inverse of a polynomial $1/(a\chi^2+b\chi+c)$ is used as an offset function to fit $f(\chi) - 0.5(\chi - 0.5)$ in Figure A.7.1b, which shows reasonably good agreement with the data, with a = 38.8, b = 7.2 and c = 3.7. It will be interesting to assess whether this result can be used as an empirical $f(\chi)$ expression for other related energy barrier problems concerning block copolymer micelles.

References

(1) Elias, H.-G.; Bareiss, R.; Watterson, J. G. *Adv. Polym. Sci.* **1973**, *11*, 111-204.

(2) Tanaka, K.; Waki, H.; Ido, Y.; Akita, S.; Yoshida, Y.; Yoshida, T.; Matsuo, T. *Rapid Commun. Mass Spectrom.* **1988**, *2*, 151-153.

(3) Karas, M.; Bahr, U. *Trends in Analytical Chemistry* **1990**, *9*, 321-325.

(4) Schrepp, W.; Pasch, H. *MALDI-TOF Mass Spectrometry of Synthetic Polymers*, Springer-Verlag: Berlin Heidelberg, 2003.

(5) Knochenmuss, R. *Analyst* **2006**, *131*, 966-986.

(6) Nielen, M. W. F. *Mass Spectrom. Rev.* **1999**, *18*, 309-344.

(7) Hilker, B.; Clifford, K. J.; Sauter, A. D., Jr.; Sauter, A. D., III; Gauthier, T.; Harmon, J. P. *Polymer* **2009**, *50*, 1015-1024.

(8) Kavitha, A. A.; Singha, N. K. *Macromol. Chem. Phys.* **2009**, *210*, 1536-1543.

(9) Watanabe, T.; Nakanishi, K.; Ozawa, T.; Kawasaki, H.; Ute, K.; Arakawa, R. *Rapid Commun. Mass Spectrom.* **2010**, *24*, 1835-1841.

(10) Wyzgoski, F. J.; Polce, M. J.; Wesdemiotis, C.; Arnould, M. A. *J. Polym. Sci.: Part A* **2007**, *45*, 2161-2171.

(11) Nakamura, Y.; Kitada, Y.; Kobayashi, Y.; Ray, B.; Yamago, S. *Macromolecules* **2011**, *44*, 8388-8397.

(12) Karas, M.; Bachmann, D.; Bahr, U.; Hillenkamp, F. *Int. J. Mass Spectrom. Ion Proc.* **1987**, *78*, 53-68.

(13) Schnöll-Bitai, I.; Hrebicek, T.; Rizzi, A. *Macromol. Chem. Phys.* **2007**, *208*, 485-495.

(14) Schriemer, D. C.; Li, L. *Anal. Chem.* **1997**, *69*, 4169-4175.

(15) Lee, H.-N.; Lodge, T. P. *J. Phys. Chem. B* **2011**, *115*, 1971-1977.

(16) Castelletto, V.; Hamley, I. W.; Pedersen, J. S. *J. Chem. Phys.* **2002**, *117*, 8124-8129.

(17) Ferry, J. D. *Viscoelastic Properties of Polymers (3rd Ed)*, Wiley: New York, 1980; pp 328-343.

(18) Ferry, J. D.; Landel, R. F. *Kolloid-Zeitschrift* **1956**, 148, 1-6.

(19) Thiagarajan, R. Modeling of Diblock Copolymers in Selective Solvents. PhD Dissertation, University of Minnesota, 2012.